eman ta zabal zazu

Universidad del País Vasco
Euskal Herriko Unibertsitatea

PhD Thesis

Rare-Earth-Noble-Metal Surface Alloys and its Interaction with Phthalocyanine Molecules

Rodrigo Castrillo Bodero

Director:

Dr. Frederik M. Schiller

Codirector:

Dra. Laura Fernández Gómez-Recuero

Año 2023

1 Abstract

This first part of this thesis is focused on the search of novel low dimensional magnetic materials that consist on monolayers (MLs) of rare-earth (RE)/ Noble-Metal (NM) surface alloys, to be more precise RE-Au_2 and RE-Ag_2 monolayers (ML). The structure of the alloys has been investigated though low energy electron diffraction (LEED) and scanning tunneling microscopy (STM). It will be shown that the new alloys present $(\sqrt{3}\times\sqrt{3})R30°$ reconstructions with a Moiré structure. The electronic structure of the alloys has been studied through several forms of photoemission spectroscopy (PES). Resonant photoemission and X-ray photoemission has been used for determination of the valence state, while angle-resolved PES (ARPES) has been used for the study of the electronic structure near the Fermi level. It will be shown that the alloys share two types of electronic structure depending on the valence state of the RE. Finally, X-ray Magnetic Circular Dichroism (XMCD) has been used to study the magnetic behavior of the alloys, in special, the anisotropy, which is determined by the selected RE.

The second part of this thesis is dedicated to the study of the metal-organic interface formed by adsorption of monolayers of organic molecules on RE noble-metal surface alloys by thermal evaporation. The specific molecules that have been adsorbed are Copper Phthalocyanines (CuPc) and Lanthanide bis-phthalocyaninato ($TbPc_2$). The growth and structure of the molecular layers have been investigated by low energy electron diffraction (LEED) and scanning tunneling microscopy (STM) techniques. The CuPc layer reveals a well ordered growth that is commensurate with the substrate, while the molecule of $TbPc_2$ presents a different scenario with some variation depending on the substrate. ARPES measurements have been performed in order to detect possible modifications in the band structure of the surface alloys upon adsorption of the molecular adlayers. In this thesis it will be shown that the molecular adsorption of these molecules is mainly by physisorption, which leaves the electronic structure of the substrate and the molecule (mostly) unaffected. Finally, XMCD measurements have been used to study the magnetic coupling of the molecule to the $REAu_2$ substrates. It will be evidenced that the substrate can enhance the anisotropy of the molecule if there is a coincidence between both molecule and substrate easy-axis direction of anisotropy.

Contents

1 Abstract....2
2 Resumen....5
3 Introduction....9
3.1 State of the art....11
3.1.1 Two-dimensional magnetism....11
3.1.2 Lanthanide-Rare earth metals....12
3.1.3 $GdAu_2$ and $GdAg_2$....15
3.1.4 Magnetic Molecules and Molecules on Ferromagnets....17
3.1.4.1 CuPc molecule....18
3.1.4.2 $TbPc_2$ molecule....19
3.2 Magnetism at surfaces....20
3.2.1 Ferromagnetism....21
3.2.2 2D Models of ferromagnetism....23
3.2.3 Magnetic anisotropy....25
3.2.3.1 Magnetocrystalline anisotropy....26
3.2.4 Remagnetization models....28
3.2.4.1 Coherent rotation model....28
3.2.4.2 Domain wall movement model....29
3.2.5 Arrot plot analysis....31
4 Experimental Techniques and Sample preparation....33
4.1 Sample Preparation and Experimental Setup....34
4.2 Substrate preparation....34
4.2.1 Single crystal substrates....34
4.2.1.1 Surface compound preparations....35
4.2.2 Molecule evaporation....36
4.2.3 Machine specifications....37
4.3 Photoemission spectroscopy....39
4.3.1 General considerations of the photoemission process....43
4.3.2 X-ray photoemission spectroscopy....45
4.3.3 Angle-resolved photoemission spectroscopy....46
4.3.4 Light generation....48
4.4 Scanning tunneling microscopy....50
4.5 Low energy electron diffraction....53
4.6 X-ray absorption spectroscopy....56
4.6.1 X-ray magnetic circular dichroism....57
5 Two-dimensional Au based surface alloys....62
5.1 Structural analysis....62
5.1.1 Trivalent $REAu_2$ surface compounds....63
5.1.2 Divalent $REAu_2$ surface compounds....69
5.1.3 Summary of the known $REAu_2$ surface compound structures....72
5.2 Electronic structure of $REAu_2$ surface alloys....73
5.2.1 Trivalent valence state in $REAu_2$....75
5.2.1.1 Core level emissions....75

5.2.1.2 Valence band emissions/electronic band structure....79
5.2.2 Divalent valence state....82
5.2.2.1 $YbAu_2$....83
5.2.2.2 $EuAu_2$....85
5.3 Magnetism in $REAu_2$ surface alloys....88
5.3.1 $HoAu_2$....89
5.3.2 $DyAu_2$....93
5.3.3 $SmAu_2$....96
5.3.4 $EuAu_2$....99
6 Two-dimensional Ag based $REAg_2$ surface alloys....104
6.1 Structure of $REAg_2$ surface alloys....104
6.2 Electronic structure....110
6.2.1 Valence band structure in $REAg_2$....114
6.3 XMCD....121
6.3.1 $HoAg_2$....121
6.3.2 $SmAg_2$....125
7 Hybrid organometallic interfaces....130
7.1 CuPc/$REAu_2$ system....130
7.1.1 Structure analysis....130
7.1.2 Electronic structure....133
7.1.3 Magnetic properties....141
7.2 $TbPc_2$/$REAu_2$ system....148
7.2.1 Structure analysis....148
7.2.2 Electronic structure....153
7.2.3 Magnetic properties....155
7.2.3.1 $TbPc_2$/$HoAu_2$ system....155
7.2.3.2 $TbPc_2$/$EuAu_2$ system....157
7.2.3.3 $TbPc_2$/ $DyAu_2$ system....161
8 Conclusions....164
9 Bibiography....167

2 Resumen

En los últimos años, el desarrollo de la industria de semiconductores ha dejado de seguir la Ley Moore[1]. Esta ley empírica predecía que el número de transistores en un circuito integrado se doblaría cada dos años. La desviación de esta tendencia se ha producido debido al continuo aumento de la dificultad de reducir el tamaños de los transistores. En particular, resulta complicada la reducción de la longitud del canal de los transistores MOSFET (transistor de efecto de campo de metal-óxido-semiconductor) llegando a encontrar problemas tales como la incapacidad de conseguir un aislamiento adecuado de la puerta[2]. Para superar estas dificultades, se han propuesto varios métodos, como substituir el silicio por semiconductores de mayor movilidad como el $GaAs_2$[3] o usar materiales de baja dimensionalidad como el grafeno[4]. Otra opción que se ha considerado, es substituir la conducción de electrones por otro portadores, como excitaciones colectivas en plasmónica[5] u ondas de espín en magnónica[6]. Pero entre ellas, destaca la espintrónica, que se basa en el control de los espines y corrientes de espín de los electrones en vez de usar solamente la carga.

Un dispositivo espintrónico se basa en el uso de corrientes de espín polarizadas, es decir que toda la corriente tiene una única dirección de espín, y el uso de sistemas sensibles a esas polarizaciones de espín. Por ese motivo, es posible la utilización de dos polarizaciones de espín como canales diferentes para doblar la cantidad de información transmisible por un único cable. El método mas simple para generar una corriente de espín polarizada es hacer pasar una corriente eléctrica por un material ferromagnético, el cual presenta una conductividad diferente dependiendo de su dirección de magnetización. Si se pone otro material ferromagnético en serie, desacoplado pero lo suficientemente cerca para que no se pierda la polarización de espín, el dispositivo resultante mostrara una fuerte diferencia de conductividad dependiendo de si ambos materiales ferromagnéticos están magnetizados en la misma dirección o en opuestas. Este efecto se llama Magneto Resistencia Gigante (GMR)[7,8], y el dispositivo resultante es la válvula de espín, el cual representó el primer gran éxito de la espintrónica. A día de hoy, la sensibilidad y versatilidad de las válvulas de espín son la base de aplicaciones como discos duros, MRAMs (memoria no volátil magnetorresistiva), brújulas electrónicas, sensores magnéticos, etc.

La espintrónica ha empezado a promover el desarrollo de la electrónica, integrando la estabilidad y la capacidad de reescritura casi-infinita de la grabación magnética. Esto resulta prometedor para el desarrollo de la electrónica de bajo consumo, nuevas arquitecturas especializadas, e incluso computación no convencional (como la computación estocástica y computación cuántica), así como sistemas de detección y medidas más sensibles basadas en el magnetismo[9]. Para el desarrollo de todas estas ideas futuras, es necesario un mejor entendimiento de los sistemas magnéticos, y el desarrollo de nuevos materiales con propiedades a medida. Es más, esos materiales se tienen que poder llevar a la nanoescala, lo que introduce un nuevo desafío para el desarrollo de la espintrónica.

En este marco, las moléculas orgánicas semiconductoras ofrecen una alternativa prometedora para la creación de dispositivos spintronicos[10]. El uso de moléculas orgánicas ofrece nuevas características no existentes en materiales inorgánicos, como mayor sensibilidad a estímulos eléctricos o ópticos externos o funcionalidades físico-químicas intrínsecas[11–13]. Los dispositivos

espintrónicos moleculares se basan en la generación, transporte y detección de portadores con espín polarizado mediante la combinación de un material ferromagnético con un semiconductor orgánico. En estos sistemas la interfaz entre los distintos materiales gobierna la transferencia de carga y la conducción de espín entre el nivel de Fermi del metal y los orbitales moleculares, actuando como un filtro adicional de espín que solamente permite el paso de electrones de una determinada orientación de espín. Varios trabajos ya han mostrado las ventajas de una interfaz ferromagnético-semiconductor orgánico y su relevancia para la inyección de espín[14,15]. De este modo, el acoplo y enlaces químicos entre el semiconductor orgánico y el metal ferromagnético da lugar a nuevos estados electrónicos híbridos con polarización de espín frecuentemente llamados "spinterface". Estos nuevos estados híbridos determinan el transporte de carga entre el metal y los orbitales moleculares solo dejando pasar electrones con una dirección de espín determinada, y actuando por tanto como un filtro de espín.

Esta tesis se centra en el estudio de materiales ferromagnéticos bidimensionales. En concreto, en las aleaciones superficiales de Tierra Rara (RE) y Metal Noble (NM). Posteriormente, se enfoca en la absorción de moléculas orgánicas magnéticas sobre estas aleaciones y los efectos de su interacción con la aleación.

La primera parte de la tesis está dedicada al estudio de nuevas aleaciones superficiales de RE-NM usando como metal noble oro ($REAu_2$) y plata ($REAg_2$). Como caso modelo, se ha usado la aleación $GdAu_2$, que ya ha sido estudiada extensivamente antes del comienzo de esta Tesis. Para la preparación de las aleaciones ya comentadas se ha procedido a la evaporación de una pequeña cantidad (un tercio de capa atómica) del átomo de RE elegida sobre un substrato de Au(111) o Ag(111) previamente limpiado mediante bombardeo de iones y recocidos (Sputtering-Annealing). En concreto, se han preparado las aleaciones $SmAu_2$, $EuAu_2$, $GdAu_2$, $HoAu_2$, $DyAu_2$ e $YbAu_2$ con oro como substrato y $SmAg_2$, $GdAg_2$ y $HoAg_2$ con plata como substrato.

La estructura y orden atómico de estas aleaciones se ha estudiado con dos técnicas: Difracción de electrones de baja energía (LEED) y microscopía de efecto túnel (STM). Tomando como ejemplo el $GdAu_2$, la estructura que presenta una monocapa de esta aleación es una reconstrucción $(\sqrt{3}\times\sqrt{3})R30°$ respecto al substrato Au(111). Es decir, se substituye un átomo de cada 3 de oro por uno de gadolinio (Gd). Esta estructura se puede ver en STM como una red hexagonal de huecos (o protuberancias, dependiendo del voltaje, la corriente y punta usadas para medir) que corresponden a los átomos de Gd. Por otro lado, se debe destacar que debido al mayor tamaño atómico de la tierra rara respecto a los átomos de Au, la monocapa de $GdAu_2$ se encuentra tensionada, y la forma de minimizar la tensión es la formación de un patrón Moiré. En el resto de aleaciones en oro se ve un comportamiento similar, formándose la reconstrucción $(\sqrt{3}\times\sqrt{3})R30°$ y además el patrón de Moiré, con un par de excepciones que se comentarán posteriormente. Al ampliar la biblioteca de aleaciones conocidas se ha observado que cuando la RE es trivalente, se distinguen 2 tipos de reconstrucciones: una $(12\times11)R4°$ en las RE ligeras (números atómicos de 57 a 63) y una $(13\times13)R0°$ para las RE pesadas (números atómicos de 64 a 70). La estructura de reconstrucción+Moiré también aparece en $SmAg_2$ y $GdAg_2$. El caso de tierras raras divalentes es más complejo, ya que el aumento de tamaño atómico (cerca del 30%)

dificulta en gran medida la relajación de la superficie. En el caso de $YbAu_2$, la relajación a través del Moiré se hace posible, pero en caso del $EuAu_2$, la tensión es demasiado alta para la formación del Moiré y en su lugar se forma una red de vacantes. En el caso de $HoAg_2$ se ha identificado un crecimiento quasicristalino. Este crecimiento ha permitido explicar las estructuras presentes en $DyAg_2$, que han sido notificadas por otros grupos de investigación, así como las estructuras atómicas reportadas sobre un el crecimiento tensionado (a temperatura mas baja) de $GdAg_2$.

La estructura electrónica de estas aleaciones has sido estudiada mediante fotoemisión. En concreto con tres variantes específicas. Primero, se ha usado espectroscopia de fotoemisión resonante (Res-PES) y fotoemisión de rayos X (XPS) para la determinación del estado de valencia, en concreto, se ha confirmado que Eu e Yb presentan un estado divalente en las aleaciones, mientras que Sm presenta un estado principalmente trivalente, aunque siempre es visible una pequeña parte divalente. Esta parte puede indicar un estado de valencia mixta inherente o la presencia de una fase divalente mezclada (como clústeres no aleados). El resto de tierras raras han mostrado un estado trivalente. Estos dos estados de valencia se han visto reflejados en dos tipos de estructura electrónica compartidas por cada valencia para cada metal noble, que han sido estudiados mediante espectroscopia de fotoemisión resuelta en angulo (ARPES). La estructura electrónica de las aleaciones trivalentes (tanto las de oro como las de plata) han permitido explicar la fuerte anisotropía magnética del $GdAu_2$ previamente reportada, así como introducir un término necesario para entender el comportamiento del resto de aleaciones. Se mostrará que la estructura electrónica de las aleaciones divalentes se puede entender como un dopado con aceptores de la estructura de las trivalentes, ademas de añadir una hibridación con los orbitales f (responsables del magnetismo). Como se verá, esta hibridación es la responsable de la fuerte anisotropía de la aleación $EuAu_2$.

Finalmente, el dicroísmo circular magnético de rayos X (XMCD) se ha usado para estudiar la respuesta magnética de las aleaciones, y en especial para el estudio de la anisotropía magnética, que viene determinada por la tierra rara usada. Se mostrará que esta anisotropía, junto con la estructura atomica y estructura electrónica de las aleaciones condiciona la respuesta magnética de las aleaciones, llegando a inducir efectos inesperados como coercitividades muy elevadas cuando los diversos factores se combinan.

La segunda parte de esta tesis esta dedicada al estudio de las interfases metal-orgánicas formadas por la absorción de monocapas de moléculas orgánicas evaporadas termicamente sobre las superficies de $REAu_2$. Específicamente, se han usado las moleculas ftalocianina de cobre (CuPc) (disponible comercialmente) y bis-ftalocianinato de terbio ($TbPc_2$) (sintética). El $TbPc_2$ fue sintetizado por Dr. G. de la Torre (Universidad Autónoma de Madrid) que tiene una elevada experiencia en la síntesis de diversas ftalocianinas.

La molécula CuPc se ha depositado sobre las superficies $GdAu_2$, $HoAu_2$ e $YbAu_2$, mientras que el $TbPc_2$ se ha adsorbido sobre $EuAu_2$, $HoAu_2$ y $DyAu_2$. El crecimiento de las moléculas ha sido estudiando mediante LEED y STM. El CuPc muestra en todos los casos un crecimiento capa a capa conmensurado con el substrato, mientras que en el caso del $TbPc_2$ el comportamiento depende del substrato. Se han llevado a cabo medidas de ARPES y XPS para detectar los cambios en la

estructura de bandas de los substratos causados por la absorción de la capa de moléculas. Se ha visto que la absorción de las moléculas es debida fundamentalmente a fisisorción, no viéndose apenas afectada la estructura electrónica del substrato ni de la molécula. Finalmente el comportamiento y acoplo magnético de las moléculas al substrato se ha estudiado mediante XMCD. Se observa que la anisotropía de las moléculas puede ser aumentada por la deposición sobre un substrato que comparta el eje fácil. En el caso de CuPc, se ha detectado un acoplo antiferromagnético entre la molécula y substratos, mientras que en el caso de $TbPc_2$, se ha detectado un acoplo ferromagnético en el substrato divalente, mientras que no hay evidencias claras de acoplo con los substratos trivalentes. Finalmente, de ha detectado un ligero aumento de la temperatura de Curie del substrato $DyAu_2$ por la absorción de la molécula $TbPc_2$.

3 Introduction

In recent years, the development of semiconductor industry and electronics no longer follows the empirical prediction given by the Moore's law[1]. Moore anticipated in 1965 that the number of transistors in an integrated circuit would double every year and would continue to do so for the next 10 years. In 1975, he revised his observation to say that this trend would continue but with a lower speed, duplication only every two years. However, the complexity of semiconductor process technology has grown over the years, which has "slowed down" Moore's Law. This deviation has been caused mainly by the miniaturization process of the systems, which has induced limitations like the capability to achieve the appropriate gate shielding in ever smaller transistors[2]. In order to beat this limits, several methods have been proposed, such as substituting silicon for higher mobility semiconductors like GaAs[3] or using the promising 2D material from graphene-like family[4]. Another option is substituting the electric switching by different transport properties like plasmonics that deals with collective electron excitations[5], or magnonics, in which spin waves are used[6]. Among such different approach, spintronics stand out. In this technology, the manipulation of electric charge and current of conventional electronics is substituted by the control of spins and spin currents.

A spintronic device operates with polarized electrons, i.e., all of the electrons have the same spin value and with systems capable of being sensitive to such polarization. For this reason, a very simple spintronic device using spin-polarized electrons can allow the transmission of a pair of signals over a single channel, doubling the bandwidth of the device. The simplest method of achieving spin-polarized electrons is to pass a current through a ferromagnetic material, which filters the electrons uniformly. If another ferromagnetic material is in series, close enough that the electron don't have time to lose the spin polarization (even though it has to be decoupled from the first), a spin valve can be constructed. In addition, it was found that depending on the magnetization directions of the ferromagnets a huge change in the electric resistance of the junction was observed. This effect is called Giant MagnetoResistance (GMR)[7,8] and has been the first success of the field of spintronics. Nowadays, the sensitivity and versatility of the spin valves is the base for the magnetic sensing in applications like hard drives, magnetoresistive random-access memory (MRAM), electronic compasses, etc.

Spintronics is called upon to promote the development of electronics by integrating the non-volatility and infinite rewritability of magnetic recording. This will lead to low power electronics, new architectures and unconventional computing methods (like stochastic computing and quantum computing) and more reliable and precise magnetic sensing[9]. For the development of all these future ideas, a better understanding of magnetic systems is required, and moreover, a further implementation of new materials with tailored properties. Furthermore, these materials have to be brought down to the nanoscale, which introduces a new challenge for the development of spintronics.

In this context, organic semiconducting molecules offer a cheap and promising alternative for the creation of spintronic based devices[10]. The use of organic molecules gives novel qualities not found

in inorganic materials due to their really unique characteristics, such as strong sensitivity to external electrical or optical stimuli and inherent physical and chemical functionality[11–13]. Molecular spintronic devices are based on the generation, transport and detection of spin polarized carriers by the combination of a ferromagnetic material with an organic semiconductor. In these systems, the interface governs the tunneling of spin and charge transfer between the Fermi level of the metal and the molecular orbitals, acting further as a spin-filter that preferentially transports electrons of a certain spin orientation. Several works have pointed out the advantages of a ferromagnetic-organic semiconductor interface and its relevance in the spin-injection[14,15]. Thus, the coupling and chemical bonds between the organic semiconductor and the ferromagnetic metal at the interface gives rise to new spin polarized hybrid electronics states. Such an interface is frequently called “spinterface”. The new spin polarized hybrid states govern the tunneling of spin and charge transfer between the Fermi level of the metal and the molecular orbitals and act as a further spin-filter that preferentially transports electrons of a certain spin orientation.

In this thesis, we have focused on the search of novel low dimensional magnetic materials that consist on monolayers (MLs) of rare-earth (RE)/Noble-Metal (NM) surface alloys, to be more precise RE-Au_2 and RE-Ag_2 monolayers (ML). In a next step, MLs of planar organic molecules have been adsorbed on top of these RE/NM surfaces in order to design metal-organic interfaces with spin order. The magnetic and electronic properties of these interfaces have been investigated analyzing the influence of the RE atoms of the substrate in the electronic and magnetic properties of the metal-organic interface.

The first part of this thesis is dedicated to the study of the RE-Au_2 and RE-Ag_2 ML systems. In a first step, the monoatomic thick RE-Au_2 and RE-Ag_2 surface alloys has been grown by electron beam evaporation of small amounts of RE atoms onto clean monocrystalline metal substrates, namely Au(111) and Ag(111). For this task, several RE atoms have been employed: Sm, Eu, Gd, Ho, Dy and Yb. The well known surface alloy of $GdAu_2$ has been taken as model case for the other alloys, because $GdAu_2$ has been extensively studied prior to this PhD thesis[16–18]. The structure of the alloys has been investigated though low energy electron diffraction (LEED) and scanning tunneling microscopy (STM). In this thesis, it will be shown that the new alloys present $(\sqrt{3}\times\sqrt{3})R30°$ reconstructions with a Moiré structure. Typically, one ML of these alloys is characterized by a highly regular Moiré superstructure with a period of about 3.5 nm. This Moiré pattern is determined by the atomic size of the RE atom. It is worth to note, that there are also some exceptions. These are the cases of $HoAg_2$ and $DyAg_2$ ML, which shows a structure that can not relax by the formation of the Moiré superstructure and therefore develops a quasi-periodic lattice of dislocation lines. The mentioned $DyAu_2$ case was investigated in Jülich some years ago[19]. The other notable exception is $EuAu_2$ ML where due to the larger ionic radius of the Eu, the Moiré superstructure is highly distorted.

The electronic structure of the alloys has been studied through photoemission spectroscopy (PES). With the help of a special form of PES, resonant photoemission spectroscopy, it will be shown that the alloys can be classified in two groups depending on the valence of the RE atoms: trivalent and divalent RE compounds. It will be visualized by angle resolved photoemission (ARPES) that the surface alloys with trivalent RE atoms share the same electronic structure near the Fermi level,

while on the divalent structures, this electronic structure is displaced due to the lack of one valence electron. Furthermore, hybridization of the RE 4f levels with the valence band is detected. As a result, the electronic structure adds an important contribution to the magnetic anisotropy of the system. Finally, X-ray Magnetic Circular Dichroism (XMCD) has been used to study the magnetic behavior of the alloys, in special, the anisotropy, which is determined by the selected RE.

The second part of this thesis is dedicated to the study of the metal-organic interface formed by adsorption of monolayers of organic molecules on RE noble surfaces by thermal evaporation. The specific molecules that have been adsorbed are Copper Phthalocyanines (CuPc) (commercially-available) and Lanthanide bis-phthalocyaninato ($TbPc_2$) (synthesized molecule). The $TbPc_2$ molecules were synthesized by Dr. G. de la Torre (Universidad Autónoma de Madrid).

CuPc has been deposited on $GdAu_2$, $HoAu_2$ and $YbAu_2$ surfaces. On the other hand, the growth of $TbPc_2$ was investigated on $EuAu_2$, $HoAu_2$ and $DyAu_2$. The growth and structure of the molecular layers have been investigated by both LEED and STM techniques. The CuPc layer reveals a well ordered growth that is commensurate with the substrate, while the molecule of $TbPc_2$ presents a different scenario with further variation depending on the substrate. ARPES measurements have been performed in order to detect possible modifications in the band structure of the surface alloys upon adsorption of the molecular adlayers. In this thesis it will be shown that the molecular adsorption of these molecules is mainly by physisorption, which leaves the electronic structure of the substrate and the molecule (mostly) unaffected. Finally, XMCD measurements have been used to study the magnetic coupling of the molecule to the $REAu_2$ substrates. It will be evidenced that the substrate can enhance the anisotropy of the molecule if there is a coincidence between both molecule and substrate easy-axis directions of anisotropy. In the case of $TbPc_2$, different interactions with the surface compounds are observed depending on the RE atom. The greatest effect in the modification of the XMCD magnetization loops is found in the system $TbPc_2/EuAu_2$, in which the magnetization of Tb couples ferromagnetically to the magnetization of Eu.

3.1 State of the art

3.1.1 Two-dimensional magnetism

Ferromagnetism in two-dimensional (2D) materials is not a new phenomena, against what it is usually claimed[20,21]. The first model of 2D ferromagnetism was proposed by Ernst Ising and Wilhelm Lenz in 1925 considering uniaxial magnetization[22]. In 1944 Lars Onsager showed that the 2D Ising model allows a ferromagnetic phase at finite temperature and gave and expression for the Curie temperature of his model[23]. Later, David Mermin and Herbert Wagner probed in 1966 that the 2D ferromagnetism is not possible in the absence of magnetic anisotropy[24]. However, years later in 1988, it was shown that an arbitrary small anisotropy is enough to allow a ferromagnetic order[25]. We should remark that up to that moment, the anisotropy in the models was considered uniaxial. In 1973, it was proven by J.M. Kosterlit and D.J. Thouless that an order-disorder transition is possible with the spins confined in the in-plane (IP) direction[26]. In any case, from all these investigations we see that the magnetic anisotropy is key for the development and engineering of 2D ferromagnetic materials.

From an experimental point of view, the 2D ferromagnetism suffered an initial delay due to the technical difficulty of obtaining 2D samples. First results were the quasi-2D ferromagnets that were formed from bulk materials of weakly coupled layers of 2D ferromagnets. The first example of this materials was K_2NiF_4, discovered in 1962[27]. After this first discovery, other materials were found giving rise to a sizable collection of different quasi-2D materials that have shown ferromagnetic or antiferromagnetic behaviors. Here, one should also mention the recent boom in new 2D van-der-Waals structures that can be prepared similar to graphene with Scotch® tape methods. Such materials include CrI_3 or Fe_xGeTe[20,21].This has lead to a renaissance of the field with an ever increasing library of 2D ferromagnets. However, the manipulation of the magnetic anisotropy in this field is still unexplored.

Thin ferromagnetic films (few nm of thickness) have also been extensively studied. These studies have allowed the discovery of the surface magnetic anisotropy, which dominates the magnetic behavior of thin films[28,29]. At the surface of these thin films, the crystalline symmetry of the material is broken and we will find reduced symmetry, lower coordination numbers and the presence of localized near-surface and interface states. These surface changes may modify the magnetocrystalline anisotropy. This effect is usually treated in theory by the introduction of a term that is called the surface magnetic anisotropy[30]. Additionally, the structural strain due to the growth of a thin film on a different substrate can further influence the magnetic anisotropy of the film itself. This means that in very thin films the surface magnetic anisotropy dominates the behavior of the whole layer. Finally, the structural strain due to the growth on a determined substrates can further change the magnetic anisotropy of the layer.

The developments in Ultra-High Vacuum (UHV) techniques made possible the evaporation of clean ultrathin films of few atomic layers. First results showed ferromagnetism in the transition metal ferromagnets (Fe,Ni) below two layer thickness[31,32]. There were also reports of ferromagnetism down to the ML limit, but the structure of the film being a single atomic layer was not addressed. Progress in this area included the report about the ferromagnetic $GdAu_2$ and $GdAg_2$ surface alloys with a clear in-plane (IP) anisotropy and Curie temperatures of 19 and 85 K, respectively[17]. The last investigations lead to the basis of the first part of this thesis, the investigations of other RE-noble metal systems with new magnetic properties.

3.1.2 Lanthanide-Rare earth metals

Lanthanide elements are a total of 15 elements with atomic numbers from 57 to 71 (La to Lu). They are called lanthanides because they appear after Lanthanum (La). They are also known as rare earths (REs). With the exception of Ce, which can exhibit tetravalent valency ($[Xe]4f^0(5d6s)^4$, lanthanide atoms can be found in two different electronic configurations: divalent or 2+ ($[Xe]4f^n(5d6s)^2$) and trivalent or 3+ ($[Xe]4f^{n-1}(5d6s)^3$) configurations. In these materials the 4f shell is successively filled by electrons, leaving the chemical properties unchanged. This implies that the RE can be substituted in the formation of compounds without further altering the material's chemistry, as long as the substituting RE shares the same valency.

Lanthanide ions have magnetic properties that are dramatically dominated by the intrinsic nature of

the 4f orbitals. The 4f wavefunctions have their highest probability of stay inside the outer three valence electrons[33] (see Figure 1). Thus, they do not directly participate in the bonding with other elements when forming a compound. Still, the 4f levels can hybridize (or mix) with the valence electrons and affect the transport and chemical properties of the RE. Due to this isolation, the RE metals follow with a reasonable precision the Hund's rules[34] for isolated atoms. Therefore, the spin and orbital momentum can be obtained as a function of the 4f filling as shown in Figure 2 and Table 1. This partial filling of the 4f orbital confers them a high magnetic moment. Even more important than the high magnetic moment is the strong spin orbit coupling (LS coupling) of the 4f electrons. Furthermore, lanthanides are characterized by an unquenched spin and orbital angular momentum and an effective LS coupling that gives rise to their strong single ion-anisotropy (with the exception of Eu^{2+}, Gd^{3+} ($4f^7$ configuration with half filled shell) and Yb^{2+}, Lu^{3+} ($4f^{14}$, completely filled). This translates in high magnetic anisotropy that is fundamental in the design of high coercive materials. Examples of such materials are the classical magnets $SmCo_5$ and NdFeB[35,36]. The high coercivity is also necessary in spintronics to achieve bistability in data storage[37]. Furthermore, the high magnetic anisotropy induced by RE atoms is necessary in order to obtain low dimensional ordered magnetism.

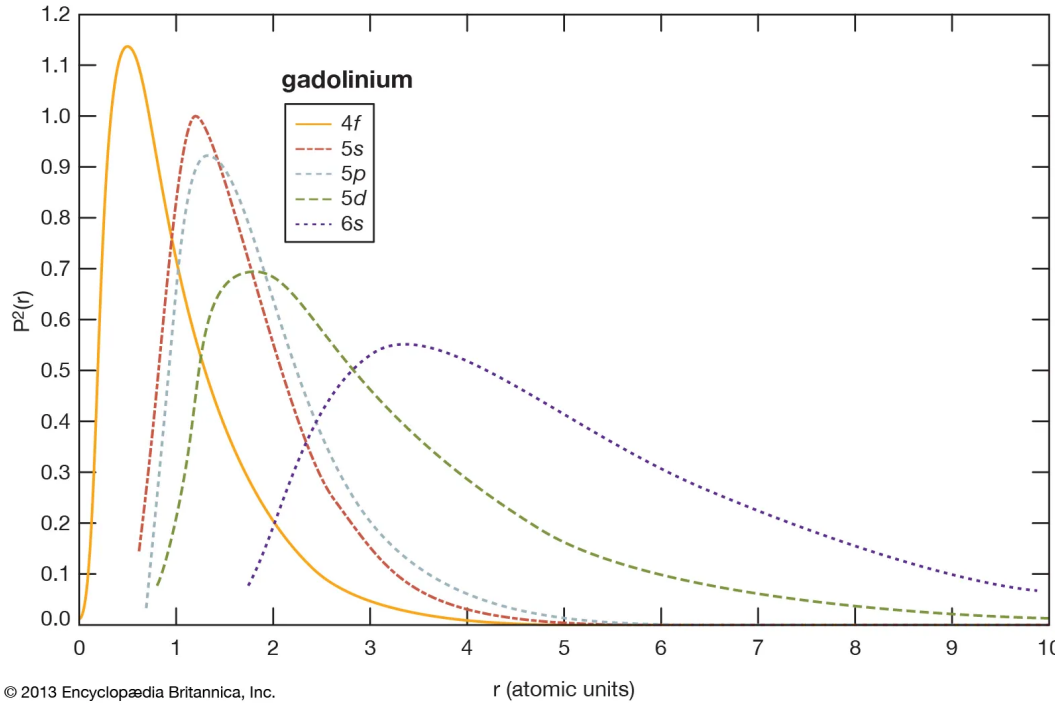

Figure 1: Radial distribution function of 4f, 5s, 5p, 5d and 6s electrons for rare earth metals, here for Gadolinium (Gd). Reproduced from ref.[33]. One observes that the 4f wavefunction is very localized therefore will not participate in chemical bonding.

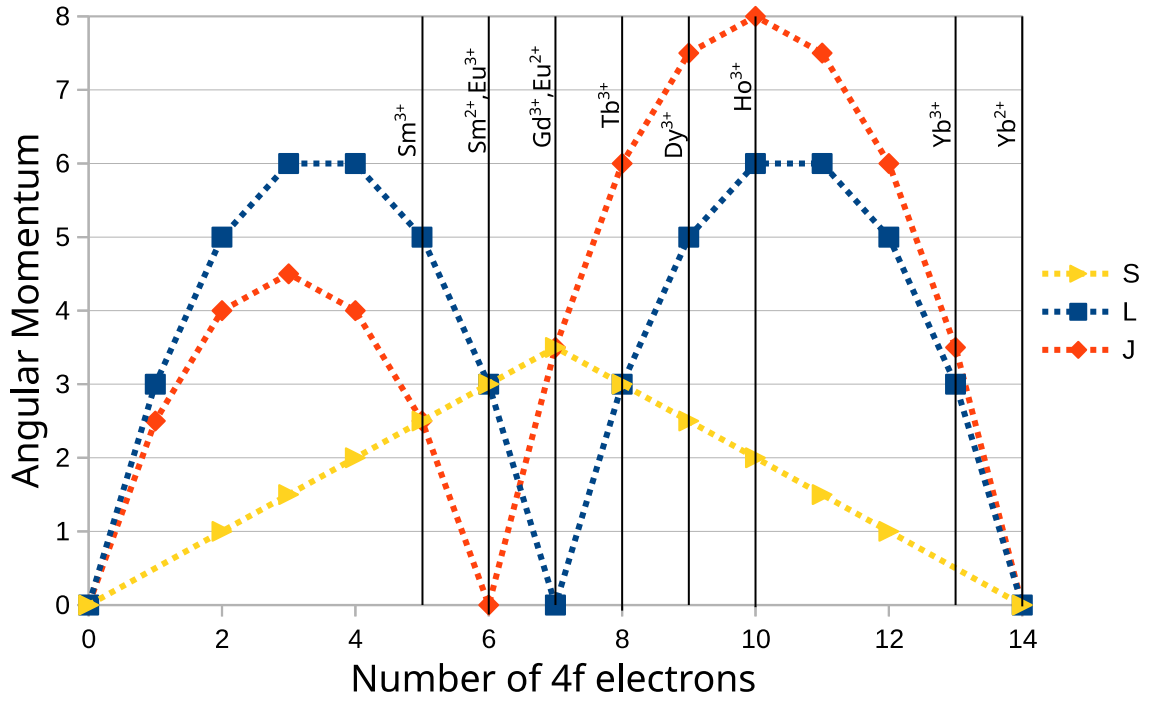

Figure 2: Spin S, orbital L, and total magnetic momentum J calculated through Hund rules for selected RE.

In this PhD thesis, Samarium (Sm), Europium (Eu), Gadolinium (Gd), Holmium (Ho), Dysprosium (Dy) and Ytterbium (Yb) have been used to form RE-Au_2 and RE-Ag_2 surface alloys. For these alloys the structure, electronic and magnetic properties of the materials have been studied. Additionally, the Terbium (Tb) ion has been also studied, as part of the $TbPc_2$ molecule. Some of the RE may be present in different valence states, and in some cases mixed valence states. Many of the magnetic properties of their compounds depends on the valence state. Gd, Ho, Dy and Tb are trivalent (+3) in (almost) all stable known compounds. Typically, Gd in metallic state is ferromagnetic at room temperature, while Dy and Ho show a complex phase diagram including exotic orders like helimagnetism[38,39]. Tb trivalent state confers the $TbPc_2$ molecule high magnetic moment and anisotropy (see section 3.1.4.2). Sm can present a mixed state of divalent (+2) or trivalent (+3) valence states. The most clear example is the Sm metal, where Sm atoms at the surface are divalent but trivalent in the bulk[40]. The divalent component presents a resultant magnetic moment equal to zero, thus Sm^{2+} it is non magnetic, while the trivalent Sm^{3+} shows an unusual small magnetic moment due to the almost compensation of spin and orbital moments. The Eu ion also presents both divalent and trivalent mixed valence states in its compounds. The trivalent configuration results in the loss of magnetic moment, while the divalent configuration reveals a magnetic moment without orbital moment (only spin). An example for the latter is the EuO ferromagnetic insulator[41]. Finally, the Yb ion is a further exception of the typical 4f filling, displaying in most cases a divalent state, in which the f-shell is completely filled, even though in some cases it can also be trivalent (see Table 1). Therefore, the Yb^{2+} ion is the only of these materials that does not present a magnetic response. In metallic state, Yb compounds reveal weak

Pauli paramagnetism.

Table 1: Spin S, orbital L, and total magnetic momentum J calculated through Hund rules for selected RE. Adapted from ref. [42].

Element	Filling	Spectroscopic term	S	L	J	$g\cdot\sqrt{J\cdot(J+1)}$
Sm^{3+}	$4f^5$	$^6H_{5/2}$	5/2	5	5/2	0.84
Sm^{2+}	$4f^6$	$^7F_0$	3	3	0	0
Eu^{3+}	$4f^6$	$^7F_0$	3	3	0	0
Eu^{2+}	$4f^7$	$^8S_{7/2}$	7/2	0	7/2	7.94
Gd^{3+}	$4f^7$	$^8S_{7/2}$	7/2	0	7/2	7.94
Dy^{3+}	$4f^9$	$^6H_{15/2}$	5/2	5	15/2	10.63
Ho^{3+}	$4f^{10}$	$^5I_8$	2	6	8	10.60
Yb^{3+}	$4f^{13}$	$^7F_{7/2}$	1/2	3	7/2	4.54
Yb^{2+}	$4f^{14}$	$^1S_0$	0	0	0	0

3.1.3 $GdAu_2$ and $GdAg_2$

In this section we will start with a brief introduction to the structural and magnetic characteristics of the family of the surface alloys RE-NM_2. $GdAu_2$ is the first case of this family of alloys[16]. It initially attracted attention because of the regular Moiré modulation and the ferromagnetic behavior that displayed a strong IP anisotropy and a Curie temperature of 19 K, in spite of being a ML[43].

This Moiré modulation resulted of interest as nanopattern for the growth of ordered arrays of Co dots[44,45] and the enhancement of their anisotropy due to antiferromagnetic coupling to the $GdAu_2$ substrate. Further works introduced the $LaAu_2$, $CeAu_2$, $GdAg_2$ and $GdCu_2$ alloys[46–48]. A bit later, an independent work on the intercalation of Eu below a graphene layer grown on a niquel surface reported ferromagnetic behavior of a $(\sqrt{3}\times\sqrt{3})R30°$ phase[49]. Nevertheless, its structure and magnetic properties were not fully addressed. In 2016 our group published a work stating that the $GdAg_2$ surface alloy presents surprising high Curie temperature of 85 K [17] for a ML (2D system), and its magnetic behavior was compared with the one of the $GdAu_2$ ML, as can be seen in Figure 3. Still, even though the article showed the strong IP easy axis of $GdAu_2$ monolayers, the source of this anisotropy was not addressed in this work. Only recently we have addressed the source of the in-plane easy axis of anisotropy of $GdAu_2$[50] and proved that it is caused by the “sd” valence states (as will be shown in section 5.2.1.2). Further works have experimentally demonstrated that the alloys presents domain structure[18] in a similar way as a 3D ferromagnet. Last, our group also has shown a soft modification of the Curie temperature of $GdAu_2$ due to adsorption of molecules on top of the surface compound[51]. $GdAg_2$ has also been studied because its electronic structure reveals possible topological features[52].

In both $GdAg_2$ and $GdAu_2$, the magnetic coupling between RE atoms was attributed to a RKKY exchange mechanism. The higher Curie temperature T_C in $GdAg_2$ compared to $GdAu_2$ was justified by an increased density of states (DOS) in the case of $GdAg_2$ at the Fermi level. In both cases, the materials are extremely soft ferromagnets, with coercive fields of about 0.2mT for $GdAu_2$ and 0.1 mT for $GdAg_2$ in the IP direction according to MOKE[17] measurements shown in Figure 3.

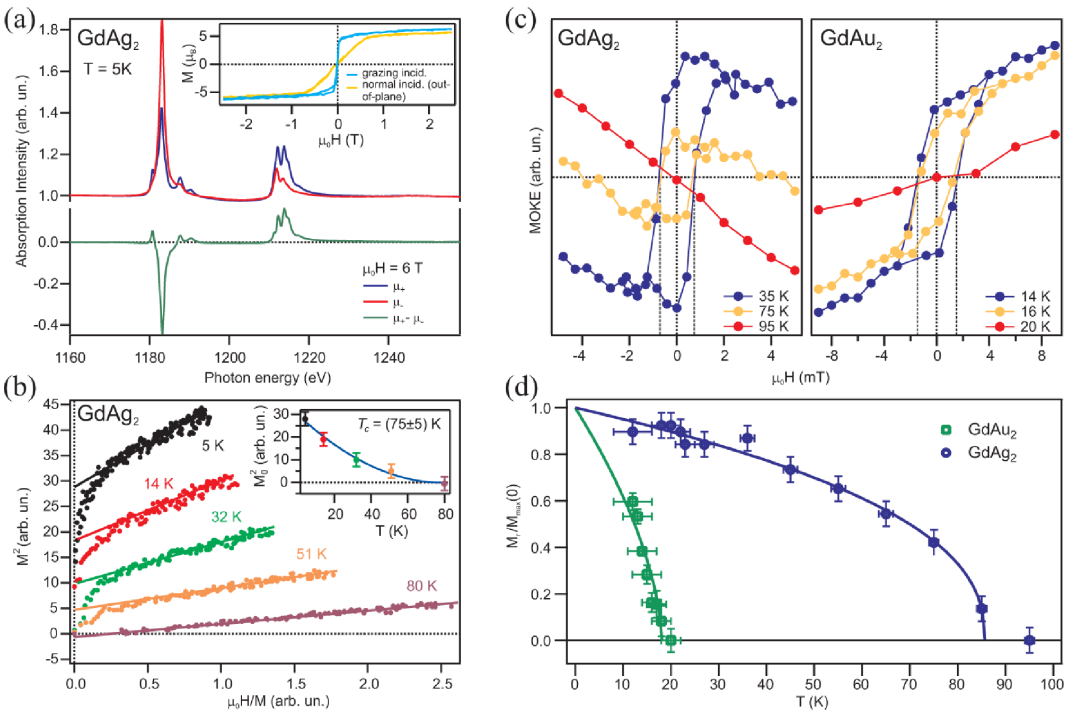

Figure 3: Ferromagnetic transition in $GdAg_2$ and $GdAu_2$: (a) X-ray absorption spectra (normal incidence) of a $GdAg_2$ monolayer taken at T = 5K and μ_0H = 6T, at the Gd $M_{4,5}$ edge with light of different helicity (top), and the resulting X-ray magnetic circular dichroism (XMCD) difference spectrum (bottom). Inset: magnetization curve obtained from the M_5 absorption peak recorded as a function of the applied field. (b) Arrot plot analysis derived from the out-of-plane XMCD hysteresis loops at different temperatures. (c) Magneto-optical Kerr effect (MOKE) loops for $GdAg_2$ and $GdAu_2$ recorded at several temperatures. (d) Remanent magnetization at zero applied field, as derived from the MOKE loops. The exponential fit of the data intersects the horizontal axis at the respective Curie temperatures for $GdAu_2$ T_C = (19±5) K and $GdAg_2$ T_C = (85±6) K, respectively. Reproduced from [17].

$GdAu_2$ and $GdAg_2$ are prepared by the evaporation of small amounts of Gd on Au and Ag surfaces, respectively. Only the atoms of the substrate metal (Au, Ag) that are located at the surface participate in the formation of the surface compound. The resulting surface compound typically displays 1ML of thickness and a Moiré reconstruction, as commented above. This surface compound is formed by substituting one out of 3 atoms of the noble metal by a Gd atom, forming a $(\sqrt{3}\times\sqrt{3})R30°$ reconstruction. Furthermore, in order to accommodate the higher atomic radii of the Gd atoms, a reconstruction of the surface forming a Moiré pattern takes place[53]. This Moiré lattice is detected in STM images as a topographical modulation that appears as higher and lower

areas periodically distributed with a hexagonal arrangement, as can be observed in the STM image of Figure 4. This image presents the typical situation of $REAu_2$, here the 1ML of $SmAu_2$ studied in our group [54] that is identical to the $GdAu_2$ case. This alloy and Moiré formation is also detected by LEED measurements (Figure 4). There, one observes new intense spots that correspond to the periodicity of the $REAu_2$ compound, namely a $(\sqrt{3}\times\sqrt{3})R30°$ structure (marked in red) and the Moiré pattern that can be seen as a hexagonal corona of secondary spots that appear around the main spots of the surface compound (marked in yellow).

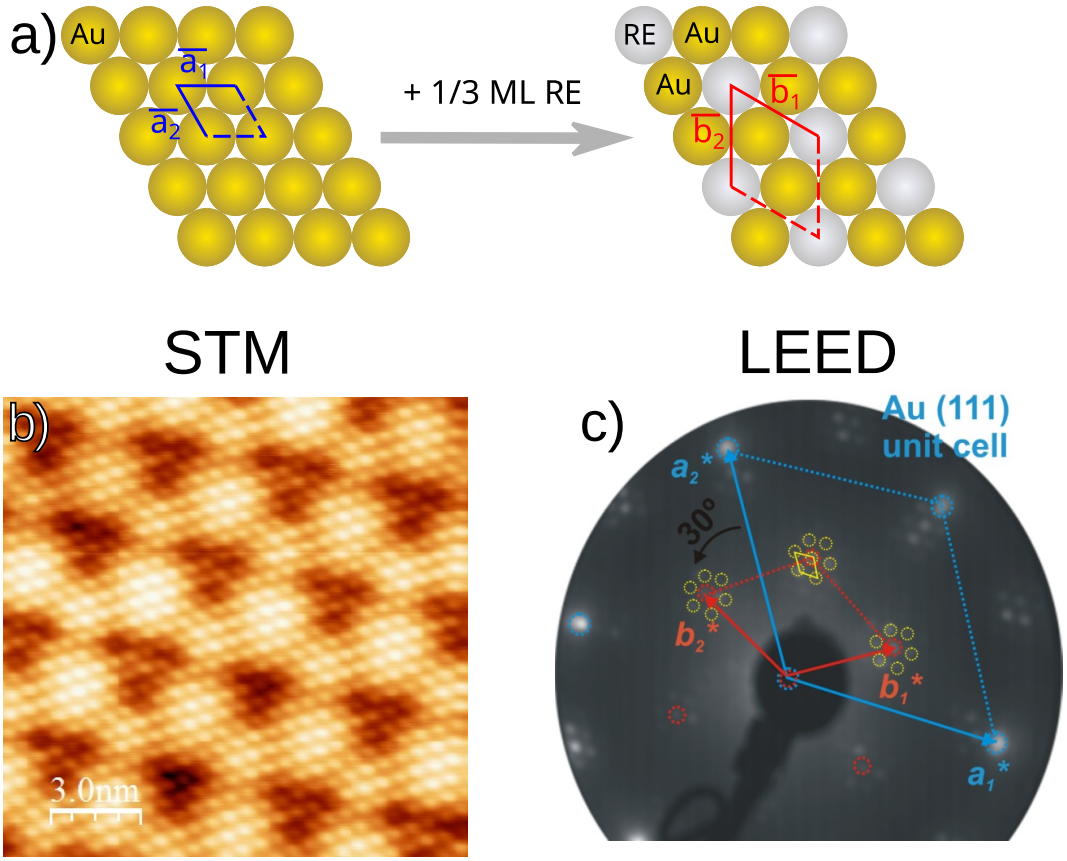

Figure 4: Structure of the RE-NM_2 surface compounds: a) Model of atomic organization prior and after RE deposition. b) STM image of $SmAu_2$ showing the long-range Moiré formation as depressions. The RE atoms are seen as short-range protrusions. c) LEED Pattern of $SmAu_2$. The Au(111) unit cell is marked in blue, the alloy unit cell is marked in red, and the Moiré reconstruction is marked in yellow. Adapted from [54].

3.1.4 Magnetic Molecules and Molecules on Ferromagnets

As it was commented above, the need to develop new electronics beyond silicon has increased attention to spintronics and hence to the development of new materials able to store the spin state of electrons and that make its manipulation possible. In terms of material, one limitation is the demanded size reduction, which affects the behavior of conventional ferromagnetic materials, loosing their hysteresis and leading to a superparamagnetic behavior[55]. Moreover, it is difficult to

modify this class of material in a predictable manner, usually consisting in substitution of magnetic atoms, resulting in completely change of the properties, often accompanied by losing the magnetic order.

An alternative to these problems is the organic-spintronics[56–58], which makes use of magnetic organic molecules. The great advantage of using organic molecules is that they can be custom-designed in the laboratory. Thus, their properties can be further tuned as needed by incorporating magnetic ions or radicals into their structure.

The contact point of the two types of materials, or as it will be called from this point on, the interface, is a necessary part in the application of any material, whether it is needed only as a support structure or to exploit its properties. It should be pointed out that in all cases the interface affects the material properties, although in many macroscopic cases where the relative volume affected is a minor part, it can be neglected. At the nanoscale, however, interfaces can no longer be neglected, since the volume affected by the interface is the major part of the system. In this work we are studying systems formed by the adsorption of organic molecules on metallic ferromagnets, i.e., this implies that we will focus on interfaces. Depending on the interaction established between the ferromagnet and the molecule we have different scenarios. A strong electron interaction with hybridization of the states of the organic molecules with the metal will produce a new set of spin polarized states. Example of this interaction are 3d transition metal centered phthalocyanines (M-Pc) on 3d transition metal ferromagnets like Ni or Co[59–61], Alq_3 molecules on cobalt[62] as well as C_{60} on 3d metal surfaces that are not ferromagnetic (Mn, Cu) but such surfaces become ferromagnetic after molecular adsorption[63,64]. In the case of a weak interaction, the interface effects will be dominated by Van der Waals forces, causing only a slight perturbation of the molecule and metal states. This type on interaction is usually referred as physisorption.

Two molecules have been used throughout this thesis, both from the Phthalocyanine (Pc) family: Copper Phthalocyanine (CuPc) and terbium(III) bis(phthalocyaninato) ($TbPc_2$). In the following, their basic properties will be addressed.

3.1.4.1 CuPc molecule

Copper Phthalocyanine (CuPc) is one of the most studied organic semiconductor. It is characterized by its chemical stability and it has been considered of interest in optoelectronics[65–68] and spintronics[59,69,70]. It is a 3d-metal centered phthalocyanine with a square planar four fold-symmetry (D_{4h}) that incorporate a Cu atom as the center of the organic ligand, as it is seen in Figure 5a). In general, in the isolated transition metal phthalocyanines the D_{4h} symmetry group transforms the degenerate 3d metal orbitals in three singlet states b_{2g} (d_{xy}), b_{1g} ($d_{x^2-y^2}$), a_{1g} (d_{z^2}), and one doublet state e_g ($d_{xz}, d_{yz}=d_{\pi}$)[71]. Depending on their energy positions, these orbitals mix to a different degree with the *2p* states of the C and N atoms of the molecular frame. In the case of CuPc, its peculiarity is that the Cu-derived outer level b_{1g} ($d_{x^2-y^2}$) is occupied by one electron, and positioned in the gap between the Pc highest occupied (HOMO) and lowest unoccupied molecular levels (LUMO). For this reason, the CuPc molecule is a model system with spin ½ and a

single d hole[72]. Upon adsorption of a CuPc monolayer on a metallic surface its spin ½ remains, contrary to other 3d-metal phthalocyanines, in which the magnetic moment is screened or lost upon surface adsorption[73–76]. The robustness of the magnetism in CuPc monolayers adsorbed on surfaces is explained by the planar symmetry of the b_{1g} singlet state, which couples weakly to the metal electrons. Moreover, this molecule is characterized by a strong anisotropy with an easy axis perpendicular to the molecular plane[77]. Several works have already reported a flat lying adsorption and a highly ordered growth on simple metal surfaces. In all these cases a ML of CuPc reveals an out-of-plane (OOP) magnetic easy axis with a large anisotropy[77,78]. These results point the interest of CuPc molecules for molecular spintronics, taking into account the robustness of its magnetic moment.

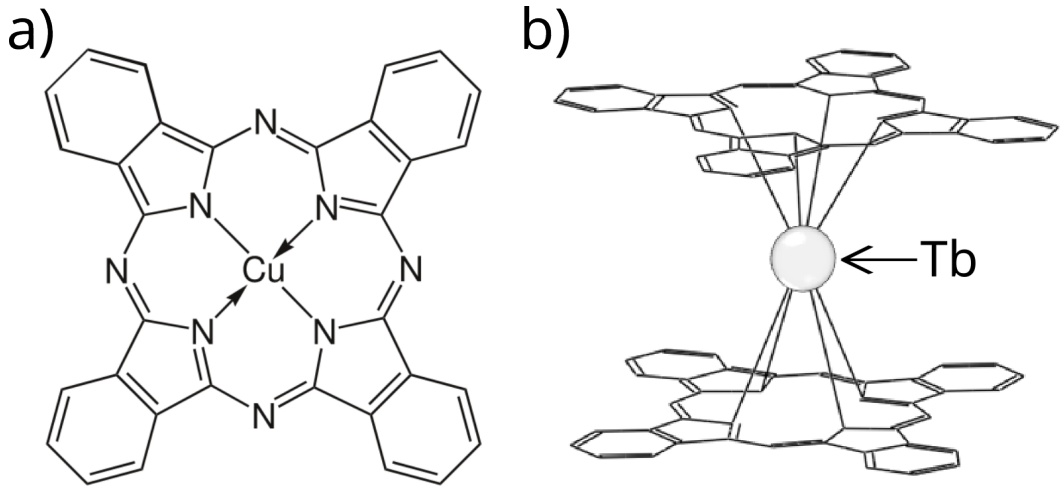

Figure 5: Structure of the phthalocyanine molecules used in this work, a) CuPc molecule, reproduced from[79], b) $TbPc_2$ molecule, reproduced from[80].

3.1.4.2 $TbPc_2$ molecule

The $TbPc_2$ molecule presents a double-decker system formed by two phthalocyanines (P_c) coordinating a Tb^{3+} ion[42,81–84] (see Fig. 5b)). The complex is characterized by a strong uniaxial anisotropy with the easy axis of the magnetization oriented perpendicular to the Pc plane. It is a lanthanide-based molecule and it is considered as a single molecular magnet (SMM). SMMs are characterized by the fact that they retain their magnetization upon removal of the external applied magnetic field. Its SMM properties were reported the first time by Ishikawa and coworkers in 2003[81]. $TbPc_2$ is of particular interest due to their large barrier to magnetic relaxation and high blocking temperatures, compared to traditional single molecule magnets based on transition metals[85]. In the neutral molecule, the Tb(III) ion exhibits an electronic spin state of $J=6\,\mu_b$. The two Pc macrocycles host an unpaired electron delocalized over the Pc ligands. The easy-axis-type magnetic anisotropy imposes an energy barrier of ≈ 65meV for magnetization reversal[86], which is the largest within the whole series of lanthanide-Pc_2 SMMs[82,83]. The first excited state lies at quite high energy. This creates a deep double well potential for the magnetization, with the minima in the

opposite magnetization directions (up and down) separated by a high energy barrier. As a result of this potential, isolated molecules achieve long relaxation times, although decoherence is possible due to processes like quantum tunneling of magnetization[87]. Magnetization loops openings (hysteresis) have been observed after molecular deposition on SiO[88]. Nevertheless, it is worth noting that the opening in the hysteresis loop of $TbPc_2$ disappear[81,89] when the molecules are adsorbed on a metal. In this case decoherence channels open due to the possibility of scattering with the conduction electrons of the metal, causing the slow dynamics of $TbPc_2$ to be lost[90]. Furthermore, it should be mentioned that $TbPc_2$ can couple to ferromagnetic substrates following the magnetization of the substrate[80,91,92] and can couple to antiferromagnets revealing an exchange bias behavior[93].

3.2 Magnetism at surfaces

In the modern quantum mechanical framework, the magnetic behavior of a materials is defined by the behavior of the angular momentum of the electrons in that material. This angular momentum consists in the sum of two terms: the orbital and the spin angular momentum. In a first approximation both values can be obtained by means of Hund rules [34,94], in which the values for each element is given by the occupation of the orbitals. This method gives good values for most rare earths (RE), which have localized 4f orbitals, although it generally overestimates the values of the orbital and the spin angular momentum for d orbitals. This is due to the fact that the Hund rules consider isolated atoms, which is a decent approximation for the localized orbitals in RE material but is not so well suited for transition metals. The cause of this is that in transition metals the d orbitals give rise to (ferro-) magnetism. The lateral extension of d-levels in 3d metals is less localized than the 4f ones in RE metals, therefore the former ones may hybridize with the valence band and form chemical bonds (in the case of insulators) or non-localized states (in metals). This hybridization will break the symmetry of the orbitals, quenching the orbital moment of the forming atoms. Additionally, the orbital hybridization will tend to pair electrons with opposite spin that in the free atom would be unpaired. This electron pairing is the reason because most known materials are non-magnetic.

The materials without magnetic moments are called diamagnets. They are characterized by a very small magnetization that opposes to the applied field. The origin of the diamagnetic behavior arises from slight deformations of the electron trajectories due to the applied magnetic field. This response occurs in all materials, but is not detected due to the much stronger response caused by the orientation of magnetic moments if they are present.

Regarding materials with unpaired electrons and therefore showing a magnetic moment, we find different types depending on whether the magnetic moments are ordered or disordered. In the case of disordered magnetic moments we talk about paramagnets. In paramagnetic materials the free magnetic moments align parallel to an applied magnetic field. However, when there is no external magnetic field, these magnetic moments are randomly oriented. These materials are characterized by the strong effect of the thermal energy that induces disorder and tend to counteract the alignment with the applied magnetic field.

In this thesis we are mainly interested in ordered magnetic materials. In this case, the magnetic

moments of atoms or molecules align in a regular patter due to the exchange interaction (Pauli exclusion) with the neighboring spins. When the neighboring spins are pointing in opposite directions we have an antiferromagnetic material, the total magnetization will be zero. Generally, antiferromagnetic order may exist at sufficiently low temperatures, but vanishes at and above the Néel temperature (named after Louis Néel). Antiferromagnetic materials reveal a highly anisotropic paramagnetic-like behavior, showing small magnetization under applied field perpendicular to the antiparallel magnetic moments of the antiferromagnet. In the crystallographic directions parallel to the magnetic moments no magnetization can be detected.

When the neighboring magnetic moments or spins are parallel aligned we have a ferromagnetic material. Other type of magnetic order is the ferrimagnetism. In that case, there are two lattices of spins of different species in opposite directions, but as the chemical species are different, and so their magnetic moments, the latices are uncompensated. Note that a ferrimagnetic material, for many phenomena, can be modeled as a ferromagnetic material, considering the resulting magnetic unit cell as a whole, “as an artificial atom”.

The source of magnetic order in these materials is the exchange interactions resulting from the Pauli exclusion principle that is applied to overlapping electrons. In a first intuitive idea, this coupling would be limited to directly overlapping electrons, but a deeper analysis indicates that this coupling can also be mediated trough other electrons. Some examples of this are the antiferromagnetic manganese oxide (MnO), in which the manganese atoms are coupled by the oxygen between them (indirect coupling) or the magnetite (Fe_3O_4) in which the coupling between the trivalent and divalent iron is meditated though an oxygen (superexchange coupling[95]). A more interesting example is the RKKY mechanism[96], in which the conduction electrons (with energies close to the Fermi level) archive a small spin polarization. The latter can propagate the coupling over several nm[97]. “Magnets” that we use in daily applications are always ferrimagnets or ferromagnets that show magnetization without an applied field, or a strong magnetization under small applied fields.

3.2.1 Ferromagnetism

In a ferromagnetic material, we have basically a lattice of spins all pointing in the same direction. As a result, the material will reveal a magnetization, even if no magnetic field is applied. A bulk piece of ferromagnetic material is commonly divided into tiny regions called magnetic domains. Within each domain, the spins are aligned, but the spins of separate domains point in different directions. Hence, their magnetic fields tend to cancel out.

In order to reduce the magnetostatic energy produced by the dipole-dipole interaction between all the magnetic moments within the material magnetic domains will be formed. This dipole-dipole interaction happens at a long range scale, which causes a growth with the domain size. This situation is opposite to the exchange interaction, which typically acts on short range (few atoms) and is approximately independent of domain size. This creates a competition between the exchange coupling that orders the spins in the short range, and the dipole-dipole interaction that disorders them. As a result, the ferromagnetic material splits into many domains. Inside of the domain all spins are ordered and point in one direction (minimizing the exchange coupling energy). Each

magnetic domain vector, however, can point in a different direction (minimizing the dipole-dipole interaction energy). As a final point (as will be shown in section 3.2.4.2) the structure of this domains will depend on the history of the material (thermal treatments, magnetizations, etc), that may give rise to hysteresis and allows a non-zero magnetization although no external magnetic field is applied (remanence).

The ferromagnetic ordering of the material is also conditioned by the temperature having a transition from ferromagnetic state to a paramagnetic state at a certain temperature that is called Curie Temperature (T_c). This transition temperature is one of the main characteristics of a ferromagnetic material, defining its range of use in terms of temperature. Ferromagnetic materials can show also complex phase transitions from ferromagnetic to antiferromagnetic order depending on temperature and/or applied magnetic field.

Apart from the spin-spin exchange interaction, the spin-orbit coupling SOC has to be introduced to explain the ordering of the orbital momentum and the anisotropic behavior of the magnetic materials. If only the spin would be considered, no difference in the magnetic behavior would exist between the different crystallographic directions. This SOC term comes from relativistic corrections to the energy of the electrons. Due to the complexity of this term it is usually approximated by considering the magnetic interaction between the spin moment $\vec{S}$ and the angular moment $\vec{L}$. The usual expression for energy related to SOC is $E=\xi\cdot\vec{L}\cdot\vec{S}$, where ξ represents a parameter that depends on the orbital. As a remark, the SOC term will be zero if the orbital moment is zero.

One of the most important characteristic features of the ferromagnets is the magnetic hysteresis. The magnetic hysteresis is the dependence of the magnetization on the previous state of the magnetization. From the hysteresis loops two important parameters can be extracted: coercive field H_C and remanence M_R. M_R is the magnetization remaining in the material after the removal of the applied magnetic field. The coercive field (H_C) is the field that must be applied to the magnet in the opposite direction in order to demagnetize it completely. M_R and H_C are indicated in the hysteresis loop that is shown in Figure 6. In this loops the saturation magnetization of the material is also indicated. More details about the origin of the hysteresis will be explained in Section 3.2.4.

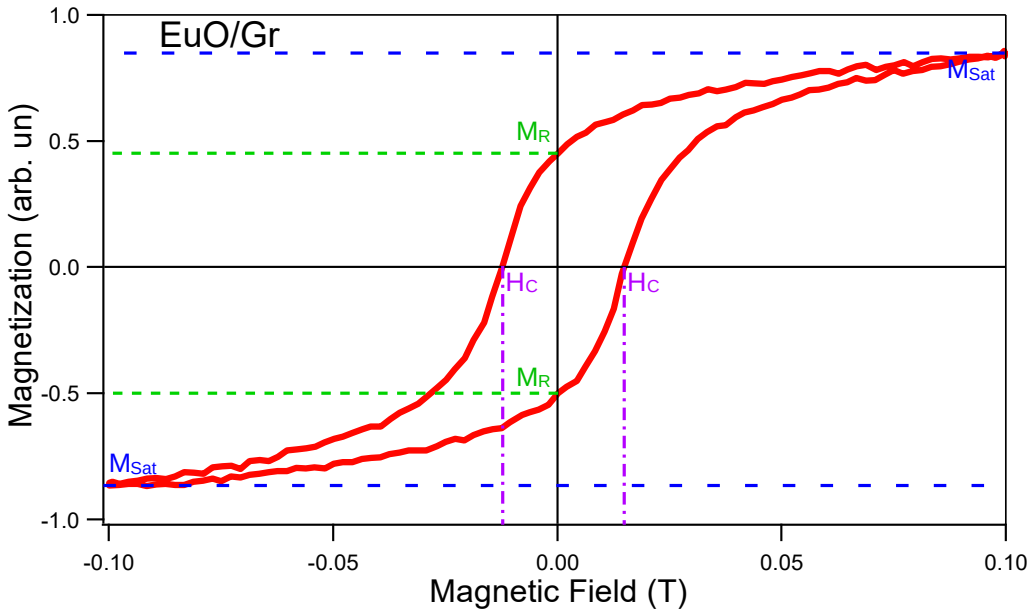

Figure 6: Hysteresis cycle of EuO grown on graphite indicating saturation magnetization (M_{sat}), coercive field (H_C) and remanence magnetization (M_R). The cycle correspond to a MOKE measurement performed on in situ grown EuO on exfoliated graphite in UHV at the STM-MOKE setup.

The most common tool to study the hysteresis is the measurement of the hysteresis cycle. In it, the magnetization is measured as a function of an applied magnetic field, which is scanned from a field enough to saturate the sample to the opposite field and back (see Figure 6). The area between the magnetization curves of the two scanning directions of the field is the energy needed to flip the magnetization. Depending on this energy, we can separate the ferromagnetic materials in soft and hard. In a soft ferromagnet, the energy required to reverse the magnetization is small. These materials are characterized by a small coercive field. On the other hand, hard ferromagnetic materials require a high energy to reverse the magnetization. They typically have large coercive fields. Soft ferromagnets are interesting in applications where the magnetization needs to be flipped fast and with low energy consumption. Another use is if the magnetization needs to follow a magnetic field, like for example in the free layers of spin valves, or the mu-metal alloy used for magnetic shielding. Hard ferromagnets with a high remanence are interesting in applications like permanent magnets and memories. This last example is of special interest, as magnetic memories show fantastic time stability and are theoretically infinite rewritable, which other memories storage technologies struggle to archive.

3.2.2 2D Models of ferromagnetism

A quite simple way to model the magnetic order of a material is to arrange it as a spin lattice. In such case, the Hamiltonian of the system will be:

$$H = \underbrace{-\sum_{i,j} J_{ij}\vec{S}_i\cdot\vec{S}_J}_{exchange\ coupling} - \underbrace{\mu_B\sum_{i,j}\vec{B}\cdot\vec{S}_i}_{interaction\ with\ external\ field} \underbrace{-K_A\sum_{i,j}\vec{u}\cdot\vec{S}_i}_{anisotropy\ energy} \quad (1)$$

Being J the coupling constant, $\vec{S}_i$ the spin momenta of the "i" atom, $\vec{B}$ the external magnetic field, $\vec{u}$ the unitary vector of the easy axis and K_A the anisotropy constant. In order to determine the temperature dependence and study phase transitions of the spin lattice, the model has to be further simplified. We will consider 3 different approximations for 2D ferromagnetic materials. In all these models a 2D lattice of spins is considered. First, we will consider the 2D Ising model, in which the spins are confined to a single axis, e.g., all atomic moments point perpendicular to the 2D plane. In the second case, the XY model, the spins are confined to a plane. The isotropic Heisenberg model in third place allows spin orientation in any direction. Additionally, to further simplify the equations, we will focus on the zero applied field case.

Under this assumptions equation 1 can be simplified to:

$$H = -\sum_{i,j} J_{ij}\vec{S}_i\cdot\vec{S}_J \quad (2)$$

Note that in this models, the anisotropy is substituted by the dimensionality of $\vec{S}$. In the Ising model we will consider that a uniaxial anisotropy is strong enough and the spins can only align in a uniaxial direction. $\vec{S}_i$ can be reduced to 1 or -1. Doing these simplifications, we arrive to the Onsager solution[23] that gives a phase transition with long range order and spontaneous magnetization. The temperature (T_C) of the phase transition can be calculated as:

$$T_C = \frac{2\cdot J}{k_B\cdot\ln\left(1+\sqrt{2}\right)} \quad (3)$$

In the XY model, a biaxial anisotropy confines the direction of the spins in a plane direction. In this case, the spins are not locked to the axis and can rotate in the plane. This model gives a phase transition, but without long range order, and as consequence also without spontaneous magnetization. This lack of spontaneous magnetization is required by the Mermin–Wagner theorem[24] which establishes that in two dimensional systems, the continuous symmetry cannot be spontaneously broken. The Ising case in contrast considers discrete magnetizations and is therefore not subject of this theorem.

Finally, we consider the isotropic Heisenberg model, where the two dimensional anisotropy is zero. In this case, there cannot be a phase transition to a ferromagnetic order at finite temperature[24], as the ferromagnetic order would imply a breaking a continuous symmetry in a 2D material, which is forbidden by Mermin–Wagner theorem[24]. Even if the ground state of the system is ferromagnetic ordered, thermal disorder does not allow the symmetry breaking of the ferromagnetic order to remain at temperatures greater than zero (T>0).

A final note about these models: all of them consider a perfect periodic defect-less spin lattice, but the introduction of defects and size limits of the real materials can cause slight or strong deviations from these ideal conditions. Nevertheless, from these models we can draw several important conclusions: (i) magnetic anisotropy is key feature in allowing 2D ferromagnetism, (ii) a material without anisotropy in the Heisenberg model cannot have magnetic order, (iii) a material with an IP

easy axis of magnetization can show magnetic order. In the ideal, defect-less case, it can not have a total magnetization in the absence of a field (absence of remanence) but in presence of defects this situation changes. In order to produce ferromagnetism, the best case is to have an OOP easy axis, in such case both, magnetic order and remanence is allowed. As was explained in the introduction (section 3.1.1), all these subjects defined a quite active field of discussion until the first 2D ferromagnets were confirmed[43].

3.2.3 Magnetic anisotropy

As it has been seen before, the magnetic anisotropy is necessary in the 2D materials to obtain a ferromagnetic order. In analogy to the dielectric response, the magnetic anisotropy can be described as the variation in the magnetization of the material depending on the direction of the applied field. In terms of modeling, it is the difference in energy in a material that is caused by a change in the direction of magnetization. We will consider two sources of anisotropy: the effect of the shape of the magnet (shape anisotropy) and the effect of the crystalline structure (magnetocrystalline anisotropy).

The shape anisotropy is the difference in energy caused by the induced magnetic field of a magnetic material against the magnetization in the material. This field is called demagnetization field and is highly dependent on the shape of the sample. This term is purely magnetostatic. It is easy to calculate and engineer. In the case of an uniaxial sample this anisotropy is:

$$K_{shape} = \frac{1}{2} \cdot \mu_0 M^2 (N_x - N_z) \tag{4}$$

μ_0 is the vacuum permeability, M the magnetization, and N_x N_z the demagnetization factors. These demagnetization factors are the proportionality factor between the magnetization of the material and the demagnetization field it generates in each corresponding magnetization direction. These factors N_x and N_z are specific of each specific shape. In the case of an "infinite disc", which is equivalent to the 2D material, the demagnetization factor will be $N_z = 1$ and $N_x = 0$. As a consequence, the demagnetization field will oppose the magnetization on the OOP direction but will not affect the IP direction. Therefore, in a 2D material the shape anisotropy will always contribute to an IP easy axis. As an example relevant for this thesis we can calculate that for the case of $GdAu_2$. In order to evade the calculation of *M* in a 2D material, which cannot be defined properly, we can estimate the demagnetization field as the field seen by a Gd atom created by the surrounding first neighboring Gd atoms (due to the $1/d^4$ decay of the dipolar field with the distance, second neighbors contribution will be negligible), that will be given by:

$$B = \sum \frac{\mu_0}{4 \cdot \pi} \cdot \frac{m}{d^3} = 6 \cdot \frac{\mu_0}{4 \cdot \pi} \cdot \frac{7.9 \cdot \mu_B}{(0.54\,nm)^3} = 30\,mT \tag{5}$$

Here, μ_0 is the vacuum permeability and μ_B the Bohr magneton. This 30mT value contrast with the reported difference of about 1T[17] approaching saturation in the OOP direction, while it saturates at near-zero field in the IP direction (see inset in Fig. 3a)). From this example we can conclude that the observed anisotropy values cannot be explained by the shape anisotropy, but acts as a small

correction.

3.2.3.1 Magnetocrystalline anisotropy

The magnetocrystalline anisotropy is the term induced by the crystal structure of the material. In order to simplify the explanation, we will split it in two terms, the crystal field anisotropy and the band anisotropy.

Here, we will focus on the 4f electrons that are of interest to this thesis. Crystal field anisotropy is the energy difference caused by the electrostatic interaction between electrons in the orbitals responsible for the magnetic moment and the rest of the electrons in the material. From the spherical harmonics treatment of the atomic levels it can be deduced that the shape and orientation of an orbital is conditioned by its magnetic momentum and its direction, which implies that the orientation of a shell like the 4f is correlated to its orbital momentum direction. Furthermore, the spin-orbit coupling will orient the spin momentum to the orbital. If now we take into account the filling (following Hund rules), we will see that the SOC will induce the spin, orbital and total momentum to be aligned to the symmetry direction of the whole 4f shell. As result, the magnetic momentum will be correlated to the orbital shape and its orientation. In order to simplify the treatment, the multipolar treatment can be applied. That way, the charge distribution and the associated fields of the 4f orbitals and the structure (the rest of the electrons) can be described by the monopolar, dipolar, quadrupole, etc. terms at the center of the 4f orbital. Due to the spherical symmetry of the monopolar terms, the latter does not have an associated direction and so it can be omitted. The center of the 4f orbital is also the inversion center of symmetry. This fact causes that the dipolar term of the 4f moments is zero, and due to the orthogonality of the multipolar terms, the dipolar term of the rest of the material will not have any effect. Therefore, the first relevant terms of the anisotropy will be the quadrupolar term. Having a look to the higher orders than the quadrupolar terms of the multipolar treatment, we will see that these contributions are much smaller. As a consequence, such higher order terms will only be considered when the quadrupolar term is zero. The quadrupolar term will be zero in cubic crystal structures due to their symmetry, but in most crystal structures it has a non-zero value. Due to the strong asymmetry of a surface (or an interface) the quadrupolar term there will not be zero, and as consequence, we can limit the treatment to the quadrupolar term only. The quadrupolar term of the orbital is given by the shape of the electron distribution of the orbital, which in turn is given by the electron filling. As an example, for trivalent Sm, Gd and Ho, we will have an electron 4f population of $4f^5$, $4f^7$ and $4f^{10}$, respectively. The shape of the $4f^5$ orbital in Sm is prolate, and so the quadrupolar term will be positive. On the other hand, the shape of the $4f^7$ orbital is spherical and hence the quadrupolar term will be 0. In contrast, for the $4f^{10}$ orbital of Ho, the shape is oblate, which in turn causes a negative quadrupolar moment[42]. This orbital shapes can be seen in Figure 7.

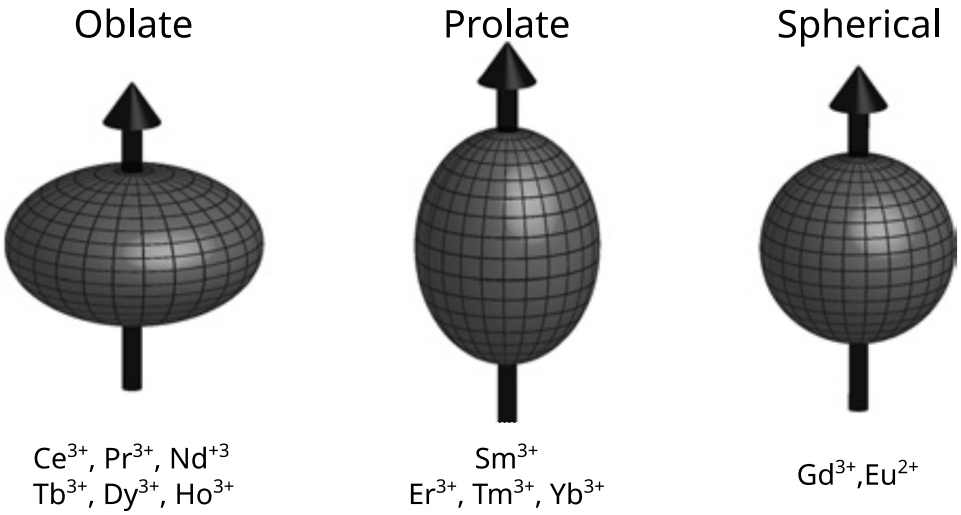

Figure 7: Orbital shape of the Lanthanide RE. Reproduced from[42].

Band anisotropy is the energy difference caused by the changes in the band structure due to differences in the direction of magnetization. The energy associated with the band anisotropy (magnetic anisotropy energy of MAE) can be calculated according to Equation 6 [50,98]. The source of the MAE is the unquenched *L* moment of the atomic orbitals after hybridization. In the same way as in the single atom orbitals, *L* is fixed to the geometry of the hybrid orbitals. Including the SOC causes the breakdown of spin degeneration. The resulting bands will now present a well defined total momentum (*J*) and will be split depending on the directions of the spin. The breakdown of degeneration is expected to be noted mostly at band crossings. These point are expected to open band gaps that are different for each magnetization direction. Introducing such gaps in the MAE (equation 6) will cause two situations. If the band gaps fall far from the Fermi level E_F, its effect to the MAE is small since the bands contributions above and bellow the gaps will be compensated. Nevertheless, when such band gaps appear close or at E_F, the contribution in each polarization will not neccessarly be compensated, and as consequence, it can show important differences. This leads to differences in the total energy of the system depending on the direction of magnetization, the MAE.

$$MAE = \sum_{K,N} \epsilon^{X}_{K,N} \cdot F_{FD} \cdot \left(E^{X}_{K,N} - Ef^{X}\right) - \sum_{K,N} \epsilon^{X}_{K,N} \cdot F_{FD} \cdot \left(E^{Z}_{K,N} - Ef^{Z}\right) \quad (6)$$

F_{FD} is the Fermi-Dirac distribution, Ef^{X} the Fermi level for in-plane (IP) spin polarization, Ef^{Z} defines the Fermi level for an out-of-plane (OOP) spin polarization, *K* the momentum index (*K*-point) and *N* the band index (or quantum number that identifies each band), $\epsilon^{X}_{K,N}$ and $\epsilon^{Z}_{K,N}$ are the density of states at a given *K* and *N* for the IP (*X*) and OOP (*Z*) spin polarizations, respectively. $E^{X}_{K,N}$ and $E^{Z}_{K,N}$ are the energy for the associated *K* and *N* for the IP and OOP spin polarizations, respectively.

For both, the crystal field and the band anisotropy, the need of SOC is clear, as it represents the coupling between the orbital shape and the spin polarization directions. The strong SOC of the RE atoms is the reason for their use in most of the permanent magnets nowadays. Te RE atoms provide a high anisotropy, which allows a high remanence, coercivity and high magnetization characteristics.

An important remark to do is that the magnetocrystalline anisotropy is conditioned by the anisotropy of the crystalline structure. This can be seen for example in the usually low anisotropy of cubic cell ferromagnets, like iron, nickel or fcc cobalt while the anisotropy increases in hcp cobalt. This anisotropy of hcp cobalt can be further exploited by the introduction of Sm (with large SOC). From such "doping" we arrive at the highly magnetic anisotropic Sm-Co magnets. A more interesting way for us to create highly anisotropic crystalline structure is by working at interfaces. An example of this are thin ferromagnetic films (few nm). Therein, the anisotropy generated at the interfaces overcome the contribution of the rest of the material[28,29]. This effect is usually referred a surface anisotropy[30].

3.2.4 Remagnetization models

It was already stated that magnetism in samples results not only from the atomic level but is modified strongly by the creation of magnetic domains that lower the total energy of the system. In order to understand the change of magnetization in a material we will consider two models. In the simplest model, the *coherent rotation model* we consider the rotation of the magnetization of a domain as a single unit. The second model refers to *domain wall movement*. In the latter, the magnetization rotation is given by the change of the domain structure. In both cases, the magnetization of a sample is the sum of the magnetizations of the domains.

3.2.4.1 Coherent rotation model

In the coherent rotation model (Stoner–Wohlfarth model), the absolute magnetization value of the domain is fixed and it is only allowed to change its direction. Thus, the energy of the system will be:

$$E \propto K_A \cdot \sin^2(\varphi - \theta) + M_{sat} \cdot B \cdot \cos(\varphi) \tag{7}$$

K_A represents the anisotropy constant, M_{sat} the saturation magnetization, B the magnetic induction field, φ the angle between the magnetization and the magnetic induction field, and θ the angle between the field and the easy axis of magnetization. Depending on the relations between these parameters, this model produces two energy minima at zero applied field (see Figure 8). These minima define the direction of easy axis of magnetization. This means, that at zero applied field the magnetization state stays aligned to the direction of the easy-axis of the material. The application of a magnetic field in the opposite direction to the magnetization of the sample induces that the magnetization does not follow the field until a critical field value, the coercive field, is reached. In this model, the coercive field at zero temperature is of the order of:

$$H_C = 2 \cdot K_A / M_{sat} \tag{8}$$

In this case the only minima of energy is found in the field direction. By introducing temperature in the model in a simplified way, we can estimate a coercive field of $H_C=(2\cdot K_A-k_B\cdot T)/M_{sat}$, and, as can be seen, the coercive field is lowered as the temperature increases. Thus, the energy barrier can be overcome by thermal activation processes.

It should also be noted that the energy barrier for the coherent rotation depends on the volume of the domain. In a simple approximation, the energy barrier depends linearly on the domain size, but in most real cases the anisotropy at the domain surface can cause a deviation from that behavior. In general, the energy barrier will be proportional to the domain size. As result of this, a domain size reduction will have two effects, first, the coercivity will be reduced with the domain size. Second, if the domain is small enough, there will be a temperature above which the thermal energy will overcome the energy barrier, without losing the ferromagnetic order. That temperature is called blocking temperature T_B. Above T_B, the magnetization of the domain will be able to rotate freely and follow the magnetic field, giving rise to a phase called superparamagnetic phase.

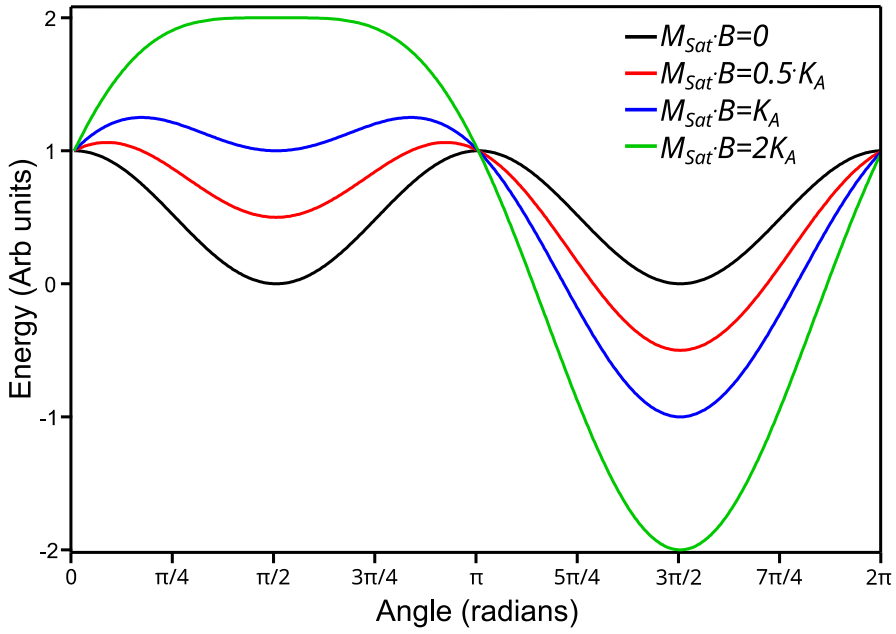

Figure 8: Energy of the a ferromagnetic domain modeled by equation 7 for different relations of anisotropy and magnetic field.

The coherent rotation model works fine for single domain ferromagnets, like nanoparticles[99] or even some classical composite ferromagnets that consists of ferromagnetic particles of few μm inside a non-magnetic matrix[100]. In homogeneous ferromagnets, however, the coercive field arising from this model is usually overestimated. This is due to the remagnetization processes consisting on domain wall movement explained next.

3.2.4.2 Domain wall movement model

In most cases of homogeneous ferromagnets, the remagnetization will happen because of domain

wall (DW) motion. The domain wall are the frontiers between domains with different magnetization. In this case, the direction of the magnetization of the domains does not change by small applied fields, only the domain walls move. Hence, when a small magnetic field is applied, the domain walls move in order to increase the size of the domain magnetized closest to the direction of the applied magnetic field. Consequently, the size of the domains pointing in other directions will be gradually reduced. From the imbalance in the size of the domains with different magnetization direction, an average magnetization results, even if there are still domains pointing in opposing directions. This process is illustrated in Figure 9. After removing the applied magnetic field, the domain walls try to move back to their original state with an averaged magnetization that is zero. The presence of defects in the material may block the domain wall motion. Different defects like dislocations, discontinuities, etc, will anchor the domain walls (domain wall pinning), producing two consequences. The first one is that one has to apply a magnetic field to provide energy to allow the domain wall to jump between the defects leading to coercivity. The second consequence is that the thermal energy will not be enough to completely disorder the magnetic structure. After field removal, the total magnetization of the material will not return to zero, giving rise to remanence. Putting these two consequences together, we see that the domain wall pinning will cause the magnetic material to have coercivity. A small remark should be made in relation with the XY model (section 3.2.2). The introduction of defects of the material (not included in the original model) allows magnetization by blocking of the structure in analogous way to the DW pinning.

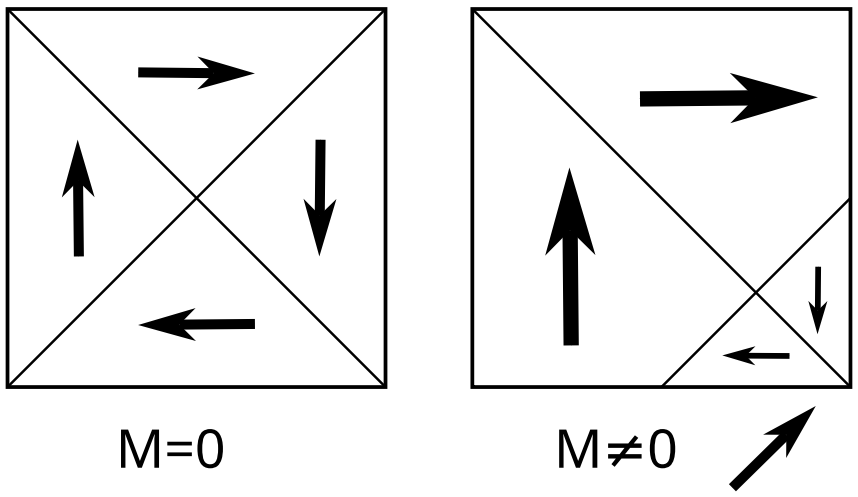

Figure 9: Illustration of compensated magnetic field structure showing 0 magnetization and uncompensated magnetic structure leading to a total magnetization.

In the domain wall motion, the anisotropy is also critical for the coercive field of the material. The anisotropy directly increases the energy required to move the domain walls. In a simplified way, we can consider that the domain wall movement behaves similarly to domain rotation, i.e., there is a barrier to flip the magnetization that is proportional to the anisotropy. Then, we can expect that for low anisotropy cases, the DW will move almost free, and with that, the domain structure will

change in order for the magnetization to follow the applied magnetic field. On the other hand, for high anisotropy systems, the magnetic field (or thermal energy) will have to overcome an energy barrier created by the anisotropy to move the domain wall. This will translate in a resistance for the magnetization to follow the applied field, or what is the same, causing coercivity in the material.

3.2.5 Arrot plot analysis

The Arrot plot analysis is a method for the determination of a ferromagnetic order. It was introduced by A. Arrot in 1957[101]. This method is based on the analysis of the Magnetic Isotherms. The temperature dependence of the magnetization introduced in this article is:

$$H = A\cdot\left(\frac{T-T_C}{T_1}\right)\cdot M + B\cdot M^3 + C\cdot M^5 + \cdots \tag{9}$$

H represents the applied magnetic field, M the magnetization, T the temperature, T_C the Curie temperature and T_1, A, B, C, etc are empirical constants. By considering the series only to third order and dividing by the magnetization, it can be rewritten as:

$$\begin{aligned} \frac{H}{M} &= M_0^2 + B\cdot M^2 \\ M_0^2 &= A\cdot\left(\frac{T-T_C}{T_1}\right) \end{aligned} \tag{10}$$

From there, by determining M_0^2 as a function of temperature, the Curie temperature T_C can be determined. To do so, the first step is plotting the squared magnetization values vs the applied field divided by the magnetization values (see Figure 10b)). Then, the high field values (high H/M values) are fitted by a linear fit. The M^2 values at $H/M=0$, namely M_0^2, are in the last point (Figure 10c)) displayed vs the measurement temperature. Finally, the Curie temperature can be determined by fitting the obtained M_0^2 values as a function of measurement temperature and search for $M^2=0$ crossing by a linear or quadratic fit.

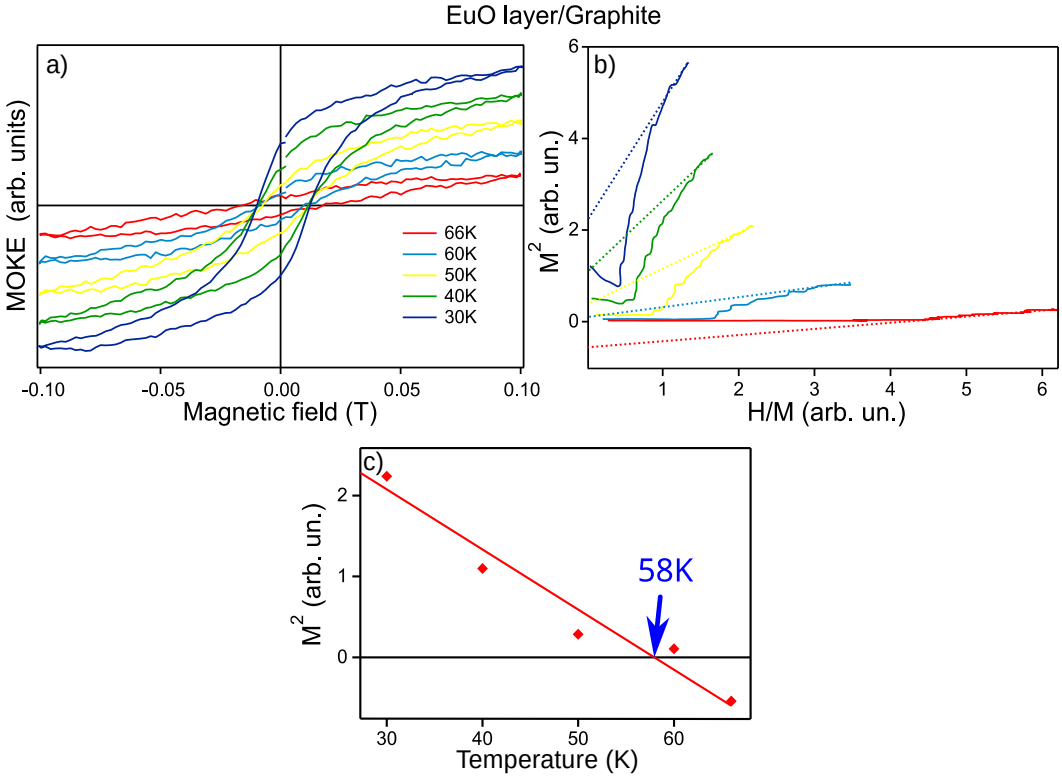

Figure 10: Temperature dependence of hysteresis loops for EuO measured by MOKE technique at the laboratory STM/MOKE system: a) Magnetization curves as a function of sample temperature, b) Arrot plot analysis: M^2 vs H/M curves and their high field fits (dotted lines). The H/M=0 crossing points are used in c) to determine the Curie temperature T_C of the EuO system.

This method of determination of magnetic order is used in the present thesis as the method for extracting T_C from the magnetic measurement carried out by X-ray Magnetic Circular Dichroism (XMCD). Other methods, like analysis of susceptibility or field cooling vs zero field cooling or permittivity variation with temperature cannot be easily applied due to technical issues like beam stability, relatively high noise-to-signal ratio of the technique and the limitations imposed by the cryostat.

4 Experimental Techniques and Sample preparation

Several experimental techniques have been used to study the rare earths/noble metal (RE/NM) surface alloys and the interfaces formed after deposition of molecules. One type of techniques is referred to as photoelectron spectroscopies. The chemical properties have been mainly studied by X-ray Photoemission Spectroscopy (XPS) while the electronic structure has been studied though Angle-Resolved Photo-Electron Spectroscopy (ARPES). Prior to such spectroscopical methods the structure have been analyzed by Low Energy Electron Diffraction (LEED) which has also been used to evaluate the quality of the prepared samples. A more in depth study of the structure was later carried out by Scanning Tunneling Microscopy (STM). Finally, the magnetic behavior of the samples was studied by the use of X-ray Magnetic Circular Dichroism (XMCD) which relies on synchrotron based X-ray absorption spectroscopy (XAS). In order to apply all these techniques, Ultra-High-Vacuum (UHV) environment was required. First, to ensure the cleanliness of the sample, and second to be able to use electrons as probes in the mentioned techniques. The alloys were prepared by direct evaporation of Rare-Earths (RE) on the hot and previously cleaned Noble Metal (NM) surfaces. After the alloys formation, a MonoLayer (ML) of the selected molecules were evaporated on top. All the details related to the experiments will be explained in this chapter.

UHV means that the pressure during the experiments should be less than 1×10^{-9}mbar. In fundamental investigations as the one considered here, one important aspect is the cleanliness of the sample to ensure the exclusion of any contamination. In the case of surfaces, this is especially critical, due to the fact that we are studying single atomic layers at the surface of a sample. Under ambient conditions or even inside a clean room, the atomic layer at the surface of a material would get contaminated from dust, air, water, or any other component inside the atmosphere that may get in contact to the sample. An additional reason for the need of UHV conditions is related to the sample surface reactivity. Some surfaces can be oxidized almost instantly at ambient conditions. If instead of ambient pressure we use UHV, there is less possibility that the sample gets contaminated or reacts with anything after being prepared, as there is “nearly nothing” that can come in contact to the surface. However, this statement is not entirely true, also in UHV there are still rest gas atoms. The composition of the rest gas atoms in the UHV chamber depends on the experimental setup, pumping system, previous use, etc. In UHV vacuum systems, the aim is always to have the lowest possible pressure, therefore different vacuum pumps are combined in the same experimental setups. From thermodynamic argumentation[102], one can extract that a very reactive surface (we speak in form of sticking coefficient) get fully covered by rest gas atoms in 1 second at a pressure of 1×10^{-6} mbar. As an example, in most of the here described experimental setups, the base pressure is 1×10^{-10} mbar, this means that in 10.000s (2.7h) the sample is fully covered even in such good conditions. If we allow a “contamination level” of 5%, this level is reached after 500 seconds or roughly 10 minutes. Moreover, the experimental techniques that we use here for sample characterization usually requires long measurement time, even the sample transfer process to the analysis chamber after preparation consumes already this time frame. The reason why we are still able to measure our prepared samples is that these surfaces are not so reactive (lower sticking coefficient), which allows the measurement of the surface properties. In any case, even in UHV systems, the pressure and

possible contamination from rest gas atoms is a very important aspect that has to be considered always and cleanliness should be controlled several times during an experiment.

Additionally, only UHV conditions allow us to use some of the characterization techniques that would not be possible to use in other environments. The clearest examples are electron based techniques. These techniques can usually not be used outside the UHV range. The electrons would suffer scattering and absorption within the gas, which changes their energy and direction or directly eliminate the electron and hence the information. The result of this is that the electron would not be able to carry information of the sample to the detectors or in the case of electron diffraction the electron would not even reach the sample. On the contrary, this electron property of being easily scattered is particularly useful for surface science, as it allows obtaining information for the last layer of the sample, the surface, due to the above mentioned small electron mean free path.

4.1 Sample Preparation and Experimental Setup

In the here considered field of material science, several methods for sample preparations are available. Often, samples are prepared from specialized groups that just do this process. Then these samples are re-examined by spectroscopy experts (e.g., our group). However, for all the here investigated materials such an approach is not possible. This has to do with the fact, that the surface compounds of RE materials are very reactive and completely oxidize in less than a millisecond under normal atmospheric conditions. Therefore, all systems of this thesis are prepared in-situ that requires much more effort and tools to check for the correct growth procedure and sample compositions. Preparation of the samples was carried out under ultrahigh vacuum conditions due to the mentioned high reactivity of the lanthanides to avoid contamination of the surfaces. The typical UHV range that we have is of approximately 1×10^{-10}mbar.

4.2 Substrate preparation

4.2.1 Single crystal substrates

In this thesis, two noble metal single crystalline substrates, namely Au(111) and Ag(111), have been used. The preparation of the surfaces was carried out by several Ar^+ ion sputtering and annealing processes. In the sputtering process the sample is bombarded with noble gas ions that have enough energy to remove atoms of the surface of the sample. A noble gas (most often Ar, sometimes Ne) must be used to prevent any possible chemical reaction with the sample. In the sputter gun, the noble gas atoms are ionized and accelerated with an electric field between 500 and 1500V. This way, contaminating atoms as well as surface atoms are removed from the sample. The second part of the process consists of annealing the metallic substrate. In this process the sample is heated to a temperature that is high enough to allow mobility of the surface atoms in order to heal the destroyed surface after the sputtering process and additionally to remove the noble gas atoms that may have been incorporated by the sputtering process into the sample. Of course, this annealing temperature has to be below the melting temperature of the sample. The annealing temperature of Au during this thesis was 800K. In the case of Ag, 740K were sufficient to form the required large

terraces of the (111) surface.

4.2.1.1 Surface compound preparations

The rare-earth noble-metal surface compounds RE-NM_2 are prepared by depositing RE atoms on the Ag(111) or Au(111) surfaces. For the preparation of 1ML of the RE-MN_2, one requires the evaporation of about one third of a monolayer of the RE material on a previous clean NM surface. This process is necessary to reach the adequate stoichiometry. Previous investigations found out that a better surface quality is achieved, when the substrate is hold at an elevated temperature[17,47,103]. This means that for a new surface compound, i.e., new RE or new NM, first the growth process had to be investigated. For this purpose, the deposition of the RE atoms have been performed at a certain sample temperature during the RE deposition process. Then, analysis methods like low energy electron diffraction or scanning tunneling microscopy is carried out. At the end the sample is cleaned and the preparation process is repeated at a different temperature until the best preparation temperature is obtained. The optimized heating temperatures are noted in Table 2. To evaporate the RE atoms, temperatures in the range of 600K to 1200K has to be achieved. This will depend on the RE atom. Figure 11 shows a top view from one of the RE evaporators that was built up for this thesis. In order to evaporate the RE atoms, a piece of the RE metal is inserted into a refractory metal crucible (usually molybdenum) that is heated by electron bombardment. The electrons are emitted from a heated tungsten filament and accelerated by applying a positive high voltage to the crucible. The RE evaporation was calibrated using a quartz microbalance setup or checked by other means, like the mentioned growth preparation techniques or even by photoemission testing the disappearance of special features of the substrate electronic band structure like the Au and Ag Shockley surface state emissions[104]. Note that after each preparation experiment, the RE atoms must be removed in order to preserve a clean metal surface for future experiments. This cleaning process must be done carefully, as the RE atoms tend to diffuse into the bulk sample at higher temperature. The way to do that is by long sputtering processes to ensure that all the RE atoms have been removed. It should be mentioned, that after several evaporation, it may be difficult to completely remove the RE from the substrate, and traces of the RE that have diffused into the bulk may resurface after annealing. In order to completely remove this traces, the only solution consist of re-polishing the sample, removing several hundreds of microns of the material.

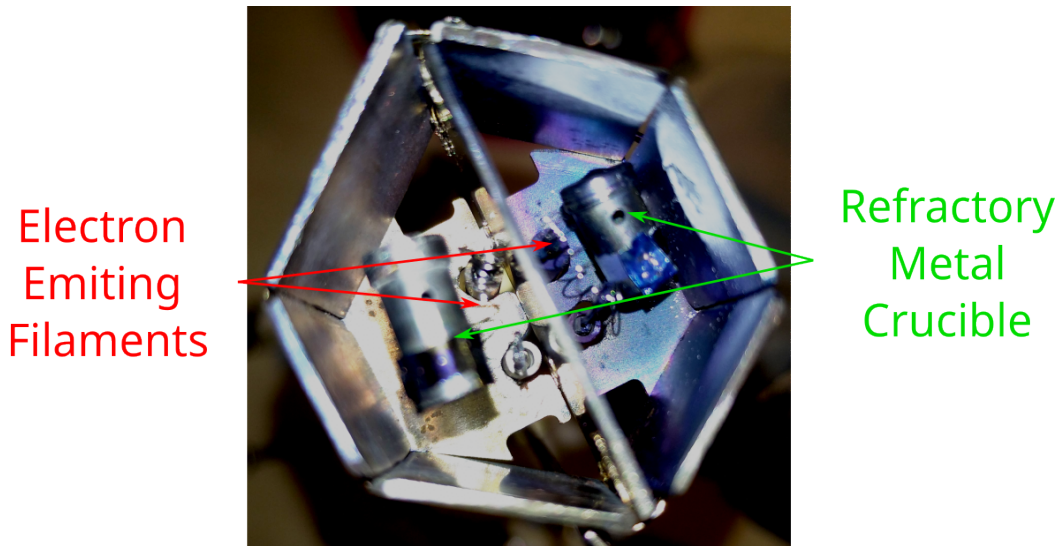

Figure 11: Knudsen cell type evaporator for deposition of two different RE materials in a single evaporator. The high voltage electron beam heating allows to reach the high temperatures needed for evaporating the REs.

Table 2 Optimized substrate temperatures during RE evaporation for the formation of 1 ML of RE-NM_2 surface alloys.

	Au(111)	Ag(111)
Sm	563K	523K
Eu	500K	------
Gd	650K	650K
Dy	620K	620K
Ho	620K	620K
Yb	570K	------

4.2.2 Molecule evaporation

The evaporation of the molecules has been performed in UHV using home-made evaporators specifically for molecules. The molecules were inserted in a crucible, either a quartz or boron nitride (BN) crucible (Figure 12a)) or in a different type of evaporator in a Ta pocket (Figure 12b)). Then the crucibles were heated until the molecules evaporate. In the first case, the molecules are inserted in the ceramic crucibles with a conductor coil around. In the second case, a tantalum crucible supported on a SiC chip acts as heater. The molecular deposition occurs when flowing a current though the coil or chip. The evaporated molecules were CuPc and $TbPc_2$, respectively. The addition of a thermoelement to the metallic crucibles of the metal evaporator (Figure 11) was avoided for security reasons. For the molecular evaporators however, a K-type thermocouple was added to better control the evaporator temperature and the deposition. We found that the temperature of evaporation of CuPc is 590K, and hence somewhat lower compared to the evaporation temperature of $TbPc_2$, which was 690K. In order to obtain a monolayer (ML), several attempts of evaporation have to be made and checked on a clean substrate (in this case mostly Au(111)) by LEED and STM until a desired thickness is obtained.

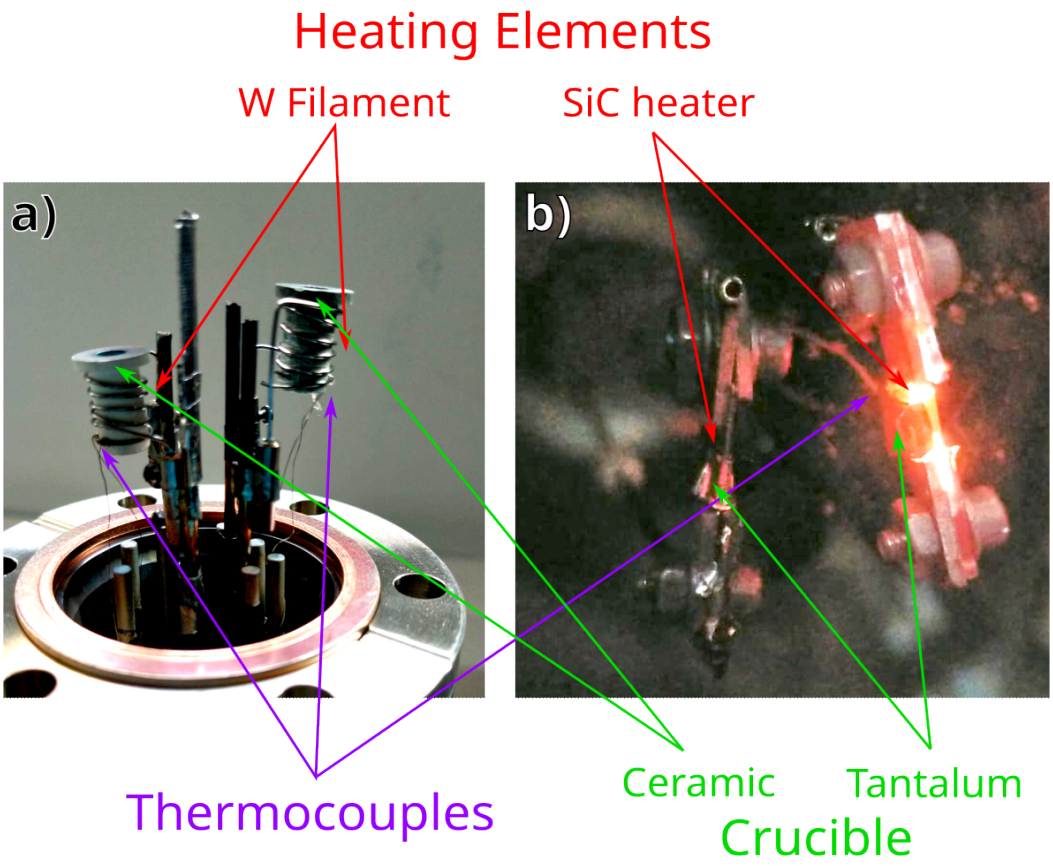

Figure 12: Different types of molecular evaporators used. a) Ceramic crucible evaporator with a tungsten coil filament (side view) and b) Tantalum pocket evaporator attached to a SiC heating element (top view).

4.2.3 Machine specifications

The experiments were performed partially in San Sebastian in the laboratories of the Material Physics Center (CFM) and in different beamlines of several European synchrotrons like ALBA (Barcelona), Soleil (France) and Elettra (Italy).

In San Sebastian two vacuum systems were used, the first system is dedicated to STM and ARPES/XPS and a secondary system that is dedicated to STM and MOKE.

The ARPES/STM setup is formed by four chambers: a preparation chamber, an analysis chamber for LEED and STM, a second preparation, and an analysis chamber for ARPES/XPS, see Figure 13 for details. The first preparation chamber is equipped with sample sputtering, sample heating, and several fixed RE evaporators. Additionally, there are available interchangeable ports with valves for introduction of additional evaporators, vacuum suitcases, or other UHV devices. Furthermore, the first preparation chamber has a load-lock for fast introduction/removal of samples. The base pressure in this chamber is 3×10^{-10} mbar. As indicated by the name, this chamber is used for general preparations, as the sample cleaning, RE evaporations, and molecule evaporation carried for this thesis. Directly connected to this chamber there is the STM/LEED chamber. This chamber is

equipped with a commercial Omicron LEED and a variable temperature STM from the same company (VT-STM). Usually, the STM is operated at room temperature (RT), but can be brought down to 70K by liquid nitrogen cooling. The base pressure in this chamber is 1×10^{-10} mbar. This STM/LEED chamber is furthermore connected to a double chamber setup dedicated to ARPES/XPS. This part is arranged with a preparation chamber on the top and an analysis chamber at the bottom. Both chambers share a rotatable manipulator with a closed cycle cryostat reaching temperatures below 120K and an additional electron bombardment heating stage for sample annealing. Due to the shared manipulator the preparation chamber is limited to clean preparation. In this case, the preparation chamber only has available fixed evaporator. The ARPES analysis chamber has three main components: a gas discharge lamp together with a toroidal monochromator, an electron energy analyzer, and an X-ray source. All these components are from SPECS company. The gas discharge lamp with its monochromator forms a 45º angle to the analyzer. It is usually used with He as discharge gas. The toroidal monochromator is used to select the emission line. In this thesis, mainly a photon energy of 21.22eV (HeI_α) was used with an energy width below 1.5meV. The X-ray source is a monochromatized Al K_α light from a commercial microfocus setup (SPECS Focus 600). The latter ensures a small light spot (<0.5mm).

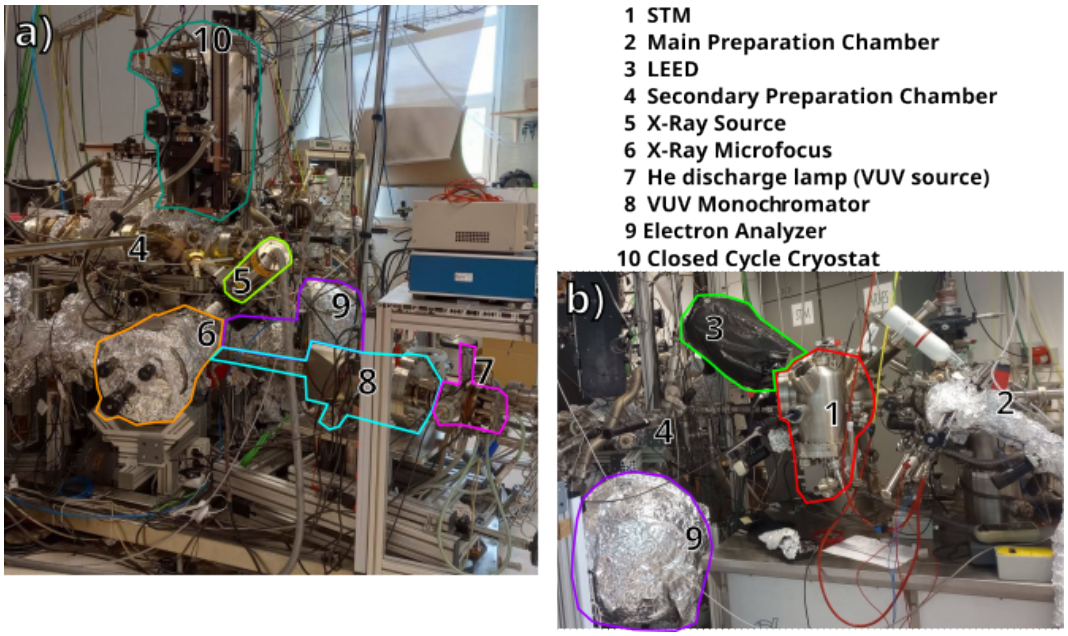

Figure 13: The ARPES-STM chambers setup. The equipment is divided into two semi-independent systems: a) ARPES/XPS and b) STM/LEED double chambers.

The STM/MOKE setup is the second experimental station in San Sebastian used during the thesis. It consists of two chambers: one dedicated to sample cleaning with a LEED setup and MOKE tools (LEED/MOKE chamber). The second chamber is used for STM experiments and there also evaporations were carried out (STM chamber). The LEED/MOKE chamber contains two manipulators, one electron bombardment manipulator for sample cleaning by sputtering/annealing and one for the Omicron LEED. Additionally, the chamber has a manipulator for surface sensitive MOKE. The latter contains a sample holder with a closed cycle cryostat capable of operation in a range from 30K to 400K. Furthermore the chamber has soft iron cores that guides magnetic fields

from the coils mounted outside the UHV system. Last, there are special optical windows for bringing in and out the light for the MOKE experiment. One can mount an external optical setup for MOKE characterization of the sample, capable of archiving monolayer sensitivity. This LEED/MOKE chamber is separated from the STM/LEED chamber by a valve. The latter is equipped with a (VT-Omicron) STM and evaporators for RE, molecules and some transition metals. We furthermore added an interchangeable port for connection of additional evaporators or a vacuum suitcase to carry out vacuum transfers of samples into the ARPES/STM system or synchrotron radiation centers. The base pressure in this chamber is 5×10^{-10}mbar.

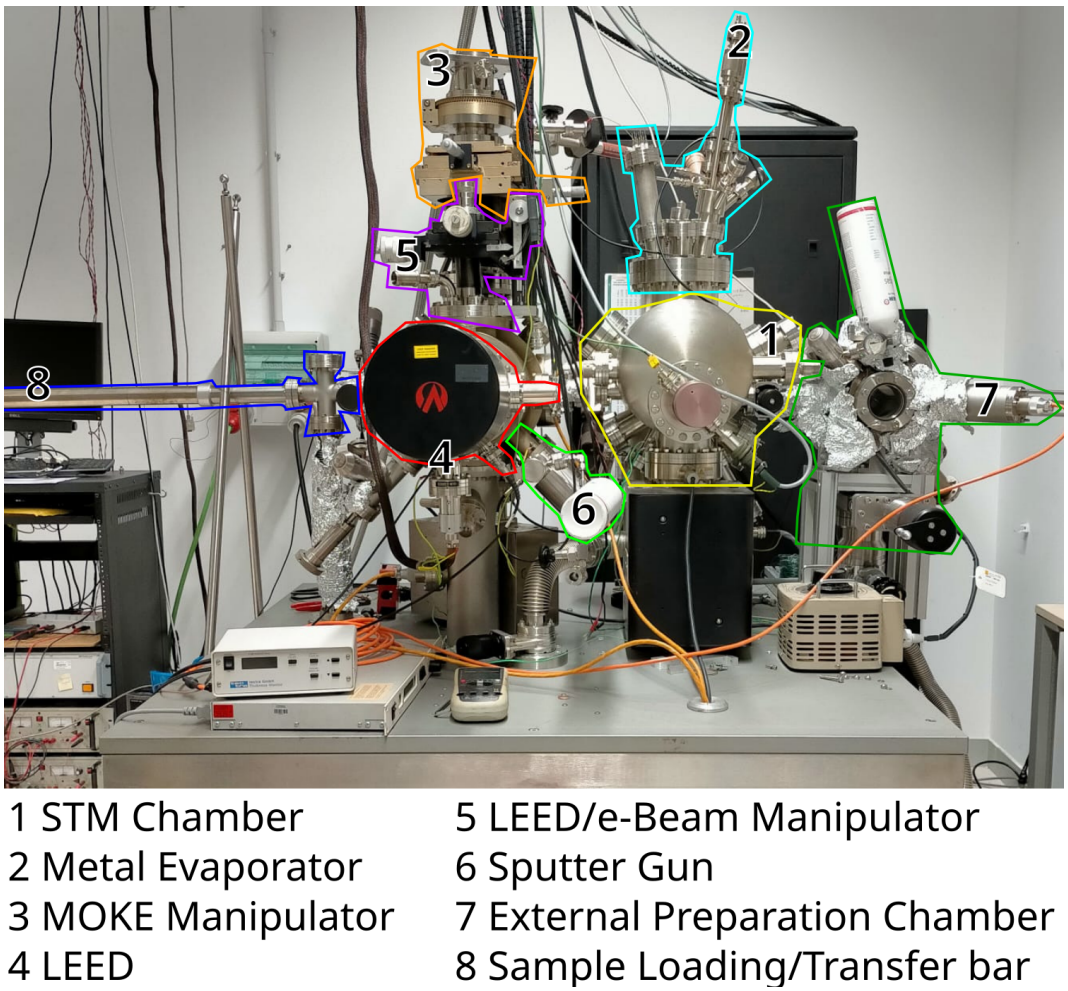

Figure 14: The MOKE-STM system setup. It is divided into two chambers, one dedicated to MOKE, LEED and sputtering/annealing (left side) and another chamber dedicated to STM and evaporation of metals. Additionally, at the moment the image was taken, a removable chamber (7) dedicated to high temperature preparations was mounted.

4.3 Photoemission spectroscopy

Photoemission spectroscopy (PES) is an experimental technique based on the photoelectric effect. This effect was discovered by Hertz in 1887[105] and later explained by Einstein in 1905[106]. It was the first time that the quantum nature of light was revealed. The photoelectric effect consists in the fact

that light illuminates a sample and excites electrons. In the PES technique, these electrons (sometimes called photoelectrons) are then collected as a function of their energy. The spectroscopy was discovered by K. Siegbahn in 1966 and was originally called Electron Spectroscopy for Chemical Analysis (ESCA) [107].

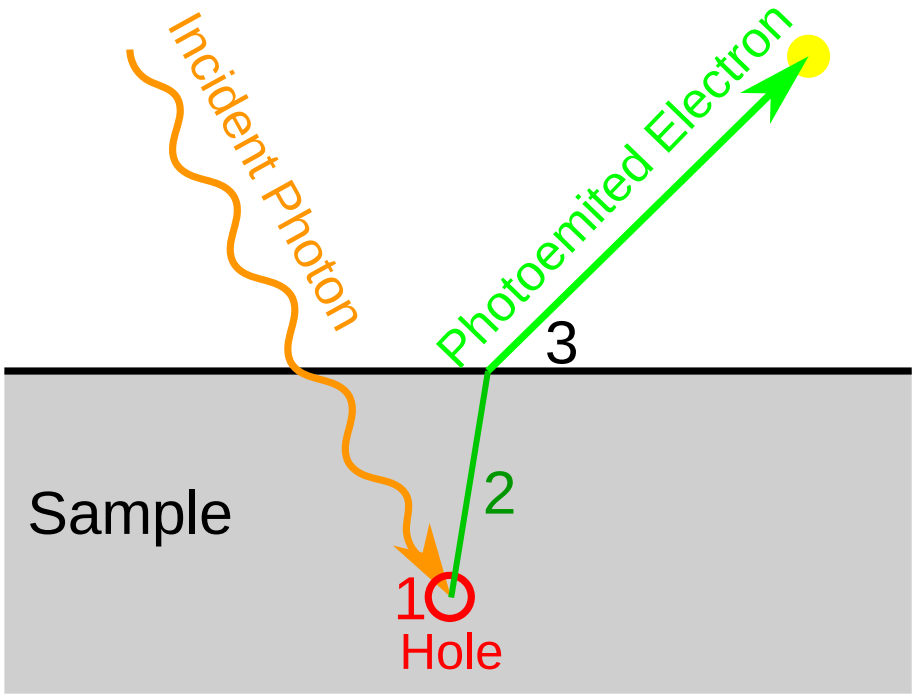

Figure 15: Illustration of the photoemission process in the three steps model. In the step 1, the photon excites the electron producing a hole. The step 2 consists on the transport of the electron to the surface. In step 3 the electron escapes from the sample.

It is important to mention that photoemission is a multi-step process. The process consists of three main steps that will be described in detail. The first part describes the excitation of an electron located in the inner shell or the valence band of the material to an empty state above the Fermi level. Details on specific possible excitation will be explained in the following section. There are other two steps to take into account, the transport of the electron to the surface, and the escape of the electron from the sample. In the second step, the electron can suffer absorption or inelastic scattering, causing some of the electrons to lose part of its energy or even disappear completely. The distance that the electron can travel without losing its energy is known as mean free path λ and it is of the order of a few layers of atoms and depends on the kinetic energy of the electron. A universal curve that is shown in Figure 16 describes this behavior. Although the curve is often referred to as a universal curve, one can see that the mean free path suffers deviations from the "universal behavior" due to different characteristics of the materials. Independent of such small deviations, a photoelectron with an energy in the order of 10-100 eV has an escape depth (mean free path) in the order of few angstroms (Å) that give rise to surface sensitive PES. However if the energies are in the order of several hundreds of eV or even keV, the electrons have escape depths (mean free path) up to few nm allowing more bulk sensitive PES. In the present work, as our region of interest is the

last layer of the sample (the surface), the low energy range was used to ensure surface sensitivity. In this context, it has to be repeated that UHV conditions are completely necessary to ensure a small mean free path. At higher gas pressures part of the electrons will be absorbed and only very few would reach the detector.

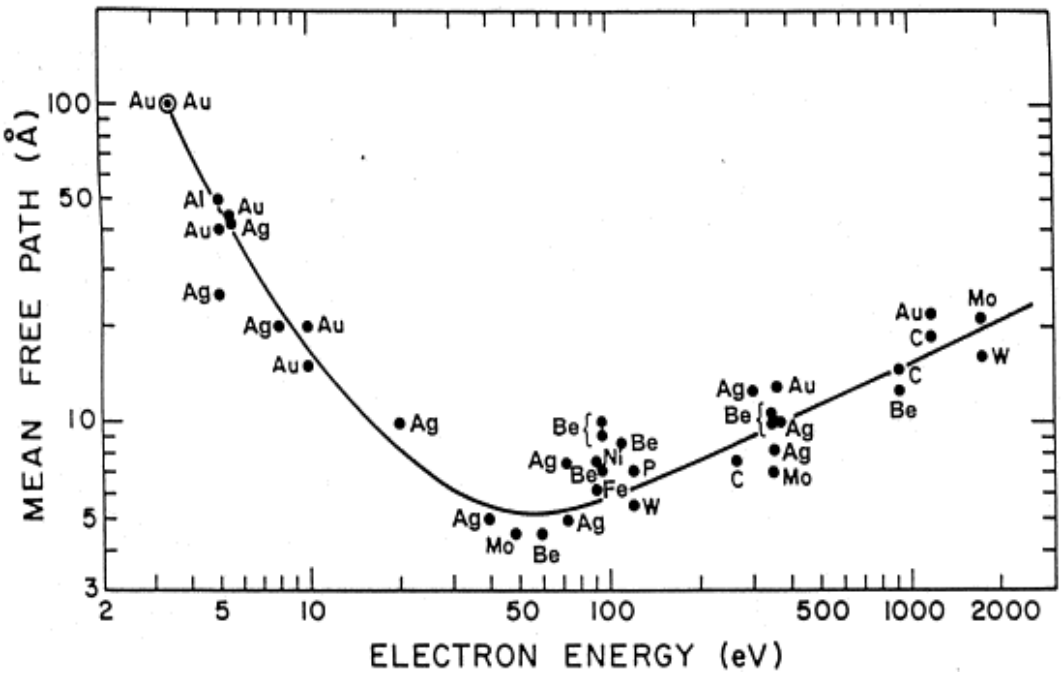

Figure 16: Inelastic mean free path of the electron in different materials as a function of the detected electron energy. Reproduced from[108].

Finally, as this curve is mostly universal, it can be used to determine the thickness of a thin layer grown on a certain substrate if the film grows layer-by-layer:

$$D = \lambda \cdot \ln\left(\frac{I}{I_0}\right) \tag{11}$$

Here D is the thickness of the adsorbed thin layer, I the detected electron intensity upon thin layer deposition, I_0 the detected electron intensity prior to the thin layer deposition and λ the mean free path for the kinetic energy of the corresponding electrons.

The third (and last) step of the photoemission process consists of the electron escape from the sample. Here, the electron has to overcome the energy difference between being inside the metal and in vacuum. This difference is called work function. It depends on the material as well as on the surface characteristics. In pure metals, the crystal orientation plays an important role. It is known that the work function grows with the surface atomic density[109]. For metals, onto which some structure (layer or islands) have been grown, the work function will be affected. This can be via the dipolar moment of the structure itself[110], via doping of the surface (e.g. evaporation of alkali, earth alkaline, and rare earth metals on the sample) or modification of charge distribution of the surface (and so polarization of the surface)[111–113].

One possibility for the determination of electron energies is an electron analyzer. There are several ways of operation depending on its construction (time of flight, deceleration, deflection[113]). The most common electron detector used in fundamental research (in UHV conditions) is based on the use of electron deviation through electromagnetic fields. In photoemission, electrostatic analyzers are preferred for simplicity of construction and versatility. They are formed by two metallic surfaces separated by a vacuum space that has an entrance and an exit slit that is designed to allow electrons to travel through it. Between those metallic surfaces a potential (pass energy) is applied. An electron that enters though the entrance slit will only arrive to the exit slit if it has a determined energy, which depends on the potential applied between the metallic surfaces. This way, an electron energy can be selected by choosing the voltage between the metal surfaces. Note that the electron counter is then placed behind the exit slit. Different geometries may be used, but the most common is a hemispherical analyzer shown in Figure 17. It consists of two concentric metallic hemispheres with the entrance and exit slit in diametrical opposed points. This type of analyzer preserves the momentum of the electrons after passing while archiving high energy resolution[114,115]. By the addition of a 2D detector behind the exit slit, it is possible to resolve at the same time the energy (in the radial direction) and the momentum (in the perpendicular direction) of all the electrons inside approx. one tenth of the selected pass energy range. In order to increase the number of detected electrons, it is common to introduce an electron multiplier like a micro-channelplate (or a channeltron if only one channel is used). The higher signal numbers improve the signal to noise ratio. The pass energy of the electrons can be changed by modifying the potential between the two hemispheres of the photoelectron analyzer. The pass energy and the slit size will determine the resolution of the analyzer.

The usual way of scanning the energy is using a retarding plate in the electron lens system at the entrance of the analyzer in order to adjust the energy of the electrons to the pass energy range. In the present thesis, several models of hemispherical analyzers equipped with channelplate detectors have been used. Specifically, a SPECS 150 analyzer was used in our home lab, Scienta 200 and R4000 analyzers in the VUV-photoemission beamline of Elettra synchrotron and in Cassiopée beamline of Soleil synchrotron, respectively.

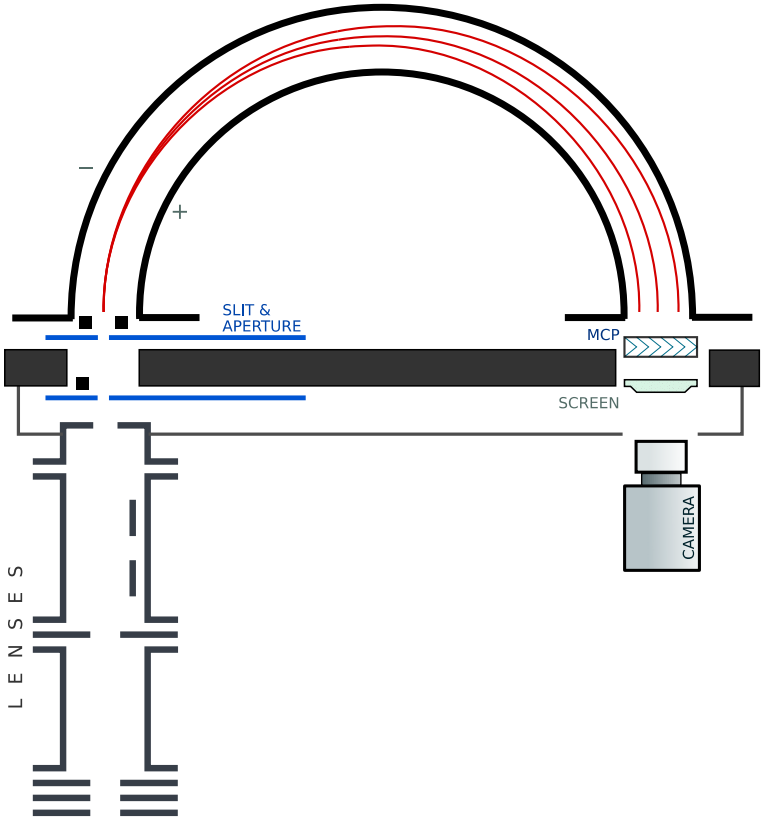

Figure 17: Hemispherical electron analyzer schematics. Reproduced from[116].

4.3.1 General considerations of the photoemission process

During sample illumination there are two kind of processes that can lead to emission of electrons: the photoemission and the Auger process. In the direct photoemission process, one electron of an atom absorbs a photon with an energy higher than the difference to the vacuum energy (=binding energy of that electronic level + work function), and it is extracted from the sample, leaving the sample in an excited state. By conservation of energy, the energy of the electron extracted from the sample is related to the difference from the energy of the photon (hν) and the binding energy E_B of the electron. By measuring the kinetic energy of the electron E_{kin}, the binding energy can be determined as following:

$$E_B = h\nu - E_{kin} - W_A \tag{12}$$

being W_A the work function of the analyzer. Due to the difficulty of determining the analyzer work function, a more practical definition is used:

$$E_B = E_{kin} - E_{kin}(E_F) \tag{13}$$

Here, we set by definition that at the Fermi level, the binding energy is zero. This way, the determination of the work functions and possible errors in the photon energy are solved by referring all energies to the Fermi level.

The second electron emission process is the so called Auger process (also Auger-Meitner effect) originally discovered by Lise Meitner[117] but later associated to the french scientist Pierre Auger. In this process, one photon removes an electron from an inner shell (IS) of an atom via a direct photoemission process and leaves that atom in an excited state. This initial process is followed by an electron decaying from a higher shell (HS) filling that hole. The energy of the transition $E_A = E_{HS} - E_{IS}$ can be either emitted as a photon (this is then called X-ray emission) or it is transferred to another electron with a lower binding energy, which acquires enough energy to escape to the vacuum. This second process is the so-called Auger emission. In order that such a process can happen, the decaying electron and the electron being emitted need to have a strong coupling in order for the energy to be transferred between them. This makes the most likely transitions those with the decaying electron and the emitted electron coming from the same level. By this way, the kinetic energy of the electron that is emitted is related to the difference between the energy of the transition minus the binding energy of the emitted electron (E_{B2}):

$$E_{kin} = E_A - E_{B2} - W_A \tag{14}$$

As the energy of the emitted electron doesn't depend on the energy of the photon, this process can be easily distinguished from the direct photoemission process by the use of two different photon energies.

There is a particular case of coherent Auger emission that should be mentioned, especially because within this work it is relevant for a photoemission process called Resonant Photoemission. In the coherent Auger process, the photon energy is chosen to be identical to the sum of the binding energy and the energy of a partially *empty* level, approximately when the photon energy equals a binding energy of a transition $h\nu = E_A$. The excited electron is transferred into this empty level leaving the atom excited and with a high probability for decaying of that electron back into the original level. If the transition occurs for the same shell, i.e., the same principal quantum number *n* (e.g., 4d→4f transition) the decay probability trough Auger emission will be enhanced (Coster-Kronig process[118]). The probability of the Auger electron increases even more for Auger processes with the decaying and leaving electron from the same sub-shell, i.e., with the same orbital angular momentum quantum numbers *l*. Such a process is called a Super-Coster-Kronig process[118]. In general, the total process can be summarized as an electron of a filled core-shell that is excited into a partially-filled shell and decays back to the original state. Then, it gives its energy to another electron of the partially-filled shell (see Figure 18). Taking into account that all the process is elastic, the energy of the final excited electron will be the same as if it was directly excited by the photon, that is, its binding energy will be given by Eq. 12.

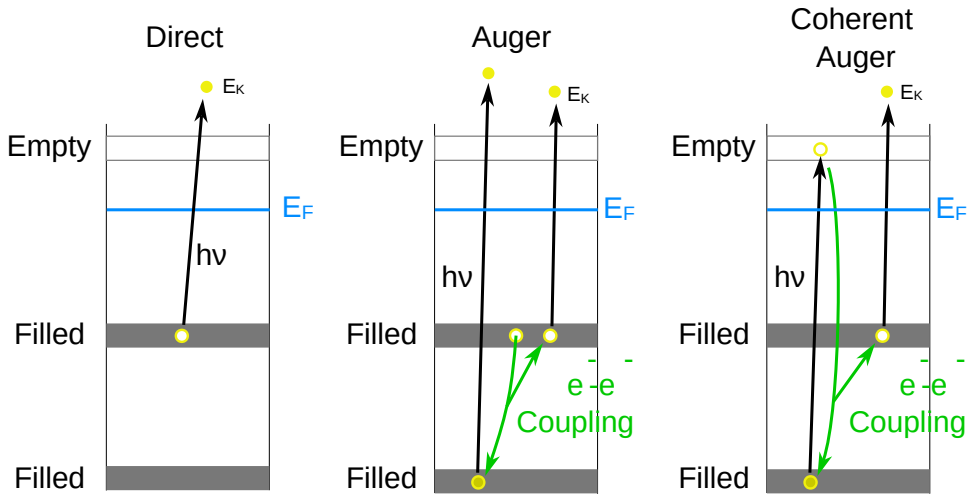

Figure 18: Different electron emission processes observed in a photoemission experiment.

When the photon energy is chosen around the appropriate absorption edge (4d→4f in our case of interest) all three processes will occur. This will lead to a Fano interference[119] between the direct photoemission (continuous transition) and the Coherent Auger process (discrete transition). This creates an enhancement of the photoemission intensity at the resonance energy with a strongly asymmetric profile as a function of the photon energy. Consequently, Resonant Photoemission can be carried out by measuring with a photon energy at the maximum of the interference (on-resonance) and at a photon energy below the absorption threshold (off resonance)[120–123]. This method presents several advantages. First, it allows to obtain a higher photoemission intensity for a certain electronic level compared to direct photoemission. Second, by taking the difference between on- and off-resonance, the contribution of the selected core level can be separated from the rest of the spectra. The drawback is, that due to the need of having an excitation inside a shell in a partially filled core level or in a sightly hybridized band, resonant photoemission is not applicable in most atoms. But if it can be applied, it is extremely useful as for the case of the lanthanides that will be investigated here. We will see the advantages of this method in sections 5.2 and 6.2.

4.3.2 X-ray photoemission spectroscopy

X-ray photoemission spectroscopy (XPS) (or the historical name of Electron Spectroscopy for Chemical Analysis (ESCA)) is used as a chemical analysis tool to study the core level electrons of the elements. In order to excite the core levels, generally photon energies above 100eV are used. This photon energy range correspond to the soft X-rays, which gives the name to this technique. Since the core level energy positions are specific for each element, one can identify clearly the elements that compose a material. Although the deep core levels are strongly bound to the cores, their energy suffer small deviations induced by the electron cloud surrounding them. Therefore, the XPS technique results extremely powerful, since a chemical interaction changes the number and energy of the surrounding electron cloud. These small deviations of the core levels energy are

related to the atom environment and possible chemical interactions with other neighboring atoms.

There are different effects that can induce a change in the core level energy. One of the main effects that induce a change in the core level energy of an atom in a material is due to a change of its valence. Usually, this effect is detected by a large core level energy shift that is due to the transference of an electron from a shallow core level to the valence band or vice versa. This process induces a strong change in the e^--e^- interaction, which produces a big difference in the electron energies. In this thesis, it will be later shown that this situation is observed in the change of valence in Samarium from divalent to trivalent (sections 5.2.1.1 and 6.2). Such a reduction in the number of electrons in the 4f shell produces a reduction of the shielding of the nuclear charge, which changes the potential that the electrons see. The latter cause that the energy needed to extract the electron from the core levels increases their binding energy, this will be further explained in sections 5.2 and 6.2. Another effect that can be detected as a core level shift is related to modifications of the chemical environment of the atoms. An example of that is the binding energy change observed in the C atom depending on its bonding. For example, there is a difference between a C-C bond or a C-N bond related to the fractional charge that the nitrogen atom takes from the C sp valence level. The latter will sightly reduce the shielding in C 1s level, and hence there is a slight increase in its binding energy (section 7.1.2).

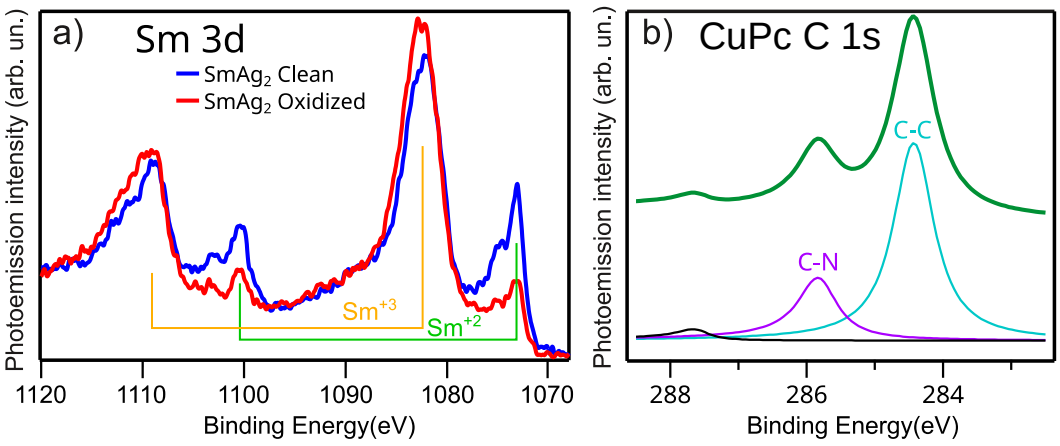

Figure 19: Different effects that cause a shift in the core level energy. a) change of valence of a part of Sm atoms in a monolayer of $SmAg_2$ due to partial oxidation. The oxidized Sm in the sample reduces the divalent component in the alloy by forming trivalent Samarium oxide. b) C 1s core level of CuPc that presents different emission energies due to the different chemical environment of C in the molecule. C bonded to nitrogen (C-N) appears at slightly higher binding energy than the C bonded to C (C-C).

4.3.3 Angle-resolved photoemission spectroscopy

Another particular case of photoemission spectroscopy is Angle Resolved Photoemission Spectroscopy (ARPES). It is characterized by the simultaneous determination of the electron energy and the electron emission angles from the surface. In ARPES, the energy and momentum of the electrons inside the material will be determined. This spectroscopy technique samples the material in the reciprocal (momentum) space. It constitutes a direct determination of the band structure of the

material, or from a different point of view, the dispersion relation of the electrons in the material. In the fist perspective, it constitutes a fingerprint of the interactions established between the electrons and the structure of the material. It is worth to note that except of the most simple cases, frequently complex simulations/calculations are requires to disentangle the electron behavior and allow an interpretation of the results.

If we analyze the momentum and energy conservation of the excitation process we will have to fulfill:

$$k_f = k_i + k_{photon} \tag{15}$$

$$E(k_f) = E(k_i) + h\nu \tag{16}$$

Here, k_f is the momentum of the excited electron in the final state, k_i the moment of the electron before excitation (initial state), and k_{photon} the momentum of the incident photon causing the excitation. Considering that the electron momentum inside of the material shows periodicity in the *k*-space range of the inverse of the lattice parameter due to Bloch's theorem[94] and that the lattice parameters is in the order of Å, our region of interest will be of an order of magnitude of $1\,\mathring{A}^{-1}$. If we now apply the De Broglie relation to the photon[124], the photon momentum k_{photon} for a photon energy around 20 eV, will be of the order of $0.001\,\mathring{A}^{-1}$. Therefore, it is reasonable to state that the excitation of the electron will not change its moment.

Next, we will explain what will happen during electron transport to the surface. We will only consider the electrons that have not lost its energy, i.e., only direct emissions ignoring for the moment inelastic scattering. During the escape from the surface, it is worth to separate the electron momentum in parallel and perpendicular components to the surface. Approximating the surface as a potential barrier, in the parallel component we will not have change of momentum as that direction is invariant under translation. In the perpendicular direction, however, due to the discontinuity caused by the potential barrier, a contribution to the perpendicular momentum needs to be added. In this thesis, mainly two-dimensional surface related systems will be investigated. In the 2D case, the confinement of the electrons in the direction normal to the surface causes a broad momentum distribution in that direction. This broad distribution of momenta removes the need to examine the momentum conservation in the normal direction. This way, in this work only the momentum parallel to the surface will be examined.

With that in mind and by applying the relations between the momentum and kinetic energy of the free electron outside of the material ($E = \hbar^2 \cdot k^2/(2m_e)$), we can determine the parallel momentum inside the material as:

$$k_{||} = \frac{1}{\hbar}\sqrt{(2 \cdot m_e E_K)} \cdot \sin(\theta) \tag{17}$$

Here $k_{||}$ denotes the electron momentum parallel to the surface, m_e the electron mass, E_K the electron kinetic energy and θ the angle of emission of the electron with respect to the normal of the surface and $E_K = \hbar\omega - W_S - E_{bin}$ with W_S the sample work function. Since all these values are known from the experiment, the momentum can be extracted from each measurement point. As a

result, photoemission then give us a mapping of the band structure as the photoemission intensity distribution in energy versus momentum.

4.3.4 Light generation

There are different ways to generate the necessary photons for the photoemission process. During this work, X-ray vacuum tubes, discharge lamps and synchrotron radiation is used. In X-ray tubes, firstly a few keV *electron* beam is directed to a metal target of a certain material. In the same way as in the photoelectric or the Auger process, an inner lying core electron is removed and this process is followed by electron recombination from higher energy shells giving rise to Auger electron and/or X-ray emission. In our case now, we are only interested in the X-ray emission. To eliminate Auger electrons, usually a filter in the form of a thin foil is used. The characteristic of this process is that there are fixed emission lines determined by the anode material. Choosing an adequate material, like Al or Mg, the number of emission lines (photon energies) can be reduce to a single one. In this work, the sources had an aluminum cathode. Furthermore, bremsstrahlung radiation is generated. It has a broad spectrum but due to the low intensity achievable for a monochromatic beam, is not used as a light source for photoemission. It is easy to eliminate by a high pass filter. The result is an x-ray beam with a well-defined energy distribution (around 1eV), which is suitable for most chemical analysis experiments. It is necessary to mention that these sources have a limited maximum intensity, usually defined by how efficient is the heat dissipation of the target. The sources are compact and relatively cheap, therefore adequate for laboratory use. In order to get higher flux beams or tunable wavelengths, it is necessary to use synchrotron sources. Coming back to our laboratory source, we have to mention that here a special source has been used that has two additional specialties. First, the source use a monochromator, and second the light spot is concentrated in a so-called micro-size spot. The latter is slightly misleading since the spot size is in the 500μm size, not in a few μm range. In any case, this is already a big advantage, normal X-ray tubes have spot sizes of several mm. The monochromator is used to filter out small side lines of the photon energy (e.g., Al K_β light) that results in a better energy resolution (0.2eV instead of 1eV) of the photon source.

As seen in Figure 2, kinetic energies of approx. 20-200eV are the ones with very high surface sensitivity. This means that surface sensitivity for valence band requires photon energies in the range of low energy X-rays or ultraviolet light. Such photon energies can be generated trough two common ways, gas discharge lamps and again synchrotrons. In the gas discharge lamp an inert gas plasma is created within a gas cell at a certain pressure. The plasma is usually generated from a discharge of electrons emitted from a filament or cathode accelerated by a voltage of about 100 V. This leads to inner shell electron losses and electron decay from higher energy levels leading to photon emission of light according to the difference of the involved electron levels. One common chosen gas, and the one used in this thesis, is helium. It has several photon energy emissions, the most intense one at 21.22eV[125] with a very low linewidth called He I_α or simply He I emission. There are less intense emissions, here I want to mention only two, He I_β, at a photon energy of 23.1eV and He II_α with 40.8eV. In order to do not mix emissions from the different photon energies, sometimes a monochromator is used to be able to separate the photon energies. This is the case of the described experiments during this work. As in the case of X-ray vacuum tubes, the maximum light intensity is limited by the construction of the lamp.

In a synchrotron, light is generated through bending of a high energy (GeV) electron beam (or other charged subatomic particles in special cases). This bending is done though either a simple bending magnet or a undulator. The first just applies a constant magnetic field and generate a broad spectral distribution up to a maximum energy set by the applied field and the electrons energy. In a undulator (see Figure 20), the magnetic field that changes the electron path is set to form a sinusoidal trajectory in such a way that the emission of the extreme point of the trajectory interfere. As an effect of this path, the spectral distribution is centered in a maximum that is selected by the intensity of the field and that can be modified by changing the gap of the undulator. By tuning this magnetic field intensity, the emission can be selected to maximize the intensity in the photon energy needed for the experiment. Furthermore, by changing the phase (either mechanically or electronically in newer models) between the rows of magnets, the polarization of the generated light can selected. More information can be found in [126,127].

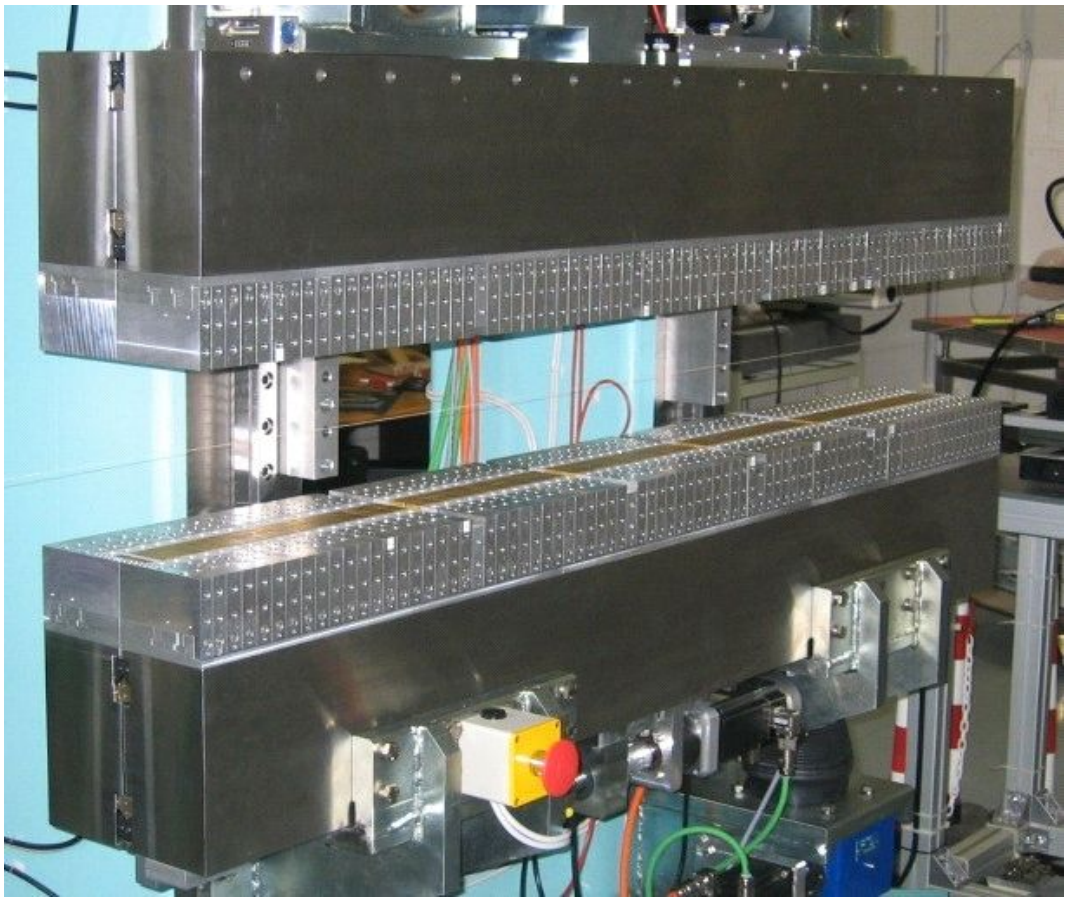

Figure 20: Apple II high photon energy HU60 undulator. The undulator is built from rows of alternated magnetization direction of permanent magnets which create a periodic alternating magnetic field. This field is designed to give the electrons a sinusoidal trajectory which creates interference of the photons emitted by their trajectory bending. Reproduced from [128].

Independent of the insert used, in both undulator and bending magnet beamlines, an optical system

is needed to deliver the light towards the sample. The first device after the undulator has to be a set of heat resistant mirrors to absorb the raw power of the photon beam (hundreds of W) and focus the beam into the entrance slit of the monochromator. Due to the need of dissipating high power without deformation, this mirrors are usually refrigerated. After that, the monochromator is placed. There are different types of monochromators, but in all cases the monochromatization is based on diffraction of the light by a grating, with the specific construction of the grating adapted to the needs of the experiment. It is also possible that several gratings exist that can be exchanged in order to cover a higher photon energy range. The energy resolution of the light will be set by this monochromator. It will depend on the grating linespacing as well as on the entrance and exit slits gap. The reduction of the beam photon energy width (mostly due to a closure of the exit slit) will also reduce the beam intensity, so a compromise between the energy resolution, signal to noise ratio and measurement time has to be found. Finally after the monochromator, additional optical elements/set of mirrors may exist to bring the light from the monochromator to the sample. These mirrors will also have the function of focusing the beam, and will determine the spot size at the sample position. A usual construction uses two bendable mirror that allow adjusting the beam size in the horizontal and vertical direction independently.

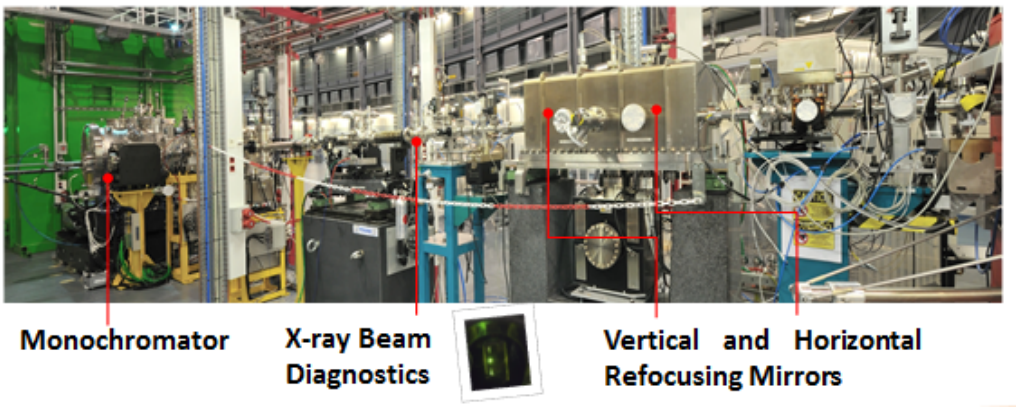

Figure 21: Beamline optics of BOREAS Beamline of Alba synchrotron that was used for X-ray absorption and XMCD measurements. The optics are composed of a heat absorber set of mirrors (not seen in the figure) a variable spacing plane grating monochromator, and a second set of bendable mirrors in a Kirkpatrick-Baez geometry to focus the X-ray beam on the sample. Reproduced from [129].

4.4 Scanning tunneling microscopy

Scanning tunneling microscopy (STM) is a real space non-optical microscopy that was developed by Gerd Binnig and Heinrich Rohrer in 1981[130]. A complete overview of STM is beyond the scope of this chapter but the most critical points will be introduced here. Extended details about STM principles can be found in [131]. In the following we will mainly focus on the working principle of STM. This technique is based basically on two particular concepts: the scanning probe microscopy (SPM), and the quantum tunneling process. The SPM is the base of many different microscopy techniques and relies on the movement of a probe over the surface of a sample in order to record a

certain property of the sample. The tunneling process consists in the fact that an electron crosses a thin energy barrier that is higher than the energy of the electron[132]. This process is forbidden in classical physics, but it is an effect that is allowed in quantum-mechanics. In this process, a current between two conductors that are not in direct contact is established. The probability of tunneling T of the electron is expressed in Eq. 18. It decays exponentially with the distance between the two conductors.

$$T = \exp\left(-\frac{2 \cdot d}{\hbar} \cdot \sqrt{2 \cdot m_e \cdot (E_{Ba} - E)}\right) \tag{18}$$

Here, d is the distance of the barrier, m_e the mass of the electron, E_{Ba} the energy barrier and E the electron energy.

With that in mind, a STM apparatus consists of an atomically sharp tip that is approached very close (distance in the order of nm) to the surface of a sample in order to establish a tunneling current that is used to image the sample surface. A schematic representation of the STM mechanism is given in Figure 22. The STM tip is moved by piezoelectric motors in three directions, being able to scan in the X and Y directions (in the plane of the surface), but also in the Z direction, which is the direction perpendicular to the sample surface.

There are two common methods to scan the surface: a) keeping a constant height between tip and sample surface and recording the current (constant height mode) or b) adapting (and recording) the Z position (height) of the tip while keeping a constant current (constant current mode). In the present thesis, the second method has been used. In order to maintain a constant tunneling current while scanning across a the sample surface, the STM tip height (distance between STM tip and sample surface) has to be adjusted. The feedback loop is the mechanism that corrects the tiny differences in the voltage output of the piezo-motor drive by comparing it with the demanded set-point value. The feedback mechanism is crucial because it tries to adjust the tip-sample distance during measurement by maintaining the tunneling current. In this configuration, the risk of hitting the sample surface due to the presence of different features like steps, clusters, etc. is minimized by the constant adjustment of the tip-sample distance.

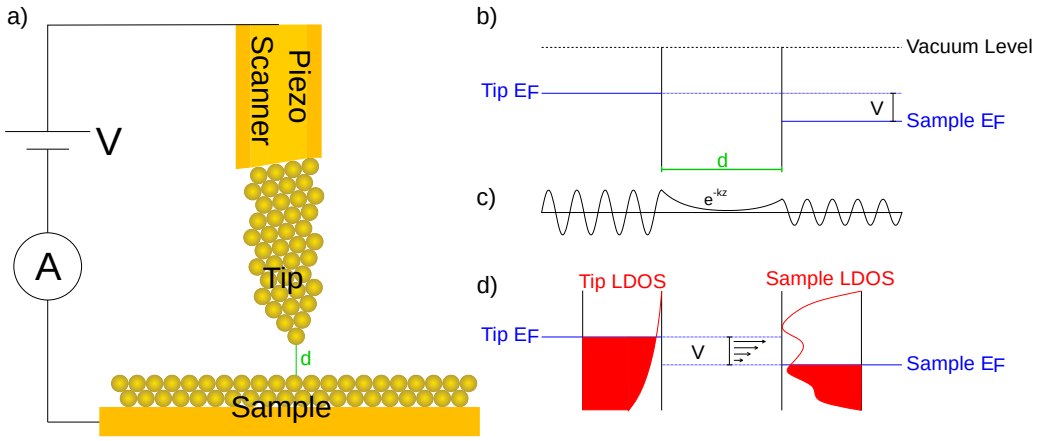

Figure 22:Basic working principle of STM. a) Scheme of the STM tip fixed to a piezoelectric scanner, the investigated sample and the electric circuit applied between both. b) diagram of the electron tunneling process established by the proximity of sample and STM tip, c) the associated electron wavefunctions. d) diagram of the scanning tunneling spectroscopy (STS) process consisting of a tip with a smooth local density of states (LDOS) to determine the LDOS of the sample. Inspired by [47].

Until here, the only parameter we have considered in the tunneling process is the tip-sample distance. As it is shown in Eq. 18, by recording the tip position in a constant current mode, the sample topology should be obtained. Nevertheless, another consideration has to be made with respect to the electronic structure of the sample. Following Bardeen quantum tunneling formalism[133] and applying it to STM geometry, Tersoff and Hamann introduced an Eq. for the STM current [134]:

$$I(V) \propto \int_0^V \rho_T(E-V)\cdot\rho_S(E)\cdot T(E,V,d) \tag{19}$$

With I being the tunnel current, ρ_T the tip local density of states (LDOS), that is, the number of electronic states at a determined energy position. ρ_S is the sample LDOS, T the transmission probability and V the applied voltage.

From Eq. 19 we can see that the intensity as function of the applied voltage is proportional to the correlation function between the density of states of the tip and sample. This has several consequences. To start with, the measured current depends completely on the tip density of states (DOS), which in turn depends on the characteristics of the tip. Usually, the tip LDOS is unknown, which produces severe limits of the modeling and interpretation of the technique. In most cases, it can be partially solved by choosing a tip with a smooth (as constant and featureless as possible) density of states. This can be archived by testing the tip on a known sample. The second consequence of Eq. 19 is that the tunnel current will be proportional to the local density of states (LDOS) of the sample at the applied voltage with respect to the Fermi level. This means, that the STM measurements are influenced by the shape of the atomic or molecular orbitals. By changing the scanning voltage, different features corresponding to different orbitals (or bands) can be

visualized. Another consequence of Eq. 19 is that by scanning the voltage while fixing the position of the tip, the local density of states of the area under the tip can be determined. This method is called scanning tunneling spectroscopy (STS) and is specially interesting in the case of molecules. This dependence on both the scanning voltage and tip characteristics can cause an apparent change on the topography of the sample due to a change of the scanning voltage or a change of the tip. The latter can spontaneously happen during the scanning, like the tip losing an atom or taking it from the surface, or can be forced by application of a voltage pulse or indenting the tip on the sample to improve the imaging.

4.5 Low energy electron diffraction

Low Energy Electron Diffraction (LEED) is a diffraction technique that is sensitive to the surface of the sample. Similar to other diffraction techniques (X-rays, neutrons) the pattern formed by the elastic scattering (here of low energy electrons) on a sample is used to obtain symmetries (rotational and translational) of the studied sample.

As all diffraction techniques, it relies on the wavelength of the probe, that must be of the order of the size of the structures to be studied. Taking the de-Broglie relation[135] and the energy of non-relativistic particles, the wavelength of the electron follows Eq. 20. Here, distances vary from the order of angstroms to nanometers, that means energies from tenths to hundreds of electron-volts. Producing electrons with these energies is relatively easy as they can be generated with a hot filament that emits the electrons and an accelerating voltage to give them the energy, even though optics are necessary to keep the beam focused and collimated. The de-Broglie wavelength λ of the electron as a function of the electron energy E_K is expressed by (h Planck's constant, m_e electron mass):

$$\lambda = \frac{h}{\sqrt{(2 m_e E_K)}} \tag{20}$$

As mention before, the chosen range of energy from this equation cause that electrons interact strongly at the surface, with penetration of few Å, see Figure 16. This makes the technique very surface sensitive, which means, that it allows us to study the surface of the sample, rather than the bulk.

The LEED pattern is formed by the interference of the electrons scattered by each atom. Determining the intensity of electrons as a function of the angle is a complex problem (requires a complete theoretical study), but the determination of the angles at which we will have intensity is quite simple, as it is only necessary to solve the interference. As usual in interference problems, it is easier to solve the problem in reciprocal space.

In the reciprocal space, we will define the reciprocal lattice $\vec{g}_i$ of a real space 2D lattice as:

$$\vec{g}_i = \frac{2 \cdot \pi \cdot (\vec{a}_j \times \vec{n})}{|\vec{a}_i \times \vec{a}_j|} \quad j = 1, 2 \tag{21}$$

With $\vec{a}_1, \vec{a}_2$ the real space vectors defining the lattice, and $\vec{n}$ the unitary vector normal to the lattice. The Laue conditions, which express the conditions required for diffraction to occur, in a two dimensional system are given by:,

$$(\vec{k}_i - \vec{k}_f)\cdot\vec{g}_i = 2\cdot\pi\cdot m \quad i = 1,2 \tag{22}$$

with *m* being an integer value. Furthermore, we consider only elastic scattering processes with energy conservation. This means:

$$|\vec{k}_f| = |\vec{k}_i| \tag{23}$$

The Laue condition and energy conservation leads to the Ewald sphere construction (Figure 23) and results in diffraction rods that represent the lateral projection of the reciprocal lattice of the surface. The initial momentum vector $\vec{k}_i$ is drawn ending at the origin of the reciprocal lattice, thus, a circle of radius $|\vec{k}_i|$ will contain all the possible $\vec{k}_f$, according to energy conservation. The intersection between the circle and the rods results in the $\vec{k}_f$ vectors that fulfill the Laue conditions and generate the diffraction pattern.

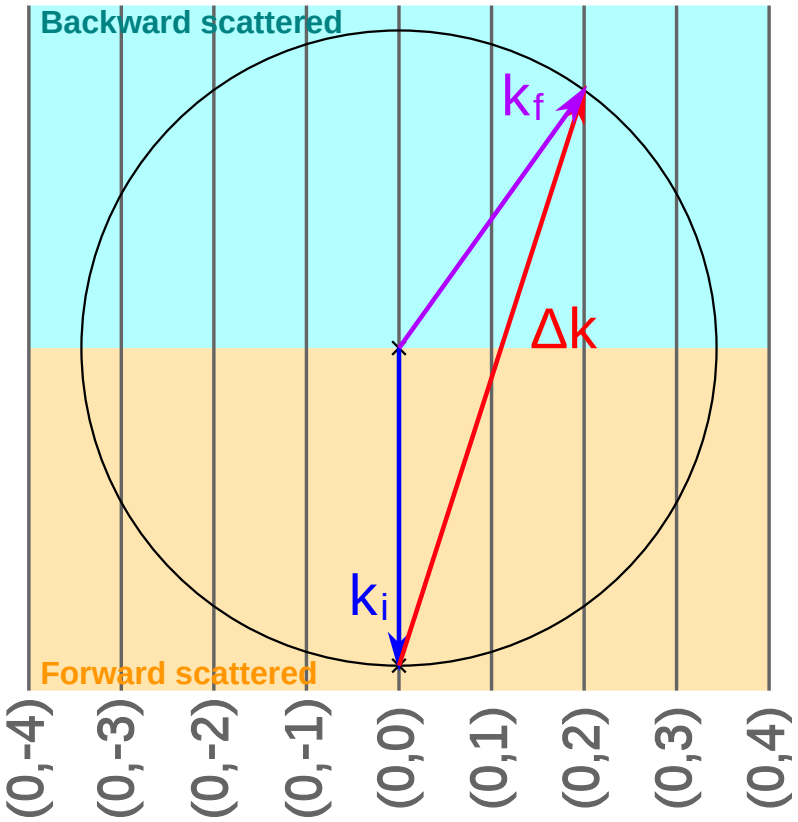

Figure 23: Ewald sphere geometric construction projected on the (0,2) direction.

The experimental setup for LEED measurements consists on two important components. The first one is the electron gun that generates the electrons and focuses them onto the sample by an optical system and the second one consists on several grids and a fluorescent screen (Fig. 24).

The generation of electrons is made by a filament of a high melting point metal that is heated by passing a current thought it. This heating gives rise to some electrons with enough energy that escape from the filament. The application of a voltage between the filament and a ring shaped anode accelerates the electrons to the chosen energy. Finally, electromagnetic lenses are used to focus and collimate the electron beam onto the sample. The focus of the beam allows a reduction of the beam spot on the sample. The collimation of the beam is important, else the diffraction peaks will be broadened for the distribution of angles of the diffracted beam.

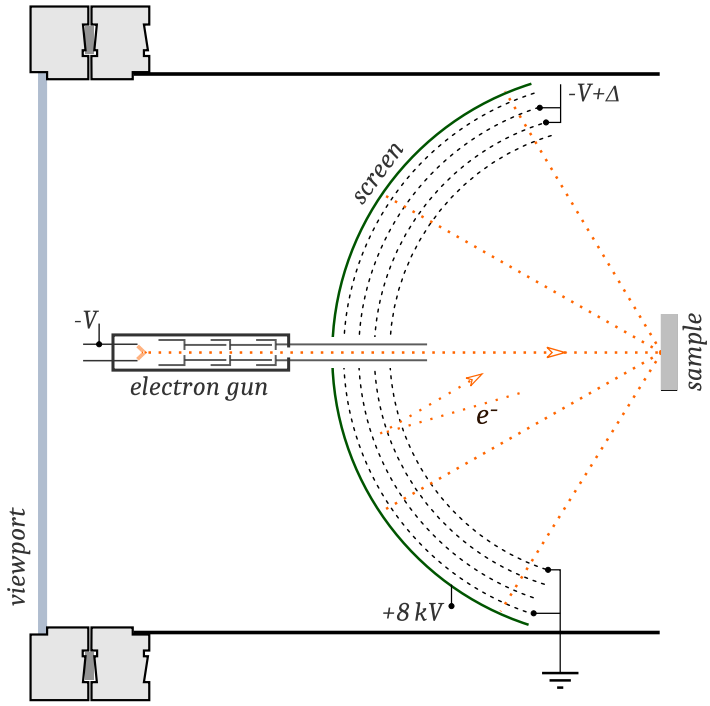

Figure 24: LEED instrument schematic diagram. The electron gun emits a collimated beam of electrons that is scattered by the sample. The scattered electron have to pass a set of grids that apply a high pass filter removing the inelastic scattered electrons and accelerating them to high voltage towards a fluorescent screen. The impacts of the electrons with the screen can then be registered with a camera from the backside viewport. Reproduced from [136].

The detection of the electron diffraction is made in a fluorescent screen detector, to which a high voltage of 5kV-8kV is given to attract and accelerate the diffracted electrons. Just in front of the screen a set of 3 or 4 metallic grids are located. To the inner grids a voltage is applied to reflect the inelastic scattered electrons, which form a large part of the background of the diffracted pattern. The first and last grids are grounded. They shield the sample and the screen from possible effects that come from the inner grids.

4.6 X-ray absorption spectroscopy

X-ray absorption spectroscopy is a versatile technique for the physico-chemical characterization of a sample. As photoemission, it is a photon-in/electron-out spectroscopy routinely used for study of bulk materials but also for surfaces and interfaces. First, the most important difference from photoemission is that XAS proves the empty electronic states, instead of the filled ones. Another difference is that in this technique, instead of keeping a fixed photon energy and scanning in the electron energy, in this case the total generated current is measured as a function of a variable photon energy. The energy of the photon used has to be varied in the range from hundred to thousands eV, which makes XAS nowadays only possible at synchrotron facilities.

XAS is based on the determination of the absorption coefficient of the sample as a function of the photon energy using X-rays as radiation light. An x-ray photon is absorbed, which produces that a core electron is excited to an unoccupied valence band. The absorption coefficient of the material smoothly decreases with increasing photon energy when the photon energy does not match a defined core level excitation. However, when the photon energy matches a core level excitation, there is an abrupt increase in the accessible density of states, which creates a sharp enhancement of the absorption coefficient. Considering the photon energy, we find at the lower energies side the absorption threshold. There, we get a peak structure that reflects the transitions from core levels to empty states. This range is referred as Near Edge X-ray Absorption Fine Structure (NEXAFS). Increasing the energy range, we find transitions to the continuum of empty states of the material. In this range of energy the absorption coefficient is determined by the scattering of the excited electrons by the structure of the material. This last range is called Extended X-ray absorption fine structure (EXAFS). The latter defines a quite common technique to obtain information about the local environment of a certain atoms (distances, bonding) but will not be used in this thesis. We will focus only on the NEXAFS or sometimes simply called X-ray absorption (XAS) process.

The probability W of transition of the electron from a core level to an empty state (absorption cross section) can be defined by the Fermi´s Golden rule[124,137]. In this case it describes the transitions from an initial core state $\langle \Phi_i \rangle$ to a final electronic state $\langle \Phi_f \rangle$.

$$W = \frac{2 \cdot \pi}{\hbar} \cdot \langle \Phi_f | T | \Phi_i \rangle^2 \cdot \delta(E_f - E_i - h\omega) \tag{24}$$

$\delta(E_f - E_i - h\omega)$ indicates that the transition is only possible if the incident photon matches the energy between initial E_i and final E_f states (conservation of energy). The $\langle \Phi_f | T | \Phi_i \rangle$ term requires further comment. This term is the incident photon operator connecting the initial and final states. Due to its complexity, this operator is usually treated in the multipolar approximation. Following the multipolar development of the electric field, this operator can be separated into orthogonal poles. From them usually only the electric dipole is considered, even though several works have shown that the magnetic dipole can also be of importance in nanoestructures[138,139]. In general, higher order terms are omitted as the probability of their transitions is usually several orders of magnitude lower (in the order of 10^{-3} to 10^{-6} times the dipolar probabilities). With this consideration, the allowed transitions will be the ones defined by the dipolar operator. The electric dipole selection rules are the following:

linear polarization:	$\Delta j = 0, \pm 1$	$\Delta l = \pm 1$	$\Delta s = 0$	$\Delta m_l = 0$	$\Delta m_s = 0$
circular left *polarization*:	$\Delta j = 0, \pm 1$	$\Delta l = \pm 1$	$\Delta s = 0$	$\Delta m_l = -1$	$\Delta m_s = 0$
circular right *polarization*:	$\Delta j = 0, \pm 1$	$\Delta l = \pm 1$	$\Delta s = 0$	$\Delta m_l = +1$	$\Delta m_s = 0$

One of the main implications of the selection rules is that a transition is allowed if the spin state of the initial and final states are identical. Another consequence is that the absorption of light imposes a change in the angular momentum of the exited electron. These two rules will be fundamental for the understanding of the XAS and magnetic dichroism.

In analogy to XPS photoemission, core levels XAS is a fingerprint of the chemical composition of the sample and the absorption peaks are element specific. In contrast to XPS, in XAS, instead of scanning in the energy of the photoemitted electrons, the scanning is done by measuring the absorption cross section as a function of the incident photon energy. To remember, it is worth noting that XAS gives information about the unoccupied electron states. This contrasts with the photoemission experiments, which gives information about the occupied electronic states.

In the present thesis, total absorption yield detection was used. In this mode, the absorption is determined by measuring the total current emitted by the sample due to illumination with the monochromatic light beam. This current is dominated by emission of secondary electrons produced by internal Auger decay of the excited states and posterior scattering of the electrons. This secondary electrons have low energy (from meV to few eV) which have much larger penetration length/mean free path (in the order of few nm, see Figure 16) than the primary electrons. Whit this in mind, the obtained information corresponds to few nanometer from the sample surface. This also means that XAS is not so surface-sensitive like the ARPES, XPS or LEED techniques, but still quite sensitive to the surface.

4.6.1 X-ray magnetic circular dichroism

X-ray Magnetic Circular Dichroism (XMCD) is a special case of X-ray absorption spectroscopy. It consists on measuring the absorption coefficient difference between right and left circularly polarized light on a core level absorption edge in a sample most often combined with applied magnetic fields. In order to do this, a sample is illuminated with a monochromatic X-ray beam that is circularly polarized (right and left). For a selected photon energy, the dichroism is the difference in the absorption cross section between circularly right and left polarization. XMCD keeps the chemical sensitivity due to the use of a core level transition, which is specific of each chemical species but adds information of the magnetic state.

If we return to the dipole selection rules introduced earlier, we see that the spin of the excited electrons does not change. The circularly polarized light transfers its angular momentum to the electron. Right circularly polarized light (C+) increases the m_l momentum value of the electron by one, while left circularly polarized light (C-) reduces it by one. A second condition has now to be considered. For NEXAFS, in order for an electron to be excited, it needs an unoccupied final state. As was introduced in section 3.2.1, magnetic samples have an imbalance in the LDOS of the unoccupied states. This also causes an imbalance in the transition into these unoccupied states and hence an imbalance in the absorption coefficient. As a result, the final states after the X-ray

transition reveal a spin-polarization that is opposite to the magnetization of the material. This means that the intensity in the XMCD signal is proportional to the magnetization. Experimentally, in XMCD one measures two (or more) XAS spectra with left and right circularly polarized light directly one after other. It is important to say that there are also instabilities in the beamline as well as in the synchrotron light that requires that such measurement sequence (usually C+, C-, C-, C+) has to be repeated several times for small signal asymmetries.

Figure 25 represents graphically the electron transition. In this case, the $M_{4,5}$ edge of one RE material (here Gd) is shown since this material class is the main focus of this thesis. Note, that the measurement here was carried out for Gd in a ferromagnetic state. The corresponding electric dipole transition occurs from the 3d core level to the unoccupied 4f level. Fig. 25a) shows the model of the absorption of the $M_{4,5}$ transition, indicating the main contributions to each final spin state depending on the polarization of the material. Due to the preservation of the spin, we can completely separate the transitions in the excited electron spin. In Fig. 25b), the XMCD spectra of Gd is shown, which presents a completely spin polarized 4f core level due to its half filling. As we can see, when we magnetize the material in a direction, we reduce the number of holes it the 4f level in the parallel direction, and we increase the number of holes in the anti-parallel direction. Furthermore, we have to take into account the transition probabilities of C+ and C- light (defined in the magnetic field direction). As a result, at the M_5 absorption edge, the probability of transition will be higher for the C- transition, and at the M_4 transition the C+ spectrum is enhanced[140,141].

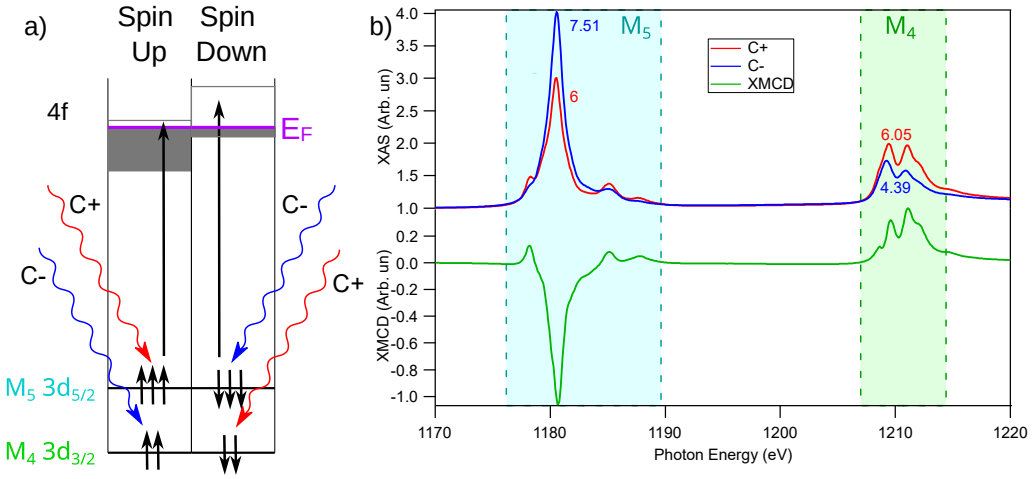

Figure 25: Description of XMCD for RE $M_{4,5}$ transition depicting the dominating incident polarization for each final spin state. a) Scheme of the absorption process separated by spin polarization and indicating the dominant polarization for each transition. b) XMCD spectra of Gd $M_{4,5}$ in $GdAu_2$ indicating the integrated areas of the peaks.

Due to the focus of this work towards RE based material (i.e., the rare-earth noble-metal alloys and the $TbPc_2$ single molecule magnet), deviations from the dipolar selection rules has to be considered. This last problem usually is not of importance in the case of transition metals, but in the case of the RE it has to be taken into account. In the RE atoms, the high magnetic moment together with the strong spin-orbit coupling allow that the magnetic dipolar transition reach a similar order of

magnitude as the electric dipolar term or will be even enhanced by the anisotropy in the charge distribution of involved core levels[142,143]. This last problem will breakdown the sum rule analysis typically used to obtain the orbital and spin moments in the transition metals[141,144].

The basic setup for XAS-XMCD measurement in Total Electron Yield (TY) detection is depicted in Figure 26. It includes the energy-tunable polarized monochromatic beam, a metallic grid (here Au-mesh), the sample for which temperature and angle respect to the beam can be controlled, a coil for generation of variable magnetic fields, and electrometers for the grid and the sample current measurements. The mesh and the sample have to be electrical insulated in order for the charge to pass through the electrometers. One has to take into account that the optical elements of the beamline also undergo similar NEXAFS and EXAFS absorption that may cause an inconstant number of photons. In order to remove such effects, the Total electron yield current of the sample has to be normalized. For this purpose, usually a gold mesh behind the last mirror of the beamline is used. For most of the here used transition range energies, Au presents a relatively flat XAS signal and is therefore adequate for such normalization. The correct absorption signal is then the measured TY current of the sample divided by the TY current of the mesh. The rotation of the sample allows to carry out measurements in different sample orientations with respect to the beam and applied magnetic field. During this thesis, the applied field direction was always parallel (or anti-parallel) to the beam. Furthermore, two geometries were used. One is the so called out-of-plane (OOP) geometry. Here, the incidence of light and applied magnetic field is normal to the sample surface. The other one is called in-plane (IP) geometry with the beam and applied field applied forming a 70º angle with the normal of the sample surface. In IP geometry it is not possible to rotate to 90º because in such a case the beam would be parallel to the surface. Already the use of angles higher than 70º makes the alignment of the sample difficult and unreliable, as the surface section becomes too small to be well aligned and there is a certain risk to illuminate the sides of the sample as the spot size in the sample increases a lot.

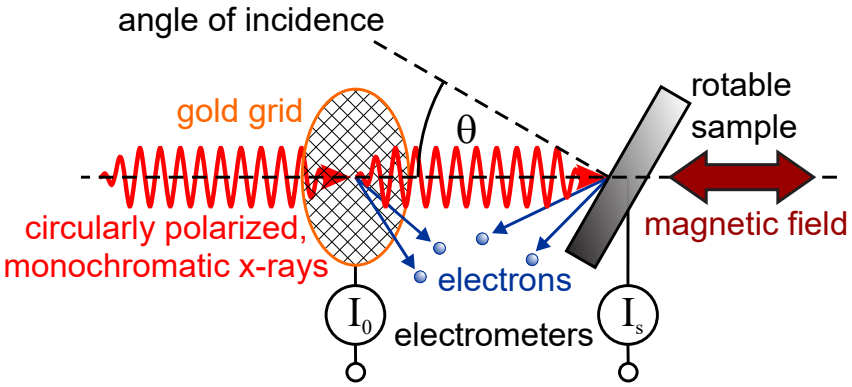

Figure 26: Schematic drawing of the experimental setups used for XAS and XMCD measurements with definition of the light incidence angle θ. Reproduced from[140].

XMCD spectra are measured by recording the X-ray absorption intensity as a function of the photon energy, which is scanned around the absorption edge of interest. These measurements are performed

separately with both polarizations, C+ and C-, for a fixed applied magnetic field. As a result, we obtain absorption spectra measured with C-, and C+, the XAS spectra is the sum of both polarization spectra (“C+” + “C-”), the XMCD spectra is the difference of the absorption spectra for “C+” - “C-”. From the XAS, C+ and C- spectra the information of the chemical state and core level filling can be extracted. The XMCD spectra carries the information of the magnetization, and orbital and spin magnetic moments.

An additional type of measurement consists in taking the magnetization signal as a function of the applied field. Such type of magnetization curved here we will call hysteresis loops. Hysteresis loops are obtained by measuring the XMCD signal as a function of the applied magnetic field, which is scanned in a loop from the maximum positive to negative field, e.g, from +6T to -6T, and then back to the positive field. In order to do so, first the maximum of the XMCD signal has to be determined. One light polarization, e.g. C+, is chosen. Then the signal at the energy corresponding to this maximum and at an energy position before the transition (for normalization) is taken. The field value is changed and the next point measured. This is continuously done until the maximum negative field is reached. Then the TY intensities for the same two photon energies are taken when the field is slowly increased back to the starting field. Once there, the light polarization is changed and the loop is repeated. This method can be as fast as the sweeping of the magnetic field allows. The change of the applied field in the superconducting coils has to be slow, therefore a complete magnetization curve takes long time (around 1 hour). The disadvantage of such slow measurements is that conditions of the sample and in the beamline can change. Such measurements depend very strongly on the stability of the synchrotron and the beamline. This causes that often magnetization loops are quite noisy. Specially, in the case of rare-earth materials the measurements are difficult, since the monochromator is continuously changed between edge and pre-edge position and the exact motor position is not so well defined. On sharp XMCD peaks as the ones for the RE, a small deviation from the edge energy has tremendous effects. Additionally, at low field, the trajectory of the electrons change drastically, causing a fast increase or decrease of the electron yield leading to not reliable values close to zero field. In the usual method of measurement, the field is sweep at a constant rate and the peak and pre-peak are measured alternatively. In such a case, the peak and pre-peak are measured at slightly different times and fields. This makes that at low field, the signals cannot be properly normalized and this method does not work. To solve this, one can measure the low field range of the hysteresis point-by-point as complete XMCD spectra. Nevertheless, this approach requires very long measuring times that are often not available. But, by such a way a full XMCD hysteresis loop can be obtained. Again, such a procedure requires very long measurement time, therefore this method was only applied in a quite limited amount of experiments and only when the continuous measurement method was not giving enough signal-to-noise ratio. Here, it was applied for $CuPc/REAu_2$ (section 7.1.3) and $TbPc_2/REAu_2$ (section 7.2.3).

One important point in the properties of magnetic materials is the critical temperature of the magnetic transition, for ferromagnetic materials the Curie temperature T_C, for anti-ferromagnetic materials the Néel temperature T_N. For this purpose, one requires to measure the magnetic properties as a function of temperature. A good option would be to measure the remanence as a function of temperature. The remanence is the magnetic moment of the sample after removing an applied field.

Nevertheless, for materials with a very small remanence as the 2D films measured here, this procedure is uncertain. Another possibility is to measure the continuous hysteresis loops for several temperatures. This is more reliable but requires time. Furthermore, there are technical limitations to stabilize temperatures in the cryostat in a temperature range between 4 and 20K. In total, several hours are required to measure such magnetization loops in a reliable way for extracting the critical temperature. The analysis method for the extraction of such a critical temperature, the so-called Arrot plot analysis[101] is further described in section 3.2.5.

5 Two-dimensional Au based surface alloys

5.1 Structural analysis

The structural investigations of the RE-Au surface compounds has been focused on 1ML $REAu_2$, although several ML thick films can be obtained[16,46]. For the bulk, the phase diagram of Gd-Au shows a complex solubility of the two metals by the existence of at least 6 known intermetallics. On the surface, though, the number of known phases is smaller. Two stable phases have been achieved for Gd, a monolayer and a trigon phase[16,103]. As mention in section 3.1.3, $GdAu_2$ monolayer is formed after deposition of 1/3 of a ML of Gd on an Au(111) substrate being heated to 720K. In the case of an insufficient evaporation time, the sample will present a mix of patches of continuous $REAu_2$ Moiré and trigons. The trigon phase is formed by small nuclei (cores) of the $GdAu_2$ phase separated by wavy discommensuration lines that incorporate a small amount of Gd. This discommensuration lines cause a repulsion between the nodes, enforcing the cores to order in a lattice with a periodicity of (90 ± 6)Å[45]. On even shorter evaporations, instead of formation of the trigon phase, this cores will seat on the protrusions of the herringbone, causing its deformation. This proves that the discommensuration lines seen in the trigon phase are nothing but the deformed Au(111) herringbone. This limitation of the possible phases at the surface already tells us that the structure of $GdAu_2$ shows a particularly high stability due to a minimization of its surface energy.

To analyze the ordering of the samples, two mathematical transformations have been used: the Fourier Transform (FT) and the Self Correlation (SC).

The Fourier Transform is a fundamental mathematical transformation defined as:

$$FT(\omega,\phi)=\iint f(x,y)\cdot e^{i\cdot 2\cdot\pi\cdot(x\cdot\omega+y\cdot\phi)}\cdot dx\cdot dy \tag{25}$$

A simple way to understand this transformation is that it converts a function from real space into the momentum space (reciprocal space). This transformation has several interests to us, first, a complex periodic structure in real space will transform into a lattice of delta functions in reciprocal space, which allows a relatively simple way to determine symmetries and periodicities of samples. The second property of interest is that Laue conditions of diffraction is easier to follow in reciprocal space. This is the same as to say that for an image of a sample with atomic resolution (like the ones obtained by STM), the diffraction pattern can be calculated by applying the Fourier transform to the image[135].

The self correlation function (SCF) is given by equation:

$$SC(x',y')=\iint f(x+x',y+y')\cdot f(x,y)dx\cdot dy \tag{26}$$

The meaning of the SCF, in simple terms, is the correlation of a signal *f* with a displaced copy of itself as a function of the displacement. In terms of structural analysis, this means that this transformation marks the lattice periodicity while removing the motive. This function is of special interest in the case of the analysis of Moiré patterns (and other long distance periodicities) as the outcome are more intensely marked compared to the FFT and the maximums give clear defined

nodes of the lattice that are difficult to establish in the original images due to the large number of atoms. Even more, this transformation keeps the result in real space, which allows to easily compare the result of the analysis back to the original image to contrast and identify features. Another property of interest in this function is that in reciprocal space, it's FFT becomes the square of the original FFT, i.e., $FFT(SCF)=FFT^2$.

Additionally we will introduce the matrix notation for the reconstructions that we will use during this thesis. The reconstruction will be given by the matrix *M* that fulfills:

$$\vec{b}=M\cdot\vec{a}$$
$$\begin{pmatrix} b_0 \\ b_1 \end{pmatrix}=\begin{pmatrix} m_{0,0} & m_{0,1} \\ m_{1,0} & m_{1,1} \end{pmatrix}\cdot\begin{pmatrix} a_0 \\ a_1 \end{pmatrix} \quad (27)$$

This means, this matrix establishes the relation between the original lattice with basic vector $\vec{a}$ and the reconstruction with $\vec{b}$. The way to obtain this matrix then, is finding how to write the reconstruction lattice in terms of the original lattice, which usually can be done simply by overlapping both lattices, finding nodes, write them in terms of the lattice vectors, and finally reducing the matrix to the simplest form.

5.1.1 Trivalent $REAu_2$ surface compounds

The LEED patterns of all the trivalent $REAu_2$ alloys of this thesis grown on Au(111) are shown in Figure 27. As mentioned earlier, the $(\sqrt{3}\times\sqrt{3})R30^o$ and the Moiré reconstruction appears. In the LEED pattern of $DyAu_2$, Figure 27b), the surface lattice of the "Au(111) surface" in the reciprocal lattice is drawn in red, the surface unit cell of the $(\sqrt{3}\times\sqrt{3})R30^o$ reconstruction in blue. The diffraction spots of the $(\sqrt{3}\times\sqrt{3})R30^o$ are surrounded by satellite diffraction spots (drawn in yellow) corresponding to a short periodicity lattice in reciprocal space, meaning larger distances in real space. They correspond to the diffraction caused by the Moiré reconstruction.

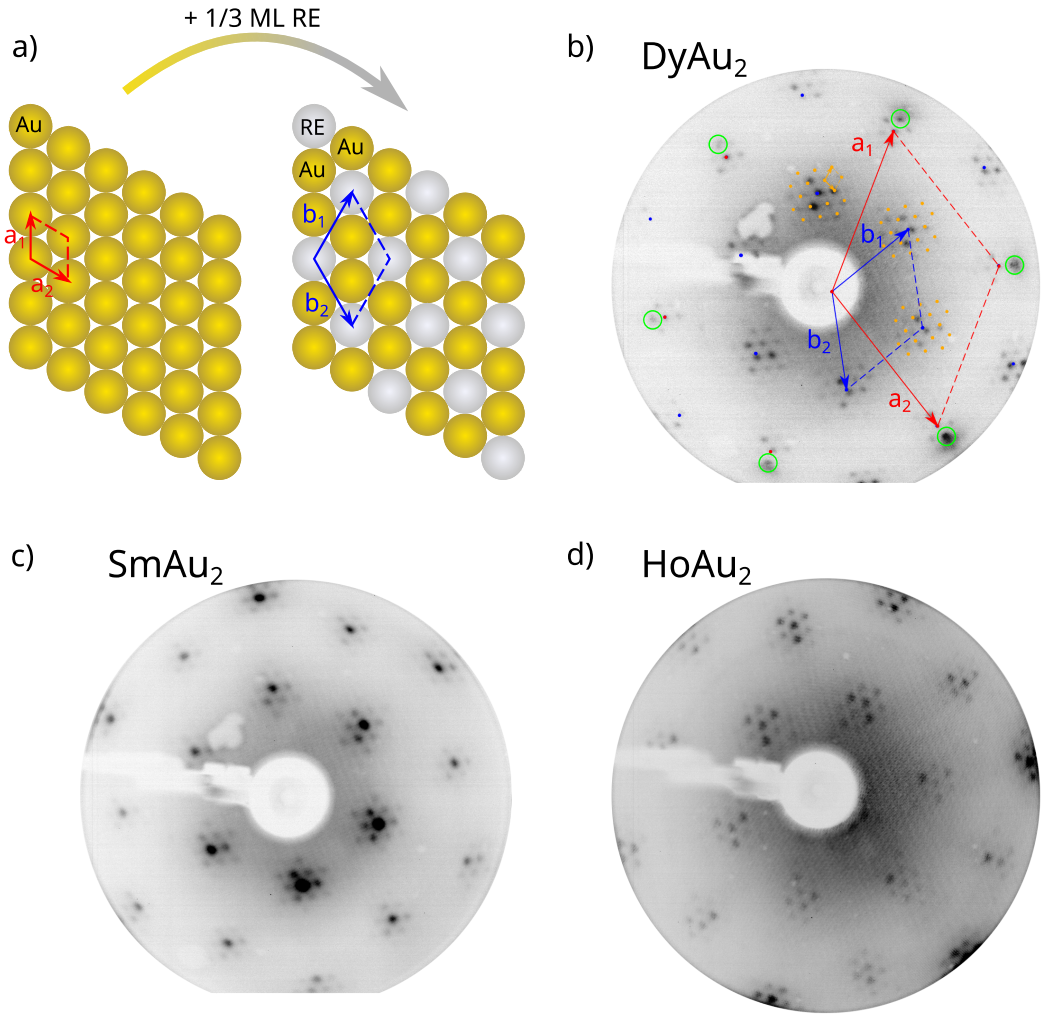

Figure 27: a) Model of a $REAu_2$ surface alloy structure without consideration of the Moiré lattice. b), c), d) LEED Pattern of $DyAu_2$, $SmAu_2$ and $HoAu_2$. The Au(111) surface lattice vectors are marked on red, the $(\sqrt{3}\times\sqrt{3})R30°$ lattice in blue, and the Moiré lattice in orange. The electron energy was set to 60eV for $DyAu_2$ and $SmAu_2$ and 53eV for $HoAu_2$.

In the model of Figure 28, the formation of the LEED pattern will be explained. The $(13\times13)R0^o$ Moiré superstructure in real space is formed by superposition of two hexagonal lattices with appropriate different lattice parameters. The first of this lattice represents the Au(111) lattice (in grey) and the second is a $(13/12)(\sqrt{3}\times\sqrt{3})R30^o$ reconstruction with respect to the substrate and represents the alloy lattice (in blue). From now on, for simplicity, we will refer to all the alloy lattice as a $(\sqrt{3}\times\sqrt{3})R30^o$, even though is not strictly correct. As can be seen, both lattices coincide in the points marked in purple, corresponding to a $(13\times13)R0^o$ lattice, which corresponds to the Moiré. Once this real space structure is understood, we can apply the Fourier transform to get the structure in the reciprocal space, or as was explained before, obtain the LEED pattern. First, in the reciprocal space (seen in the diffraction pattern) one can appreciate a lattice factor of $\sqrt{3}$ and a rotation of the lattice by 30º, called a $(\sqrt{3}\times\sqrt{3})R30^o$ superstructure. Finally, the Moiré superstructure is observed by a small periodicity lattice (in purple) in the reciprocal

space.

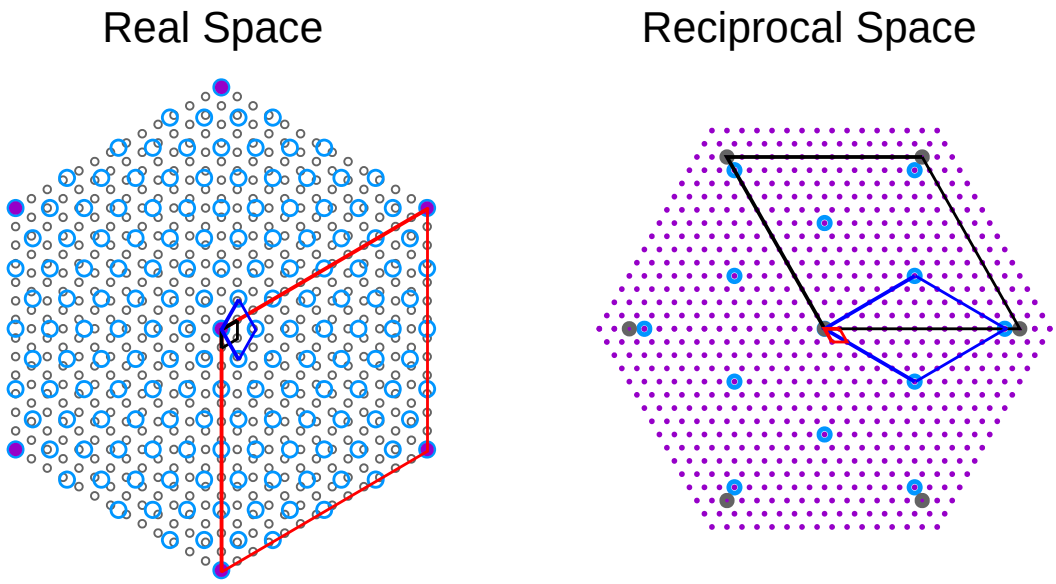

Figure 28: Formation of the Moiré pattern due to superimposition of two lattices with lattice mismatch in real space (Left panel, lattice one: grey atoms; lattice two: blue atoms; Moiré: purple and the corresponding reciprocal space lattice (right panel).

After explaining in detail the model, we can compare the LEED pattern with the model. The main difference between the experiment (Figure 27) and the model (Figure 28) is the amount of visible orders of diffraction of the Moiré. In the experiment only up to the second diffraction order can be seen around the alloy spots. This difference is caused by two reasons, (i) electron scattering probability and (ii) defects. Electron scattering factor is the probability of the electron to be scattered at a given relation of incidence and emission angles. It is determined by charge distribution of the sample. In the low energy regime used for LEED, it is sensitive to small variations, which makes it fundamentally difficult to calculate, as the electronic structure has to be known with high precision. Apart from the dependence on the electronic structure it also shows a strong dependence with the beam energy, and as a result, a change of the electron energy will not only change the scaling of the reciprocal lattice but also the spot intensity. On the other hand side, defects (vacancies, dislocations, size limit of domains, etc.) cause a deviation from perfect order of the lattice giving rise to locally incorrect scattering phase and intensity. As defects we also include jumps in the local superstructure, i.e., a local (10×10) side by side to a (11×11) structure. Such a scenario results in a local order but not in a long range order. This refers to the amount of defects and also to different domains of the Moiré lattice of the sample. Therefore, the quality and sharpness of the Moiré seen in the LEED pattern is a good indication about the quality of the prepared sample. With the adequate electron energy the Au(111) periodicity can be seen over-imposed to one of the Moiré spots (marked in green in Figure 27b)).

LEED gives a quite good idea about the periodic order in the surface, but to obtain the atoms (or molecules) position, as well as other fine details, often scanning tunneling microscopy is better suited. Figures 29a) and b) display STM measurements performed on $HoAu_2$. From these

measurements it is possible to extract the different periodicities observed in the $HoAu_2$ layer. There is one large distance of several nm (tenths of atoms) and one short distance, close to atom size. The short periodicity is formed by an ordered array of small holes. This periodicity can be measured directly in the reciprocal space after executing the FFT of the STM image (Figure 29c)). It presents a rhomboid cell with two unit vectors of 5,4Å and an angle of 120º between the vectors. This value corresponds within experimental error to a $(13/12)(\sqrt{3}\times\sqrt{3})R30^{o}$ reconstruction on Au. Such a superstructure compares well with the structure obtained by LEED and previous works on $REAu_2$[2–5]. Based on that, we can assign that the holes correspond to the position of the Ho atoms. As shown in reference [17] this "texture" is not arising from the topography of the sample but from the used tunneling conditions, especially the tip shape, tunneling current and bias voltage (see section 4.4). Another tunneling current or bias may change the appearance and the Au atoms would be imaged.

$HoAu_2$ STM

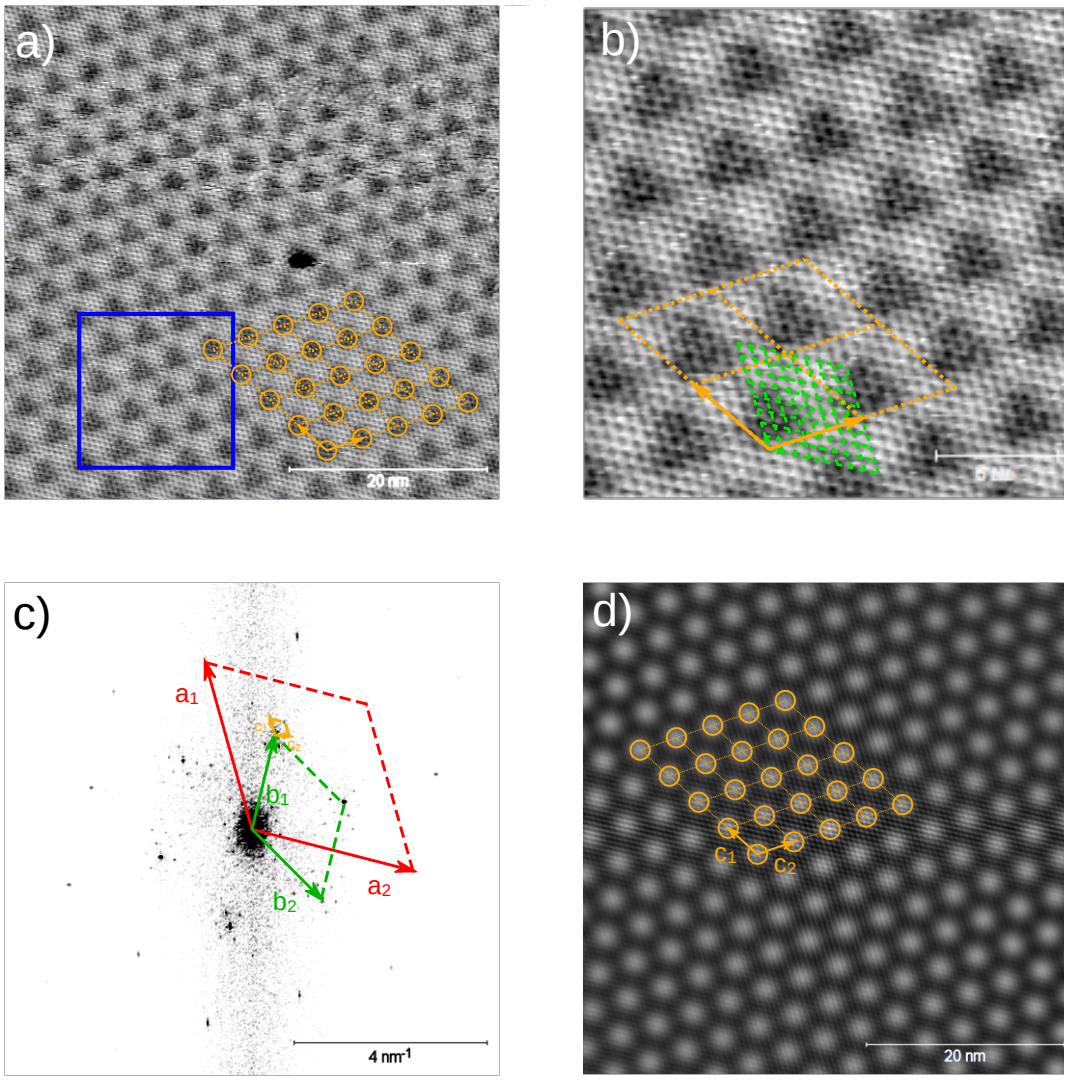

Figure 29: a) STM images of the $HoAu_2$ surface alloy revealing the Moiré undulation and the Ho atoms as black holes (image size 50×50 nm^2, tip voltage 0.85 V, target current 0.3nA.) b) Amplification of the area marked in blue in a), (size 20×20 nm^2, tip voltage 0.85 V, target current 0.3nA.). c) Fourier transform of a) showing the Au(111) surface periodicity in red, the alloy periodicity in green, and the Moiré marked in orange. d) Self correlation of a), the Moiré lattice is marked in orange and can be compared to the STM images in a) and b).

On the long, few nm range one observes a Moiré lattice in the form of a second periodic cell. In order to easily measure this cell, the self correlation function (SCF, Eq. 26) has been used. As was previously explained, that operation marks periodicity in such a way that the lattice can be measured by regression of the maxima (Figure 29d)). That lattice is marked in orange, and shows good correspondence to the original STM image. From that calculation, a lattice of constant of $(3.90 \pm 0.05)\,nm$ is obtained.

Trivalent RE atoms can be classified depending on their 4f orbital filling. On one hand side are the

RE atoms with the 4f half filled or with more than seven 4f electrons. This list includes Gd, Tb, Dy, Ho, and Er that we describe as heavy REs and on the other hand those with less than half filled 4f shell, like for example La, Ce, or Sm. The latter RE are considered as light RE atoms. The classification in the two groups is directly related to the RE atom radii. For the light RE atoms the radius is slightly larger than in the heavy RE ones due to the lanthanide contaction[145]. All the previously reported trivalent heavy $REAu_2$ ($TbAu_2$, $ErAu_2$[146] and DyAu[19]), as well as $HoAu_2$ studied here show Moiré lattices that can be described by $(13\times13)R0^o$. Such a structure can be extracted from atomic resolution images similarly the one in Figure 29b) for the case of $HoAu_2$. For this purpose one compares the lattices of the Moiré undulation and the RE periodicity. In the $HoAu_2$ case, the repetition in the Moiré occurs each 13 atoms of the Au substrate, confirming that the Moiré is commensurate. For the tri-valent light $REAu_2$ surface compounds, the Moiré lattice can be locally described as $(12.4\times12.4)R4.7^o$. Figure 30a) shows a STM image of $SmAu_2$. In general, the STM measurements performed on $REAu_2$ surfaces with light RE atoms (La, Ce) show a local rotation of 4.7°[46]. This small rotation with respect to the substrate is randomly distributed forming domains of few unit cells of the Moiré. This small variations of the Moiré periodicity with respect to the commensurate structures of the heavy RE-Au_2 surface alloys is not visible by LEED due to reduced size of the different domains in the Moiré, which do not contain enough unit cells to produce differentiated diffraction spots in LEED. Therefore in LEED the total average rotation is zero.

A writing of the reconstruction in matrix form allows for more clarity. Table 3 discloses the reconstruction matrix detected for each of the studied $REAu_2$ surfaces by our group and others. It is noticed that for all the trivalent RE, the Moiré is commensurate as all the matrix elements are integers. This point also probes that the observed rotation in the surface compounds with light RE atoms is not a random misalignment, but a precise value required for the adjustment of the $REAu_2$ overlayer to the Au(111) surface. This factor changes the type of reconstruction from $(13\times13)R0^o$ in the case of heavy RE to $(12.4\times12.4)R4.7^o$ for the light ones. The latter is a consequence of the slightly larger RE atoms of the light RE.

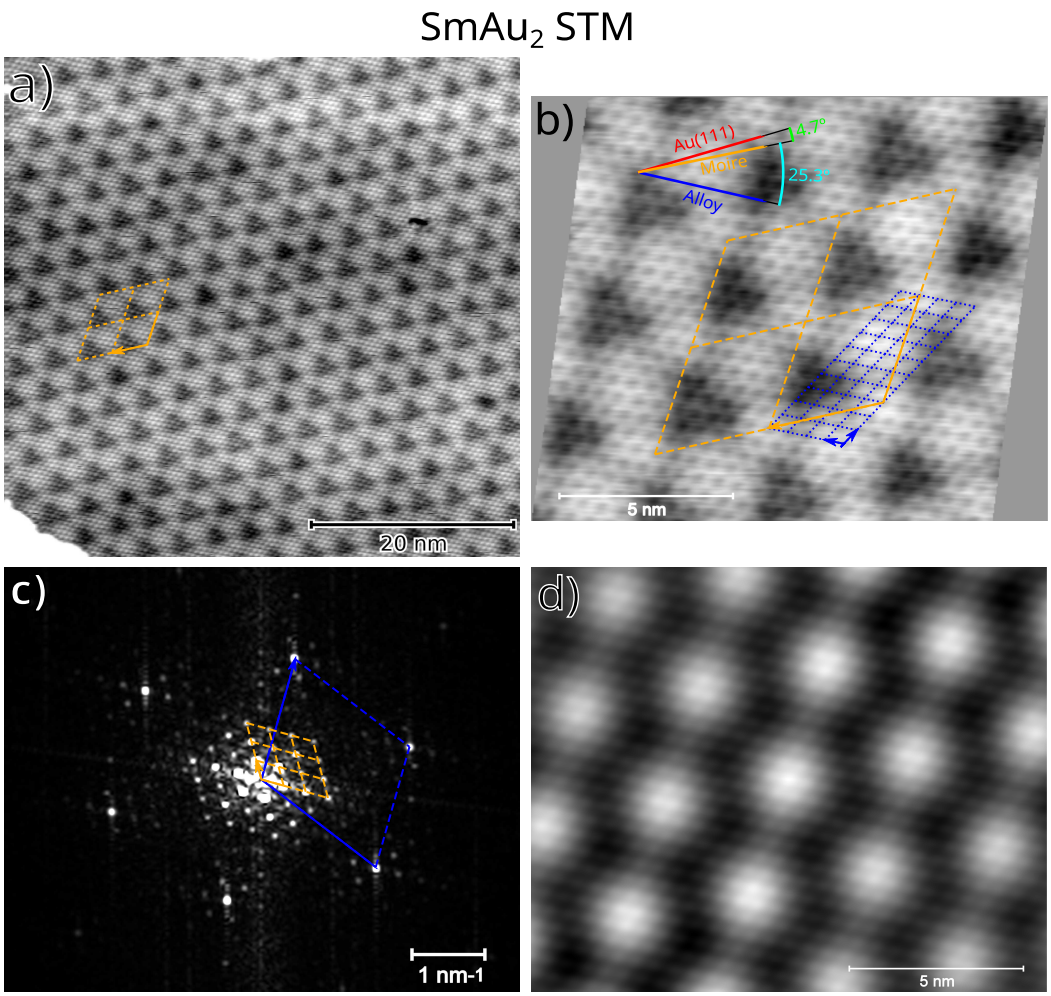

Figure 30: a) Large scale area STM image of $SmAu_2$ showing the high quality of the growth (image size 50×50nm², tip voltage -1.5V, tunnel current 0.3nA), b) STM image of $SmAu_2$ alloy showing Moiré undulation and the Sm atoms as black holes (image size 30×25nm², tip voltage -1.5V, tunnel current 0.3nA). c) Fourier transformation of a). d) Self Correlation of a). In the images the alloy periodicity is drawn in blue, and the Moiré lattice in orange.

5.1.2 Divalent $REAu_2$ surface compounds

In the case of the divalent RE atoms, their structure description has to be addressed apart, as their structure is different from the trivalent cases. The main reason is that the atomic radii expands about a 30% in the case of the divalent atoms with respect to the trivalent ones[147]. This huge expansion means that the previous mentioned Moiré reconstructions observed in $REAu_2$ surfaces formed with trivalent RE atoms cannot fit the larger atoms of the divalent RE atoms. In this work, the two divalent RE atoms were studied: Yb and Eu.

Similar to the case of the trivalent RE, in the divalent RE atoms there are also two groups, the light and heavy RE cases. Although the groups have only one member here, being Eu the light RE and Yb the heavy RE. The Yb size is relatively small and would allow the formation of a periodic alloy without defects. In the long range (Figure 31a)), the surface shows a similar Moiré pattern to the

ones of the trivalent $REAu_2$ alloys. It can also be seen that the LEED pattern is formed by the $(\sqrt{3}x\sqrt{3})R30^o$ alloy and a $(13\times13)R0°$ Moiré superlattice. A more detailed inspection, however, shows that the Moiré lattice does not match the alloy, as equivalent positions in the Moiré would have been occupied alternatively by a RE and a gold atom (following a Au-Au-RE periodic sequence, see Fig 31e)). Nevertheless, as stated before, only one species is imaged with a certain voltage or current. This means that the Moiré is commensurate to the Au(111) but not to the $YbAu_2$ lattice. Finally, the superlattice is best described by a $(13\times12)R4.7°$ reconstruction. The reconstruction matrix with respect to the alloy is more complicated than before but has rational numbers (in molecular surface science such coincidence lattice are characterized as Coincidence II[148]). This means that the lattice coincidence with the Au(111) substrate site does not have preference between the Yb or the Au atoms of the alloy.

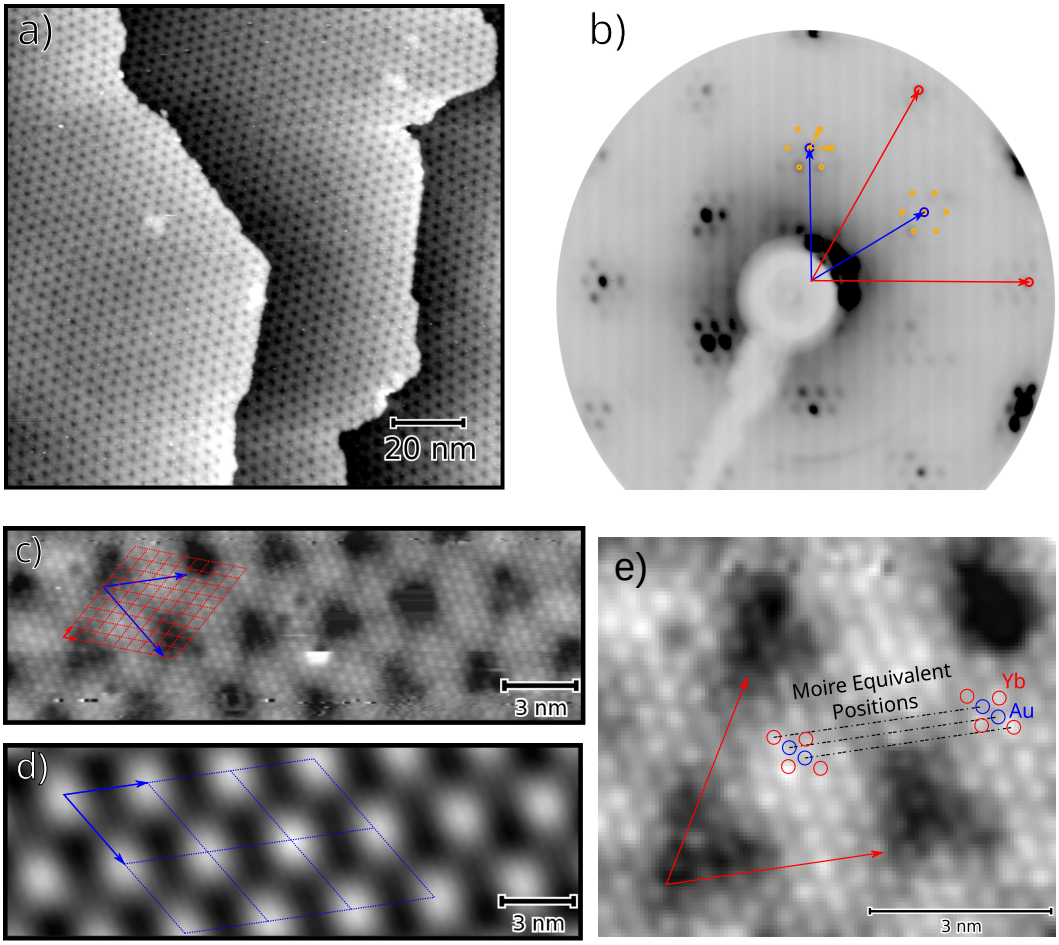

Figure 31: STM images of $YbAu_2$ a) Large scale image showing the Moiré order on long distance (image size: 150×143nm², tip voltage -1.2V, tunnel current 1.4nA). b) LEED pattern of $YbAu_2$ revealing the Au(111) lattice (in red), the alloy lattice (in blue) and the Moiré reconstruction (in orange), c) atomic resolved image of the alloy showing periodic depressions and the RE atoms as white points. This change of the the texture could be related to the higher number of available electronic states due to divalent character or due to a change of the tip (see section 4.4). The alloy lattice is marked in red (image size: 23.9×7.7nm², tip voltage -1.2V, tunnel current 1.4nA). d) Self correlation of b), the Moiré lattice is marked in blue. e) zoom of c) (7×7nm², tip voltage -1.2V, tunnel current 1.4nA) indicating the Moiré lattice and the switching of the element in the equivalent positions of the Moiré.

For $EuAu_2$, the lattice distortion is too high to relax by the formation of just a "simple" Moiré lattice. In this case, we see a nearly flat surface that is relaxed by the formation of atomic "vacancies" of different nature that induce the topographic depressions observed in the surface (see Figure 32a)). The depressions are formed by an average of 7 atoms, but the exact number varies from 3 to 10 vacancies. Additionally, the shape of the depressions is also variable. Moreover, an analysis of the depth (Figure 32b)) of the "vacancies" indicates that only a limited set of values is possible (40, 60, 90 and 110pm). These numbers do not match an atomic layer thickness (236pm in Au[149]) implying that the "vacancies" cannot be formed by a missing atom in the surface. Rather than

a surface vacant, it can be supposed that the relaxation of the surface tension is released by the formation of a vacant in a subsurface layer and a bending of the surface layer to accommodate to that vacant. Additionally, there are single “vacancies” randomly distributed in the surface. Finally, as can be seen in the SCF (Figure 32c)) that the depressions (not the vacancies) are distributed in an ordered pattern, producing the Moiré-like spots in LEED (Figure 32d)), similar to the ones of the trivalent alloys of the previous section (5.1.1). From the analysis of the STM image following the atom and depression lattice (in the SCF image) we can extract a surface reconstruction of $(11.5\times11.5)R4.3°$ which, as can be seen in the matrix form in Table 3, has integers in the transformation matrix with the alloy, showing again that it is commensurate to the Au(111) substrate.

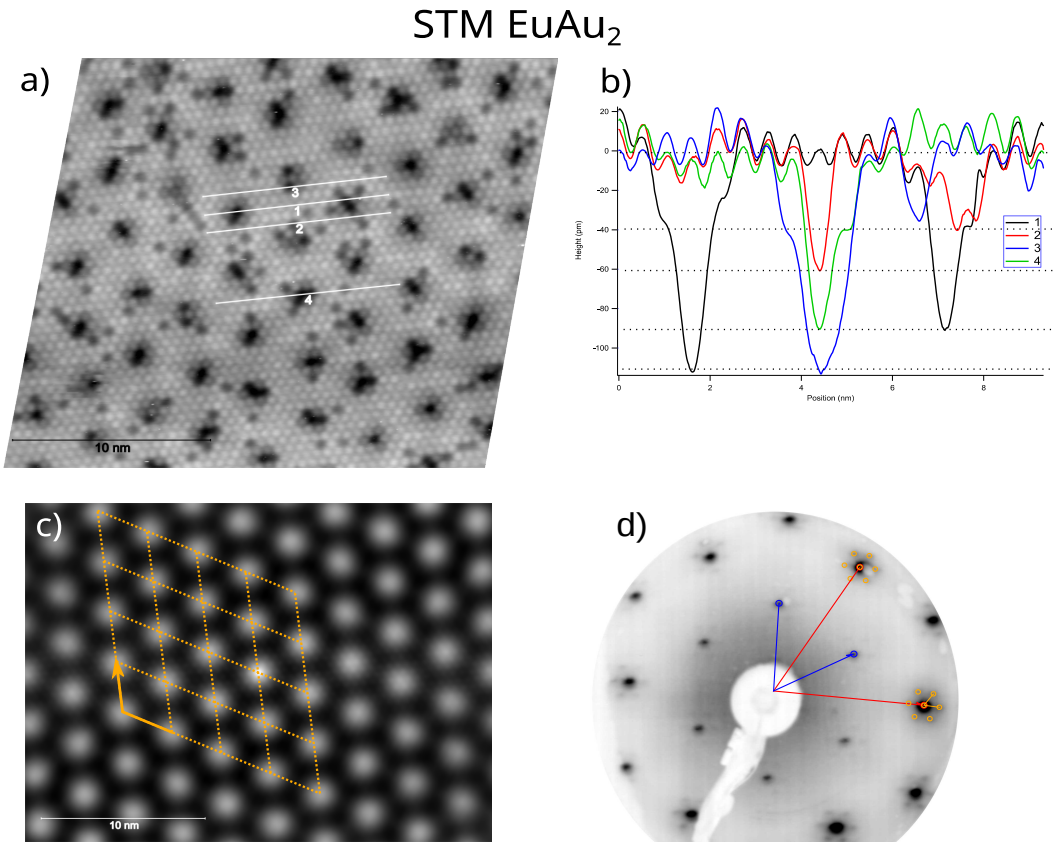

Figure 32: a) STM image of $EuAu_2$ alloy showing periodic depressions and the RE atoms as white protrusions (image size 28.5×22nm² tip voltage -1.5V, tunnel current 0.3nA). b) Depth profiles taken at the marked positions in a). c) Self correlation of a), the Moiré periodicity is drawn in orange. d) LEED pattern of $EuAu_2$ showing the alloy spots and the faint Moiré periodicity .

5.1.3 Summary of the known $REAu_2$ surface compound structures

The structures of the $SmAu_2$, $EuAu_2$, $DyAu_2$, $HoAu_2$ and $YbAu_2$ have been studied in this thesis. Additionally, $LaAu_2$[46], $CeAu_2$[46], $GdAu_2$[16], $DyAu_2$[19], $TbAu_2$[146] and $ErAu_2$[146] surface compounds have been reported in the literature. A summary of the $REAu_2$ alloys structure can now be compiled and is presented in Table 3. From the results we can draw several conclusions. First, in all cases, the ML

shows an alloy lattice described (approximately) as $(\sqrt{3}\times\sqrt{3})R30°$. Second, the strain created by the larger atom diameter of RE with respect to Au is relaxed by the formation of a Moiré lattice, except in the $EuAu_2$ case. In the latter, the Eu atom diameter is too large due to its divalent character and the structure cannot be relaxed by the formation of the Moiré. In the case of Yb, even if the atom diameter is larger due to divalent character, it is still small enough to be compensated by a Moiré. Third, in the case of trivalent RE, there are two possible Moire reconstructions, for less than half filled 4f shell (light) RE atoms a $(12.4\times12.4)R4.7°$ structure and for heavy RE we observe a $(13\times13)R0°$ superlattice.

Table 3 Structure of the $REAu_2$ alloys

$REAu_2$	Valence	Type of Superlattice	Alloy Lattice	Moiré (referred to Alloy) (local)	Moiré (referred to Au) (local)
$LaAu_2$[46]	+3	Moiré	$(12/11)(\sqrt{3}\times\sqrt{3})R30^o$	$\begin{pmatrix} 7 & -3 \\ -3 & 4 \end{pmatrix}$	$\begin{pmatrix} 12 & 1 \\ 1 & 11 \end{pmatrix}$
$CeAu_2$[46]	+3	Moiré	$(12/11)(\sqrt{3}\times\sqrt{3})R30^o$		
$SmAu_2$	+3	Moiré	$(12/11)(\sqrt{3}\times\sqrt{3})R30^o$		
$EuAu_2$	+2	Vacancies lattice	$(12/11)(\sqrt{3}\times\sqrt{3})R30^o$	$\begin{pmatrix} 23/3 & 10/3 \\ -10/3 & 13/3 \end{pmatrix}$	$\begin{pmatrix} 11 & -1 \\ 1 & 12 \end{pmatrix}$
$GdAu_2$	+3	Moiré	$(13/12)(\sqrt{3}\times\sqrt{3})R30^o$	$\begin{pmatrix} 8 & 4 \\ -4 & 4 \end{pmatrix}$	$\begin{pmatrix} 13 & 0 \\ 0 & 13 \end{pmatrix}$
$TbAu_2$[146]	+3	Moiré	$(13/12)(\sqrt{3}\times\sqrt{3})R30^o$		
$DyAu_2$	+3	Moiré	$(13/12)(\sqrt{3}\times\sqrt{3})R30^o$		
$HoAu_2$	+3	Moiré	$(13/12)(\sqrt{3}\times\sqrt{3})R30^o$		
$ErAu_2$[146]	+3	Moiré	$(13/12)(\sqrt{3}\times\sqrt{3})R30^o$		
$YbAu_2$	+2	Moiré Coincidence -II with the alloy	$(13/12)(\sqrt{3}\times\sqrt{3})R30^o$	$\begin{pmatrix} 25/3 & 14/3 \\ -14/3 & 11/3 \end{pmatrix}$	$\begin{pmatrix} 13 & 1 \\ -1 & 12 \end{pmatrix}$

5.2 Electronic structure of $REAu_2$ surface alloys

The electronic structure of $REAu_2$ monolayers (RE=Ho, Sm, Yb, Eu) has been studied by Photoemission spectroscopy (PES). On one hand side, the inner shell electrons were mainly investigated by X-ray photoemission spectroscopy, on the other hand side, the valence band was mostly probed with ultraviolet light, specially in the form of angle-resolved photoemission spectroscopy (ARPES). Figure 33 shows as an example a XPS overview spectrum of $SmAu_2$ revealing the composition of the sample. The x-axis is the energy scale in binding energy (E_B) referred to the Fermi level (E_F), i.e. E_F = 0eV. This XPS spectrum was measured using monochromatized Al K_α light at hν = 1486.7eV in our home laboratory. With this photon energy, the accessible range of energy starts approx. at E_B = 1400eV and goes beyond E_F. In the energy

range above 1400eV the electron emission is dominated by secondary electrons due to inelastic processes that reaches very high levels and can damage the detector. Therefore binding energy ranges close to the excitation energy should be excluded. Au substrate emissions corresponding to the 4s, 4p, 4d, 4f, 5p core levels, and the Au MNN Auger emission can be clearly identified. In such a survey or overview spectrum, the experimental setting is tuned to high throughput and therefore poor resolution. As a consequence, the measurements are not capable of resolving bulk and surface components. Apart from the Au, Sm emissions corresponding to the 3d and 4d, and the Sm MNN Auger emission can be observed. Their intensity is much smaller compared to the emissions of Au. Additionally, Sm 4f and Au 5d emissions appear in the valence band region close to E_F, but both are mixed and cannot be identified separately. The cross section of Sm 3d, 4s, 4p, 5s and 5p is too small to produce a discernible peak with the selected photon energy. Deeper lying core levels are not accessible with the selected photon energy.

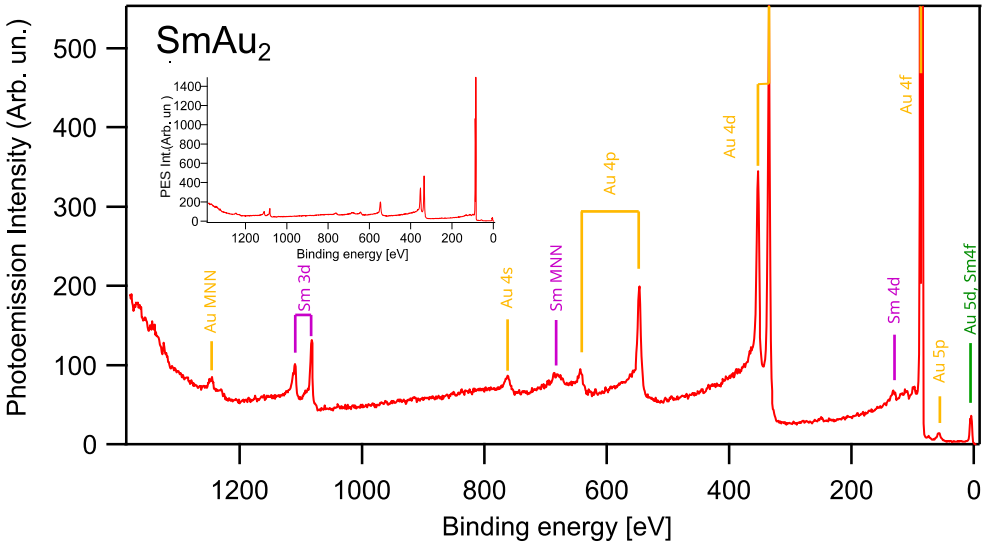

Figure 33: XPS overview photoemission spectra of $SmAu_2$ sample excited by Al K_α X-ray source. Emission lines of Au are marked in yellow, emission lines of Sm are marked in purple. The Au 5d and Sm 4f are superposed and marked in green. Peaks were assigned according to ref.[150–152]*. The indicated spectrum is cut from the complete survey (inset) to better differentiate the small Au and Sm levels.*

Depending on the rare-earth metal and its environment, the valence of the RE metal can be divalent (2+), trivalent (3+) or tetravalent (4+). The 4+ valence may occur only for Ce atoms that will not be discussed here. Most of RE metals are usually found in the 3+ situation. Only for Sm, Eu, and Yb divalent or mixed-valent (2+, 3+) configurations are observed. The valence state of the RE is a relevant factor that define many of the properties of these compounds. With respect to the here investigated photoemission spectra, the valency affects possible hybridization effects between the RE 4f core level and the valence band structure of the compounds. In the photoemission spectrum we will see that the trivalent REs don't show hybridization of the slightly deeper laying 4f shell and the valence bands near E_F. In the latter case, the valence band is dominated by s,d bands. In the case

of the divalent compounds, however, the valence band structure revels hybridization with the 4f band, producing hybrid s,d,f bands.

5.2.1 Trivalent valence state in $REAu_2$

In this section, it will be shown that $GdAu_2$ and $HoAu_2$ are surface compounds where the rare-earth atom are completely trivalent while $SmAu_2$ is almost completely trivalent. We will discuss the effect of the valency to the RE atoms on band structure, 4f orbitals and finally on the electronic and magnetic properties.

5.2.1.1 Core level emissions

The valence state of the RE atom for each $REAu_2$ compound can be extracted from the analysis of its core level emissions. Here, the 3d, 4f, and 5p core levels were investigated for the above mentioned $REAu_2$ surface compounds. Figure 34 shows the photoemission spectra of the 4f and 5p core level regions for $SmAu_2$, $GdAu_2$ and $HoAu_2$ MLs. The spectra were measured at Cassiopée (Sm) and VUV-Photoemission (Gd, Ho) beamlines of Soleil and Elettra synchrotrons in Paris and Trieste, respectively. In order to separate the 4f core level emission from other electronic states in the valence band region of the surface compound and the Au substrate emission (mainly 5d), spectra were acquired at photon energies corresponding to on- and off-resonant photoemission of the corresponding RE material[122].

In Figure 34a) the process of the resonant photoemission is briefly pictured. As was shown in section 4.3.1, this process is the result of the interference of two contributions, a direct photoemission and a Coherent Auger photoemission process. In the first process, the photon directly excites an electron from the 4f shell into the vacuum with a kinetic energy corresponding to the energy of the photon minus the binding energy and its work function. The second process (Coherent Auger emission) consists of a sequence of two steps. First, an electron of the 4d shell is promoted into an empty state of the 4f shell. This process can be measured and is called X-ray absorption spectroscopy (XAS, see section 4.6). In the inset of Figure 34b) one observes the X-ray absorption spectra at the mentioned edge for Sm in the $SmAu_2$ monolayer case. There is a strong jump in the spectrum at hν = 140eV for the $4d \rightarrow 4f$ X-ray absorption edge corresponding to trivalent Sm. Additionally, in this XAS spectrum we can observe that there is a small pre-peak at 136 eV corresponding to the very same $4d \rightarrow 4f$ transition of divalent Sm. In a second step, the hole can be filled with an electron that decays back to the original state transferring its energy to another electron of the 4f shell that leaves the atom at the same energy as the directly excited photoelectron (Super-Coster-Kronig process[118]).

This situation is shown in Figure 34b) for the $SmAu_2$ case. For photon energies below the XAS threshold no 4d hole is generated, and as consequence no Auger process can occur. We have a normal photoemission spectrum (red) with strong emission of the Au 5d electrons and some weaker contributions from the rare-earth 6s, 5d and 4f electrons. If we now tune the photon energy to resonant photoemission with hν = 141eV we observe a strong enhancement at approx. 6, 8, and 10eV binding energy while the Au 5d emission drops. For comparison, the calculated trivalent Sm multiplet structure in the intermediate coupling regime[153] is included on the bottom part of Figure

34b) as a solid black curve. The binding energy of the calculated spectrum has been shifted to fit the experimental values. We observe a quite good coincidence to the experiment confirming that the new emissions at the higher binding energy side correspond to trivalent Sm. Additionally, one observes a small enhancement of spectral features close to the Fermi level. One can better observe them by a multiplication of the spectra as shown on the right of the figure. There is a double peak (with some fine structure) at 0.3 and 1.1 eV binding energy. These emissions are strongest at the resonant photoemission energy hν = 136eV corresponding to the divalent Sm emission, while the new features at the high binding energy side are strongest for a photon energy corresponding to the 3+ resonance. Further comparison to literature results confirms the assignation of the double peak structure near E_F to divalent Sm emissions[154]. Therefore, we treat here a mixed-valent situation very close to Sm^{3+} where a small part of Sm atoms are in a divalent state. An exact relation of di- versus trivalent contribution is difficult to determine from resonant PE. Below we will see that such a number can be estimated from normal photoemission at the 3d core level.

In the cases of the RE 5p levels that were measured for $GdAu_2$ and $HoAu_2$, there is no direct resonant photoemission process due to the fact that the corresponding 5p emissions are far away from the Fermi level, see Figure 34c) and e), respectively. For these measurements, a photon energy of 136eV was used for Gd, hν = 170eV was used for Ho. As can be observed, in the case of the RE 5p peaks, these emissions also exhibit multiplets and result from final state photoemission effects[155]. In the latter cases, after photo-excitation of a 5p electron, the hole left behind interacts with the electrons in unfilled subshells resulting in different final states that lead to the observed 5p multiplet. In the $GdAu_2$ ML, Gd 4f and 5p levels are similar to the calculated and experimentally observed multiplet structures of trivalent Gd metal[156,157]. The effect of alloying with Au in the surface compound can be directly assessed by comparison to the surface core level lines in the corresponding pure RE metal crystals (i.e. Gd and Ho), where RE atoms at the surface have the same atomic coordination (ninefold). The trivalent Gd 4f and 5p lines of $GdAu_2$ are shifted to higher binding energies by 0.6eV and 0.7eV, respectively, with respect to the corresponding surface core levels in pure Gd[158]. For $HoAu_2$ the situation is very similar. In fact, the Ho 4f multiplet reveals a trivalent character and it is shifted to a higher binding energy by 0.4eV with respect to the surface component in metallic Ho[159]. The mentioned shifts can be understood as the more electronegative Au slightly reduces the charge, reducing electron-electron repulsion in the RE and lowers the energy of the levels.

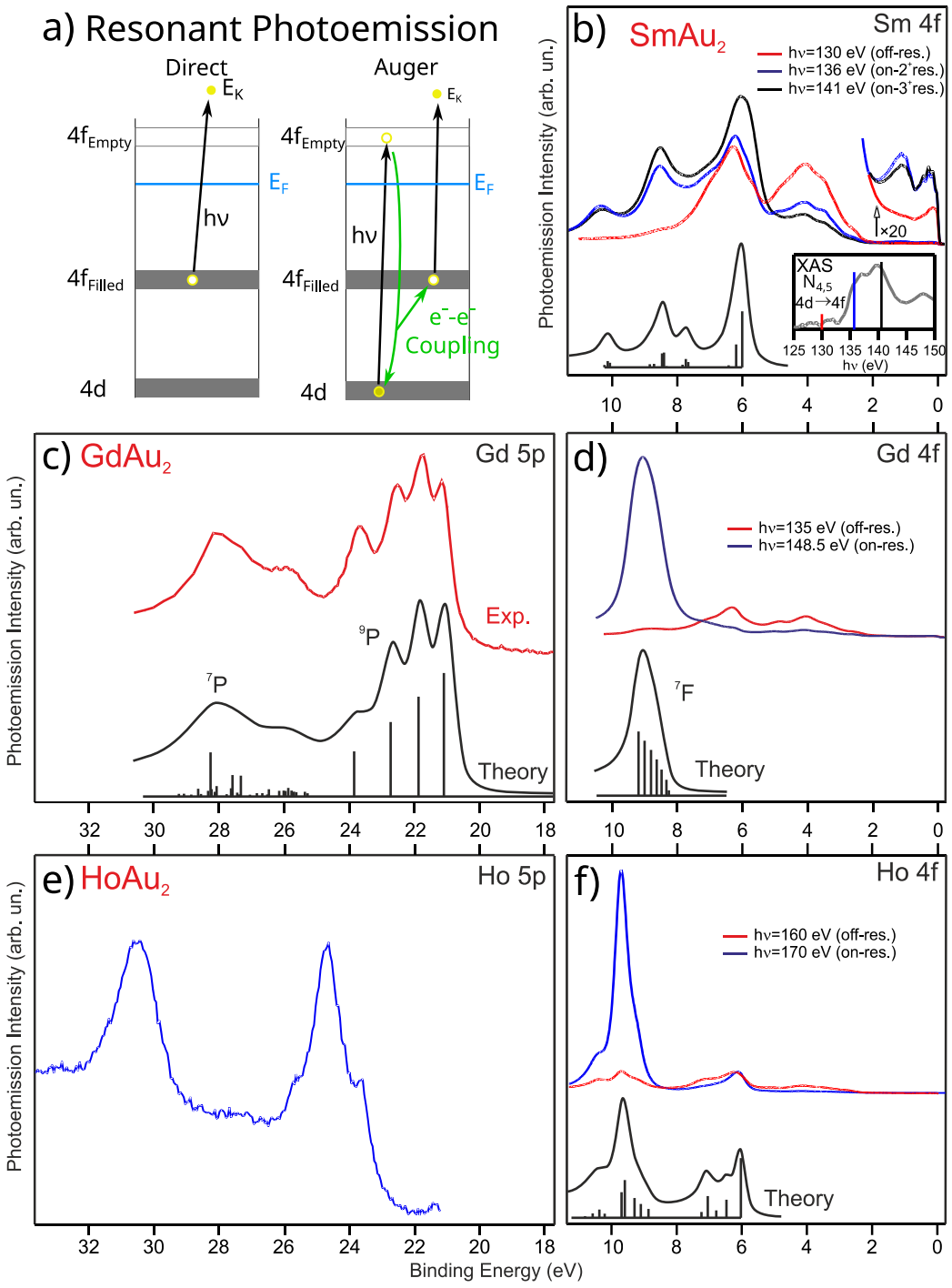

Figure 34: Resonant Photoemission at $SmAu_2$, $GdAu_2$ and $HoAu_2$: a) schematic description of the resonant photoemission process. b),d),f) On- and off-resonant photoemission of Sm, Gd and Ho 4f electrons of the valence band energy region, respectively. The black spectra are taken from reference [153] and denote calculations of the excited electrons. The inset in b) is the x-ray absorption spectra at the here studied $4d \rightarrow 4f$ absorption edge. c), e) photoemission of Gd and Ho 5p core level regions, respectively.

Further insight in the valence state of Sm atom in the $SmAu_2$ alloy has been determined from core level photoemission of the 3d core level as can be seen in Figure 35. The spectra were obtained from laboratory based measurements with a monochromatic Al K_α x-ray source. The 3d level reveals a spin orbit doublet with smaller satellite peaks. The main transition would show a multiplet structure as the 5p. However, due to the single hole of the excited states of this shell being too deep in the atom to interact with the empty valence states the multiplet here have much lower energy separation. The small satellite peaks are shakeup features associated to excitation of valence electrons into the empty 4f shell[160]. The Sm 3d emissions of $SmAu_2$ are similar to the bulk contribution of Sm metal[161] that is indicated by solid black lines in Figure 35. Nevertheless, similar to the Sm 4f multiplet emission, also in the 3d levels we observe hints for a small di-valent contributions. As was reported in ref.[154], the undercoordination of the surface atoms may result in a divalent state. In the alloy, surface Sm atoms are surrounded by Au atoms that draw charge from the Sm atom. As observed here, the resulting balance leave Sm in $SmAu_2$ in a nearly trivalent state. From our laboratory data we can integrate both, the tri- and a divalent contributions and from such an analysis the amount of divalent Sm is calculated to be approx. 2.5%. The energetic positions of divalent Sm emission are marked by blue dashed lines in Figure 35. This small divalent part may be associated to not completely alloyed samarium or not fully coordinated Sm due to defects in the growth of the $SmAu_2$ layer. Nevertheless, it is also possible that the surface is a mixed-valent compound since some divalent contribution is found in all independent preparations. The measured tri- to di-valent peak shift is $\Delta E_{3+,2+} = 8.7$eV.

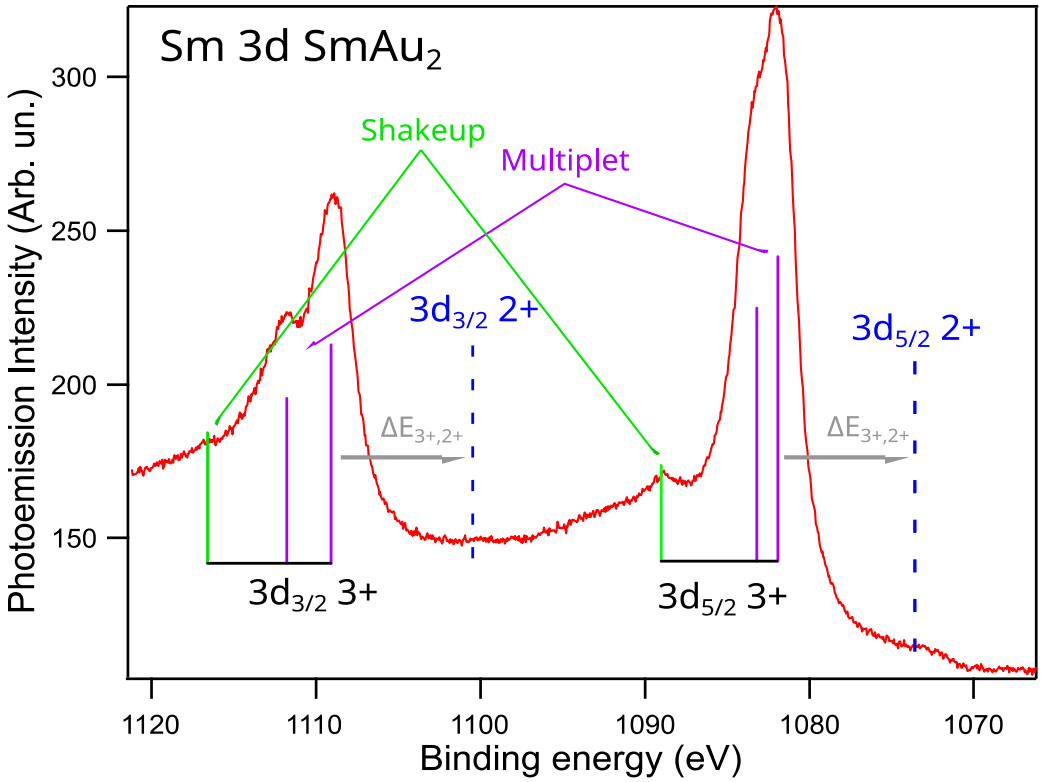

Figure 35: Photoemission spectra of the 3d core level of Sm. Emissions for the $3d_{3/2}$ and $3d_{5/2}$ can be seen. Peak positions from trivalent y divalent Sm are marked by solid black and colored (3+) as well as dashed blue lines (2+), respectively. Reference positions were taken from ref.[154].

5.2.1.2 Valence band emissions/electronic band structure

The electronic band structure of $GdAu_2$, $HoAu_2$ and $SmAu_2$ MLs on Au(111) was measured by ARPES. The band structures measured on these surface compounds are shown in Figure 36. Band structure of $GdAu_2$ was already reported in ref.[16,17,51]. From a simple look at Figure 36 one observes that the three surface compounds present a very similar band dispersion in the valence band region. This proves that the previously mentioned 3+ valence imposes the same $(6s5d)^3$ orbital contribution of the RE atoms. There are two-dimensional (2D) electronic bands visible arising from the $REAu_2$ surfaces. The 2D confined bands have been labeled as *A*, *B*, *C* and *C'* (see Figure 36) in the same way as in earlier publications, namely the $GdAu_2$ band structure[16]. The *A* band has an electron like behavior and appears in the limit of the bulk Au(111) gap, causing it to be surface confined. According to theory[17], the *A* band is formed of hybrid RE and Au bands and has similar position and dispersion as the Au(111) Shockley state but shifted towards higher binding energy. The *B* band has a hole-like behavior. It is a hybrid state with main contribution of 5d character from the Au surface atoms. The *C* band shows a nearly linear dispersion. It is best seen at the second surface Brillouin zone and crosses the Fermi level at the $\bar{\Gamma}'$ point. This band is formed from Au s,p band hybridized with the 4d bands of the RE forming a new 2D confined band. The *C'* band is formed

from umklapp processes of the Au s,p band caused by the $(\sqrt{3}\times\sqrt{3})R30°$ superstructure[162]. The rare-earth 4f core levels are not detected here due to the limited energy range used for the measurement of the band structure. As it was explained in the preceding section, these 4f core levels in the trivalent surface compounds are deeper in energy, and therefore are not seen in Figure 36. With the limited energy range of the here presented measurements we also avoid the high intensity of the Au 5d emission that would mask the low intense compound bands in that energy range. Moreover, the investigated range of energy is relevant for the magnetic properties and the electron transport near the Fermi level.

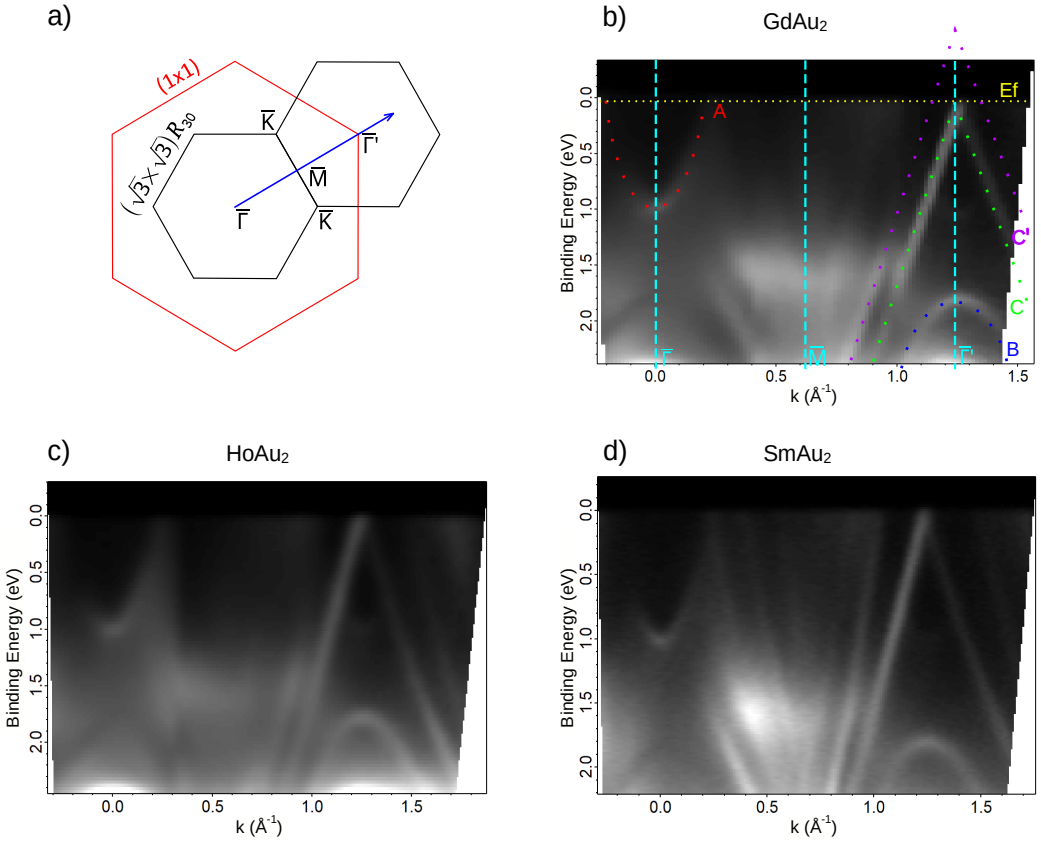

Figure: 36 ARPES 2D maps of the different trivalent $REAu_2$ surface alloys. a) schematic representation the surface Brillouin zone and the measurement direction. b)-d) $GdAu_2$, $HoAu_2$ and $SmAu_2$ ARPES intensity map, respectively. The dotted color lines in the $GdAu_2$ panel mark the different bands. Maps are taken along the $\overline{\Gamma M \Gamma'}$ direction of the surface Brillouin zone with HeI_α light ($h\nu$ = 21.22 eV).

Further analysis of the band structure was done thanks to DFT simulations carried out by Dr. M. Blanco-Rey from the University of the Basque Country[50]. Figure 37a) shows the orbital characters and spin polarities in the absence of spin-orbit coupling (SOC) for a freestanding $GdAu_2$. This is unrealistic in the sense of the experiment, but is the first access point to understand the electronic properties of the system. The α and α′ features are crossings between d_{xy} and $d_{x^2-y^2}$ (m = ±2) with the same spin polarization. The β feature corresponds to the crossing between d_{xy} and

$d_{x^2-y^2}$ bands with opposite spin polarization. In momentum (*k*)-space, according to ref.[52] the β band crossing (in 3D) is a ring shaped Weyl nodal line. Figure 37b) shows the same band structure, now including SOC calculated with IP (label *X*) and OOP (label *Z*) spin polarization for freestanding $GdAu_2$. The introduction of the SOC induces splitting of the α and α′ crossings for OOP spin polarization and splitting of the β line for IP spin polarization. Figure 37c) shows the band structure with SOC calculated with IP and OOP spin including 3ML of Au(111) as a substrate material (slab calculation). This situation is much closer to the real experiment, a slab of 4 layers including the surface compound and 3 substrate layers. Such a slab causes an increasing number of electronic bands. However, as can be seen, the RE-Au band character and gap openings are not modified by the inclusion of the substrate. This probes the 2D character of the bands and the exchange mechanism confinement to the alloy layer.

As shown in section 3.2.3.1, the MAE is obtained from the spin-orientation-dependent band energy contribution to the total energy of the system. It is calculated by integrating the energy of the electrons up to the Fermi level for each of the spin polarization directions. It should be remembered that the Fermi level is dependent on the spin polarization, as well as the electron filling. To evaluate the contribution of the bands, instead of being represented in terms of binding energy, it is usually represented in terms of electron filling. We take as a criterion (established in formula 5) that positive MAE means lower energy of the OOP spin polarization and negative MAE lower energy of the IP polarization. Or what is the same, positive MAE means OOP easy axis while negative MAE means IP easy axis. With this criteria established, we can pass to analyze the MAE in our case, the $GdAu_2$ (and in general the $RE^{3+}Au_2$ alloys). In this case, the main differences in the electronic structure are the α, α′ and β gap openings that are expected to dominate the MAE. Figure 37d) shows the calculated MAE as a function of the electron filling for $GdAu_2$, (i) for the free-standing layer and (ii) the $GdAu_2$ layer on 3ML of Au. This figure confirms that the gap opening features have a critical importance in the MAE. The calculation of the freestanding layer (in red dotted lines) illustrates that the gaps produce sharp peaks in the MAE. The α, α′ gaps give positive MAE, i.e., they favor OOP easy axis, while the β gap results in negative MAE, indicating that it favors IP easy axis. What has to be taken into account is that in the free-standing layers, the intrinsic sharpness (in terms of electron filling) of the features finishes right before $N_e = 0$, leading to an almost zero MAE in the neutral $GdAu_2$ isolated layer. This is a bit less strict in the case of the $GdAu_2$ on top of the 3ML Au. In the latter the hybridization of the alloy bands with the substrate broadens the gaps in terms of electron filling. This hybridization can be seen as a broadening of the peaks associated to α, α′ and β, while its position is nearly unchanged. As can be seen, the broadening of the β feature is the responsible of a negative MAE at charge neutrality. This is even the case here where the β feature does not appear exactly at the Fermi level. This negative MAE translates into an IP easy axis, which matches the previously reported IP easy axis of $GdAu_2$[17]. To summarize, we have shown that the origin of the giant anisotropy with IP easy axis of the $GdAu_2$ surface alloy are a gap openings caused by the SOC in the s-d bands of the alloy. Additionally, the s-d origin of this anisotropy implies that this contribution of band anisotropy will be present in all $RE^{3+}Au_2$ surface compounds. Finally, based on the dependence of the MAE with the electron filling, we can predict that it will be possible to further modify the magnetic anisotropy of the alloys by electron or hole

doping. For example, the easy axis could be brought into an OOP easy axis by doping with electrons, like for example alkali metals.

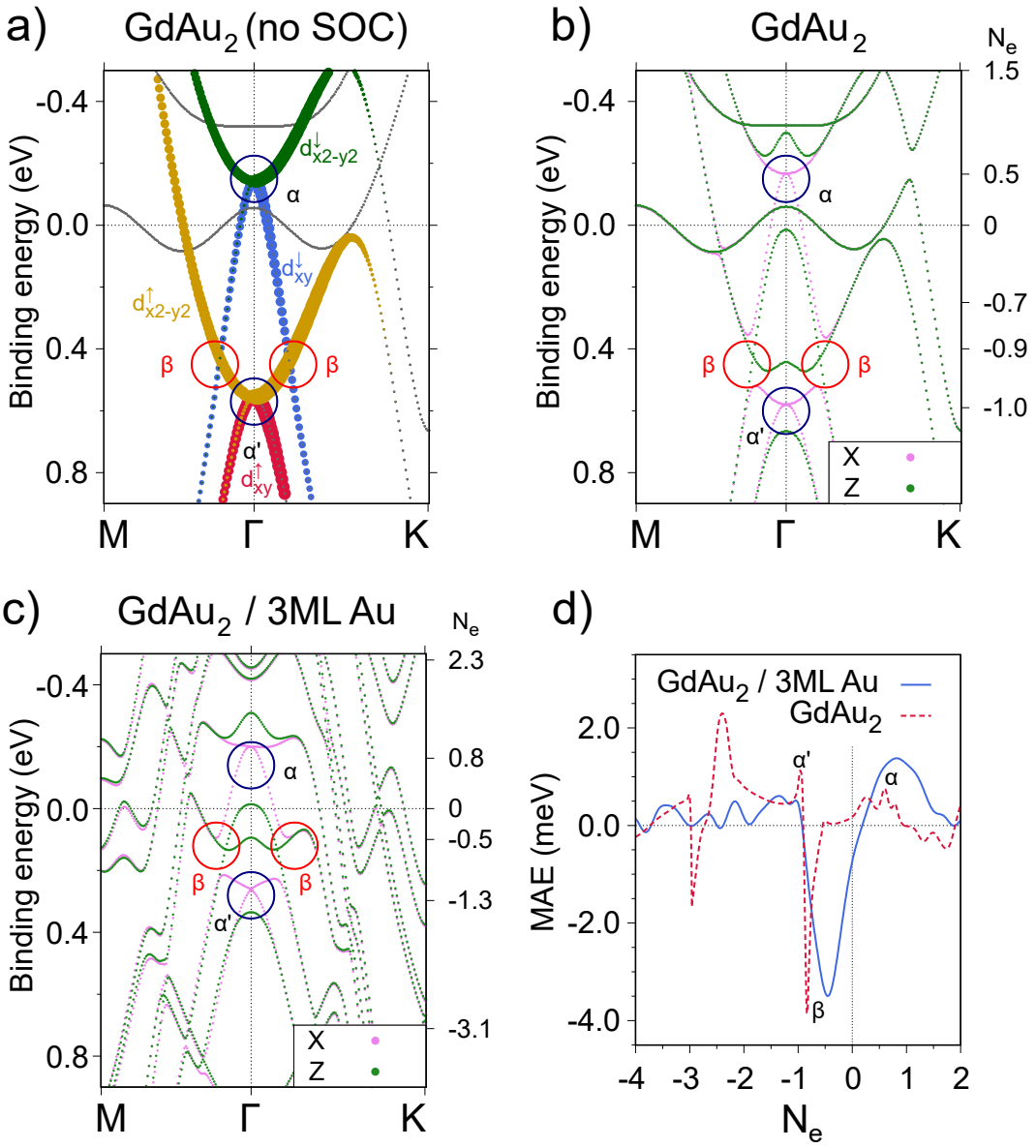

Figure 37: DFT simulated band structure of $GdAu_2$: a) freestanding layer without SOC and b) including SOC. Note that the colors indicate different directions of polarization. c) DFT simulated band structure of $GdAu_2$ supported on 3ML of Au with SOC. d) MAE calculated for $GdAu_2$ for unsupported (red) and on top 3ML of Au (blue). Negative MAE favors IP, positive MAE OOP easy axis of magnetization.

5.2.2 Divalent valence state

In this section, it will be shown that $YbAu_2$ and $EuAu_2$ are surface compounds where the rare-earth atom are nearly completely (Yb) or completely (Eu) divalent. We will discuss the effect of the

valency of the RE atoms on band structure, 4f orbitals and finally on the electronic and magnetic properties.

5.2.2.1 $YbAu_2$

The valency of the Yb atom has been determined by photoemission of the Yb 5p and 4f core levels (Figure 38). In order to verify or discard the presence of a possible trivalent contribution, resonant photoemission has been used to separate the Yb 4f and the Au 5d emissions. The resonant photoemission process was already described in section 4.3 and 5.2.1.1 In the here considered case of Yb, the used resonant excitation energy of hν = 183eV corresponds to the absorption edge of the $4d_{5/2}$ level. Note, that this resonant PE works only for tri-valent Yb. In the case of divalent Yb, no resonance process can take place. This is due to the fact that in the Auger process pictured in Figure 34a) one cannot excite an electron into unoccupied 4f levels, because they do not exist, as the band with $4f^{14}$ configuration is already completely filled. Therefore, an Auger process is not possible and as a result no resonant PE process of divalent Yb can occur. The valence state for Yb in $YbAu_2$ is deduced by directly comparing the experimental spectrum with the theoretical divalent and trivalent configurations of Yb, shown in Fig. 38b). There is a dominant divalent Yb 4f emission near E_F, although a zoom in the higher energy spectrum reveals the presence of trivalent Yb. An estimation of the average valency from resonant PE is difficult, therefore, as was previously carried out in the Sm case, a non-resonant transition will be used. Here, the Yb 5p core level is better suited for a quantitative analysis. Photoemission measurement of this core level reveals a small, but well visible, trivalent $5p_{3/2}$ emission at approx. 27eV binding energy. This binding energy discards emission from bulk Yb impurities that would occur at lower energy,[163] but rather indicates a mixed valence scenario, with a dominant divalent state and a minor trivalent contribution. One possibility for the observation is a valence fluctuation of Yb. This valence fluctuation could be seen by X-ray photoemission as a fast femtosecond-range transition process, faster than the valence fluctuation time of rare-earth ions in mixed-valence systems[164]. It is also possible that the trivalent contribution arises from a small contamination of the sample, leading to the formation of a small fraction of compounds with trivalent Yb, like Yb_2O_3. The relative peak area of the two $5p_{3/2}$ peaks in Fig. 38a) reflects an intermediate valence value ν = 2.06 of Yb in $YbAu_2$. Applying the Hund rules, divalent Yb will have zero magnetic moment, while trivalent Yb will show a magnetic moment of $4.54\,\mu_B$. With the valency value obtained, we can estimate an average magnetic moment of $0.27\,\mu_B$. Not only this magnetic moment is small but furthermore it is localized on the trivalent Yb atoms, which account for approx. 6% of the Yb. This leads to an expected diluted paramagnetic behavior of the trivalent Yb in a diamagnetic matrix.

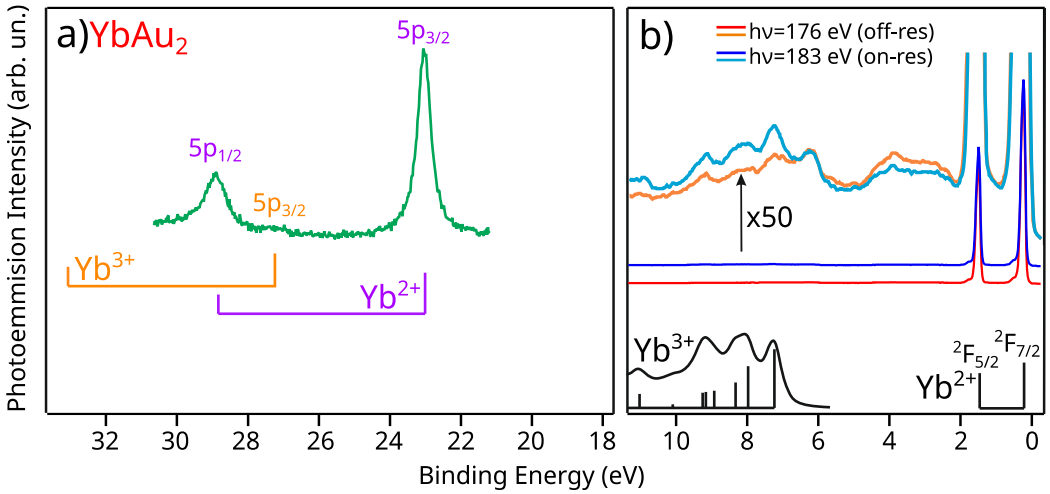

Figure 38: Photoemission of Yb core levels: a) 5p core level with the positions of the di- and tri- valent ytterbium contributions, respectively. b) Resonant photoemission of the Yb 4f levels in off- and on-resonant PES (red, blue: full spectrum; orange, light blue: high binding energy part multiplied by a factor of 50 to distinguish the tri-valent contribution). Theoretical spectra in black (below) were taken from ref.[153] *and were shifted in energy to coincide with the experimental emissions.*

The experimentally measured band structure of $YbAu_2$ is shown in Figure 39. The most visible difference with respect to the trivalent photoemission images is that due to the divalent Yb character, the 4f levels of the Yb appear as non-dispersive bands at a binding energy of approx. 1.5 and 0.25eV. Apart from these non-dispersive bands, the band structure reveals similar dispersive bands as the trivalent alloys. Therefore, we will follow the same convention to name the different bands. The *A* band has an electron like behavior and appears in the limit of the bulk Au(111) gap. This band appears slightly shifted upwards (about 0.1eV) with respect to the trivalent alloys. The *B* band has a hole-like behavior, it consists of a hybrid band from RE and Au(111) states and it is located far away from the Fermi level. The *C'* band is again formed from the Au s,p band umklapps induced by the $(\sqrt{3}\times\sqrt{3})R30°$ structure[162]. The *C* band reveals differences with respect to the trivalent case. First, it has lost its ideal conical shape, specially visible in the crossings with the Yb $4f_{7/2}$ band. In these crossings, the *C* band reveal band gaps caused by the hybridization with the $4f_{7/2}$ manifold, giving a weakly dispersive character to the 4f levels. Second, the band is displaced upwards with respect to the trivalent alloys. This implies that the *C* band is expected to have its cone 0.3eV above the Fermi level. The displacement of the *C* band can be understood when considering the valence change from trivalent to divalent. In the latter case, the lack of one valence electron acts as a dopant that shifts up the whole bands or alternatively shifts down the Fermi level. This change is more subtle in the *A* band, as this band feature has a Shockley like character, its binding energy is mostly determined by the unchanged bulk gap and the vacuum confinement.

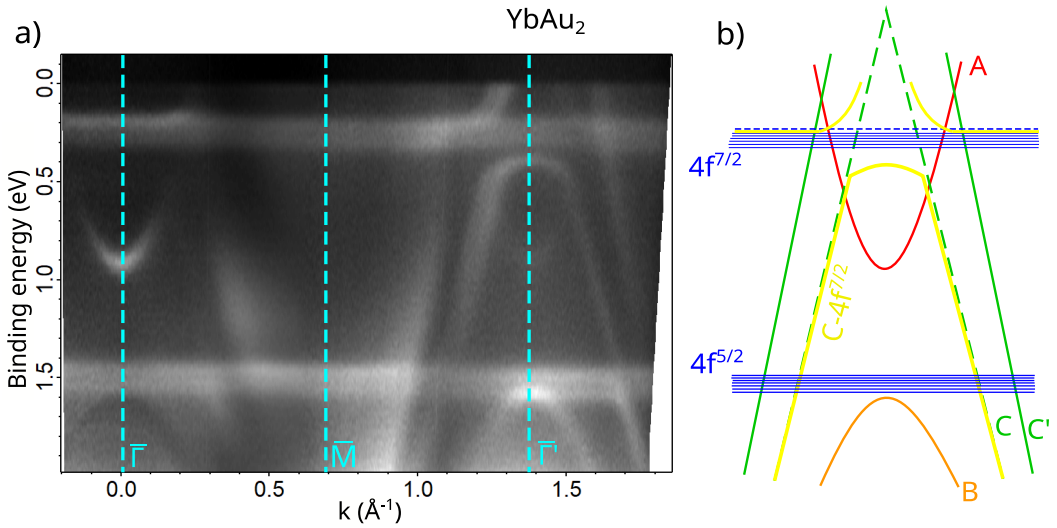

Figure 39: Band dispersion in $YbAu_2$: a) ARPES intensity mapping of $YbAu_2$. Map is taken along the $\overline{\Gamma M \Gamma'}$ direction with a phonon energy of 30eV at T = 12K. The ARPES map was taken in VUV-photoemission beamline of Elettra. b) Combined schematic representation of the bands around the $\overline{\Gamma}$ points. The green dashed lines are used to mark the bands without hybridization.

5.2.2.2 $EuAu_2$

The valency of the Eu atoms in $EuAu_2$ has been again determined by resonant photoemission at the $4d \rightarrow 4f$ absorption edge and the results are presented in Figure 40. Three photon energies have been used (i) hν = 135eV that corresponds to off-resonant photoemission (energy below the absorption edge), (ii) hν = 141eV corresponding to on-resonant PE for divalent Eu, and (iii) hν = 146eV corresponding to on-resonant photoemission of trivalent Eu. The valence state of Eu in $EuAu_2$ can be deduced from comparing the experimental spectrum with the calculated divalent configurations of Eu $4f^{2+}$, shown in the bottom part of Figure 40. One has to take into account that a possible tri-valent contribution would occur for binding energies above 2eV. Such a situation, even at the Eu^{3+} resonant photon energy is not observed. This means that in the surface compound $EuAu_2$, there is only a divalent Eu 4f emission at a binding energy of 1.1eV. In pure Eu metal such a surface emission is found at approx. 2eV binding energy. This implies a shift of 1eV towards the Fermi level due to the Au alloying[165].

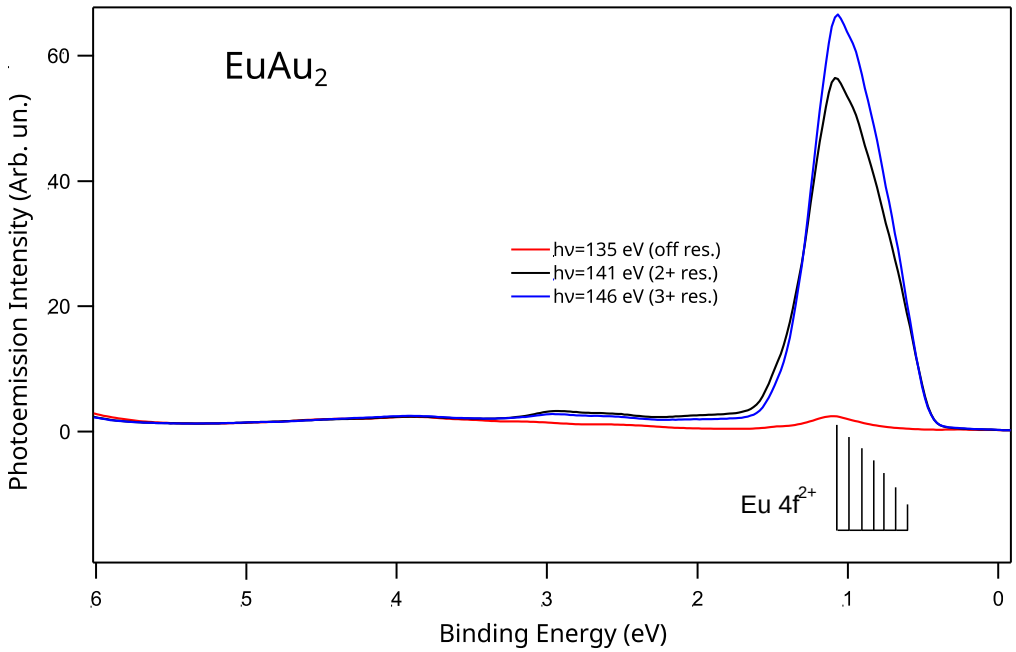

Figure 40: Resonant photoemission at the 4d→ 4f absorption edge. The off-resonance spectrum is represented in red; in blue and black the on-resonance measurements. The multiplet at the bottom indicate the calculated multiplet structure for divalent Eu 4f taken from ref.[153]*. The spectra were measured at the Cassiopeé beamline of Soleil synchrotron.*

A representative ARPES intensity map of $EuAu_2$ is shown on Figure 41. The 4f levels of Eu appear as very-weakly dispersive bands at 1.1eV. For the rest of the dispersive bands we expect a similar situation as in $YbAu_2$. In $EuAu_2$, the *A* band results to be shifted upwards 0.1eV with respect to the trivalent alloys. The *B* and *C'* bands are again unchanged. The *C* band has lost its ideal conical shape in the energy range corresponding to the crossing with the Eu 4f band. Now, the *C* band is slightly bent at the crossings (Figure 41b)) caused by the hybridization with the 4f manifold. As in $YbAu_2$, the *C* band is displaced upwards with the expected cone crossing about 0.3eV above E_F. This displacements reveals again the lowering of E_F due to the reduction of one valence electron on the Eu side.

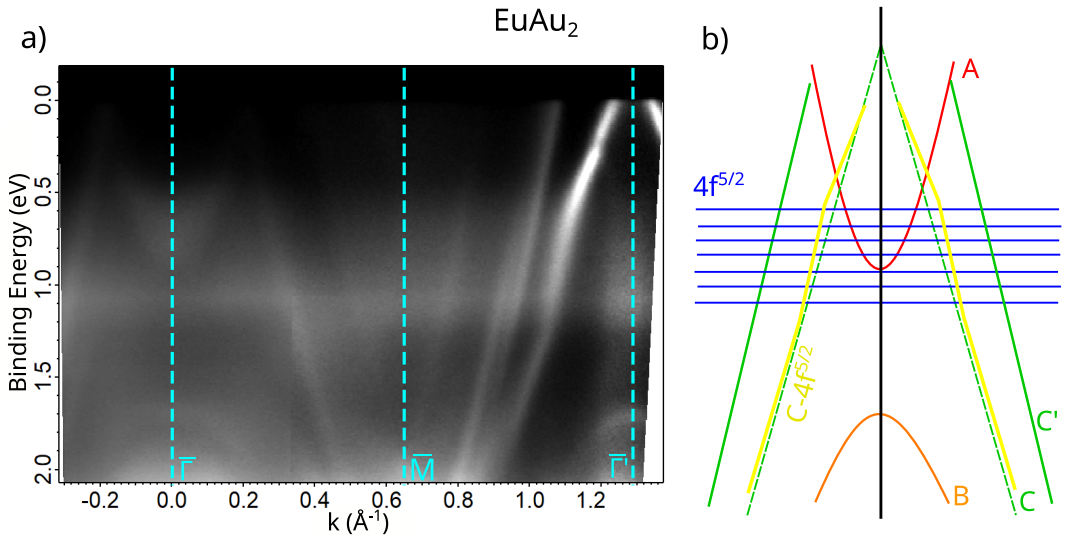

Figure 41: ARPES photoemission map of $EuAu_2$. a) Experimental photoemission intensity map taken along the $\overline{\Gamma M \Gamma'}$ direction. The mapping was obtained at VUV photoemission beamline of Elettra with a photon energy of 32 eV. b) schematic representation of the bands close to the $\overline{\Gamma}$ points. The dashed green lines are used to mark the bands without hybridization.

As in $GdAu_2$, analysis of the band structure was done thanks to DFT simulations made by Dr. M. Blanco-Rey from the University of the Basque Country[50]. Figure 42a) shows the orbital characters and spin polarities in the absence of SOC for freestanding $EuAu_2$. As in $GdAu_2$, the α and α′ designates the crossings between d_{xy} and $d_{x^2-y^2}$ (m =±2) with equal spin polarization and the β feature the crossings with opposite spin polarization. Figure 42b) shows the bands with SOC calculated with IP and OOP spin polarization for freestanding $EuAu_2$. As can be seen, all these crossings happen above E_F, so, in contrast to the case of $GdAu_2$ they fall out of the integration range of the MAE (Eq. 6) and as consequence, are not expected to contribute to the MAE. The most important change with respect to Gd is that in this case, the *C* band now obtains a certain amount of 4f character. Furthermore, the *C*-band/4f hybridization breaks the degeneracy of the Eu 4f. This causes a strong dependence of the 4f bands with the direction of the spin polarization. This can be seen in the band upshift of the 4f bands in OOP polarization (green lines in Figure 42b)) with respect to the bands with the spins polarized in the IP direction (violet in Figure 42b)). The effect can be also understood as a deviation from the sphericity of the 4f electron cloud of an isolated Eu atom leading thus to a small *L* moment that is locked in the OOP direction by the crystal field. This small *L* couples to the spin moment of the Eu 4f, creating a strong magnetic anisotropy. This deviation from sphericity can be seen in the previously mention broadening of the 4f band and the shifts with the spin polarization direction. The MAE as a function of the electron filling (N_e = 0 being charge neutrality) is displayed in Figure 42c). As a reminder, the used criteria (established in Eq. 6) here means positive MAE is assigned to lower energy of the OOP spin polarization (OOP easy axis) and negative MAE results in lower energy of the IP polarization (IP easy axis). First, in Figure 42c) it can be seen that, as expected, the α, α′ and β crossing do not have contribution because they are above E_F. Second, it can be seen that when the bands are depleted until reaching the Eu 4f shell (from N_e = -12 to N_e = -5) a huge contribution to the MAE appears (1 order of

magnitude higher than the neutral charge anisotropy). This contribution confirms the effect of hybridization breaking due to the symmetry of the 4f. Furthermore, the effect of 4f in the MAE tends to neutralize when moving towards the charge neutrality, but still a positive residue remains. This positive MAE is of about 2meV and justifies the measured strong OOP easy axis anisotropy that this alloy shows (as will be seen in section 5.3.4).

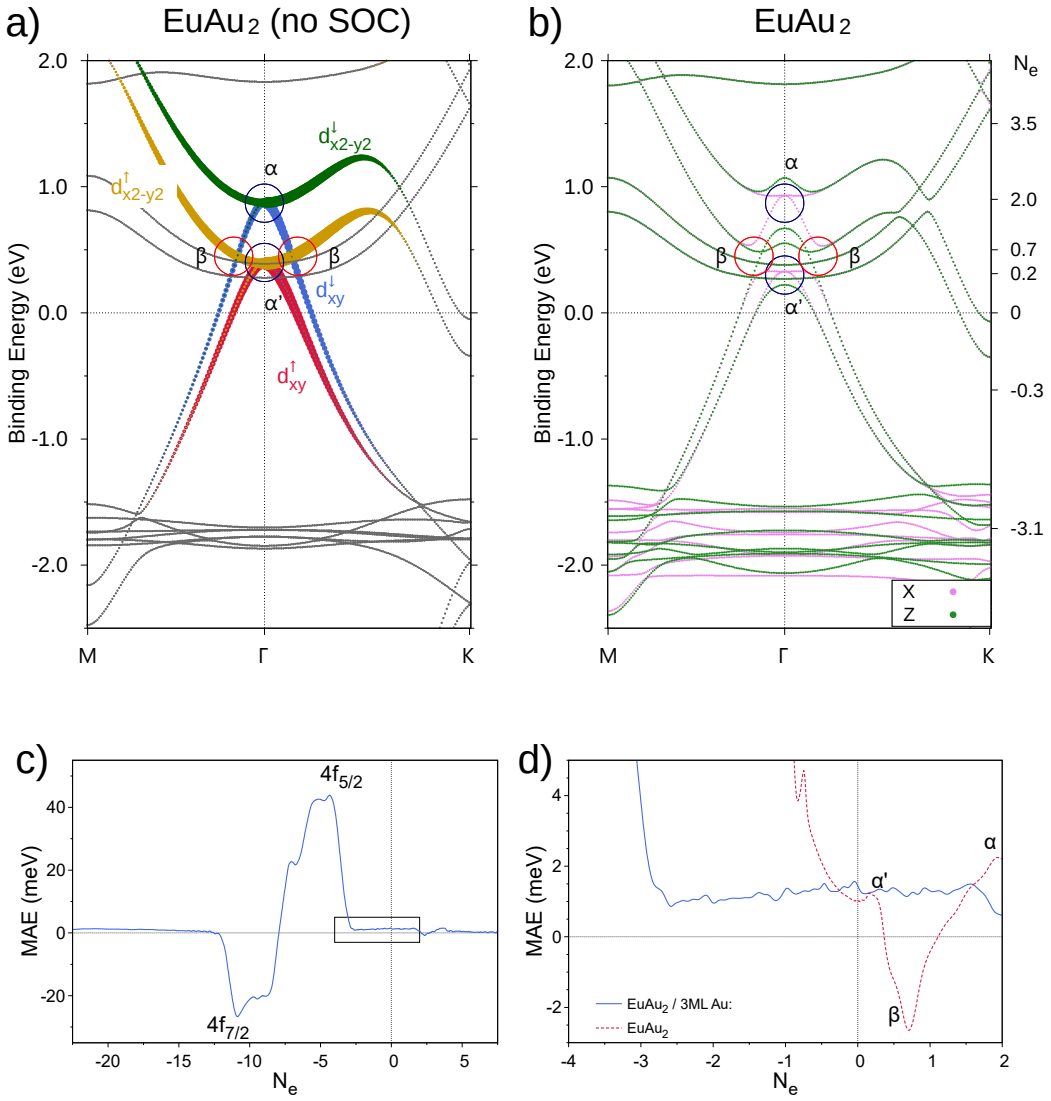

Figure 42: DFT simulated band structure of $EuAu_2$: free-standing layer a) without SOC and b) with SOC. Note that the colors indicate the directions of polarization. c) MAE calculated for $EuAu_2$ on 3ML of Au featuring the 4f contribution to anisotropy. Part d) details the MAE closer to the Fermi level revealing that the MAE contribution is a residue from the 4f hybridization. For comparison, the unsupported $EuAu_2$ in drawn as dotted red line.

5.3 Magnetism in $REAu_2$ surface alloys

The magnetic behavior of the rare-earth/noble-metal ($RE\text{-}NM_2$) surface compounds has been studied by XAS-XMCD at synchrotron radiation facilities, namely at ALBA (Barcelona, Spain) and

SOLEIL (Paris, France). Mainly two geometries have been used for this measurements dedicated to probe the in-plane and out-of plane magnetic properties. In both cases, the magnetic field has been applied in the direction of the incident beam. XAS-XMCD spectra are obtained at a fixed field by varying the incident photon energy at an absorption edge of interest, here the $M_{4,5}$ edge of the rare-earth metal. The grade of polarization in most cases has been 90%, sometimes even 99%. The XAS-XMCD has been always carried out in total yield mode, i.e., by measuring the absorption through the total emitted charge.

5.3.1 $HoAu_2$

XAS and XMCD measurements performed at a temperature of 2K and with an applied field of 6T in both geometries, IP and OOP, respectively, are shown in Figure 43. These data have been obtained at Boreas beamline at Alba. The spectra shows two peaks, associated to the M_5 and M_4 transitions, which corresponds to electron excitations from the electronic levels of $3d_{5/2}$ and $3d_{3/2}$, respectively, into the empty 4f and 6p states. This is due to the XAS adsorption rules that require a $\Delta l=+/-1$ transition. The density of states of the unoccupied p level is very small and broad compared to the 4f levels, therefore it is mainly the $3d \rightarrow 4f$ transition that is observed. This transitions have been chosen as they allow to prove the empty states of the 4f shell of the RE and so, the magnetization of the alloy. Two main differences exist between XAS and XMCD spectra from both geometries. One is a marked change of shape in the M_5 transition between IP and OOP geometry in the XAS spectra. That can be explained by considering the shape of the f-electron distribution (and the charge cloud of Ho). For spherical 4f orbitals as for the case of the $4f^7$ configuration in $GdAu_2$ or $EuAu_2$ (see below) such shape changes should not be observed. But here, with a more oblate 4f electron charge distribution the latter effect is reflected in the lineshape[42]. This lineshape indicates a preferential orientation of the 4f orbital, even at fields capable of saturating the sample. The second important difference is better seen by comparing the intensities of the two XMCD spectra. The XMDC intensity in the OOP geometry nearly doubles the value for IP geometry. This fact is a sign of an OOP easy magnetization axis. In a very simplified approximation we can estimate minimum anisotropy constant by the difference in energy at the maximum applied field (Equation 28).

$$K_A = B \cdot \mu_{Ho} \cdot \left(M_{R,OOP} - M_{R,IP} \right) \tag{28}$$

B is the applied induction field (here 6T), μ_{Ho} the magnetic moment of trivalent Ho ($10.6\,\mu_B$ [34], see table 1), $M_{R,OOP}$ and $M_{R,IP}$ the reduced magnetization, i.e., the magnetization at a specified field divided by the saturation magnetization (or the maximum magnetization achieved), here at 6T: $M_{R,OOP}$ = 1 in OOP and $M_{R,IP}$ = 0.6 in IP direction, respectively. From these numbers we can estimate the anisotropy constant per unit cell to be at least 1.5meV. As will be seen later, this value is of the order of the thermal energy at the Curie Temperature (1.8meV at 22K) indicating that the Curie temperature could be limited by the magnetic anisotropy, as expected from the consequences of the Heisenberg model (see section 3.2.2).

The shape of the XMCD spectra is consistent with the Ho^{3+} valence state[166] already determined by photoemission. That valence state is associated with a $4f^{10}$ electron configuration. As mentioned earlier, the orbital filling implies an oblate orbital shape[42] that justifies the difference in shape

between IP and OOP geometries.

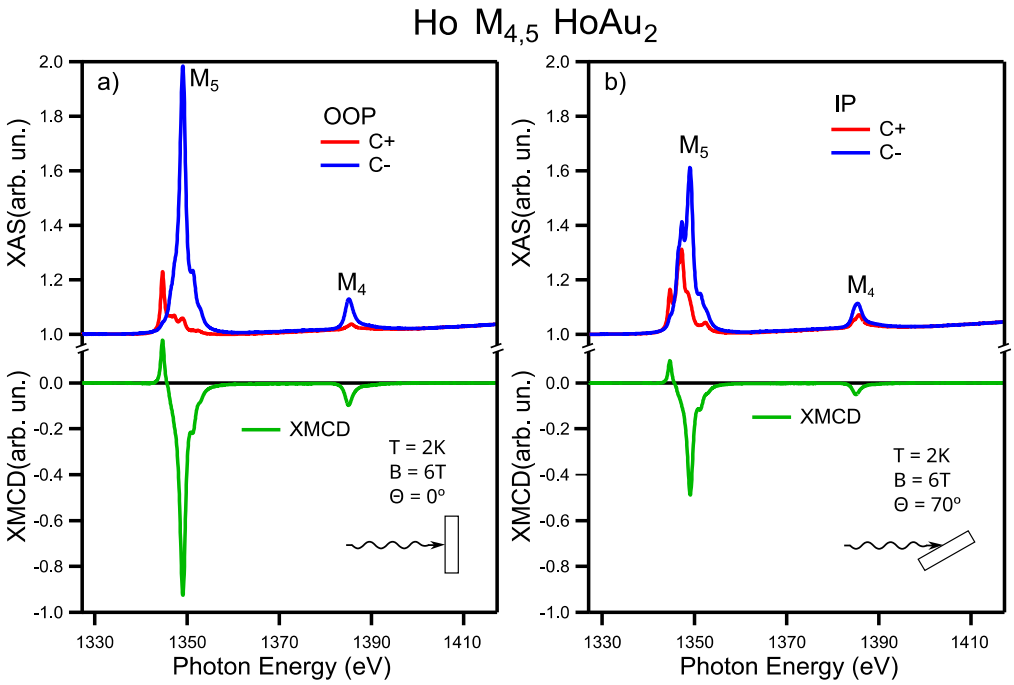

Figure 43: X-ray absorption (top) and XMCD spectra (bottom) of $HoAu_2$ measured at 6T and 2K in (a) OOP and (b) IP geometry, respectively. XAS spectra in red (blue) are measured with C+ (C-) circular polarized light. The dichroic XMCD spectra [C+]-[C-] is displayed in green.

Figure 44 shows the XMCD hysteresis loops of $HoAu_2$. There is a clear difference in the shape and in the saturation behavior among both geometries, IP and OOP. The OOP loop shows a more "square like" behavior that reaches saturation at approx. 1T, while the IP loop shows a more "S shape" behavior, that eventually reaches a linear behavior at 1.5T. This allows to define an easy and hard axis for the magnetization of $HoAu_2$. The easy axis (the lower energy state) here corresponds to the OOP direction and the hard axis to the IP direction, which results to be the high energy state. The XMCD loops doesn't display a visible hysteresis, which means that $HoAu_2$ monolayer is extremely soft ferromagnet, i.e., the energy required to change the direction of magnetization tends to zero. Due to the characteristics of the measuring method, the remanence at zero field cannot be determined, but due to the tendency of the curves can be assumed to be small.

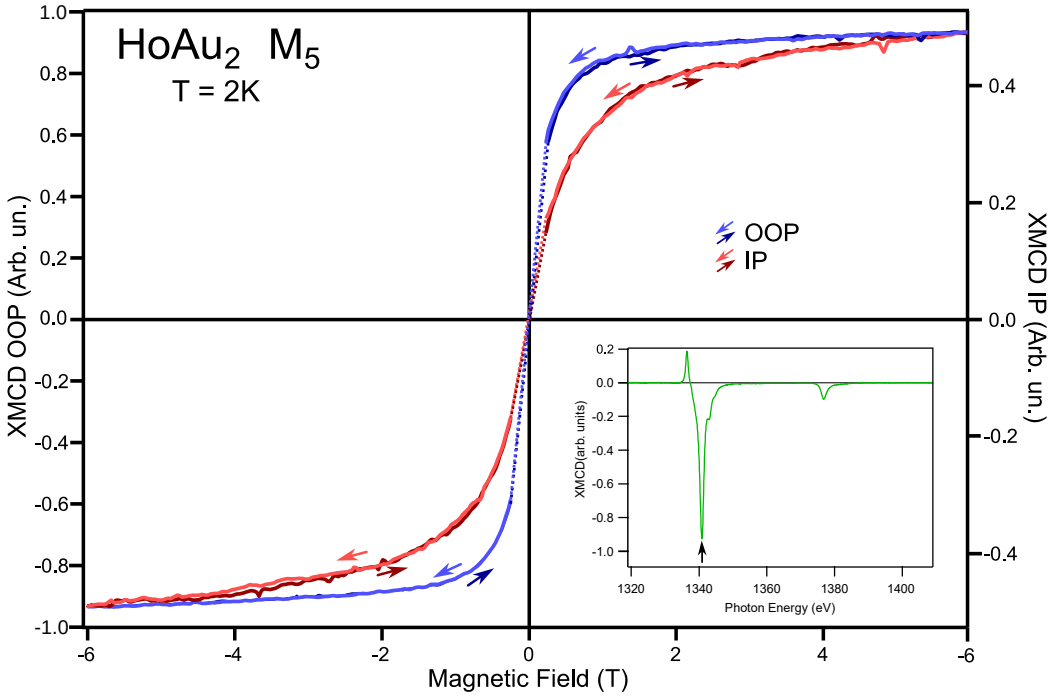

Figure 44: XMCD Hysteresis loop of $HoAu_2$ measured and normalized at 2K on the maximum of the dichroism of the M_5 transition. The shape of the loops confirms the OOP anisotropy. Note the difference of scale for the OOP and IP direction. This has been chosen in order to better see the difference in the shape of the loops. The inset shows the XMCD spectra in IP geometry marking the measurement photon energy.

As it was commented in section 3.2.3, there are two sources of anisotropy: shape and magnetocrystalline anisotropy. To shortly repeat, shape anisotropy always favor IP magnetization due to the physical shape of the samples (monolayers) but the effect is too small and in the wrong direction with respect to the seen effects. Therefore, the magnetocrystalline anisotropy results to be the most important source of anisotropy in this sample.

Following the explanations in section 3.2.3.1 we can split the magnetocrystalline anisotropy in two parts, the band anisotropy and the crystal field anisotropy. We refer to band anisotropy as the contribution of the spin polarization of the itinerant electrons of the $REAu_2$ bands near the Fermi level. In the present case, $HoAu_2$ presents Ho^{3+} valence and as was shown in section 5.1.1 shares the band structure of $GdAu_2$. Therefore we can assume that the contribution of the band anisotropy would resemble the IP easy axis as in $GdAu_2$. However, this does not correspond to the experimentally observed anisotropy in this alloy. Hence, a different term that is not present in $GdAu_2$ has to be considered.

This additional term to the $GdAu_2$ case is the crystal field anisotropy that in $HoAu_2$ is a relevant term due to the electric interaction between the Ho 4f quadrupolar moment and the electric field produced by the rest of the electrons of the material. As it was commented above, the Ho $4f^{10}$ electron distribution has an oblate shape[42] that causes a negative quadrupole moment. This is different to the case of Gd, where the electron cloud has a spherical shape and consequently the

quadrupole term vanishes. The presence of a non-zero 4f quadrupolar term allows an important crystal field anisotropy contribution. From the experimental observation that the easy axis of the $HoAu_2$ is OOP, and the band contribution is IP, we can deduce that the crystal field contribution dominates over the band contribution and favors an OOP easy axis. The OOP easy axis together with the Ho 4f negative quadrupole moment allow us to assign a positive quadrupole crystal field in the direction normal to the surface for the $REAu_2$ structure. Finally if we consider that this crystal field is fixing the symmetry axis of the 4f orbital in the OOP direction, each of the subshells will also have a fixed direction, which will modify excitation probability of each individual transition and so, it can explain the shape difference in the XAS spectra between the IP and OOP geometries. This could be confirmed by future simulations of the XAS spectroscopy.

Considering the observed strong anisotropy, the hysteresis will be further analyzed. We will start from the simplest remagnetization model, the coherent rotation (see section 3.2.4.1). Applying Eq. 7 (section 3.2.4.1) with an anisotropy constant of 1.5meV from the estimation above, we would expect a coercive field on the order of 2 T. This is not the case, and the deviation of the prediction of this model can be understood by the fact that the high magnetic moment of Ho requires formation of small domains to minimize the energy (section 3.2.1). Such a domain wall structure has already been reported in the case of $GdAu_2$[18]. On a domain wall motion model, coercivity would be expected to be caused by pinning of the domain walls at defects, which become pinning centers (see section 3.2.4.2). Apart from presenting adequate characteristics (anisotropy or variation of interatomic coupling), the pinning center density has to be high enough. If the number is too small, the domains wall will anchor only on few defects, which will not produce enough energy advantage to keep the magnetic domain blocked. As was shown in section 5.1.1 the $HoAu_2$ alloy grown on monocrystalline Au(111) presents an almost defect-free structure. The result of this is a lack of pining centers to lock the magnetic domain walls. As a consequence, the magnetic structure will change in order to follow the magnetic field. To summarize, even if the alloy shows the most favorable easy axis for forming a 2D magnetic hard material, $HoAu_2$ does not present enough density of defects to allow a measurable remanence in XMCD technique.

In order to determine the Curie temperature of the alloy, the temperature dependence of the hysteresis loops has been measured. Figure 45 displays the results of this experiment. The curves show a smooth transition from a “square shape” toward linear paramagnetism as the sample temperature is increased. To determine properly the Curie temperature T_c, the chosen analysis method has been the Arrot Plot methodology (see section 3.2.5), that can be seen in Figure 45b). The advantage of this method is the possibility to determine the presence of magnetic order in the limit of near-zero coercivity. Moreover, the methodology is not sensitive to the measurement procedure (like field cooling vs zero field cooling for example[167,168]) and can be easily applied to XMCD results. It consists in plotting the squared magnetization values vs the applied field divided by the magnetization values (see Figure 45b)). Here, the magnetization values are exchanged by the XMCD values that are proportional to the magnetization. Then, the high field values (high H/M values) are fitted by a linear fit. The M^2-values at H/M=0, namely M_0^2, are in the last point (Figure 45c)) plotted vs the measurement temperature. The resulting fit (here second order) that crosses the $M_0^2 = 0$ line gives then the Curie temperature T_C. The Curie temperature determined by this method

corresponds to T_C = 22K. This temperature is slightly higher than the Curie temperature measured on $GdAu_2$ of T_C = 19K[17].

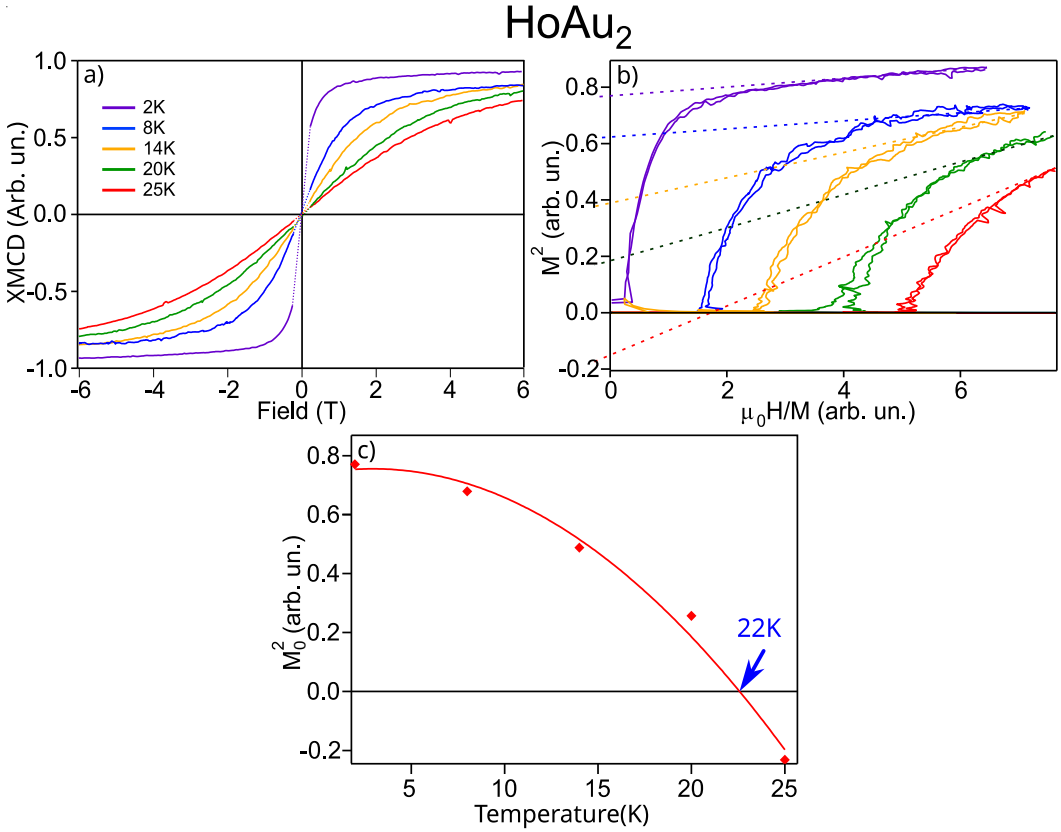

Figure 45: Temperature dependence of hysteresis loops for $HoAu_2$: a) magnetization curves as a function of sample temperature, b) Arrot plot M^2 vs H/M curves and their high field fits (dotted lines). The H/M=0 crossing points are used in c) to determine the Curie temperature T_C of the $HoAu_2$ system.

5.3.2 $DyAu_2$

XAS and XMCD measurements performed at a temperature of 4K and with an applied field of 6T in both geometries, IP and OOP, respectively, are shown in Figure 46. Data were obtained at Deimos beamline of SOLEIL synchrotron. As in $HoAu_2$ the spectra show two peaks, associated to the M_5 ($3d_{5/2}$) and M_4 ($3d_{3/2}$) transitions. Again, the density of states of the unoccupied p level is very small and mainly the 3d→4f transition is observed, allowing to prove the 4f shell of the RE and with it, also the magnetization of the alloy. $DyAu_2$ shows similar differences between geometries as $HoAu_2$. One is the marked change of shape in the M_5 transition between IP and OOP geometry, and as in the previous case, is caused by the non-spherical shape of the f-electron charge cloud of Dy. As in Ho, it is indicative of the orientation of the 4f level of Dy, even at saturation. By comparing the intensities of the two XMCD spectra it can be seen that in the OOP geometry, the intensity is almost doubled. This indicates an OOP easy magnetization axis.

The form of the XMCD spectra[166] indicates that the RE is trivalent (Dy^{3+}). This valence is associated with the $4f^9$ electron configuration, which has an oblate orbital shape.

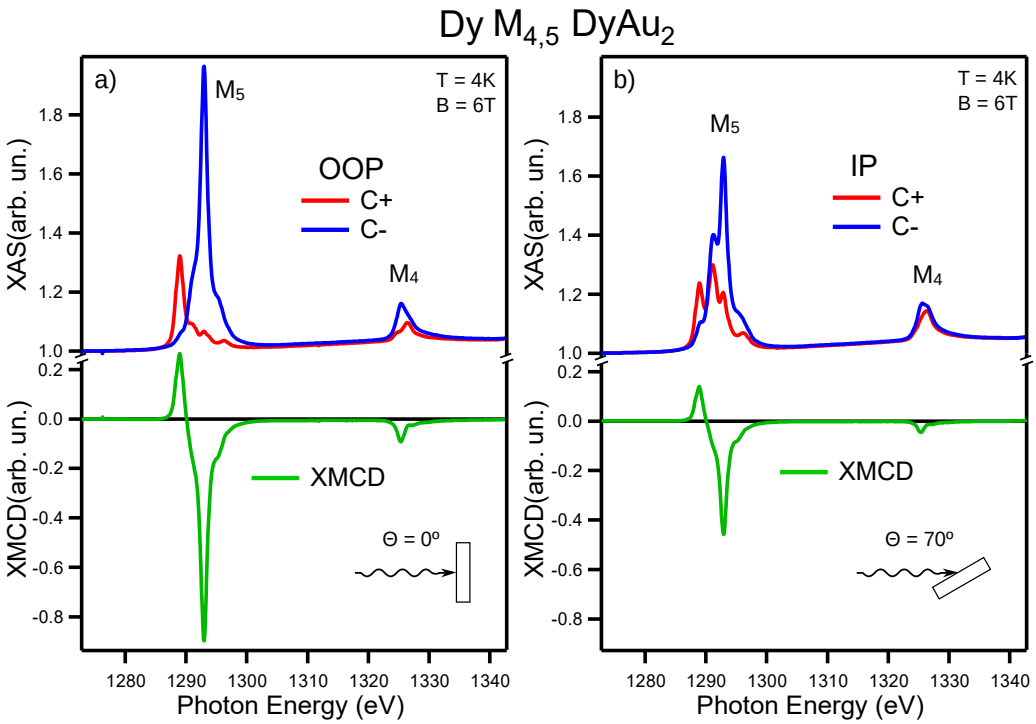

Figure 46: X-ray absorption (top) and XMCD spectra (bottom) of $DyAu_2$ measured at 6T and 4K in (a) OOP and (b) IP geometry, respectively. XAS spectra in red (blue) are measured with C+ (C-) circular polarized light. The dichroic XMCD spectra [C+]-[C-] is displayed in green.

Figure 47 shows the XMCD loops of $DyAu_2$. Similarly to $HoAu_2$, in OOP geometry we see a "square like" loop that saturates at approx. 1T. The magnetization curves in IP geometry shows a more "S shape" like curve form that does not saturate below 6T. We again attribute the observations to an OOP easy axis of magnetization. As it is observed in the XMCD loops, $DyAu_2$ does not reveal hysteresis opening in the measured region of the loop detectable with XMCD technique, resulting to be a soft ferromagnet, similarly to $HoAu_2$. As previously mentioned (see section 4.6.1), due to the characteristics of the measuring method, the remanence at zero field cannot be well determined and has to be measured apart.

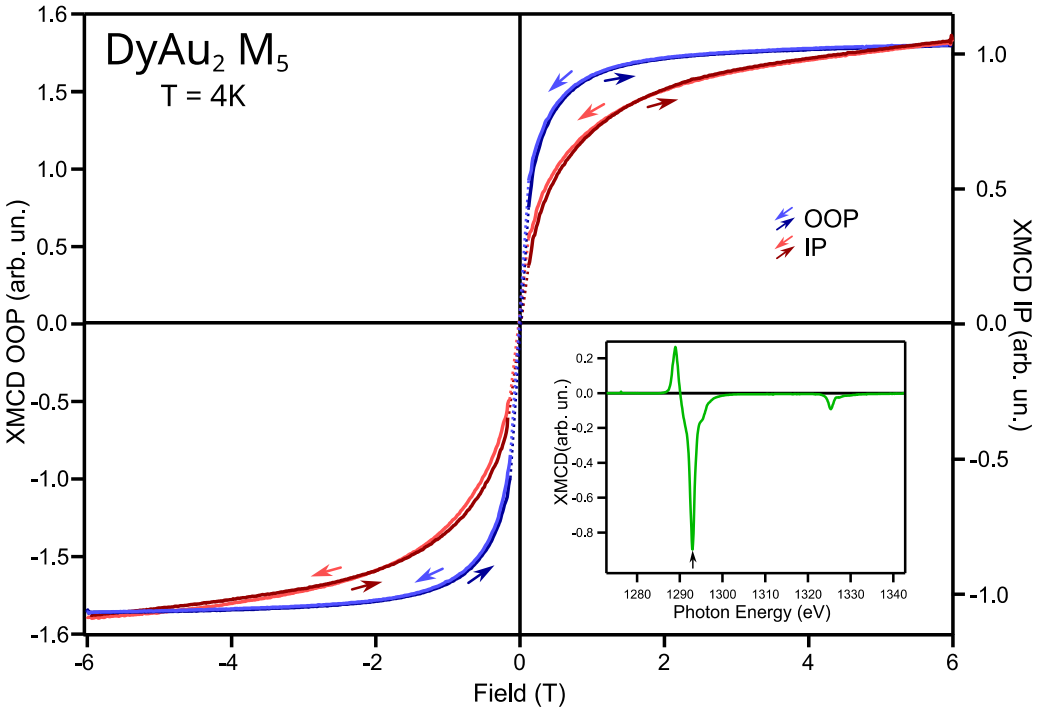

Figure 47: XMCD Hysteresis loop of $DyAu_2$ measured at 4K on the main peak of the M_5 transition. The shape of the loops confirms the OOP anisotropy. Note the difference of scale for the OOP and IP direction. The inset shows the XMCD spectra in OOP geometries marking the measurement photon energy.

On the origin of anisotropy, we can draw the same conclusion as for $HoAu_2$. Shape anisotropy results irrelevant as its magnitude its well below the observed effects. Taking into account that we have Dy with +3 valence, we can consider that $DyAu_2$ shares the $GdAu_2$ and $HoAu_2$ (RE^{3+}-Au_2) band structure. If this is the case, then we should have an IP easy axis of magnetization resulting from the band anisotropy term, contrary to the observations.

About the crystal field anisotropy, as in the case of Ho, the trivalent Dy 4f shell has oblate electron distribution[42], which causes a negative quadrupole moment. As was deduced from the $HoAu_2$ experiment (section 5.3.1), the structure of $REAu_2$ imposes a positive quadrupole moment that acts on the RE 4f orbital. If we apply the electrostatic interaction of both quadrupolar moments, we see again that the symmetry axis of the oblate Dy 4f electron distribution will have an OOP preferential orientation. This orientation of the symmetry axis translates into a maximum *L* moment in the OOP direction and so in an OOP magnetic easy axis. As this easy axis is the experimentally observed one, we can deduce that this term is dominating the magnetic anisotropy of the alloy. As in $HoAu_2$, the fixing of the symmetry direction of the oblate Dy 4f orbital by the crystal field would explain the shape difference in the XAS spectra between the geometries.

Following the same deduction as in $HoAu_2$, we can immediately see that coherent rotation is not a good model for the re-magnetization of $DyAu_2$, as the experiment does not show strong coercivity and the high magnetic moment of Dy will promote the formation of small magnetic domains. As has been shown in ref.[19], the $DyAu_2$ alloy also grows (almost) defect free, which has as consequence a lack of pinning points for the magnetic domain walls.

In order to determine the Curie temperature T_C of $DyAu_2$, several hysteresis loops have been measured at various temperatures, and the Arrot plot methodology (see sections 3.2.5 and 5.3.1) has been used (see Figure 10). As can be seen in the loops of Figure 48a), there is a smooth transition from a "square like" loop at the lowest temperatures towards an "S" shape with the increase of temperature and finally the curves change towards a more "linear" paramagnetic behavior. Figures 48b) and c) show the Arrot plot and linear fit used to extract the Curie temperature. The extracted T_C for $DyAu_2$ was of 24.5K, slightly higher than the Curie temperatures of $GdAu_2$ (19K) and $HoAu_2$ (22K).

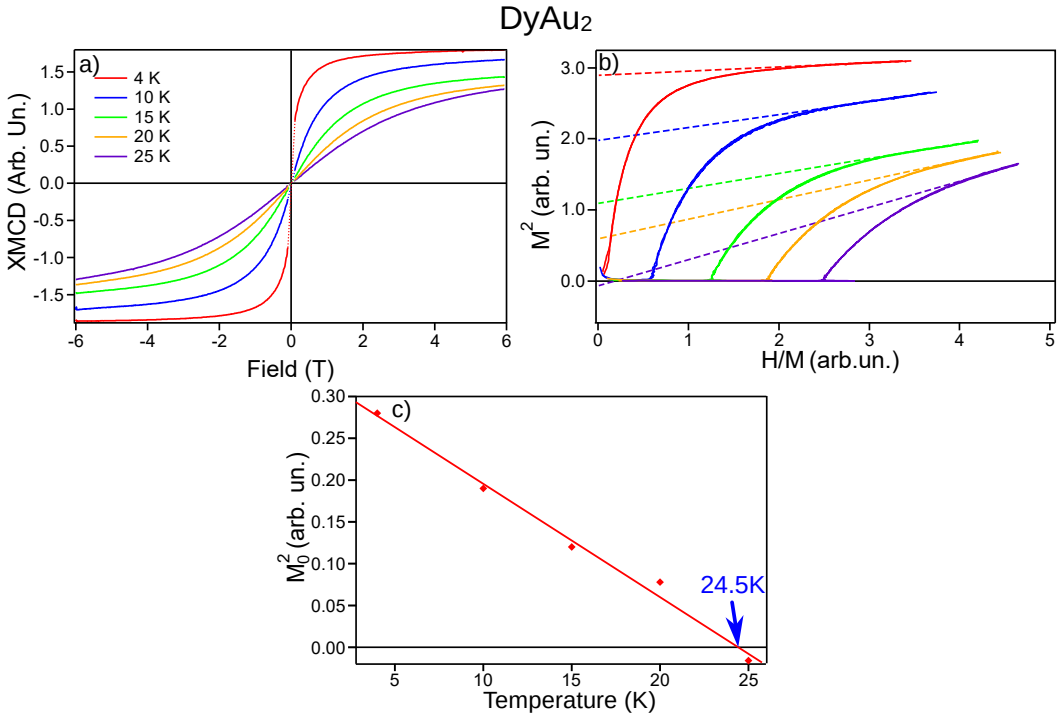

Figure 48: Temperature dependence of hysteresis loops for $DyAu_2$: a) magnetization curves as a function of sample temperature, b) Arrot plot M^2 vs H/M curves and their high field fits (dotted lines). The H/M=0 crossing points are used in c) to determine the Curie temperature T_C of the $HoAu_2$ system.

5.3.3 $SmAu_2$

XAS and XMCD measurements performed on a $SmAu_2$ monolayer at 6T and 2K are shown in Figure 49. These data have been obtained at Boreas beamline at Alba. In the same way as the previous alloys, the spectra reveal two peaks, associated to the M_5 ($3d_{5/2}$) and M_4 ($3d_{3/2}$) transitions into the empty 4f shell, as the transition probability to the 6p shell is low and broad. As before, this allows to prove the magnetization of the alloy through the 4f empty states. In this case, the difference in shape between the geometries in the XAS spectra is not as marked but a small difference is still present, mainly visible in the M_4 transition. As in Ho and Dy, it is indicative of a preferential direction of the 4f symmetry axis. In this alloy, the most marked difference for the XMCD spectra between geometries is the almost zero dichroism in OOP direction, while it is clearly present in the IP direction. This already indicates that the alloy has a strong anisotropy with

an IP easy axis.

The shape of the XMCD spectra confirms a mainly trivalent (Sm^{3+}) state for the RE as previously extracted from photoemission (section 5.2.1.1). This valency is linked to the $4f^5$ electron configuration, which has a prolate shape.

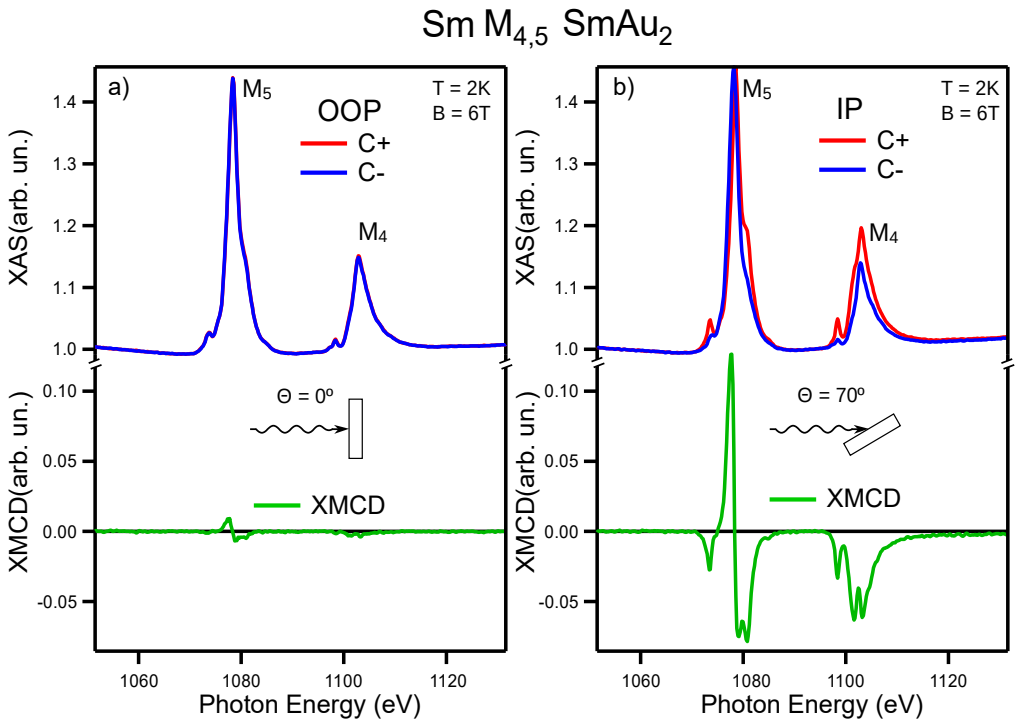

Figure 49 $M_{4,5}$ XMCD spectra of $SmAu_2$ measured at 6T and 2K. a) OOP measurements and b) IP measurements. In red (blue) we display the spectra measured with C+(C-) circular polarization of the light. The dichroic spectra is displayed in green ([C+]-[C-]).

Figure 50 shows the XMCD hysteresis loops of $SmAu_2$ at 2K. In this case, we see a "square like" loop summed to a linear response in the IP geometry, while the curves in OOP direction do not show clear magnetization. From this lack of magnetization in the OOP direction it is evident that the total effect of the anisotropy is a IP easy axis. The linear behavior could be explained by the presence of patches of paramagnetic phases, likely unalloyed Sm (see section 5.2.1.1) or Sm atoms that diffused inside the bulk due to an imperfect preparation of the sample. In this case the sample could be assumed to be already saturated for B > 0.5T. The coercive field is below 350mT.

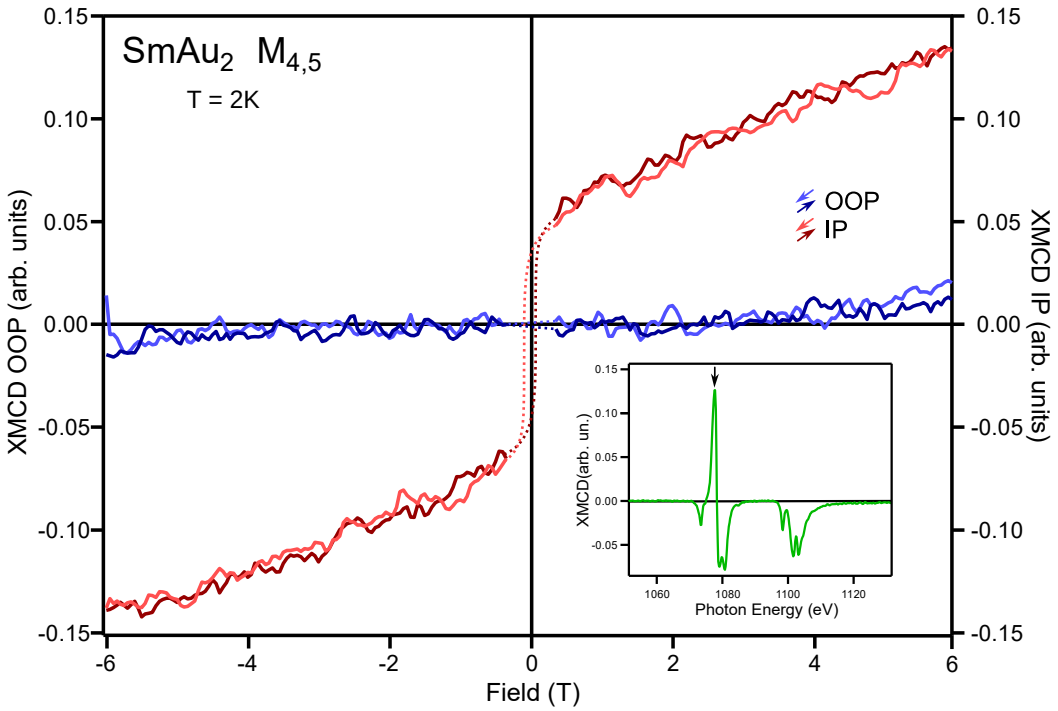

Figure 50: XMCD Hysteresis loop of $SmAu_2$ measured at 2K on the main peak of the M_5 transition. The insert shows the XMCD spectra in IP geometry marking the measurement photon energy.

About the shape anisotropy, as was shown in section 3.2.3 it is proportional to the square of the magnetic moment. If we now compare the magnetic moment obtained from the Hund Rules[34] (see table 1) of Ho^{3+} with Sm^{3+} (the Sm^{2+}magnetic moment is zero and as consequence not relevant for the discussion) we see that the moment of Sm is below 1/10 of the Ho moment. These two things together imply the shape anisotropy in $SmAu_2$ is below 1/100 of the one of $HoAu_2$, which as was previously shown was small and not relevant. As consequence, the shape anisotropy on $SmAu_2$ will be irrelevant. Sharing the band structure with the rest of the tri-valent $REAu_2$ ($GdAu_2$, $HoAu_2$) surface compounds (section 5.2.1.2) it is safe to assume that the band anisotropy will also favor in plane easy axis.

As previously was shown in the case of Ho and Dy, the $REAu_2$ structure imposes a positive quadrupole moment to the 4f shell of the RE. While for Ho and Dy the orbital shape of the 4f was oblate, in the case of Sm the shape is prolate[42]. This change of shape implies an inversion of the direction of the quadrupole moment of the RE 4f, which in this case will be negative. Applying the electrostatic interaction of the quadrupoles, the 4f shell of Sm will minimize its electrostatic energy by situating its symmetry axis in the surface plane. This means that the magnetic moment of Sm 4f will be preferentially oriented in the IP direction. Thus, both terms of the magnetocrystalline anisotropy point to IP easy axis, which is expected to reinforce its magnitude.

For the hysteresis discussion we will consider two possibilities, prevalence of (i) coherent rotation or (ii) domain wall (DW) movement. In the coherent rotation model, the measured IP anisotropy in a 2D material allows free rotation in the plane, and, therefore, zero coercivity would be expected.

This would lead to a square like loop with switching at zero field. For the case of DW movement prevalence, coercivity would still be possible, if there exist sufficient local defects that are capable of pinning the domain walls (as explained in section 3.2.4.2, and as was already shown in $GdAu_2$ by spin resolved STM[18]). Here, both scenarios are possible, since the low magnetic momentum of Sm will favor the formation of large magnetic domains, possibly minimizing the contribution of the domain wall movement. In order to clarify this point, a detailed study in the small field region with space resolving technique (like spin resolve STM) will be necessary.

5.3.4 $EuAu_2$

The $M_{4,5}$ absorption edge XAS measurements of $EuAu_2$ monolayer is shown in Figure 51. This time data were obtained at ALBA synchrotron, BOREAS beamline. The spectrum of $EuAu_2$ is accompanied by a measurement carried on Eu_2O_3 where the Eu is in a tri-valent state. This set of measurements was taken with linear polarized light at normal incidence, in order to ensure the chemical state of Eu in the sample. In both $EuAu_2$ and Eu_2O_3 we see the peaks associated to the M_5 ($3d_{5/2}$) and M_4 ($3d_{3/2}$) transitions into the partially empty 4f shell. As can be seen, the two materials reveal clear differences, indicating a variation of the contributing empty shells and an energy displacement of the 4f shell respectively. From that it is clear that the chemical state of Eu in both samples is different. Taking into account that Eu_2O_3 presents a trivalent state, and that Eu can only present di- or trivalent valence states, we can conclude only from this measurement that Eu in $EuAu_2$ is divalent. Further comparison to bibliography confirms this deduction, as $EuAu_2$ matches previous spectra of divalent species[169,170]. This is consistent with the di-valent valence of europium already obtained by photoemission (Section 5.2.2.2).

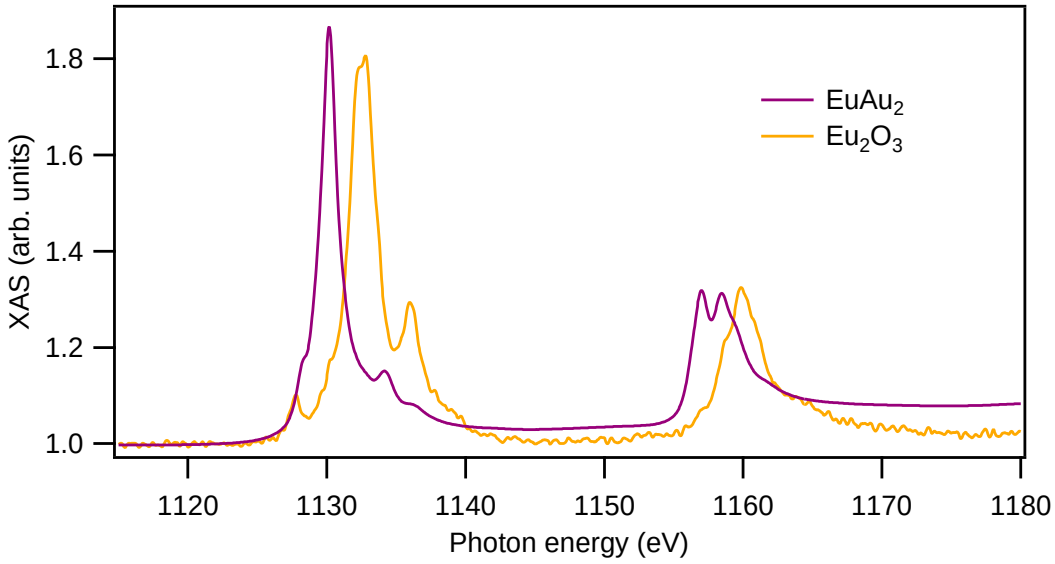

Figure 51: X-ray absorption spectra taken with linear horizontal polarized light at normal incidence geometry for $EuAu_2$ and Eu_2O_3. One can see the spectra of completely divalent Eu in $EuAu_2$ and trivalent Eu in Eu_2O_3. Reference spectra of Eu in different compounds can be found in ref.[166,169,170].

Once that the valency of Eu is clear, we can continue the study of $EuAu_2$. Figure 52 shows the XAS-XMCD spectra of $EuAu_2$ (taken with circular polarization) at 6T and 2K, both in OOP and IP geometries. In contrast to $HoAu_2$, $DyAu_2$ and $SmAu_2$, there are no differences in XAS between IP and OOP geometries. The lack of change of shape of the transition is expected since Eu^{2+} 4f orbital is spherical and, therefore, the orbital should not reveal any preferred orientation. Furthermore, there isn't a strong difference in the dichroism signal (XMCD) when the sample is saturated. This is also expected, as the orbital momentum of Eu^{2+} is 0 (L = 0) eliminating the contribution of the 4f spin orbit to the magnetic anisotropy.

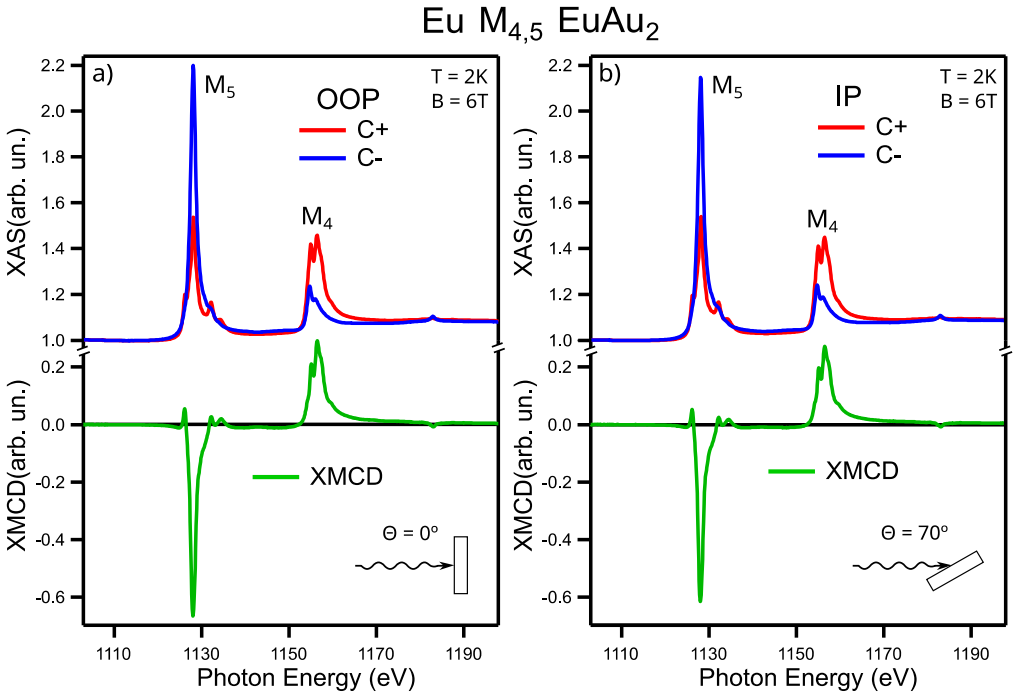

Figure 52: XAS and XMCD spectra at Eu $M_{4,5}$ of $EuAu_2$ measured at 6T and 2K . a) OOP and b) IP measurements of the XAS for C+(C-) circular polarization, red (blue), respectively. The dichroic XMCD spectra [C+]-[C-] is presented in green.

XMCD hysteresis loops of $EuAu_2$ were taken at 2K and at a photon energy corresponding to the maximum of the M_5 transition and is shown in Figure 53. In this case we see a rather "square like" loop with a jump in the near zero field for both geometries, with the IP geometry loop having a smoother "S" like behavior with much lower magnetization at low fields. This shape indicates a clear OOP easy axis. At 6T applied field the sample has reached magnetic saturation in both geometries. The dichroic XMCD signal in saturation is nearly identical. The XAS and XMCD signals after removing the field (after saturating the sample applying 6T) was measured separately (not shown). In the case of OOP geometry, this remanence signal corresponds to 72% of the saturation magnetization, while for IP geometry, it corresponds only to a 26% of saturation.

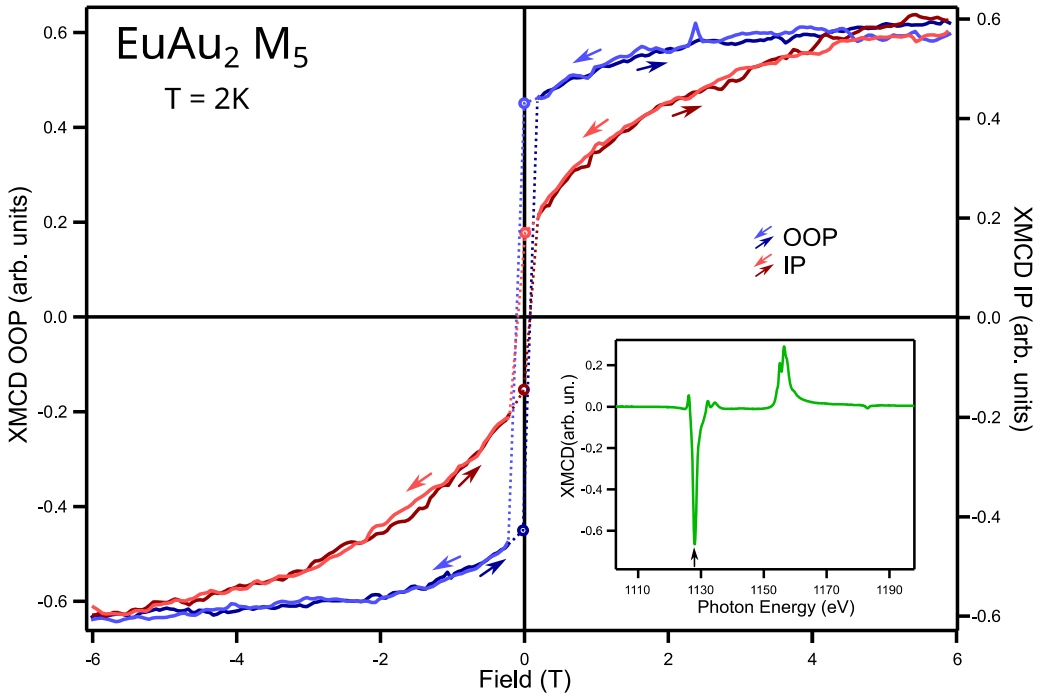

Figure 53: Eu M_5 XMCD Hysteresis loop of $EuAu_2$ measured at 2K at the maximum of the M_5 transition. Zero field points were taken manually and added to the graph as circular marker. The inset shows the XMCD spectra in IP geometries marking the measurement photon energy.

As for the rest of the RE-Au_2 surface alloys, we will analyze the source of the observed anisotropy. As before, shape anisotropy contribution probes to be irrelevant, as the magnitude and direction does not match the measured effect. For the crystal field contribution, we have to remember that Eu is di-valent, i.e., the 4f shell is half filled ($4f^7$). This implies that the 4f electron cloud has a spherical shape and no quadrupole moment or preferential direction for the orbital, which leads to a zero crystal field contribution.

On the band anisotropy, as it was shown in section 5.2.2.2, it is caused by 4f-5d hybridization. There, we probed that the 4f levels in Eu^{2+} are situated right below the Fermi level, hybridizing with the valence band and inducing a strong break of the 4f subshell degeneracy. As a consequence of this degeneracy breaking, the OOP direction becomes favorable direction of spin polarization, or what is the same the magnetic easy axis. As commented also in section 5.2.2.2, it can also be seen as a breaking of the spherical symmetry leading to an effective $L \neq 0$ and, as consequence causing the measured OOP easy axis.

In the following we will discuss the remanence observed in Figure 53. Let us start by the simplest re-magnetization model, the coherent rotation of domains. Due to the OOP easy axis, coercivity would be expected in the OOP direction but not in the IP. This would explain the remanence values in the OOP direction but does not explain the IP case. The coherent rotation only gives remanence in the easy axis direction. With that in mind, remanence in another direction will be given by the OOP component of the magnetization, that is, the projection of the magnetization on that direction [cos(θ)]. Due to the incidence angle of the measurement light beam, the projection will appear

again, giving as results a $\cos^2(\theta)$ contribution of the OOP magnetization. In our IP case, the incidence and field angle θ to the normal is 70° giving as result, a maximum remanence in the coherent rotation model of 9%, too small for the observed value. On the other hand, the 1 meV band anisotropy estimated by DFT simulation[50] (section 5.2.1.2) would cause a much higher coercivity in the OOP direction (of the order of 2T). Next, we consider the domain wall motion model. As in Gd, Ho and Dy, the high magnetic moment favors the formation of small magnetic domains. Here, coercivity would be expected to be caused by pinning of the domain wall motion at defects (section 3.2.4.2). As seen by the STM microscopy, the sample presents a periodic lattice of defects that are assumed to break the coordination of the alloy. These defects can cause local effects, like different easy axis and weakening of the coupling, and acting as highly effective domain wall pinning centers. This also explains the remanence in the hard axis of $EuAu_2$. This is reinforced by the lack of remanence in the hard axis of $GdAu_2$[17], which grows without defects. To summarize, the seen remanence (and the associated coercivity) is caused by pinning of domain walls on the defect lattice of the alloy.

As for the rest of the surface compounds, the Curie temperature T_C has been determined by the measurement of XMCD loops at different temperatures. In this case, this temperature dependence was taken in the hard axis of the sample (IP geometry) and the analysis is shown in Figure 54. The Arrot plot analysis has been used to extract T_C. The Curie temperature determined by this method has been 13K, a lower value than the Curie temperature of $GdAu_2$ (19K), $HoAu_2$ (22K) and $DyAu_2$ (24.5K).

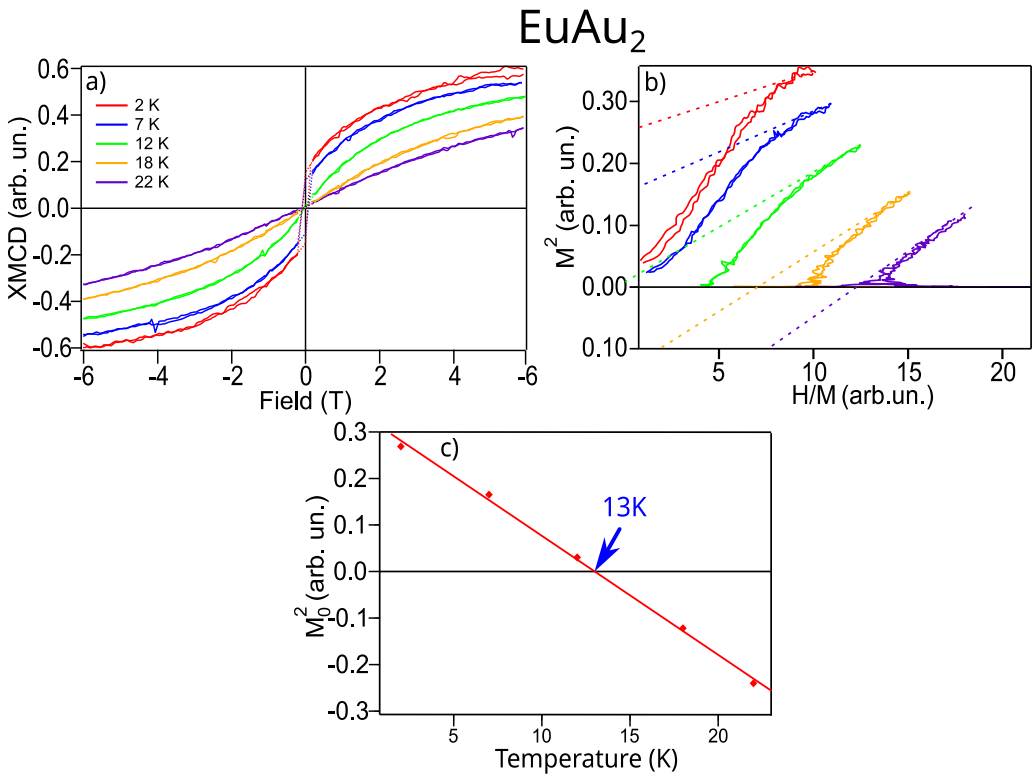

Figure 54: Temperature dependence of hysteresis loops for $EuAu_2$: a) magnetization curves as a function of sample temperature, b) Arrot plot M^2 vs H/M curves and their high field fits (dotted lines). The H/M=0 crossing points are used in c) to determine the Curie temperature T_C of the $EuAu_2$ system.

6 Two-dimensional Ag based $REAg_2$ surface alloys

6.1 Structure of $REAg_2$ surface alloys

For the case of RE alloys on Ag(111), LEED shows two types of patterns (Figure 55). The first case, would be the one corresponding to $SmAg_2$, with the $(\sqrt{3}\times\sqrt{3})R30°$ + Moiré reconstruction already explained in section 5.1.1 and also reported for $GdAg_2$[17]. By careful analysis of the LEED pattern we can extract a $(10\times10)R0°$ Moiré reconstruction with respect to the Ag(111). However, it should be noted that due to the LEED screen curvature and the order of magnitude of difference between the Moiré spots and the Ag(111), the precision of this calculation is limited. For the case of $HoAg_2$, the pattern becomes much more complex. On a first glance, it appears similar just changing the hexagonal shape of the Moiré spots (marked in orange) to a diamond-like shape. Further inspection, though, reveals that we can see that the expected first order spots of the alloy (in blue) are split into two peaks. This splitting in not only limited to the alloy spots, but also to the substrate spots, i.e., Ag(111) spots (in red) also results to be split. Additionally, new intense spots (marked in green) have been formed at a position that would be the second order diffraction of the $(\sqrt{3}\times\sqrt{3})R30^o$. Note that the spots around the $(\sqrt{3}\times\sqrt{3})R30^o$, the Ag(111) substrate spots and the second order diffraction looks different. This is unusual in LEED diffraction patterns where the basic units repeat for higher orders. The Moiré spots can be described approximately by a $(14.5\times14.5)R0^o$ superlattice with respect to the Ag(111) substrate. The same or very similar LEED pattern has also been reported in $DyAg_2$[19]. The authors there claim the formation of anti-phase domains as the source of the splitting of the alloy spots. Nevertheless, the authors in this publication are not able to explain the splitting of the substrate spots, or the formation of the intense higher order spots that are marked in green.

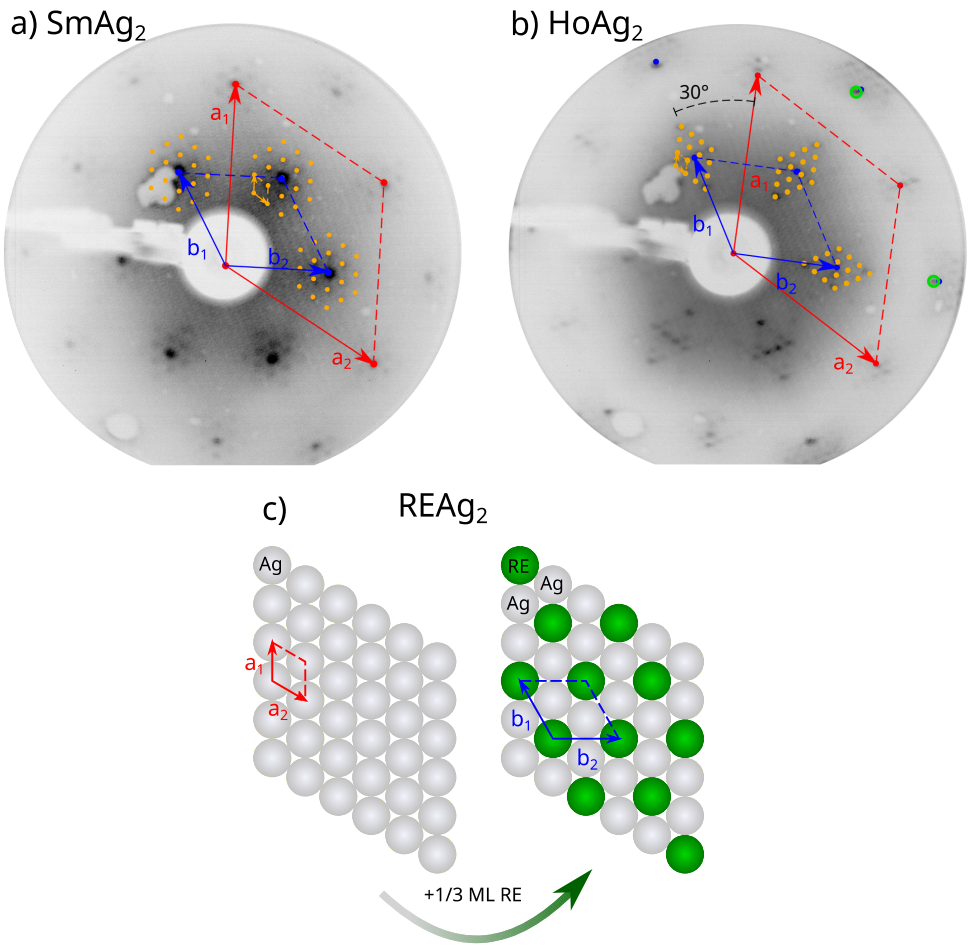

Figure 55: a), b) LEED Pattern of $SmAg_2$ and $HoAg_2$, respectively. The beam energy was 60 eV. c) Model of alloy structure, in red lattice of Ag(111) surface. In blue we mark the lattice of the $(\sqrt{3}\times\sqrt{3})R30^o$ lattice, in red the Ag(111) substrate, and in orange the lattice of the Moiré reconstruction.

For this reason, here we will shortly focus on this fact. To do so, in Figure 56a) and b) we present the LEED pattern of $HoAg_2$ but at a different sample angle to appreciate better the (0,0) spot normal to the surface and at a different energy to be able to include additional diffraction spots that may be hidden for special energies. In part c) of the same figure we now present the diffraction spots extracted from the different LEED patterns. Again, a simple translation and rotation of the spots around the $(\sqrt{3}\times\sqrt{3})R30^o$ is unable to produce the LEED pattern.

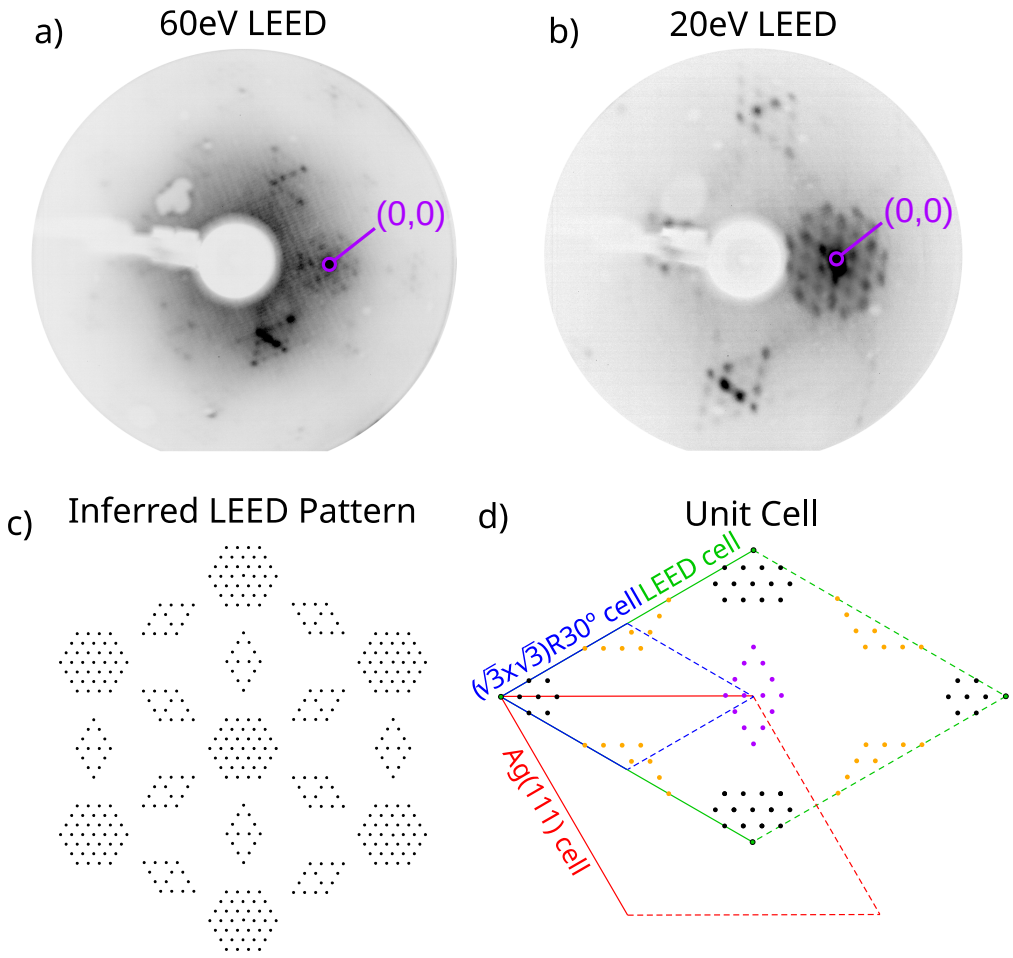

Figure 56: LEED patterns of $HoAg_2$ and subsequent analysis. a) and b) LEED patterns of $HoAg_2$ at $\theta=10^o$ from normal incidence at 60eV and 20eV beam energies. c) idealized diffraction pattern constructed by superposition of series of LEED images at different incidence angles and beam energies. d) Unit cell extracted from c), remarking the rotation of the rhombus around the Ag(111) spots (in purple) compared to the ones around the $(\sqrt{3}\times\sqrt{3})R30^o$ spot (in orange). The unit cells of the diffraction pattern is marked in green, unit cell of the alloy is marked in blue, and unit cell of Ag(111) is marked in red.

In order to clarify the source of the rather strange LEED pattern we have performed STM investigations of the $HoAg_2$ surface alloy. Figure 57 shows the atomic resolution image of the alloy with the Ho atoms as bright protrusions. It can be seen that the surface is formed of almost hexagonal tiles that are separated by dislocation lines, see also Fig. 58. Inside the tiles we can find a hexagonal lattice corresponding to the $(\sqrt{3}\times\sqrt{3})R30^o$ lattice. Additionally, there is a modulation of the depth, showing a depression in the center. The lattice constant of the white protrusions in short range are $(5.2\pm0.1)\text{Å}$, the average distance between tiles is $(4.5\pm0.4)nm$. Further analyzing Figure 57 reveals several other things to be noted. First, the tiles are not completely hexagonal. All tiles of this image are extended in one direction. The direction in which the tiles are extended is shared, at least inside a certain domain as the one of this image. Second, different types of tiles can be found, that can be classified according to the number of atoms forming the sides.

Here, each type of tile is marked with a different color. No periodic distribution of the types of tiles can be detected. We furthermore observe two types of dislocations at the borders of the tiles. A smaller amount of dislocation, marked in blue (nearly horizontal) in Figure 57, separate the protrusions at the borders of the tiles similar to a mirror line. The majority of the dislocations, however, are marked in red. These are formed by the inclusion of an additional atom row between the tile borders. This row of atoms can be seen as protrusion in Figures 57 and 58b). In that latter image only one type of the dislocation lines is visible occurring mainly in up-down orientation.

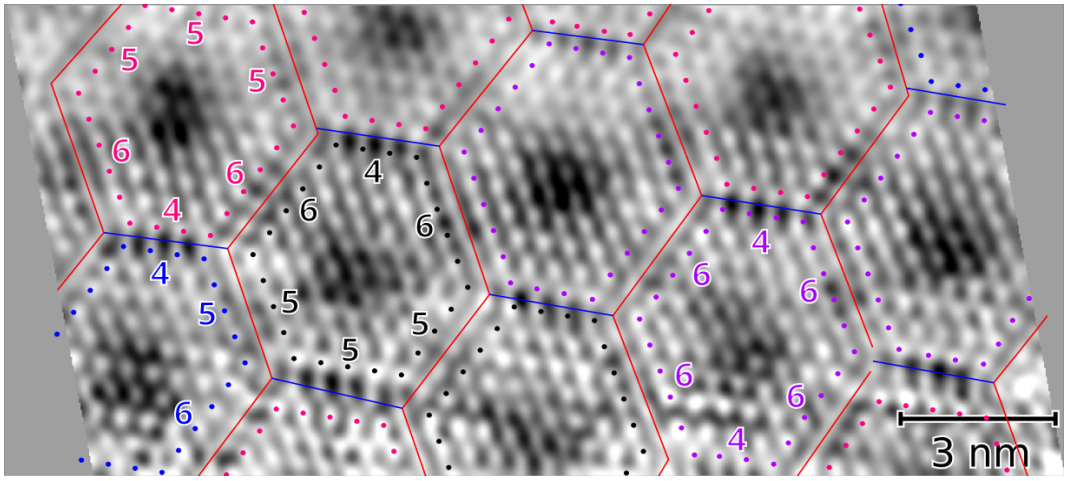

Figure 57: Analysis of the atomically resolved STM image of $HoAg_2$ (image size $20\times9nm^2$ tip voltage 1V, target current 0.3 nA) revealing multiple types of tiles (marked in different colors). The tiles can be distinguished easily by counting the atoms of the tiles borders (marked for each type of tile detected). Two types of dislocations can be detected and are marked by lines of different colors.

Furthermore, in Figure 58b) we can observe that the depression in the center of the tiles results in a Moiré-like modulation. Analyzing an even larger image, (Figure 58c)), it can be seen that the Moiré + dislocations form almost ordered domains of oblique lattice. The visible dislocation lines are running here mainly left/right, i.e., we are watching a different domain. Looking in detail, it is clear that there is not really a long-range order, as the distances between the dislocation lines are not a stable value. We can even see that some expected dislocation are missing, like the one in the center of the image. The breaking of the hexagonal symmetry seems to arise from preferential directions of the deformation of the tiles in the domains. Nevertheless, on large scale images the imperfections on the short scale are not observed anymore. Figure 58d) is the largest image taken on this surface compound. We observe a nearly hexagonal pattern. The Fourier transformation (Figure 58e)) indicate a hexagonal order that arises from the Moiré like pattern.

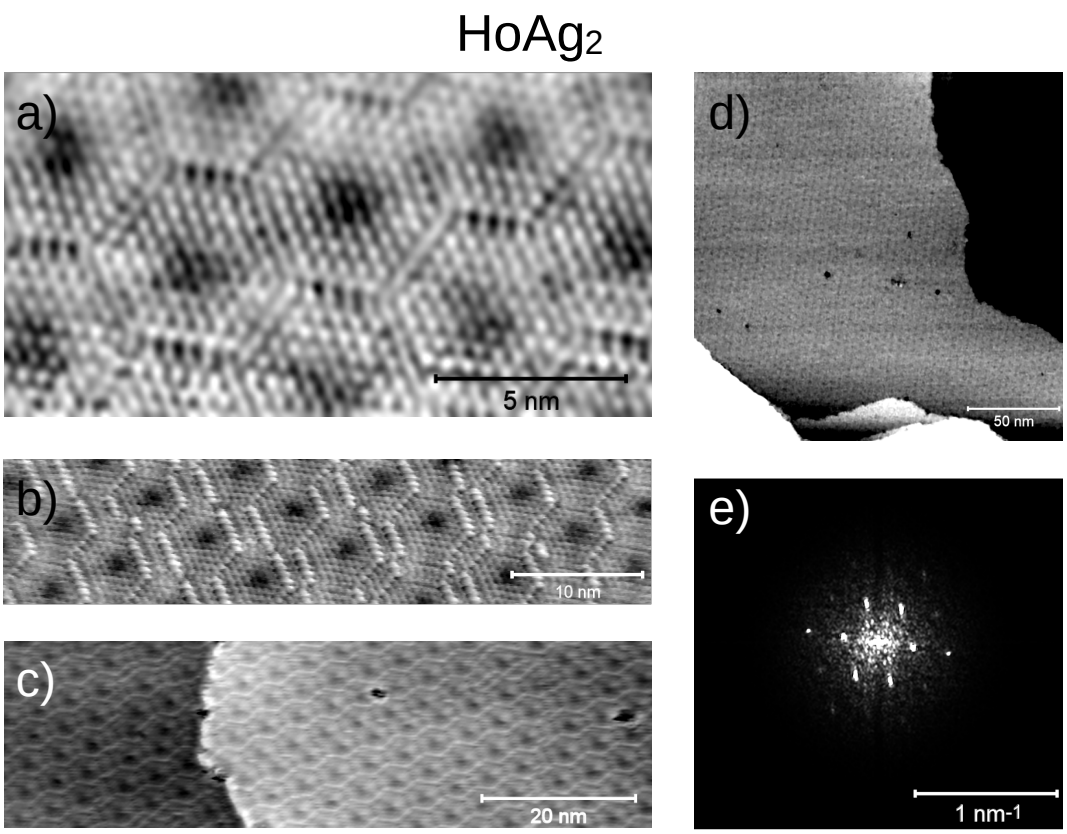

Figure 58: STM images of $HoAg_2$ revealing the "disorder and order" process from few atoms range to hundreds of nm range (tip voltage 1V, target current 0.3nA) a) image size 16×9nm², b) image size 50×10nm², c) image size 80×23nm², d) image size 200×200nm² e) Fourier transform of d) revealing a Moiré-like reconstruction.

Let us further examine the observations: The $HoAg_2$ lattice constant of 5.2Å (see above) leads to an inter-atomic distance of $5.2\,Å/\sqrt{3}=3.0\,Å$. The lattice mismatch to the underlying Ag with inter-atomic distance $4.09\,Å/\sqrt{2}=2.89\,Å$ is 3.8%. For such a misfit in a normal Moiré we expect an approx. (26×26) superstructure (1/0.0388) of 7.5nm lattice. This value is much larger than the observed 4.5nm. In Fig. 59 a model of the system is shown: in part a) the expected (26×26) Moiré lattice started from a hollow position of one Ho atom marked in the center of the image. We observe that along the [1-10] directions after several $HoAg_2$ units we get Ho atoms in top positions (marked with green circles). The hexagon that we included in Figure 59a) is a prototype of the tile observed in the STM. We see that the top positions are just outside of the tile. In Fig 59b) we modify the model and now include only the $HoAg_2$ atoms in the tile but create a structure of tiles with the measured 4.5nm Moiré-like structure. One immediately sees the difference; the top positions are completely eliminated by such a tessellation. This is the reason behind this structure, the elimination of the energetically unfavorable top positions. Such a restructuring is sometimes observed in overlayer systems[171–174] together with surface stress release.

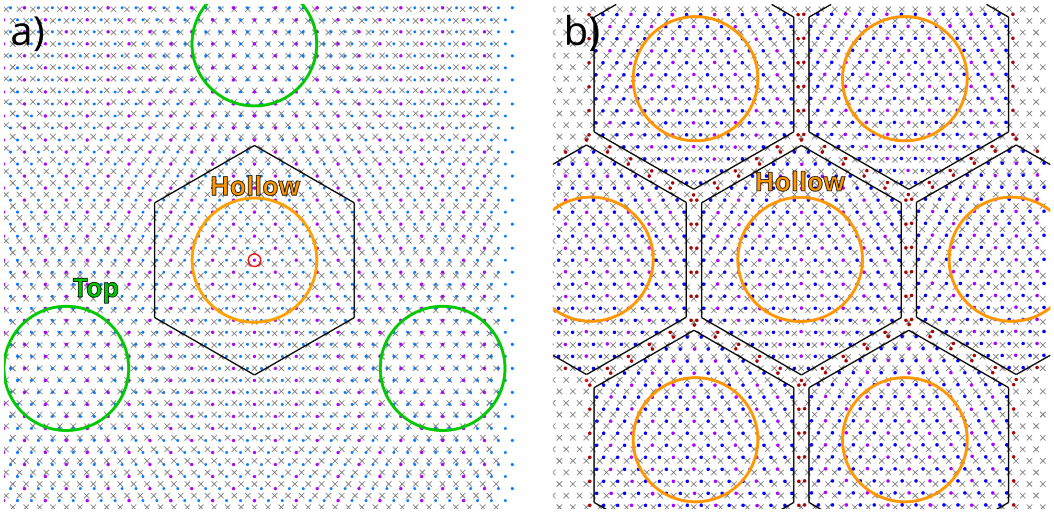

Figure 59: Simplified model of the a) Moiré structure and b) Tile structure applied to observed lattice parameters of $HoAu_2$. The construction is quite similar to Fig. 4 of ref. [19]. The main difference is that here we put the central Ho atom of the overlayer in a hollow position and are then able to observe the elimination of unfavorable top positions.

Now, we can turn back to the reciprocal space to understand the LEED pattern of Figure 55b). We start by considering the effect of the tile formation. As was shown in ref. [19], the tiles formation causes a splitting of the alloy spots. This occurs since the tiles break the coincidence of the structure with itself due to the displacements of one unit vector of the alloy. This leads to a removal of the usual $\sqrt{3}$ spots. Nevertheless, there is still a long-range coincidence after a displacement of one tile that produces the Moiré-like spots. Still, even though the alloy does not create the self-similarity of the lattice after the displacement of an alloy unit vector, it modulates the intensity of the Moiré-like spots, leading to the Moiré-like pattern being visible only were the alloy spots would be. This can be also understood by considering the LEED pattern as being formed by the diffraction of the dislocation lines. Still, these considerations imply a three-fold symmetry around the (now invisible) $(\sqrt{3}\times\sqrt{3})R30^o$ spots. In order to break this symmetry, we have to introduce an additional, lower-symmetry lattice. This may be achieved by the inclusion of non-hexagonal tiles, exactly the ones seen in the STM images. In any case, the sharp LEED pattern obtained indicates that even though no local order can be extracted from the tiles, a long range periodicity appears for the surface alloy indicating that the reconstruction is a quasi-crystalline lattice[175]. Such quasi-crystalline lattices lack of a short-range order but still reveal sharp LEED patterns and photoemission results[176,177]. This long range periodicity is caused by the repetition of similar (but not exactly equal) tiles over the surface, keeping a coherent distance between them. As the tiles have to be situated at precise positions to fit the substrate atomic structure, the average distance has to be precise for the relaxation of the surface tension.

Last, we want to mention that not only the here studied $HoAg_2$ and the $DyAg_2$ surface alloy of ref. [19] reveal such a described tessellation. Also $GdAg_2$ can present such a structure if the preparation

temperature is slightly modified[48]. In all these systems tiny variations in the alloy formation seems to influence the formation energy of the systems and their structure.

6.2 Electronic structure

We studied the electronic structure of $GdAg_2$, $HoAg_2$ and $SmAg_2$ MLs by photoemission spectroscopy. The three surface compounds reveal a similar electronic structure, which is due to the trivalent (or almost trivalent) (3+) valence state.

Figure 60 shows as an example a XPS spectra measured for $SmAg_2$, which displays the composition of the sample and probes that there is no oxygen or carbon in the sample. For the XPS measurements our laboratory-based monochromatized Al K_α X-ray source (1486.7 eV) was used. The experimental resolution of the measurement does not allow to resolve bulk and surface components if there would be any. The Sm emissions corresponding to the 3d and 4d, and the Sm MNN Auger emission can be identified, but the Sm peak results much less intense than the peaks of Ag. This is related to the small amount of Sm (1/3 ML) and to the small photoemission cross section of Sm in comparison to Ag. In the valence band energy range, the Sm 4f and Ag 4d emissions are very close in energy and appear superposed. The cross sections of Sm 4s, 4p, 5s and 5p are too small with the selected photon energy to produce discernible peaks. A detailed inspection of Figure 60 allows already a distinction of a di- and trivalent component in the Sm 3d core level. The divalent (2+) contribution on the lower binding energy side of the 3d doublet has a lower intensity and a smaller width. An integration of the individual peaks corresponding to 2+ and 3+ contributions results in a Sm^{2+} contribution of 24%.

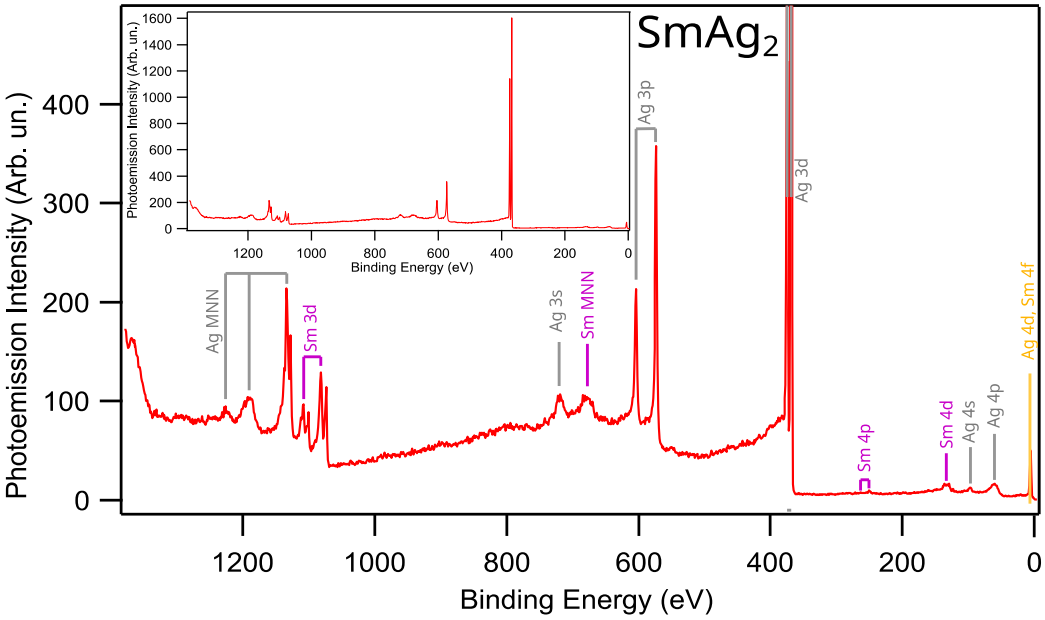

Figure 60: XPS measurement of $SmAg_2$ surface compound excited by a monochromized Al K_α X-ray source. Ag emissions are marked in grey, emission lines of Sm are marked in purple. The valence band energy range contains the Sm 4f and Ag 4d levels that are superposed and are marked in orange. Peaks were assigned according to ref.[150–152].

A more detailed investigation about the valence state in the RE-Ag_2 surface compounds focuses again on the 4f and 5p core level emissions. Figure 61 shows the photoemission spectra of the Gd 4f and 5p core level regions for $GdAg_2$ and $HoAg_2$ MLs, respectively. For further considerations, Figure 62 display the 4f levels of Sm in $SmAg_2$. The spectra were measured at the spin-ARPES setup (RGBL II) at Bessy II synchrotron in Berlin (Gd, Ho) and VUV-Photoemission beamline at Elettra in Trieste (Sm), respectively. As in the RE-gold alloys, photon energies corresponding to on- and off-resonance were used to separate the 4f core level emission from other electronic states in the valence band region of the surface compound.

In the case of the Gd 5p level of $GdAg_2$ indicated in Figure 61a) measured with a photon energy of 136 eV there is a multiplet structure that is caused by multiple final states[156]. The spectrum matches well with the theoretical expected one for a trivalent multiplet as well as with the one measured in $GdAu_2$ (Figure 34c)). The Gd 4f level measured at $GdAg_2$ in on- ($h\nu$ = 148.5 eV) and off- ($h\nu$ = 135 eV) resonance is shown on Figure 61b). As for the 5p emission, especially for the on-resonant spectrum we observe a multiplet arising from the multiplicity of excited final states that coincides well again with the theoretical trivalent multiplet and the 4f level measured for $GdAu_2$. The matching of both multiplets and the absence of a possible divalent emission indicates that Gd in $GdAg_2$ alloy is purely trivalent giving as result a $4f^7$ electronic configuration. Similar to the Au case, we can asses the effect of alloying by comparing the position with the pure metal surface that also presents ninefold coordination. The trivalent Gd 4f and 5p lines of $GdAg_2$ are shifted to higher binding energies by 0.4 eV and 0.2 eV, respectively, with respect to the corresponding surface core levels in pure metallic Gd[122]. This core level shift is slightly smaller compared to the $GdAu_2$ case,

following the lower electronegativity of Ag compared to Au[178].

For $HoAg_2$ the situation is very similar. In fact, the Ho 4f multiplet (Figure 61d)) reveals a trivalent character. In this case, the 4f emission is identical to the surface component in metallic Ho[159]. This means that the 4f emission is shifted by 0.37 eV towards lower binding energy with respect to the $HoAu_2$ case. Again, this shift is expected due to the lower electronegativity of Ag. In the experimental part, it was mentioned, that sometimes it was difficult to remove completely RE atoms from previous experiments. Here, in this Figure 61d) we can examine for such possibility. If we would have a look only on the resonance and anti-resonance of the Ho 4f level, we would not note any strange behavior. Nevertheless, here, for the prepared $HoAg_2$ layer, we added the spectrum measured at 148 eV, the on-resonance energy of Gd^{3+}. And effectively, there is an emission at 8.8eV binding energy that could correspond to Gd 4f. It is now worth to estimate in this case, how much Gd would be incorporated in the surface from this $HoAg_2$ preparation.

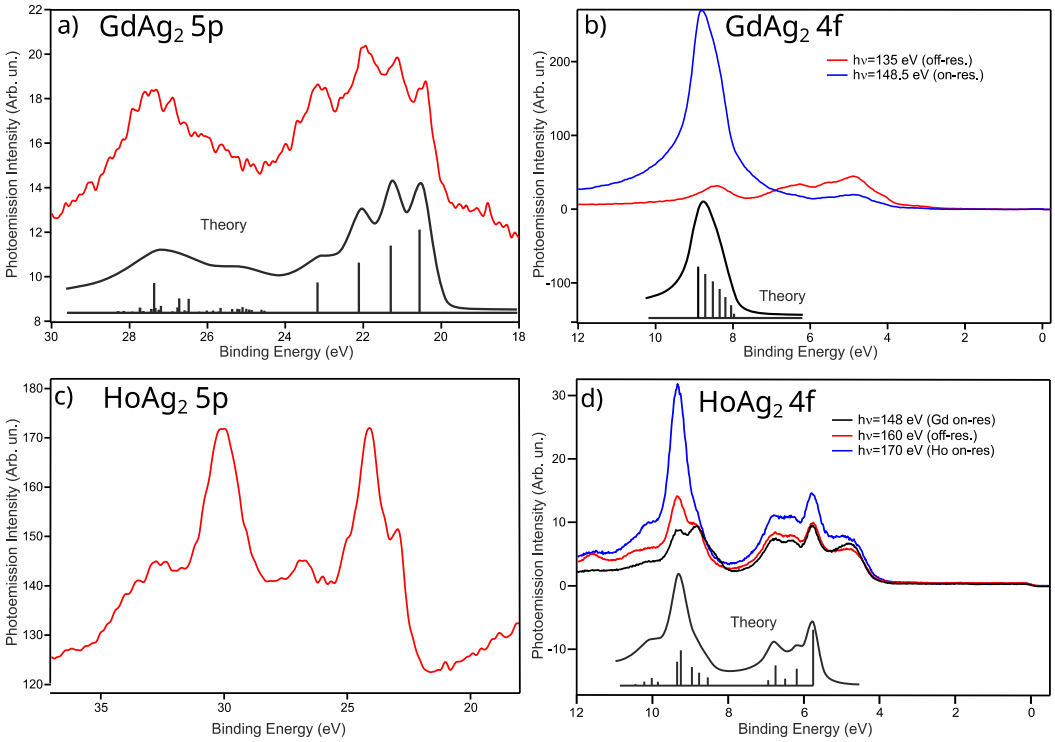

Figure 61: Resonant Photoemission of $GdAg_2$ and $HoAg_2$: a),c) photoemission of Gd and Ho 5p core level regions; b),d) On- and off-resonant photoemission of Gd and Ho electrons of the valence band energy region, respectively. The theoretical spectra below are taken from reference [153] and denote calculations of the excited electrons.

In the region of the 4d-4f resonance, the intensities of the individual terms of a 4f multiplet can strongly vary as a function of the photon energy. This is because the $4d^9$-$4f^{n+1}$ intermediate state forms a multiplet several eV wide and depends on which term of this multiplet it is excited with the chosen photon energy and how the final states arising from the Super-Coster-Kronig decay of the intermediate state before interference with the ordinary photoemission states through the Fano-Beutler resonance[119]. Outside the resonance, the intensities of the individual terms can vary

additionally due to matrix element effects, which depend on the polarization of the synchrotron radiation and the photon energy, and in the case of magnetically ordered systems also on the angle of incidence. In holmium, mainly 4M and 4K states will resonate for the peak with the high binding energy (E_B = 9.3 eV), while the shoulder at the low binding energy side (E_B = 8.8eV) is formed from 4F, 4G and 4I states[153]. The shoulder, unfortunately, coincides energetically almost exactly with the 7F final state of Gd so the question of a contamination of Ho with Gd arises and is naturally difficult to answer.

If we first look at the $GdAg_2$ spectra, we see that at the 4f resonance (hν = 148eV) the 4f emission is about 40 times stronger than at anti-resonance (named Gd on-resonant in Figure 61d)). Outside of the energy of the anti-resonance the enhancement is of approx. a factor of 20. Next, we examine the $HoAg_2$ spectra. The spectrum taken with 148eV photons consists of two peaks at about 8.8 and 9.3 eV binding energy. With hν = 160eV photons, the peak at 8.8eV forms only one shoulder, which is also faintly visible at the resonance. The calculated multiplet does indeed show Ho 4f states there at the shoulder energy. The fact that peak and shoulder are formed from different terms (terms 4M, 4K for the high binding energy peak; 4F, 4G, 4I for the shoulder) means that it would be quite possible that there are different resonant effective sections of the shoulder compared to the main peak. Such an effect can be seen in the 4I term of the multiplet at 6eV binding energy. The latter resonates only by a factor of 2. The leading peak at 9.3eV of 4M and 4K terms reveal an enhancement factor of 3 from anti-resonant to resonant. We have to take into account, that this value is 10/7 stronger than a hypothetical 4M and 4K transition in Gd due to the $4f^{10}$ (Ho) vs $4f^7$ (Gd) configurations. Thus, at hν = 148eV, per atom, the Gd 4f emission should be approximately by a factor of 60 stronger than the high energy peak of the Ho 4f. If one takes into account that below the possible Gd-derived 8.8 eV peak of the hν = 148eV spectrum there is still the shoulder of the 4F/4G/4I-Ho4f emission, the Gd contamination can only be on the order of 1%. This is in agreement to the 5p spectrum of $HoAg_2$ measured for the same sample (Figure 61c)) that does not indicate possible Gd contamination, e.g., peak emissions at 20.5 eV binding energy. This means that we can consider this preparation as a clean preparation.

We turn back to the initially presented $SmAg_2$ case, (see Figure 60). Resonant photoemission on the Sm 4f level of the $SmAg_2$ is shown in Figure 62. Similar to the case of $SmAu_2$, three photon energies have been used corresponding to the off-resonant, the Sm^{2+} on-resonant and the Sm^{3+} on-resonant photon energies of 130, 136, and 141eV, respectively. For the spectrum of the Sm^{2+} on-resonant photon energy, one observes the appearance of two emissions near the Fermi energy, while in the spectrum at the Sm^{3+} on-resonant photon energy these two peaks diminish their intensity but higher binding energy emissions between 5 and 11eV emerge. The latter multiplet structure is very similar to the $SmAu_2$ 4f(Sm^{3+}) emissions shifted 0.22eV toward lower binding energies, as expected from the lower electronegativity of Ag vs Au. The calculated multiplet is given below the experimental spectra[153]. The experimentally obtained divalent Sm 4f multiplet appears as two peaks with some fine structure at 0.3 and 1.1eV binding energy. An integration of the intensity of the divalent and trivalent multiplets, each at its resonance photon energy, yields that about a 7% of the Sm in the sample is divalent. As just explained for the $HoAg_2$ case, an exact relation of di- versus trivalent contribution is difficult to carry out for resonant PE due to the multiple terms that resonate

at different factors and energies. Therefore a reliable number cannot be given from this data set. There are two possible sources of this divalent contribution. First, formation of clusters of unalloyed samarium on the surface due to the lower preparation temperature used in the preparations on Ag. As is shown in ref.[40,179,180], Sm clusters show mixed valence with a divalent contribution that varies with the coverage. This argument is supported by the observed differences in the amount of divalent samarium between preparations. The second possible source would be the hybridization to lower energy of the 5d composed band. If this band would lower enough its energy, electrons from the 4f could be transferred to that band changing the valency. In this second case, we would have an intrinsic mixed valence in the $SmAg_2$ alloy. To clarify this, further preparations of the sample and spectroscopy measurements in similar conditions should be carried out to obtain a constant value of the contributions. Obtaining a constant value would indicate that the alloy is intrinsically mixed-valent, if the values keep differing, it could be stated that the divalent contribution is in another phase like the mentioned clusters.

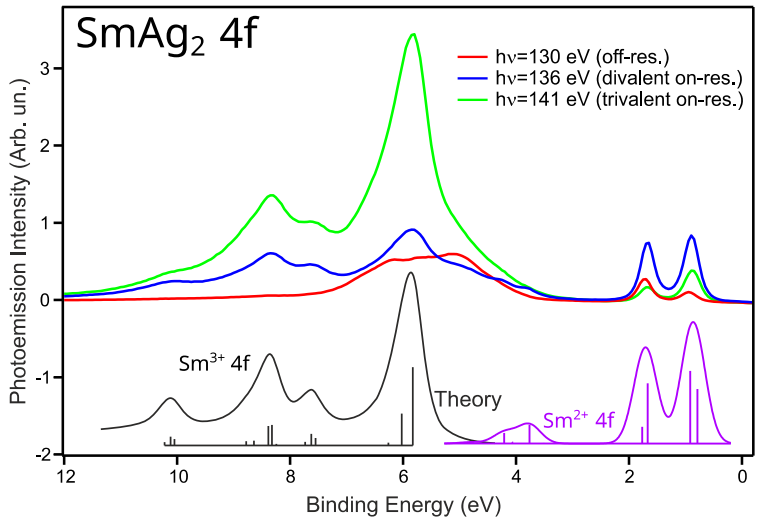

Figure 62: Resonant Photoemission on $SmAg_2$. On- and off-resonant photoemission of the trivalent and divalent chemical states of Sm 4f. The theory spectra are taken from reference [153] and denote calculations of the excited electrons.

6.2.1 Valence band structure in $REAg_2$

The valence band structure of the RE-Ag surface compounds has been investigated by angle resolved photoemission. Part of the band structure for $GdAg_2$ was already investigated earlier[17,47,52]. Nevertheless these published data are taken only above the Curie temperature T_C = 85K of the material. It is interesting to check the electronic bands below this phase transition. This analysis will be carried out here. The experiments have been performed at the VUV-Photoemission beamline at Elettra.

Figure 63 shows the ARPES photoemission intensity mapping of $GdAg_2$ taken at T = 44K (in the ferromagnetic phase, well below T_C = 85K[17]) with a photon energy hν = 26eV. We will use the same notation of the band structure as for the $REAu_2$ surface compounds. In the ARPES map, there

is no sign of the *A* band. The *B* band neither appears in the measured range (about 3eV), due to the higher binding energy of the Ag 4d that compose the *B* band. The *C'* band is formed from Ag s-p band umklapp processes at the $(\sqrt{3}\times\sqrt{3})R30^o$ structure. The *C* band shows a parabolic shape splitting in two branches when approaching the Fermi level. One branch shows the apex at 0.25eV below E_F and the other apex is located slightly above E_F. This is the first observation of spin-split bands of a rare-earth noble-metal surface compound in its ferromagnetic state. Additionally, along $\overline{\Gamma}'\overline{K}$ a band named *D* with a maxima at 0.2eV is observed that was not visible in the RE-gold surface alloys. This *D* band is degenerate with the *C* band at the $\overline{\Gamma}'$ point (α' feature).

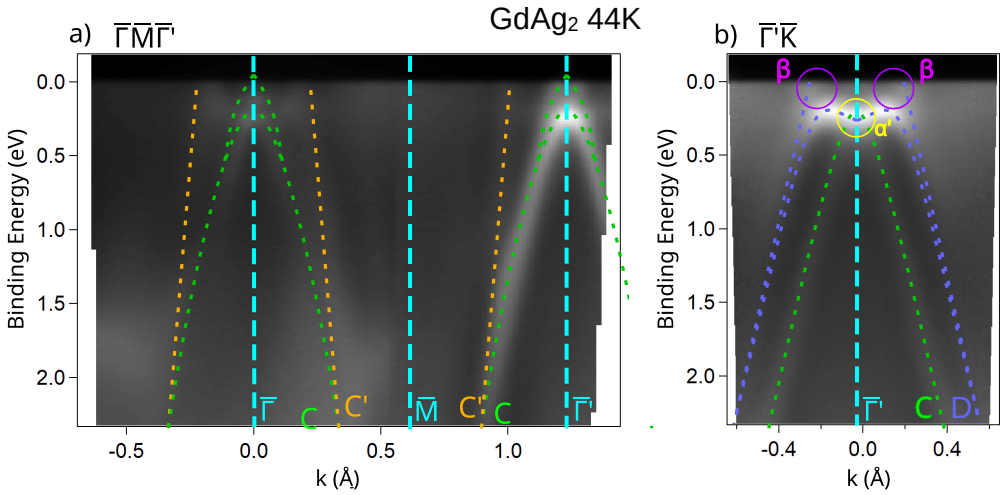

Figure 63: ARPES map of $GdAg_2$ along the $\overline{\Gamma M \Gamma}'$ direction at T = 44 K taken with a photon energy of 26 eV. The C' and C bands are marked in orange and green respectively. The D band is marked in blue.

By comparison with the previously published DFT calculations of $GdAg_2$[17] shown on Figure 64a) and b) we can assign that the *C* band corresponds to the d_{xy} band, more specifically, the upper and lower branches with the down ($d^{\downarrow}_{xy}$) and up ($d^{\uparrow}_{xy}$) spin polarizations of the band. Additionally, we can observe that the *D* band has $d^{\uparrow}_{x^2-y^2}$ character. We further observe in the calculations that the bands obtained for the free-standing layer are quite similar to the bands of the alloy on three ML of silver, again (like in $GdAu_2$) confirming the confinement of them to the alloy layer. In general, the bands of $GdAg_2$ correspond quite well to the ones of $GdAu_2$ (see Figure 36c)) but shifted in energy. This is expected as both noble metals share a $(6s5d)^3$ valence electronic structure of trivalent Gd. Taking this into account, we will proceed to compare now the band behavior to the DFT calculations *with SOC* calculation of $GdAu_2$ (see section 5.2.1.2). The main reason for this is that we do not have calculations including SOC for $GdAg_2$. As was indicated previously, the ARPES map shows that the *C* and *D* bands are degenerate at α' (crossing of $d^{\uparrow}_{xy}$ with $d^{\uparrow}_{x^2-y^2}$) and band gaps open at β (crossing of $d^{\downarrow}_{xy}$ with $d^{\uparrow}_{x^2-y^2}$). Very important, we can see in the measurement that the β gap is located very close to E_F. In $GdAu_2$, β gap opening happened for IP spin polarization. Due to the similar valence contribution of both noble metals Au and Ag, a similar correspondence is expected in $GdAu_2$ and $GdAg_2$. Band crossing gaps in different DFT calculations with SOC have been reported in ref. [52]. However, in the latter case, the energy splitting of the open

gaps does not correspond to the experiment. The above mentioned correspondence of the measured gap opening with the IP polarized DFT bands rather indicates that ferromagnetic domains are formed when cooling the sample below the Curie temperature. These domains are magnetically oriented in the IP direction. This is also consistent with the previously reported IP easy axis of the sample[17]. Joining all these indications and taking into account the lack of other significant sources of magnetic anisotropy, we conclude that the band contribution to anisotropy would be IP. If we now look at the MAE calculation of $GdAu_2$, we can position the charge neutrality at the β feature (purple line in Figure 64d)). That way, we can see that a negative MAE appears, caused by the presence of the β gap at E_F that maximizes the MAE value. This high value of the MAE can explain the reported stronger IP anisotropy of $GdAg_2$ with respect to $GdAu_2$.

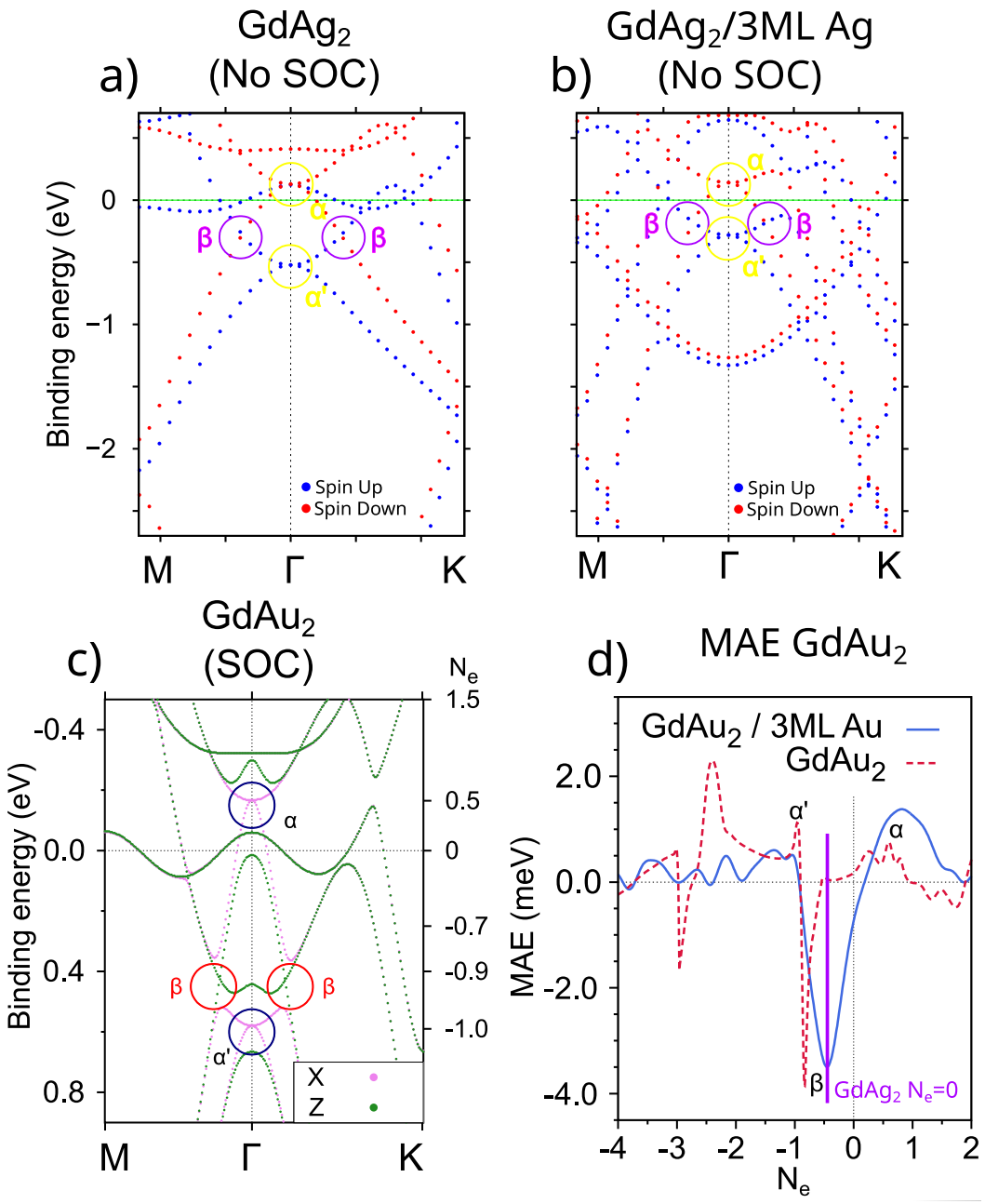

Figure 64: DFT simulated band structure of $GdAg_2$ and its relation to $GdAu_2$. a) DFT simulated layer of freestanding $GdAg_2$ layer without SOC and b) supported on 3ML of Ag. Note that the colors indicate opposite spin directions. c) DFT simulated band structure of freestanding $GdAu_2$ with SOC. Colors denote different directions of spin polarizations. d) MAE calculated for $GdAu_2$ for unsupported (red) and on top 3ML of Au (blue). The violet vertical line denotes the N_e=0 position for $GdAg_2$ taking into account that the β band gap opening in ARPES appears very close to E_F.

The ARPES valence band dispersion measurement of $SmAg_2$ is shown on Figure 65. We will also here follow the typical $REAu_2$ (see section 5.2.1.2) nomination for naming the bands. In this case, the *A* band is visible and has an electron like behavior with its minima at 0.27eV (on the limit of the

Ag(111) $\overline{\Gamma}$ gap[181]). As in the case of $GdAg_2$, the *C* and *D* bands are identified with the d_{xy} and $d^{\uparrow}_{x^2-y^2}$ bands of the DFT simulation. The *C'* band is formed from umklapp of the $(\sqrt{3}\times\sqrt{3})R30°$ reconstruction of the surface confined Ag s,p band. A very intense, non dispersive band appears at 0.9eV. It has been identified previously as Sm^{2+} $4f_{5/2}$ emissions. We do not observe band bendings or dispersion of the 4f core level emissions with *C* and *D* bands. This fact reinforces the hypothesis that the divalent samarium arises from non alloyed clusters. Nevertheless, we also observed that in $EuAu_2$ such bendings of the 4f level not always take place. Above T_C, the *C* band of $SmAg_2$ reveals a conical hole like shape with the apex cutting at E_F. The *D* band shows similar shape as in $GdAg_2$ but upward shifted, with its local minimum at 0.1eV from E_F. The *D* and *C* bands show a crossing near the minimum of the *D* band.

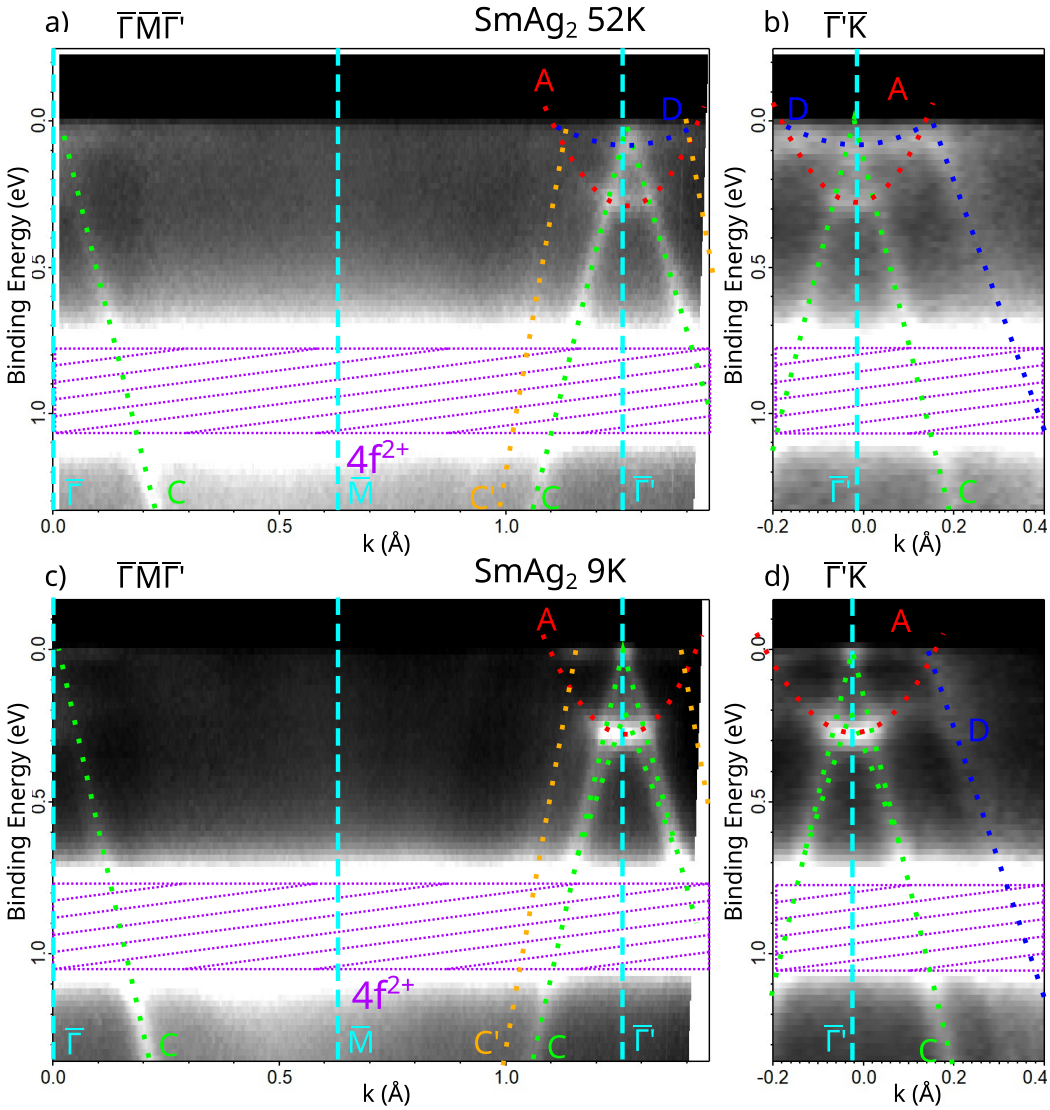

Figure 65: a)-d) ARPES photoemission intensity map of $SmAg_2$ along $\overline{\Gamma M \Gamma'}$ and $\overline{\Gamma' K'}$ direction at 52K and 9K, respectively. A schematic representation of the bands is over-imposed to the photoemission maps.

Below T_C, the *C* band splits into the $d_{xy}^{\downarrow}$ branch which has the apex slightly above E_F and the $d_{xy}^{\uparrow}$ with an apex at 0.27eV below E_F. Additionally, the *D* band shifts upward, with the band inflection now above the Fermi level and invisible to us. This means that the band degeneration of *C* and *D* bands at $\overline{\Gamma}'$ and the Fermi energy gets lifted. As the inflection is now above E_F, there is no crossing between the $d_{xy}^{\uparrow}$ branch of the *C* band and *D* band although it is possible that the *D* band is crossing the $d_{xy}^{\downarrow}$ band in the apex resulting in the intensity increase at the apex of $d_{xy}^{\downarrow}$. Comparing with the simulations on $GdAu_2$ (section 5.2.1.2), from the displacement of the *D* band above the $d_{xy}^{\uparrow}$ band (α feature in the DFT simulation), we can deduced that the domains formed after cooling below T_C are magnetized in the OOP direction. The latter could be expected due to the strong OOP easy axis of the $SmAg_2$ sample (see section 6.3.2). All these observations results from the peak fit analysis carried out above and below the Curie temperature of $SmAg_2$. The energy dispersive curves at $\overline{\Gamma}'$ are shown in Figure 66. We observe that below 25 K the shape of the *C* and *D* bands changes. The *C*/*D* bands above T_C gave rise to the photoemission peak at 80 meV binding energy. Below T_C we see a shift downward that we interpret as the majority spin branch of *C*, while the intensity close to E_F disappears as a result to an additional upward shift of the minority *C* branch above E_F. The peak fit analysis places the minority peak right above E_F by 20 meV, while the majority part moves downwards till 140 meV binding energy. Nevertheless, in order to clarify the experimental observations, specific DFT simulation will be needed to extract the band above E_F.

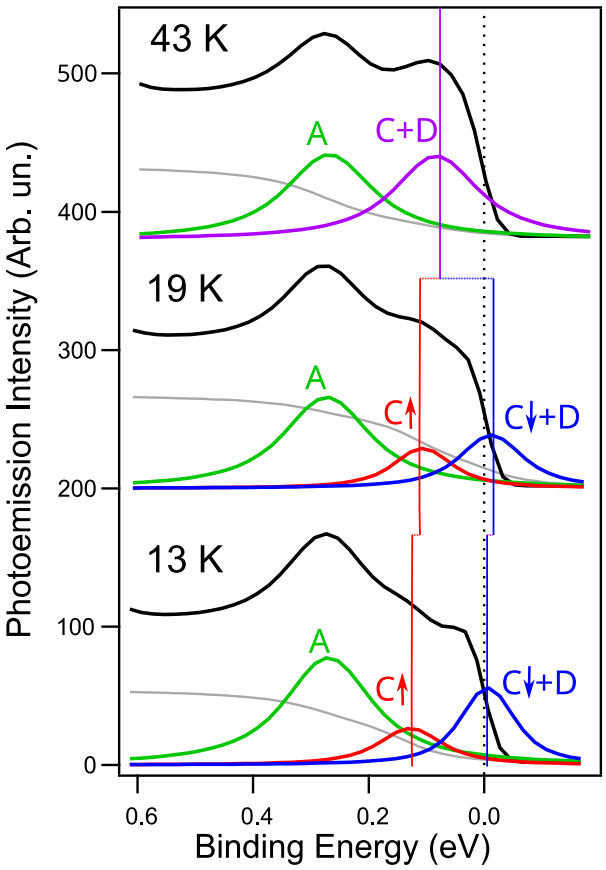

Figure 66: Peak fit analysis of photoemission spectra taken at $\overline{\Gamma'}$ *, the position corresponding to the second Brillouin zone center of* $SmAg_2$*. Spectra were taken above and below the Curie temperature. The Fermi energy was taken from the same channelplate image as the* $\overline{\Gamma'}$ *emissions, but offset to avoid band crossings. The fitting was carried out applying 4 Lorentz peaks corresponding to the rest of the* Sm^{2+} *4f at highest binding energy, the A, C majority and minority bands, respectively. C minority peak width and background was set to coincide with the majority part. A Shirley background was used to account for inelastic electrons.*

The energy dispersive curves at the $\overline{\Gamma'}$ point at all temperatures of the experiment are shown in Figure 67. The main change observed with the temperature occurs by the extinction of the small peak at approx. 0.1eV being caused by the splitting of the *C* band and upward shifting of the *D* band. We can estimate a T_c of around 30K by the fact that above that temperature the peak stops changing. This T_C value coincides well with the XMCD determined T_C, probing that the variation of the photoemission features with the temperature can be a reliable method for T_C determination. The apparent decay of intensity of the Sm^{2+} 4f peaks with the increase of temperature is caused by thermal broadening.

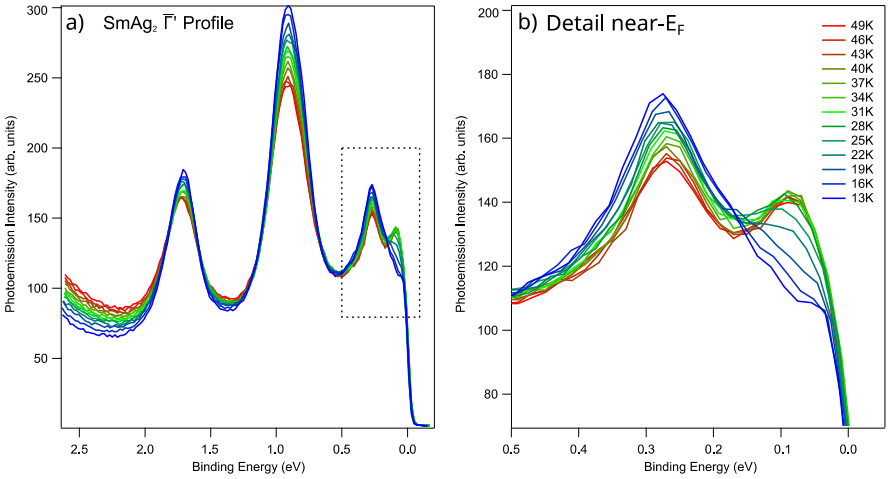

Figure 67: a) Energy dispersive curves (EDCs) as a function of temperature at the $\overline{\Gamma}'$ point of the second Brillouin zone of $SmAg_2$.

6.3 XMCD

The magnetic behavior of the rare-earth/noble-metal (RE-NM_2) surface compounds has been studied by XAS-XMCD setup at DEIMOS beamline at SOLEIL synchrotron facility (Paris, France). As in the RE-Au_2 alloys, two geometries have been used to probe the in-plane and out-of plane magnetic properties. In both cases, the magnetic field has been applied in the direction of the incident beam. XAS-XMCD spectra are obtained at a fixed field by varying the incident photon energy across the $M_{4,5}$ absorption edge of the corresponding rare-earth metal. The grade of polarization has been 90%. In all cases, the XAS-XMCD data resulted from total yield measurements of the sample current, i.e., by measuring the absorption through the total emitted charge.

6.3.1 $HoAg_2$

XAS and XMCD measurements performed at 6T and 4K in both geometries, IP and OOP, are shown in Figure 68. As in all other studied RE metals, the indicated transition arises from photon adsorption and energy transfer to electrons that are excited from occupied 3d levels. Both, M_5 and M_4 transitions are associated to excitation from the $3d_{5/2}$ and $3d_{3/2}$ levels, respectively, into the empty 4f and 6p states. However, as the 6p band is broad and weak in comparison, the observed transition can be simplified to a transition into the empty 4f levels reflecting the magnetization state of the RE. As in $HoAu_2$, the first thing we note is the shape change of the XAS between the two geometries. It can be appreciated, that the relation IP/OOP is now reversed with respect to $HoAu_2$ (see figure 43 in section 5.3.1). As before, this change of shape is associated to a preferential orientation of the 4f oblate charge distribution. From the inversion we can deduce that the symmetry axis of the 4f orbital will now be oriented in the IP direction indicating the magnetic easy axis will be IP. The increased magnetic dichroism value (factor 1.5) at IP geometry supports this easy axis assignment as well.

The form of the XMCD spectra agrees with a Ho^{3+} valence as already established by photoemission[166] (see section 5.3.1). As previously stated, orbital filling of Ho^{3+} implies an oblate orbital shape and was one of the main arguments for the high magnetic anisotropy of $HoAu_2$[42].

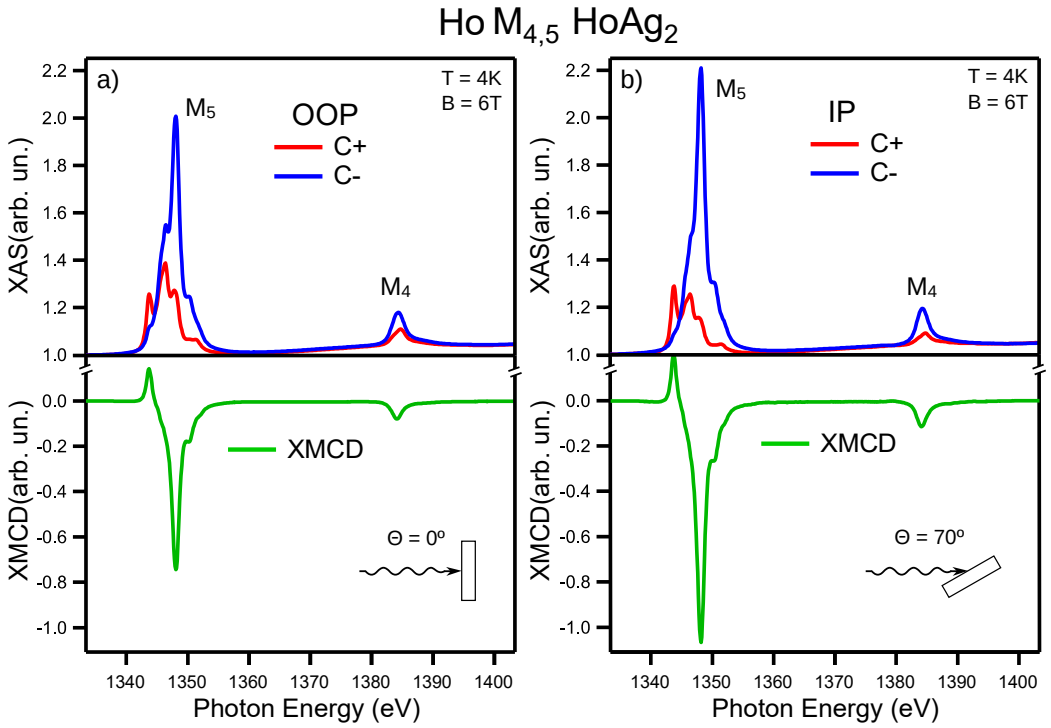

Figure 68: Ho $M_{4,5}$ XAS and XMCD spectra of $HoAg_2$ measured at 6T and 4K in a) out-of-plane and b) in-plane geometry. The higher intensity of the dichroism indicates an IP easy axis of magnetization.

The XMCD hysteresis loops of $HoAg_2$ at 4K are shown in Figure 69. In both, IP and OOP geometry, a rather "S" shape loop can be seen. Nevertheless, there are fundamental differences. First, the IP curve reveals a more pronounced change of magnetization at low fields and eventually reaches "saturation" (linear growth) at lower field than the OOP geometry. This confirms that $HoAg_2$ presents an IP easy axis of magnetization. The other, more important difference is that the loop in IP direction this time has an opening in the range from -1 to 1T. In this case, approximating the behavior by a linear interpolation of the loop around the zero field, we obtain a remanence of a 3% of saturation and a coercive field of 35mT. This linear estimation is necessary to estimate the values near zero field since the XMCD measurement method doesn't work properly there. As will be shown next, the stronger "S" shape of the loop compared to $HoAu_2$ is caused by the proximity of the measuring temperature to the Curie temperature of this alloy.

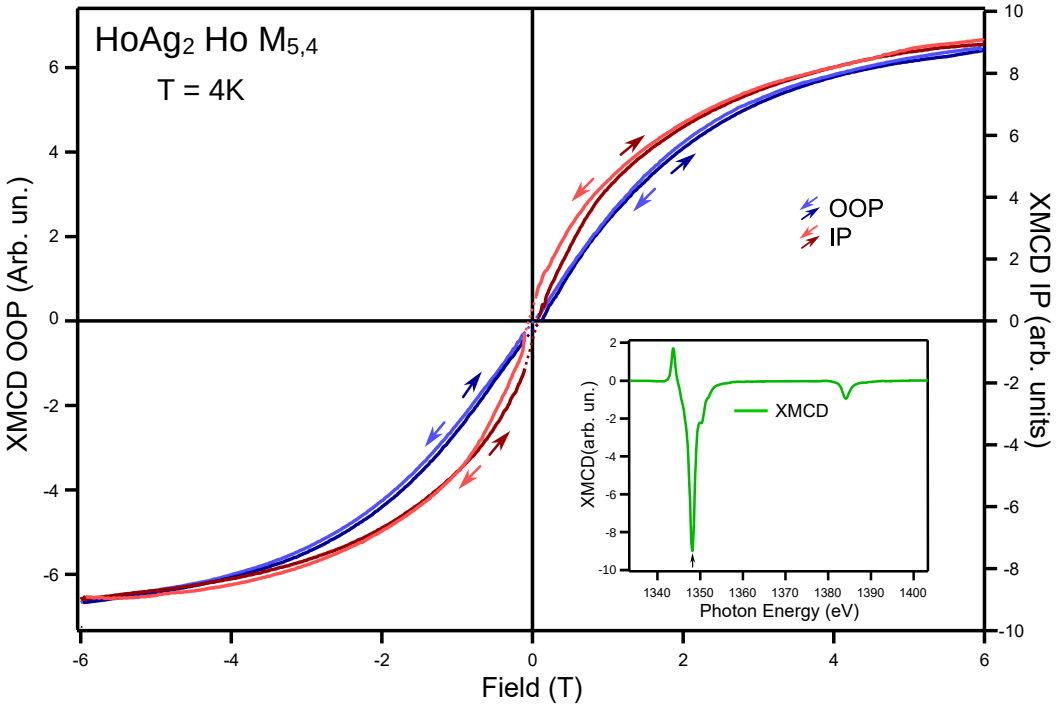

Figure 69: Ho M_5 XMCD hysteresis loop of $HoAg_2$ measured at 4 K on the maximum of the M_5 transition. The shape of the loops confirms IP anisotropy. In the IP magnetization curve, an opening can be seen at small fields. Note the difference of scale for the OOP and IP direction. The inset shows the XMCD spectra at 6T in IP geometries marking the measurement photon energy.

To further understand the source of the measured anisotropy, we will again split the magnetocrystalline anisotropy into two contributions, the band anisotropy and the crystal field anisotropy. As always, shape anisotropy contribution can be depreciated as the order of magnitude of the effects are way below the measured ones.

In the present case $HoAg_2$ presents Ho^{3+} valence and as was shown on section 5.3.1 shares the valence of $GdAg_2$ and in similar way to the $RE^{3+}Au_2$. It is expected that the shared valence will cause a similar band structure. Therefore we can assume that the contribution of the band anisotropy would be IP as in $GdAg_2$. But this term does not explain the change of shape in the $M_{4,5}$ transition as, considering the 4f is only weakly interacting and not hybridizing with the valence bands, the band anisotropy term cannot lock the symmetry axis of the orbital. To get that, the crystal field contribution is necessary.

As a short reminder, the crystal field anisotropy is given by the electrostatic interaction of the electric quadrupole associated to the charge distribution of the 4f and the quadrupole created by the charge distribution of the rest of the electrons. As it was commented for $HoAu_2$ before, in Ho^{3+} 4f shell has an oblate shape, which causes a negative quadrupole moment. The fact that in this case the symmetry axis of the 4f shell is in the in-plane direction, indicates that $HoAg_2$ creates a positive quadrupole on the RE. This means, substitution of Au to Ag in the structure has inverted the sign of the quadrupole term of the crystal field. This change is unexpected since Au and Ag present similar

electronic band structure and electron affinity. This change of sign in the quadrupole could be caused by a slight distortion of structure, e.g., a different height of the RE in the layer, or by a different intensity of the surface dipole associated to the difference in work function between Au(111) and Ag(111), but further studies will be necessary to find the source of the change.

After the analysis of the anisotropy, we can further comment on the hysteresis. As was already commented, coherent rotation in the case of Ho is not a good model, as the high magnetic momentum favors greatly the formation of small domains. Furthermore, coherent rotation cannot explain coercivity in the IP axis, because, as was commented for the case of $SmAu_2$ (see section 5.3.3) the magnetization would rotate freely in the plane. Domain wall movement, nevertheless, provides good explanation of the origin of the coercivity once we go back to the structure of the $HoAg_2$ alloy. As was seen in section 6.1 $HoAg_2$ alloy structure is formed of a quasiperiodic lattice of dislocations in which the coordination of the Au and Ho atom changes. This change of coordination imply local changes of anisotropy and exchange, which can offer favorable locations for the domain wall to stay, or said in another words, this dislocation act as “pinning centers” hindering the movement of the domain walls and stabilizing the magnetization. This effect is similar to the large remanence in $EuAu_2$, which presents also a defect-rich structure, but such pinning centers are missing in the cases of $GdAu_2$, $HoAu_2$ and $DyAu_2$ that form (almost) defect-less layers.

As a last point in this section, the T_C of $HoAg_2$ has been determined by measuring the temperature dependence of the hysteresis loop and applying the Arrot plot methodology (see section 3.2.5 and 5.3.1). Figure 70a) indicates that at the lowest temperature the loop shows clear coercivity, which is lost for higher temperatures, with the loops also evolving to a more linear behavior. Figures 70b) and c) show the Arrot plot analysis and the final linear fit used to extract the Curie temperature. The Curie temperature determined by this method is T_C = 11K, much lower than the Curie temperature of $HoAu_2$ (22K). This was again unexpected as the previous studied silver substitution, $GdAg_2$, caused an extreme increase in the T_C to 85K compared to $GdAu_2$ with T_C = 19K[17]. This implies that a more complex model than a simple RKKY will be necessary to understand the coupling in this alloys, including the structure and electronic bands of the alloy.

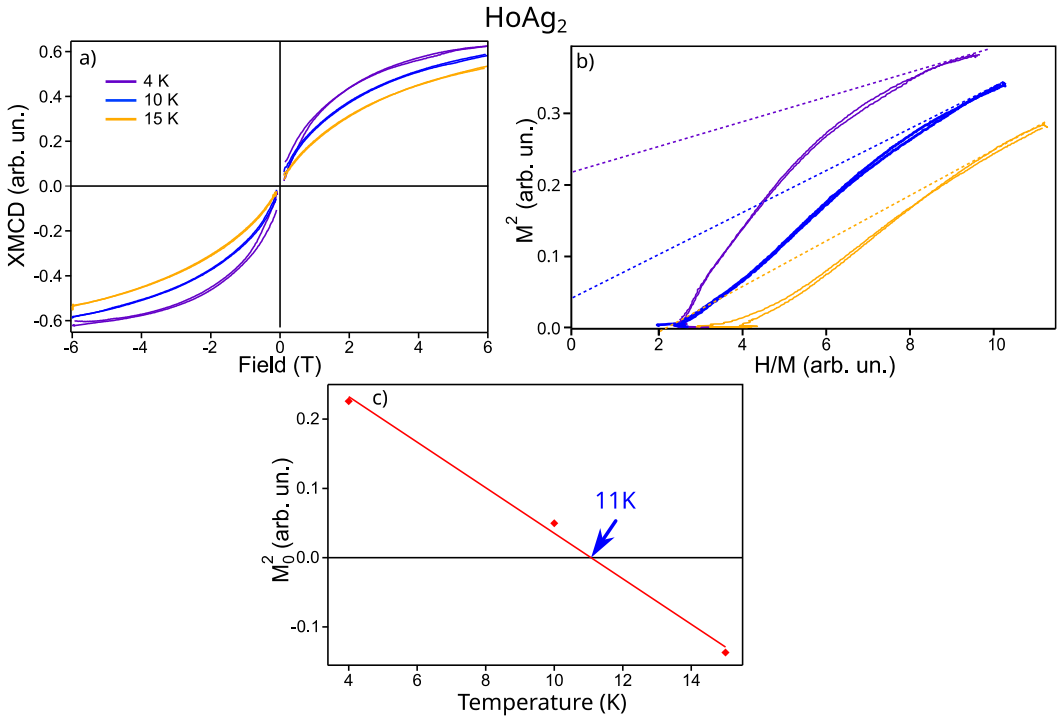

Figure 70: Temperature dependence of the hysteresis loops for $HoAg_2$: a) IP magnetization curves as a function of sample temperature, b) Arrot plot M^2 vs H/M curves and their high field fits (dotted lines). The H/M=0 crossing points are used in c) to determine the Curie temperature T_C of the $HoAg_2$ system.

6.3.2 $SmAg_2$

Sm $M_{4,5}$ XAS and XMCD measurements performed on $SmAg_2$ monolayer at 6T and 4K are shown in Figure 71. As in all previous spectra of RE, there are two transitions, the M_4 from the $3d_{3/2}$ and M_5 from $3d_{5/2}$ into the 4f shell. Again, the transition intro the 6p level has lower probability and is broad, therefore we expect no distinguishable peaks. The difference in the XAS spectra between IP and OOP geometries is faint and mostly localized in the M_4 transition. A more intense difference exists in the dichroism (XMCD). There, it can be seen that the intensity in the OOP direction is about 3 times higher. This clearly indicates that the sample reveals an OOP easy axis. This, as in $HoAg_2$, is inverted with respect to the respective $REAu_2$ alloy.

The shape of the XAS spectra is in good agreement with the one of $SmAu_2$ and the trivalent Sm of bibliography[166], but it could also hide a divalent contribution. In order to disentangle this, calculations of the absorption multiplet would be necessary. From photoemission spectroscopy we found a mixed Sm^{2+}/Sm^{3+} behavior (section 6.2). As a reminder, the dominant trivalent Sm^{3+} valence state implies a prolate shape of the 4f electron distribution. Finally, a small contamination of Eu can be appreciated (marked in violet). This $M_{4,5}$ transition from earlier Eu/Ag trial experiments can be appreciated better in the XMCD signal due to the much higher magnetic dichroism of Eu compared to Sm. Nevertheless, an estimation of the amount by integrating the XAS signal leads to a contamination level below 1.5%. This contamination arises most likely from a low amount of Eu

that may have diffused into the bulk (see section 4.2.1.1 for sample cleaning) of the Ag crystal that was not completely removed during sample cleaning.

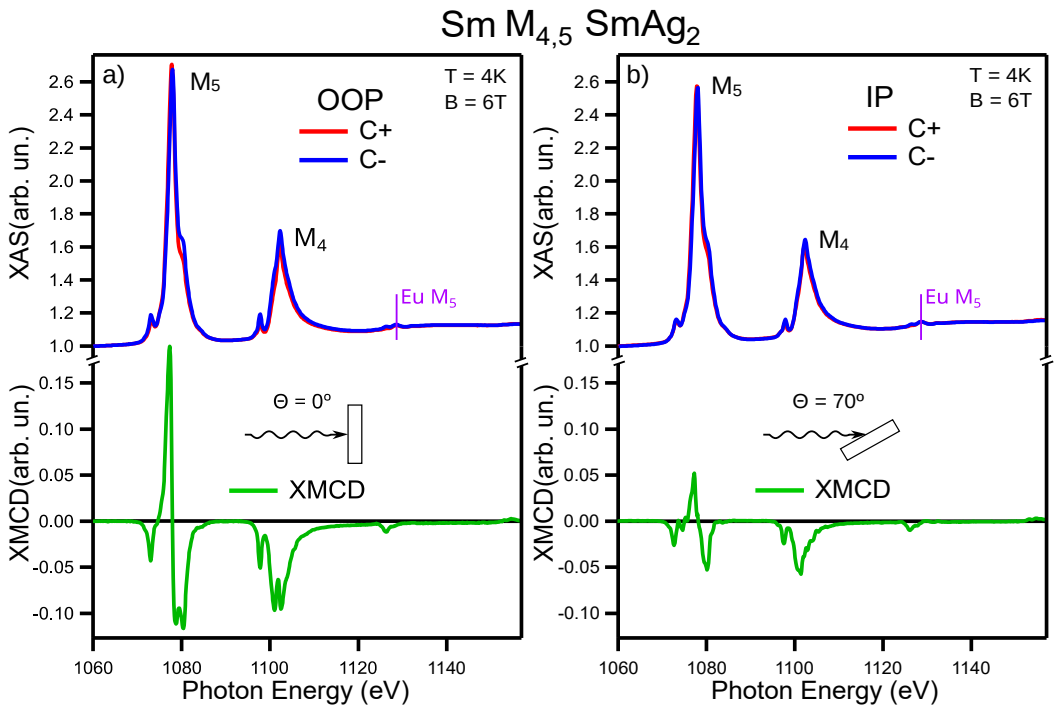

Figure 71: Sm $M_{4,5}$ XAS and XMCD spectra of $SmAg_2$ measured at 6T and 4K in a) OOP and b) IP geometry, respectively. Higher intensity of the dichroism indicates an OOP easy axis of magnetization. A small Eu contamination (contamination level of 1.5% with respect to Sm) is visible and marked in violet.

XMCD loops of $SmAg_2$ at 4K are shown in Figure 72. In the OOP loop one can immediately see a completely open loop, while in the IP direction there is only a paramagnetic behavior observed. Looking at the data in more detail, it can be observed that the linear part of both loops is parallel. From that, we can deduce that in the sample we have two phases, the alloy with highly anisotropy ferromagnetic behavior and an additional isotropic paramagnetic phase. That paramagnetic phase is most likely (and as was proposed in section 6.2) Sm at the surface without alloying but forming clusters. Such clusters can have a mixed valence whose ratio varies on the cluster amount and size[179,180]. After correcting the loops to account for this paramagnetism, what we have is an almost square loop in the OOP direction and near-zero magnetization in the IP direction (Figure 72 upper inset). It should be noted that after this correction the sample remains saturated after the field removal showing no demagnetization. We have to remark the impressive coercive field of 5.2T. To explain this behavior we have to take two aspects into consideration, (i) the anisotropy and (ii) the magnetic moment of Sm.

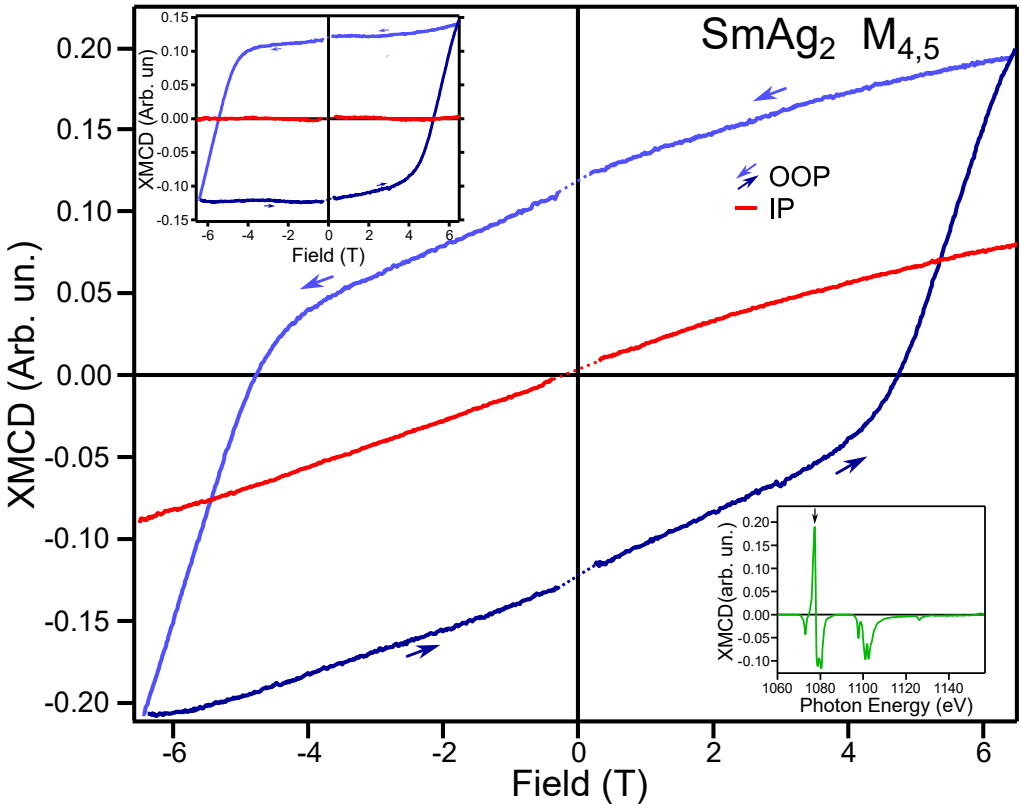

Figure 72: Sm M_5 XMCD Hysteresis loop of $SmAg_2$ measured at 4K. The curve reveal a clear "square-like" shape. Upper inset shows the loop after subtracting a paramagnetic behavior. The lower insert shows the XMCD spectra in OOP geometries marking the measurement photon energy.

As previously explained for $SmAu_2$ (section 5.3.3), the shape anisotropy can be neglected for Sm due to its small magnetic moment. Next, we split the two contributions of the magnetocrystalline anisotropy. First, we consider the band anisotropy. As an initial consideration, due to the Sm^{2+} having no magnetic momenta, from now on we will simplify the discussion by considering only the Sm^{3+} part. As we did with $HoAg_2$ (section 6.3.1) we can base the band anisotropy on the shared electronic structure of the alloys and deduce the contribution from the IP easy axis of $GdAg_2$[17] (that only has band contribution). That way, we can expect the band term to favor IP easy axis. But, this is opposite to the seen anisotropy, which means that the term dominating will be the crystal field anisotropy.

The crystal field anisotropy is the energy term introduced by the electrostatic interaction of the quadrupolar term of the magnetized 4f shell. As was seen in the case of $HoAg_2$ substitution of Au for Ag has changed the sign of the quadrupole of the crystal field to positive value. The Sm^{3+} has an oblate charge distribution that implies a positive quadrupole. The electric interaction of both quadrupoles will then favor the symmetry axis to be oriented in the OOP axis. This, together with the strong LS coupling[84] characteristic of Sm will cause the strong anisotropy with an OOP easy axis.

The second aspect that we wanted to discuss was related to the magnetic momentum of Sm that is

quite small, about 1/10 of the values of the other RE. Such a low magnetic momentum is caused by the spin and orbital moment being in opposite directions as imposed by Hund's rule. The implication of the low magnetic momentum is that the difference in energy between the momentum being parallel or anti-parallel to the magnetic field is small, since the energy is proportional to the magnetic moment. As a consequence, the sample magnetization is only affected by high fields. Specially for the case of IP magnetization direction, it implies that the magnetic field is not capable of overcoming the anisotropy barrier preventing magnetization of the sample in that direction, making the sample behave as an ideal Ising ferromagnet.

After this comments on anisotropy and magnetic moment, we can give an explanation on the cause of the extremely high coercivity. As was commented already in the case of $SmAu_2$, the low magnetic moment of samarium will favor the formation of big domains, including the possibility of a single domain. A second consideration to make is, that the high anisotropy in the OOP direction will confine the moments in that OOP direction. The consequence of this is that the domain walls will be abrupt and more difficult to move. Domain wall movement, then, will be a minor term (or even non-existent) in the re-magnetization dynamics. Removing the possibility of DW movement for the re-magnetization, we can model the system trough coherent rotation. That way, the high anisotropy imposes a high energy barrier between the two possible stable magnetization states. To flip the magnetization, it is necessary to overcome this barrier, or what is the same, either a high enough field (the coercive field) or a high enough thermal energy (reaching temperatures close to T_C) are necessary. As a reminder, in the case of $SmAu_2$ (section 5.3.3), the coherent rotation does not lead to coercivity due to the IP easy axis. The IP easy axis, confines the magnetization to the plane, but allows free rotation in it, allowing decoherence of the magnetization by the rotation of the magnetization in the plane.

As for all the other alloys, the Curie temperature has been determined by the measured temperature dependence of the hysteresis (Figure 73). The Arrot plot analysis results in a Curie temperature T_C = 30K. This is approx. a factor of 3 higher compared to $SmAu_2$ and is similar to the increase in the Gd case: T_C = 19 and 85 K for $GdAu_2$ and $GdAg_2$, respectively). In the former section on $HoAg_2$ we saw a lower T_C as in the $HoAu_2$ case. Here, we see that Ho is then rather the exception.

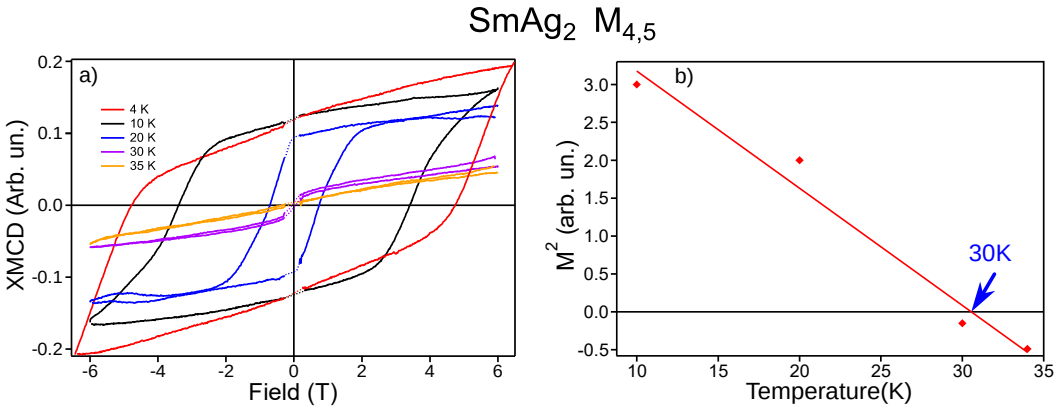

Figure 73: Temperature dependence of the hysteresis loops for $SmAu_2$: a) magnetization curves as a function of the sample temperature, b) Arrot plot analysis of the M_0^2 values to determine the T_C = 30K result.

7 Hybrid organometallic interfaces

7.1 CuPc/$REAu_2$ system

7.1.1 Structure analysis

1ML of CuPc molecules was adsorbed on several $REAu_2$ surface compounds, specifically, on $GdAu_2$, $HoAu_2$ and $YbAu_2$ monolayers. The growth and structure of CuPc on top of them was studied by low-energy electron diffraction (LEED) and scanning tunneling microscopy (STM) at room temperature. In general, the structure of the molecular layer is characterized by the formation of a densely packed molecular layer that is commensurate with the $REAu_2$ surface.

The growth of CuPc layers on $REAu_2$ shows analogous LEED patterns on all three $REAu_2$ substrates studied here. Figure 74a) to c) display LEED images from measurements of 1ML of CuPc on $HoAu_2$, $YbAu_2$ and $GdAu_2$, respectively. The CuPc molecule has a 4 fold symmetry while the $REAu_2$ surface has a 3 fold symmetry. In order to macroscopically respect the substrate symmetry, it forms 3 rotational domains. This effect on Pc overlayers grown on hexagonal surfaces is already well documented[110,182,183]. The surface unit cell of CuPc in this particular case results to be rhomboidal with a lattice parameter a=1.43nm and an angle of $\theta = 80^o$ between the two lattice vectors. It appears marked by a solid red line in Fig. 74a) for the CuPc/$HoAu_2$ case. The solid green and violet lines represent the unit cells of the other two rotational domains, which are rotated by 60º degree respect each other. Similar LEED patterns have been measured on 1ML of CuPc/$YbAu_2$ (Figure 74b)) and CuPc/$GdAu_2$ (Figure 74c)). The complex epitaxy of CuPc (four-fold symmetry) on hexagonal $REAu_2$ surfaces can be expressed by the matrix $\begin{pmatrix} 2 & 1 \\ -2 & 3 \end{pmatrix}$. This matrix only has integer values, which indicates that the growth is commesurate[148] with respect to the substrate. Considering this arrangement, the packing density of the CuPc overlayer results to be of 0.49 molecules/nm^2, very close to the value obtained in CuPc on Au(111) (0.5 molecules/nm^2)[183]. However, the unit cell of a CuPc ML adsorbed on Au(111) is a square lattice. In part d) of Fig. 74 we show the extended LEED pattern including second order diffraction spots of the molecules that can be directly be compared to the LEED images. From LEED measurements one can only evaluate the lattice and periodicity but not the adsorption sites of the atoms. Another technique is needed to solve this problem.

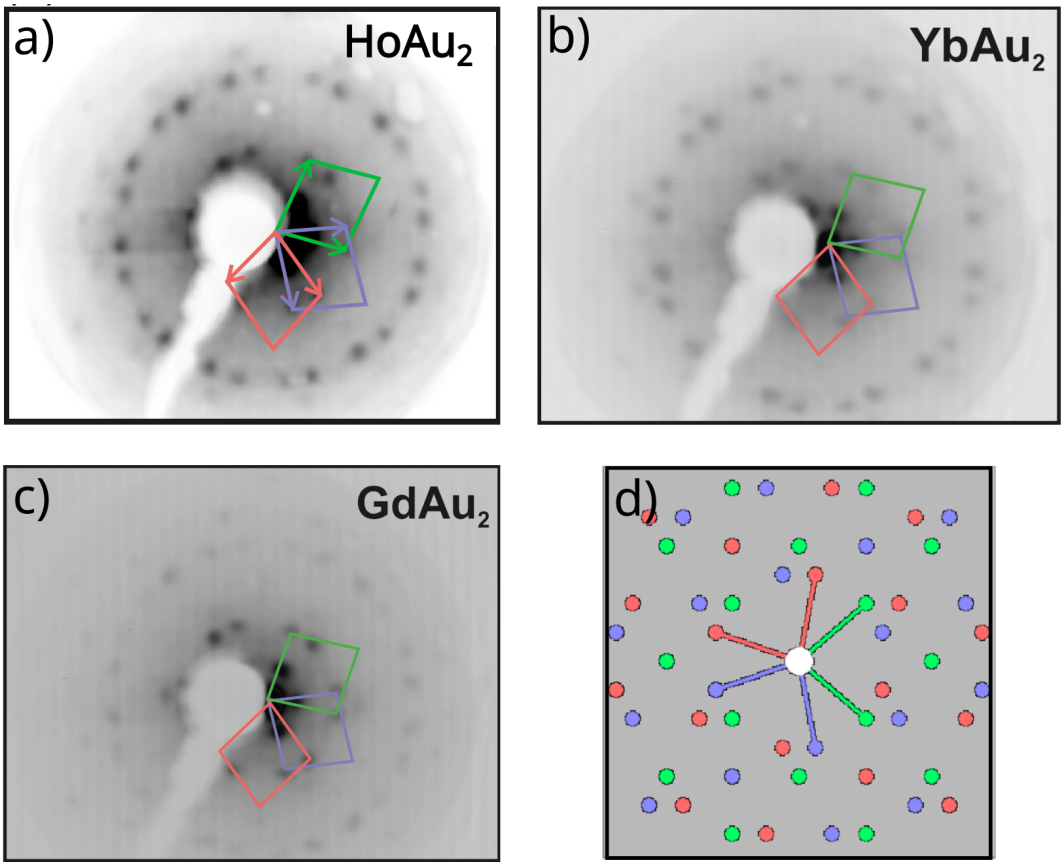

Figura 74: LEED patterns of CuPc on a) $HoAu_2$, b) $YbAu_2$ and c) $GdAu_2$ surfaces taken for an electron energy of 11.5eV. The surface unit cells of the three equivalent rotational domains are displayed (red, green and blue lines). All of them together contribute to the observed pattern. d) Simulation of the CuPc/$REAu_2$ LEED pattern carried out in "LEEDpat"[184] *up to the second order diffraction. Each rotational domain is marked in a different color: blue, green and red.*

The ordering of the molecules at the surface is confirmed by scanning tunneling microscopy (STM) measurements. Figures 75a) and b) display STM micrographs of CuPc grown on $HoAu_2$ and indicate one of the three rotational domains of the CuPc ML. The high extension of the ordered molecules on the surface with the low density of defects is a good indicator of commensurated growth. This kind of growth implies the existence of favorable sites of absorption. As in the case of LEED, the precise adsorption site of molecules cannot be determined neither by the STM technique since we observe only the top molecular layer but not the underlying one. The good quality of the CuPc layer allows the application of a Fast Fourier Transform (FFT) to the STM image of CuPc (Figure 75c)). This transformation pass the information from real space to frequency space, the resulting pattern is used to analyze the periodicity measured in the topographical images of STM. Therefore, we can compare the image obtained after the application of a FFT filter (Figure 75c)) to the LEED diffractogram of one of the three rotational domains formed in the CuPc layer on $HoAu_2$ of Fig. 74a). The self correlation function has also been used to extract the lattice constants, see

Figure 75d). This transformation allows the extraction of the lattice by marking the periodicity of the image in real space (see section 5.1) by removal of the motive (shape of the molecules) from the image in order to distinguish the Moiré periodicity of the substrate, which is marked in green. In Figure 75 the surface lattice of CuPc is marked in cyan while the Moiré periodicity of the substrates underneath is marked by green dashed lines in the FFT image.

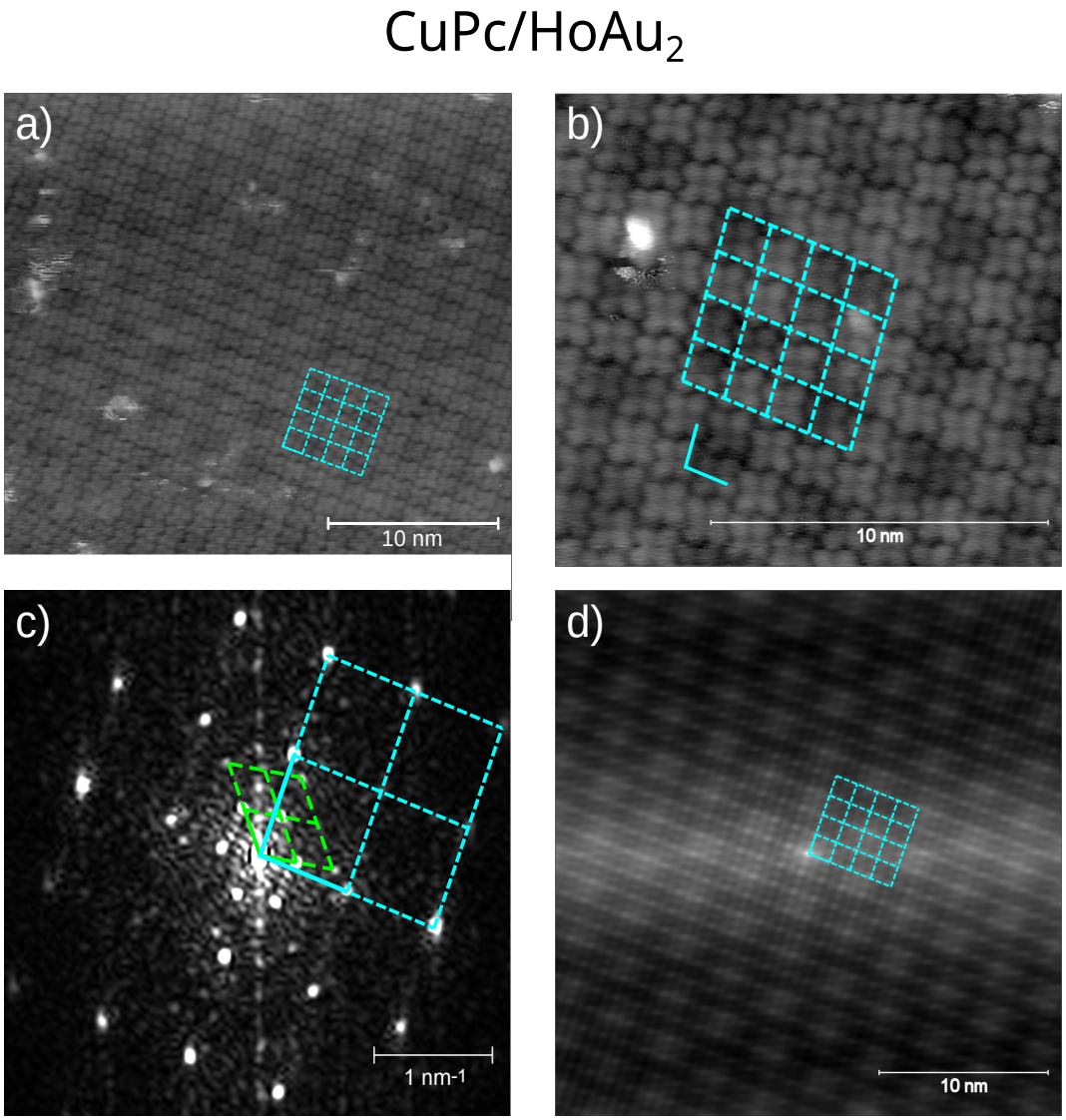

Figure 75: STM micrographs of CuPc (1ML) grown on $HoAu_2$. a) Large scan area (image 30×26nm², U = 0.5V, I = 0.2nA). One observes the ordered arrangement of the CuPc molecules. The surface unit cell of CuPc is marked in cyan. b) Zoomed area (image 15×14 nm²) to show the arrangement of the molecules. The dark areas represent the Moiré pattern of the $HoAu_2$ surface that is below the CuPc layer. The molecular unit cell is marked in cyan. c) and d) show the result after the application 2D FFT (Fast Fourier Transform) and the SCF (Self Correlation Function) of a). The sharpness of these 2 transformations shows the high precision of the periodicity of the CuPc layers. The surface unit cell of the CuPc layer is drawn in cyan, and the unit cell of the alloy is marked in green.

The same ordering of CuPc molecules is observed by STM measurements on $YbAu_2$. Fig. 76 displays a STM micrograph of CuPc grown on $YbAu_2$ and reveal the three rotational domains of the CuPc ML in a single image. The frontiers between the rotational domain are marked in yellow and blue. Figure 76b) and d) are zoom-ins of two of these domains of CuPc (areas 1 and 2). The corresponding Fourier transformed images of these STM micrographs are displayed in c) and e), respectively. The 60º degree rotation between both diffraction patterns is clearly observed, which verifies the rotational domains that have been observed in the LEED patterns. In Fig. 76a) terraces of the $YbAu_2$ alloy are observed and marked in blue. It is seen that around these terraces there is no preferential adsorption geometry in which molecules would get fixed but rather follows the growth of the layer in the adjacent domain. This indicates that step sites are not a favorable adsorption positions. This points to the fact that there are favorable adsorption sites in the surface alloy. Such favorable positions are most likely Au or RE atoms of the surface compounds.

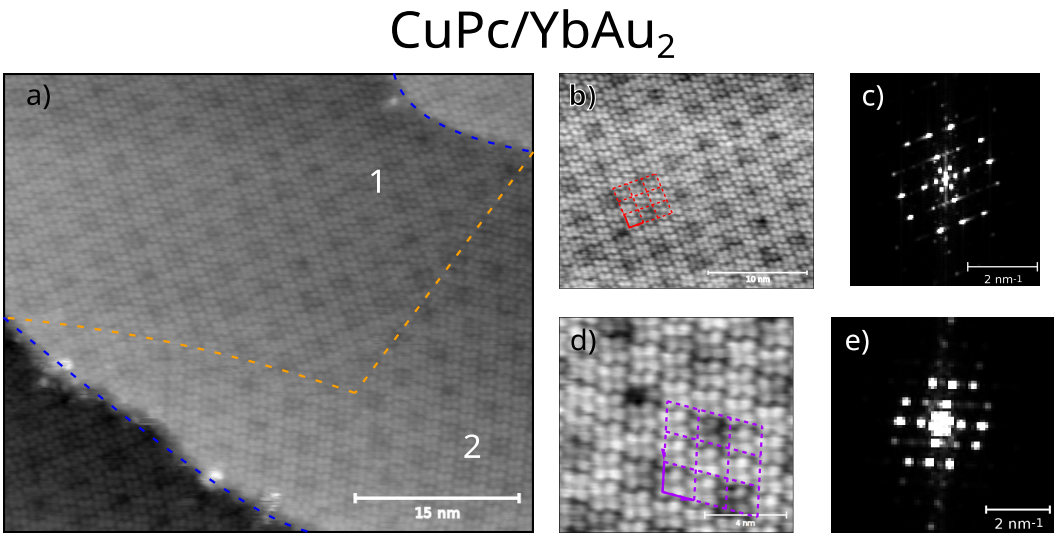

Figure 76: STM micrograph of CuPc on $YbAu_2$. a) Large area scan of the sample (image size 48×42nm², U=0.5V, I=0.2nA) showing 2 of the 3 possible rotational domains of CuPc. Terrace edges are marked in blue, crystallographic domain walls of the CuPc layer are marked in yellow. b) and d) Small scale images of areas 1 (image size 26×22nm²), and 2 (image size 10×10nm²), of part a). c) and e) show the corresponding 2D FFT of the STM images shown in c) and e).

7.1.2 Electronic structure

The valence bands of adsorbed CuPc MLs on $REAu_2$ surfaces (RE = Yb, Gd, Ho) have been investigated by angle resolved photoemission spectroscopy (ARPES).

The measurements were carried out on pristine $REAu_2$ surfaces and upon CuPc adsorption. The results are presented in Figure 77. The characteristic dispersing bands of the $REAu_2$ surfaces that have been discussed in sections 5.2.1.2 and 5.2.2.1 can be appreciated. The growth of CuPc on top introduces new non-dispersing bands that are assigned to the highest occupied orbital (HOMO) levels of the adsorbed molecule. Important to note is, however, that the $REAu_2$ band structure is still

visible although with a strongly reduced intensity due to the very surface-sensitive photoemission measurements (hν = 21.2eV, 30eV). At first glance, the band structure of the $REAu_2$ surface compounds seems to be unaffected upon CuPc adsorption, with the exception of the so-called *A* band. This band is located close to the $\bar{\Gamma}$ points and has an electron-like dispersion. It is observed that, after CuPc deposition, the *A* band binding energy (E_B) displays a small shift (δE_B) to lower energies at $\bar{\Gamma}$. This effect confirms the surface-state like character of the *A* band, which seems to be very sensitive to the adsorption of adlayers. Figure 77a), c), and e) displays the photoemission intensity mappings of electronic bands of pristine $HoAu_2$, $GdAu_2$ and $YbAu_2$, respectively, and in Figure 77b), d), and f) the same measurement after the adsorption of 1 ML of CuPc.

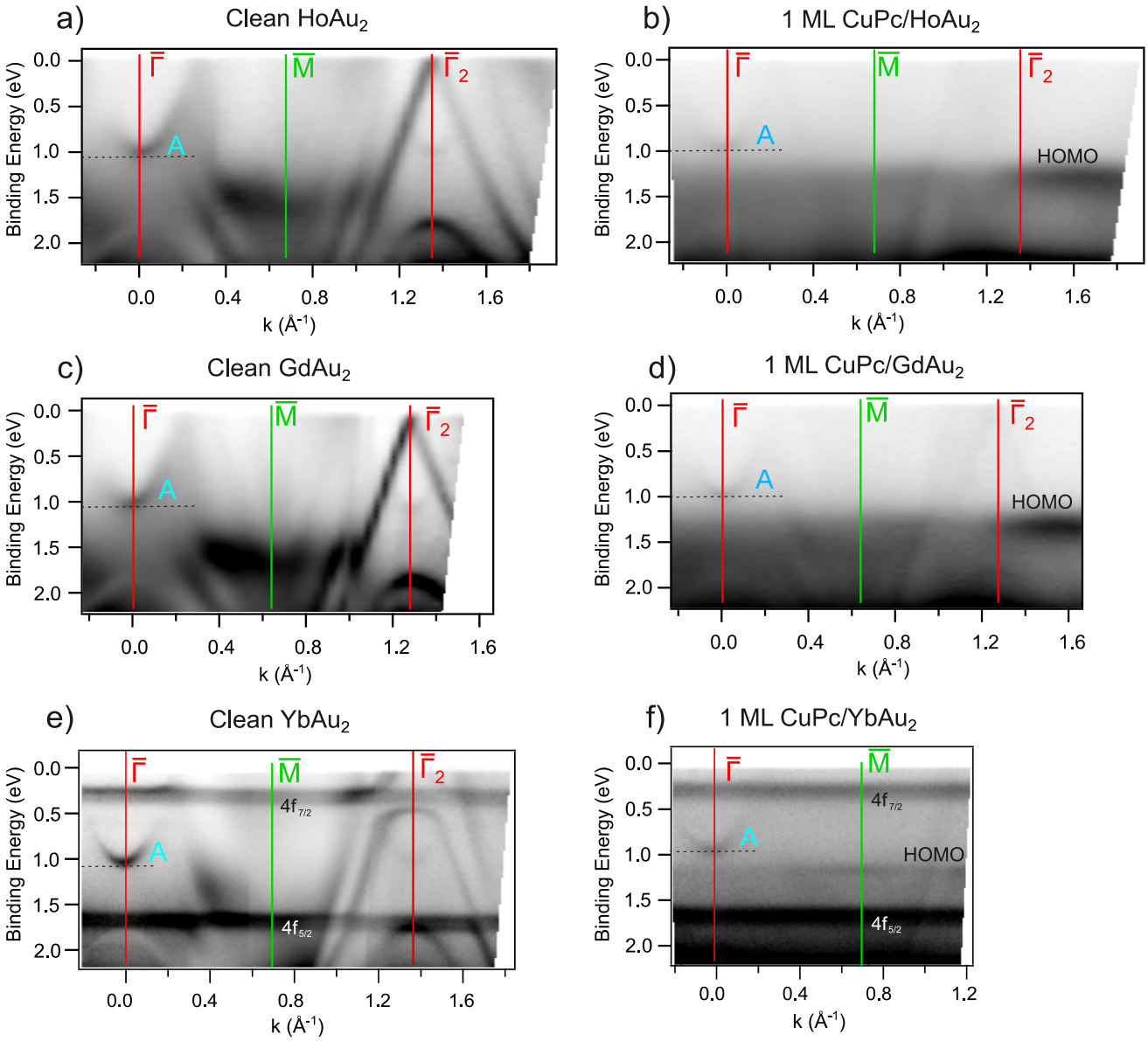

Figure 77: ARPES photoemission intensity plots along $\bar{\Gamma}\bar{M}\bar{\Gamma}_2$ *of a) pristine* $HoAu_2$*, c)* $GdAu_2$*, and e)* $YbAu_2$*, prior and in b), d), and f) after 1ML of CuPc adsorption, respectively. New, non-dispersing bands originate from the HOMO levels of the molecule.* $HoAu_2$ *and* $GdAu_2$ *experiments have been carried out at our home laboratory with HeI light, hv = 21.2eV, the* $YbAu_2$ *experiment at VUV-Photoemission beamline at Elettra synchrotron (hv = 30eV).*

Figure 78 shows the energy dispersion curves at an emission angle of 0º ($\bar{\Gamma}$ point) where one can detect the binding energy shift (ΔE_B) of the *A* bands. In the case of $YbAu_2$, E_B at the $\bar{\Gamma}$ point shifts from 0.92eV in the pristine alloy surface to 0.84eV upon CuPc adsorption, a shift of 80meV. However, for $HoAu_2$ and $GdAu_2$ E_B is shifted from 1.03eV in the pristine surface compounds to 0.99eV after CuPc deposition, the shift amounts to only 35meV. ARPES studies performed on rare-gas/Au(111) and organic molecules/Au(111) interfaces have ascribed a similar shift of the surface-state band to the pushback effect[185]. It has been shown that a universal curve can be established that relates the shift with the adlayer height above the metal surface, while the substrate work function

plays a minor role[186]. As was shown in section 5.2.1.2, the *A* band is formed upon $REAu_2$ interaction with the Au(111) support. This implies that its expansion into vacuum is smaller compared to the usual Shockley-like surface states in noble metals. This can also be understood in the universal curve as a due to higher absorption distance. Therefore, the pushback effect due to interaction with CuPc will be weaker than usual. Indeed, the observed ΔE_B values are lower than other typical shifts. For example, the Shockley state shift caused by PTCDA physisorption ranges from 0.164eV on Au(111)[187] to 0.95eV on Ag(100)[188]. The smaller shift for the CuPc layer case on $HoAu_2$ and $GdAu_2$ with respect to $YbAu_2$ is caused by a slightly higher adsorption distance of the layer in the trivalent alloys with respect to the divalent one. This was proven by the calculations carried by Dr. M. Blanco-Rey from the University of the Basque Country[189].

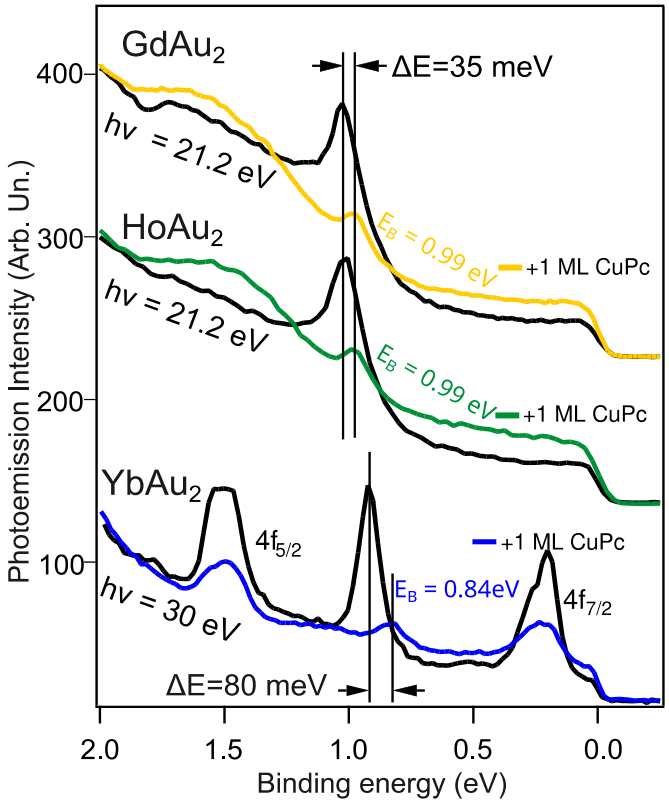

Figure 78: Normal emission photoemission measurements for $CuPc/REAu_2$ before and after CuPc adsorption. The spectra were measured on CuPc ML grown on $GdAu_2$, $HoAu_2$ and $YbAu_2$ MLs. Note also the decrease of the 4f emissions in the case of divalent $YbAu_2$.

As previously mentioned, the flat emissions from the HOMO levels is best observed at higher emission angles. The F-LUMO may get occupied for chemisorbed systems like CuPc/Ag(111)[182] or TiOPc/Ag(111) [110,190], but is unlikely to happen on physisorbed cases like CuPc/Au(111)[183]. Figure 79 shows the photoemission results at an emission angle of θ=45° of 1ML of CuPc on $HoAu_2$, $GdAu_2$ and $YbAu_2$ as well as for CuPc on pure Au(111). The latter one is used as a reference to estimate and compare energy shifts of HOMO band among the $CuPc/REAu_2$ samples. In none of the four systems, F-LUMO emissions occur below the Fermi level E_F. However, the HOMO related

features are readily seen, presenting different shifts with respect to the reference CuPc/Au(111) system. In the case of $YbAu_2$, this shift amounts to 0.26eV, while in the other two cases this value increases to approximately 0.5eV. The exact HOMO positions have been obtained after peak fit analysis using Lorentzian lines and taking into account the vibrational couplings of CuPc[191–193]. The results are presented in Table 4.

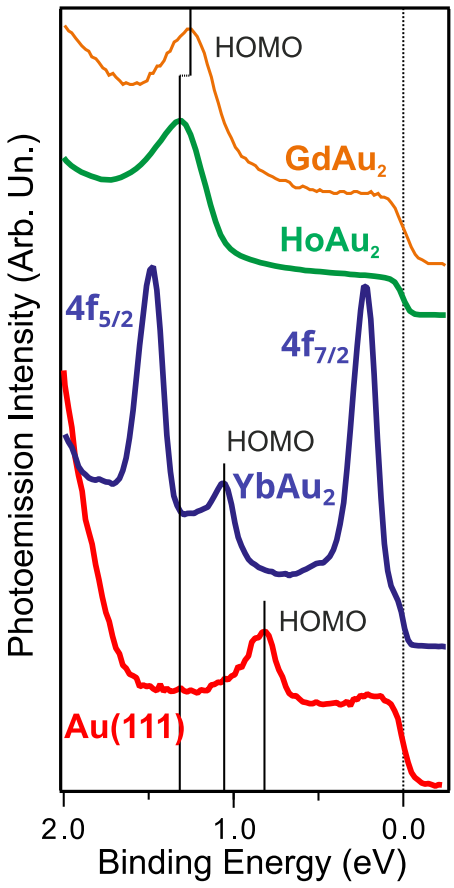

Figure 79: Photoemission measurements indicating the CuPc HOMO for CuPc/$REAu_2$ samples (RE: Gd, Ho, Yb) in comparison to CuPc/Au(111). The experiments were taken at an emission angle of 45º with a photon energy of 21.2eV (He I_α). In the Yb case, the intense 4f emissions of divalent Yb can be appreciated.

In addition, the interaction strength of CuPc with the different $REAu_2$ surfaces was studied by analyzing core levels with X-ray photoelectron spectroscopy (XPS). Figure 80 shows N 1s and C 1s core levels measured on CuPc/$HoAu_2$ and CuPc/$YbAu_2$. These core levels were measured at VUV-Photoemission beamline of the Elettra Synchrotron in Trieste, with photon energies of 520eV for N 1s and 390eV for C 1s. Core level shifts of both N 1s and C 1s to higher binding energies with respect to the CuPc/Au(111) emissions were detected (see Table 4). As in other works, the broad peak of N 1s emissions is attributed to the contribution of two non-equivalent nitrogen atoms within the Pc ligand that cannot be resolved due to the line width of the peaks[194]. In order to disentangle both contributions, a peak fit analysis was carried out using two individual Doniach-Sunjic peaks[195] of the same width, asymmetry, and Shirley background[196]. On the other hand, the analysis of the C

1s core level of CuPc reveals three different contributions: first, the strongest emission corresponds to the 24 carbon atoms of the benzene rings, second, the contribution from the 8 carbon atoms in the pyrrole structures, and third, a shakeup satellite[197]. The fit results are included in Figure 80b). Similar to the result from the HOMO level shifts, the core level shifts in CuPc/$YbAu_2$ amounts to approximately one half of those in the $HoAu_2$ and $GdAu_2$ cases with respect to the CuPc/Au(111) system. This result indicates that the $YbAu_2$ surfaces show a slightly weaker interaction compared to $GdAu_2$ and $HoAu_2$ with the CuPc molecules, taking Au(111) as a reference. The exact positions of the core levels are again included in Table 4. From all the photoemission results, and taking into account that the HOMO-LUMO gap is of the order of 3eV[198] we extract that E_F is located well inside the HOMO-LUMO molecular gap, far from the edges. In such scenario we do not expect a significant amount of charge flowing to align the Fermi level to the molecular levels.

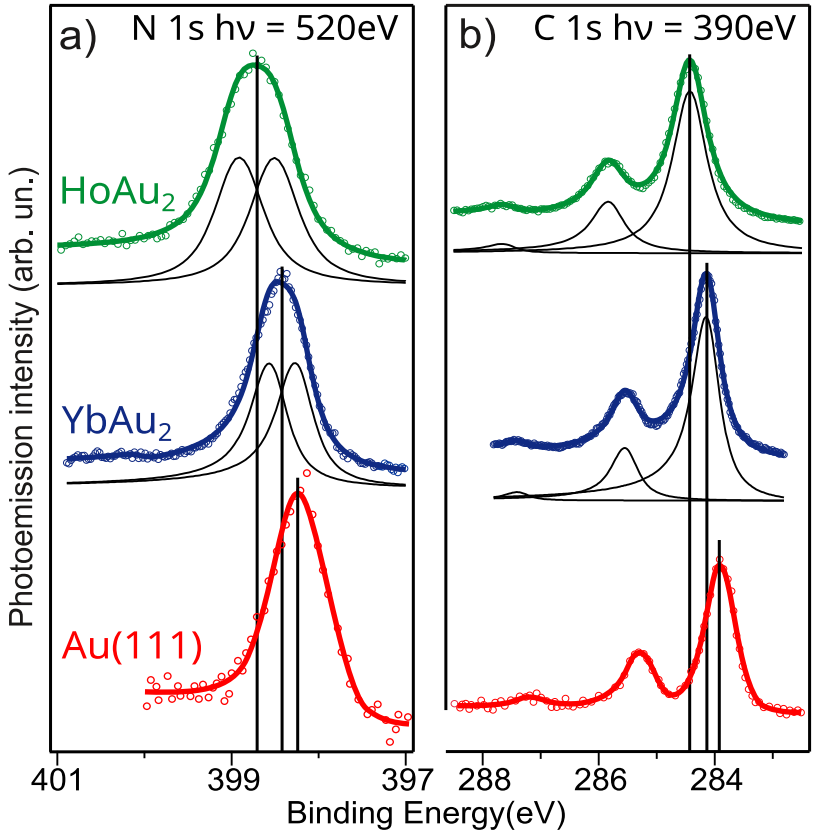

Figure 80: X-ray Photoemission measurements for CuPc/$REAu_2$ samples. a) N 1s and b) C 1s core levels of 1 ML CuPc grown on $HoAu_2$ and $YbAu_2$. For comparison N 1s and C 1s core levels of 1ML of CuPc/Au(111) are displayed as reference. The reference spectra of CuPc/Au(111) is taken from ref. [199].

Last, experimental work function (Φ) measurements were performed by photoemission spectroscopy from the cutoff of the secondary emitted electrons on pristine $REAu_2$ substrates and upon adsorption of 1ML of CuPc on top. Φ was evaluated by ARPES measurements in our laboratory using normal emission geometry and HeI_α (21.22eV) photons. In order to be able to bring the secondary electrons into the analyzer, a voltage has been applied to the sample (extraction

voltage) displacing the complete emission spectra to higher kinetic energies. Then, cutoff of the secondary emitted electrons and E_F is measured for each extraction voltage. The work function is obtained by evaluating the energy difference between the Fermi level E_F and the photoemission cutoff for several extracting voltages (5V, 10V and 15V). Several extraction voltages have been used to eliminate artifacts[200,201]. Figure 81 shows the photoemission cutoffs of the Φ measurements for the pristine $REAu_2$ and CuPc/$REAu_2$ surfaces. For simplicity, only the 15V sample potential measurements are shown. The corresponding changes in the work function ΔΦ upon CuPc adsorption on each $REAu_2$ surface is calculated with respect to the CuPc/Au(111) sample, which has been used as reference sample. The Φ values are included in table 4. The work function changes after CuPc adsorption is related to the surface dipole induced by the molecules. This dipole is caused in turn by the Pauli push-back effect, which is commonly observed in metal-organic interfaces[202–205]. This Pauli repulsion was also seen as source of the displacement of the *A* band. The highest ΔΦ values are found in the samples of CuPc/$HoAu_2$ and CuPc/$GdAu_2$. For the pristine alloys (without CuPc), Φ displays similar values for both $GdAu_2$ (4.89eV) and $HoAu_2$ (4.88eV) surfaces. However, the highest Φ is measured in $YbAu_2$ (4.98eV). This is an unexpected result considering that Yb as pure element exhibits smaller work function values than Ho and Gd due to its divalent configuration[206,207]. From table 4 we see, that ΔΦ, ΔHOMO and the changes in the core levels are directly correlated. This clearly points to a vacuum level pinning of the molecular energy levels in our samples[199,205], which means that the behavior of the samples is close to the Schottky-Mott limit[208].

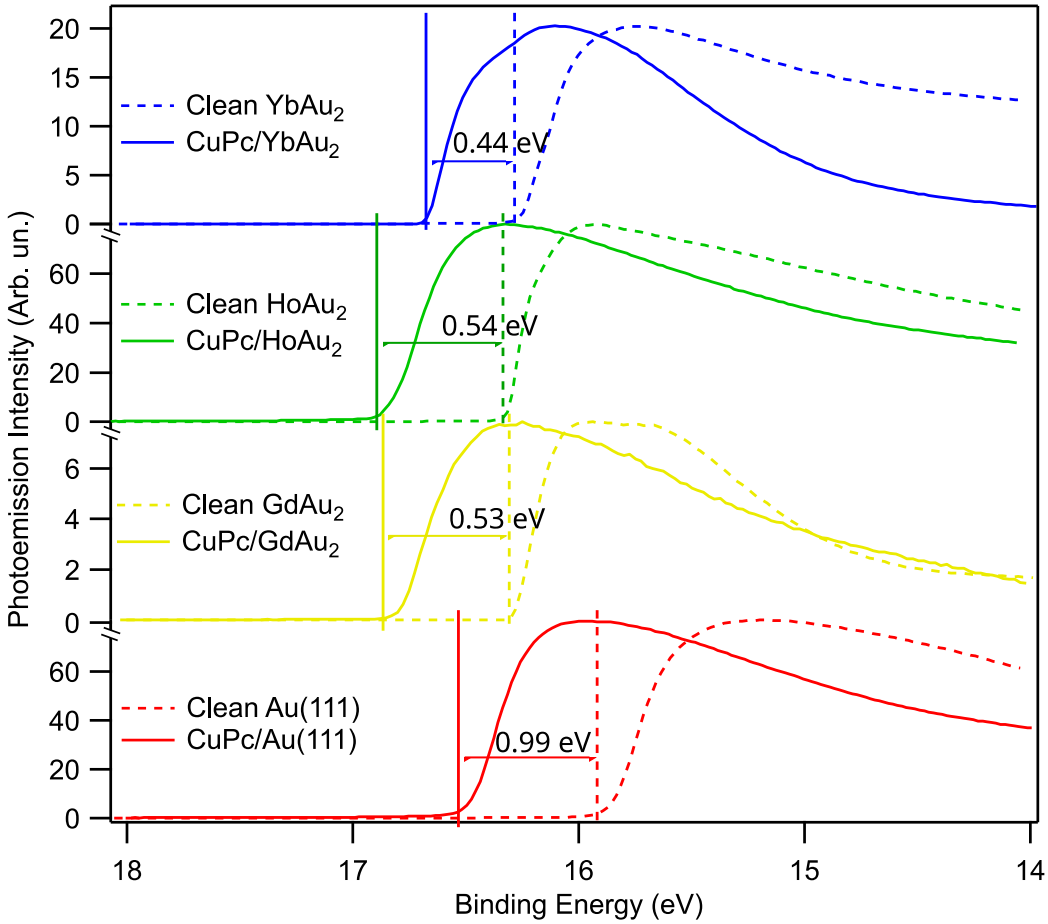

Figure 81: Photoemission cut-off measurements for CuPc/REAu₂ samples and CuPc/Au(111) (solid lines) as well as the clean substrates (dashed lines) for extraction of the work function values. Work function shifts produced by the CuPc adsorption are indicated. Measurements were taken with HeI$_\alpha$ light ($h\nu$ = 21.22eV) applying a sample voltage of 15V. The Φ shifts are included.

In order to estimate a possible LUMO energy position for our samples, we consider a molecular gap of 3eV, obtained from a combination of normal and inverse photoemission measured on CuPc/Au(111) reported in ref.[198]. CuPc on all investigated $REAu_2$ systems and on Au(111) is physisorbed, although on $REAu_2$ it reveals a slightly stronger electrostatic interaction. Therefore, the predicted bandgap for CuPc/$REAu_2$ should be close and somewhat smaller than 3eV. This argument is based on the fact that the bandgap of molecules adsorbed on surfaces becomes smaller in case of stronger interactions[205,209]. Hence, we can extract the following LUMO level positions of CuPc on the substrates: 1.92eV on $YbAu_2$, 1.73eV on $GdAu_2$, 1.67eV on $HoAu_2$ and 2.18eV on Au. It is worth to note that the energy difference between the HOMO and the Fermi level on one hand side and between the LUMO and the Fermi level on the other hand side (/HOMO E_b/-/LUMO E_B/)for $GdAu_2$ and $HoAu_2$ substrates is quite small (approx. 0.4eV), but this value doubles for $YbAu_2$ substrate (0.84eV) and is even higher for CuPc/Au(111) (1.36eV). Similar LUMO and HOMO values (neglecting the sign) mean that E_F is located close to the middle of the molecular gap. Such systems allow simultaneous injection of electrons and holes into the organic layer. Such

effect, called ambipolar injection, is key to achieve an effective electron-hole recombination in organic light-emitting FETs [210–212]. We see, that in our system (CuPc) we can tune the value of the HOMO and LUMO levels with an adequate RE element of the substrate. This opportunity opens the possibility to tune band alignment on demand.

Table 4: Binding energies E_B, core level shifts of N 1s and C 1s and binding energies measured on 1 ML CuPc grown on $REAu_2$ surface compounds for RE = Yb, Gd and Ho. The first column is the HOMO position with respect to E_F. The binding energy differences ΔE_B of these quantities are refereed to the binding energy values measured on 1 ML of CuPc on Au(111).

	HOMO E_B (eV)	HOMO shift ΔE_B (eV)	N1s E_B (eV)	N1s shift ΔE_B (eV)	C1s E_B (eV)	C1s shift ΔE_B (eV)	Φ (eV)	ΔΦ (eV)
CuPc/ $YbAu_2$	1.08	0.26	398.45	0.22	284.18	0.26	4.54	0.27
CuPc/ $GdAu_2$	1.27	0.45	398.78	0.40	284.50	0.44	4.35	0.46
CuPc/ $HoAu_2$	1.33	0.51	398.74	0.49	284.41	0.49	4.35	0.46
CuPc/ Au(111)	0.82	-	398.20	-	284.14	-	4.81	-

7.1.3 Magnetic properties

We have studied the magnetic behavior of the CuPc/$GdAu_2$ and CuPc/$HoAu_2$ interfaces with the use of synchrotron radiation at BOREAS beamline in ALBA using XMCD technique. Both systems display an unaltered ferromagnetism of the $REAu_2$ monolayer and antiferromagnetic coupling between the molecule and the $REAu_2$ layer. The strong magnetic anisotropy of the CuPc molecule is still present[77].

Figure 82 shows XAS and XMCD measurements performed on CuPc/$GdAu_2$. The spectra have been measured at the Cu $L_{2,3}$ edges at 6T and 4K, in IP and OOP geometries. The first observation is that the intensity of the spectra measured in OOP geometry is more intense than the spectra measured in IP geometry. This is caused by the high anisotropy of the CuPc molecule itself with a marked OOP easy axis of anisotropy that is perpendicular to the molecular plane. Previous measurements of the molecule on noble metal surfaces observed that the magnetic anisotropy of the molecule is caused by the strong anisotropic charge distribution within the Pc molecule[77,213]. Therefore, also here, the dichroic signal measured in the system CuPc/$GdAu_2$ in IP geometry, at the maximum applied field (6T), is much lower than in the OOP one, with about ¼ of intensity. This indicates that the strong anisotropy of the CuPc molecule is preserved under absorption on a $GdAu_2$ surface. The background observed in XAS below the Cu signal is produced by the EXAFS of the Au N_1 edge transition that depend on the incidence angle.

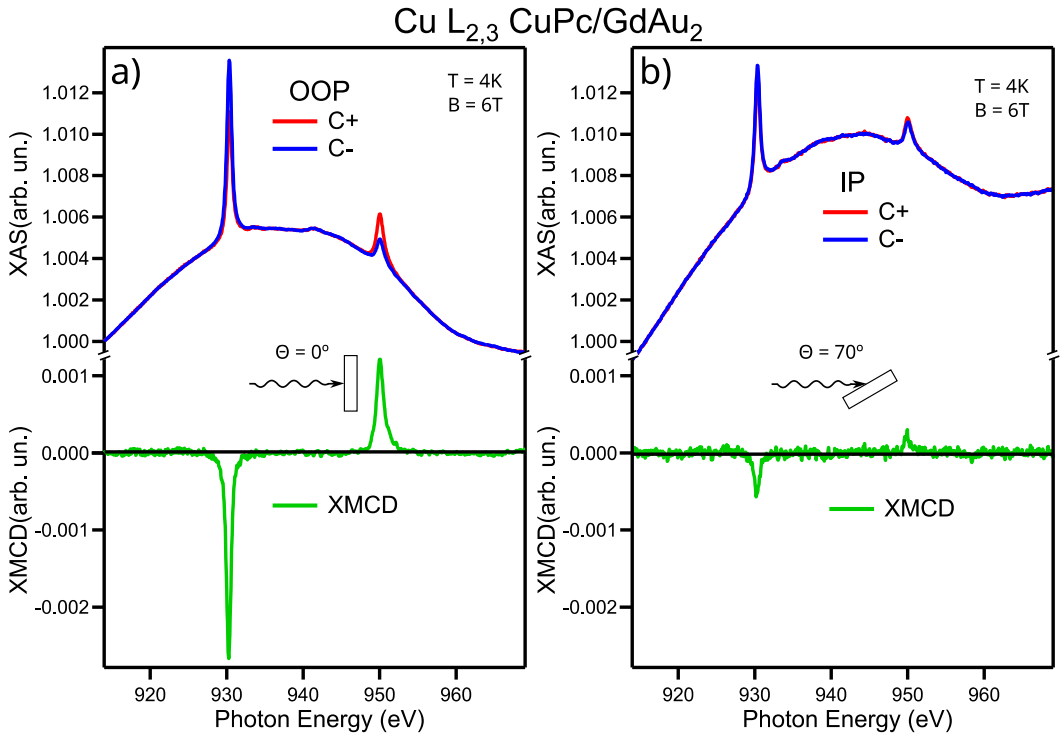

Figure 82: Cu XAS and XMCD spectra of CuPc/GdAu$_2$ measured at 6T and 4K at the Cu $L_{2,3}$ in a) OOP and b) IP geometry. XAS spectra measured with C+(C-) circular polarization are presented in red (blue), in green we mark the dichroic spectra [C+]-[C-] with a different scale.

Figure 83 shows the Cu and Gd XMCD loops of CuPc/GdAu$_2$. For this purpose the photon energy of the XMCD signal was set to the maximum of the Cu L_3 and Gd M_5 peaks. For normalization the signal was divided by a pre-peak value at hν = 925eV (Cu) and 1165eV (Gd) at each field value to account for beamline instabilities. Measurements on the Cu L_3 peak are marked in blue (OOP) and red (IP). On the other hand, the measurements on the Gd M_5 edge are marked in light blue (OOP) and yellow (IP). The GdAu$_2$ loops match reasonably well with the loops of pristine GdAu$_2$ reported in the work of Ormaza et al.[35]. This coincidence indicates that the absorption of the CuPc molecules does not affect significantly the XMCD loops of the GdAu$_2$ alloy. In the case of the XMCD loops measured on CuPc there are two different behaviors depending on the magnetization direction. In the case that the sample is magnetized IP, the magnetization is close to zero for applied magnetic fields below 1.25T. Above this field, the magnetization grows linearly. In the case that the CuPc is magnetized in OOP geometry, its magnetization is antiparallel to the magnetization of the substrate for fields below approx. 0.8T. Above this field the magnetization grows linearly following the field direction. It crosses the zero magnetization axis at an applied field of 1.1T. In Figure 84 we verify this observation by showing the XAS and XMCD spectra measured at high fields (6T) and low fields (0.5T) of the CuPc layer. The XMCD spectra reveal that at low applied fields the XMCD signal of CuPc in OOP geometry is opposed in sign to the XMCD signal at high fields. Therefore, there is an inversion of magnetization of CuPc respect to the applied magnetic field in the OOP direction pointing clearly to an antiferromagnetic coupling (J<0) of the Cu moment in CuPc to the substrate magnetic moments. However, in the IP geometry, there is an apparent absence of CuPc

magnetization at low fields.

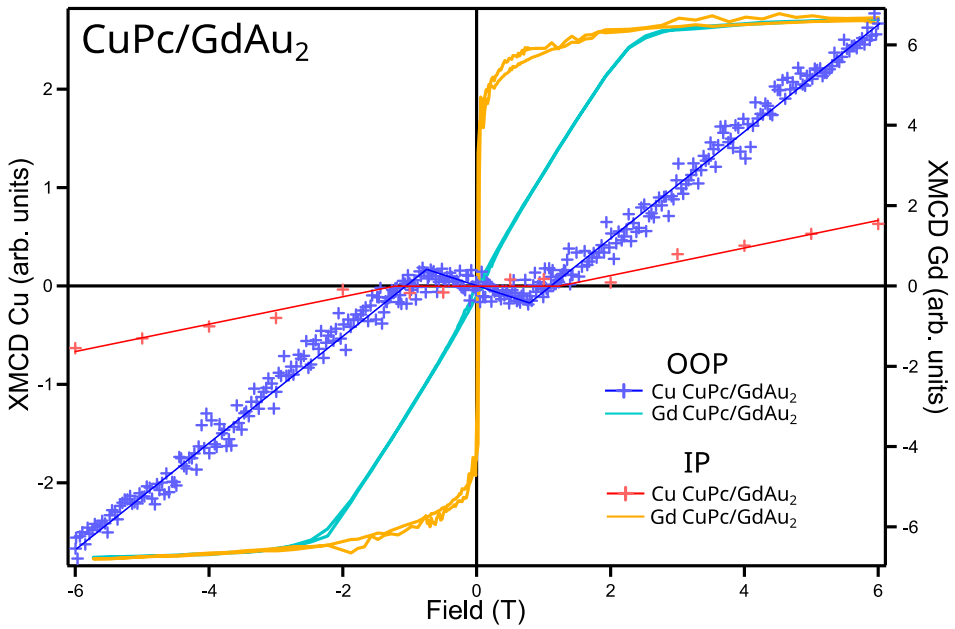

Figure 83: XMCD Hysteresis loops of 0.7ML CuPc/GdAu$_2$ measured at 4K. The measurements were performed at the Gd M_5 and at the Cu L_3 edges. The measurements of CuPc are marked in blue (OOP) and red (IP geometries), while the measurements at Gd are marked in green (OOP) and orange (IP). For the Cu measurements, solid lines has been drawn as visual guides.

In order to model the interaction of the magnetic response between the CuPc molecule and the substrates we will use a hamiltonian including three terms. The first term is the action of the applied magnetic induction field over the molecular spin (Zeeman term). The second terms relates to the exchange coupling to the surface and the intrinsic magnetic anisotropy of the molecule. In previous works on non-magnetic subtrates[77,78,213], in which there cannot be exchange coupling, the IP magnetization is much lower than the OOP. From this observation we can deduce that the intrinsic magnetic anisotropy of the molecule will be fundamental to understand the dependence of the magnetization with the measurement geometry. This anisotropy part will enter our Hamiltonian in third place. Additionally, we have to consider the anisotropy of the coupling constant (J). Due to the quenched L moment of the CuPc (as a result of the hybridization of the Cu orbital to the organic ligands) we can assume that the electron distribution of the molecule will not be affected by the spin polarization direction, and as a consequence it will not contribute to anisotropy in J. As we showed in section 5.2.1.2 the RE 4f levels lay too deep in the atom to couple directly and coupling is trough valence electrons (RKKY-like). This way, the coupling will be proportional to the density of states near the Fermi level, and, as was shown in section 5.1.1, the density of states almost equals for both magnetization directions. Taking that into account, we can approximate the exchange coupling J to be isotropic, especially when compared to the intrinsic magnetic anisotropy of CuPc. It is common in the treatment of the Pc molecules that the coupling between molecules will be depreciated as no ordered magnetism of the pure molecules has been reported. As a result of all these considerations,

the Hamiltonian of the magnetization of the molecules will be given by:

$$H = \underbrace{-\mu_B \cdot \vec{B} \cdot \vec{S_M}}_{\text{Zeeman interaction to the field}} - \underbrace{J \cdot \vec{S_M} \cdot \vec{S_S}}_{\text{Coupling to the surface}} - \underbrace{K \cdot |\vec{u} \cdot \vec{S_M}|}_{\text{Molecular anisotropy}} \tag{29}$$

H is the Hamiltonian (per molecule), J the exchange constant between the molecule and the substrate, μ_B the Bohr magneton, *K* the anisotropy constant, $\vec{u}$ the unitary vector of the easy axis of the molecule, $\vec{S_S}$ the magnetization of the surface alloy, $\vec{S_M}$ the magnetization of the molecule and $\vec{B}$ the applied field.

From now on we will make separate considerations for each magnetization direction. Starting with the easy axis of magnetization, it is immediately seen that the molecular anisotropy favors this direction. As a result, it will not affect the minimization of energy in this direction. That way, we can simplify the Hamiltonian to:

$$H = -J \cdot \vec{S_M} \cdot \vec{S_S} - \mu_B \cdot \vec{B} \cdot \vec{S_M} \tag{30}$$

In order to simplify further, we can limit the discussion to a single direction for which $\vec{S_S}$, $\vec{S_M}$ and $\vec{B}$ are colinear and we can take them as scalars. Now we can apply the canonical distribution, or in more simple and direct approach, we apply the Brillouin model solution[137]:

$$S_M \propto B_J\left(\frac{-J \cdot S_S - \mu_b \cdot B}{k_B T}\right) \tag{31}$$

k_B is the Boltzmann constant $B_J()$ is the Brilloiun function for J total moment. From this, we can see that the magnetization can be zero if:

$$J \cdot S_S = -\mu_b \cdot B \tag{32}$$

As a note, this condition can give a trivial solutions at $\vec{B}=0$ if the substrate magnetization is zero or the coupling is zero. The equation give a non-trivial solution if the coupling is antiferromagnetic ($J < 0$).

With the easy axis treated, we can now move to the hard axis data. If we go back to equation 29, we can see that in order to minimize the Hamiltonian in the hard axis, we have to fulfill that the coupling to the surface plus the effect of applied field has to overcome the molecular anisotropy, that is, the magnetization in the hard axis will not appear until:

$$\left| \underbrace{-\mu_b \cdot \vec{B} \cdot \vec{S_M}}_{\text{Zeeman interaction to the field}} \quad \underbrace{-J \cdot \vec{S_M} \cdot \vec{S_S}}_{\text{coupling to the surface}} \right| > \underbrace{K \cdot \left|\vec{S_M}\right|}_{\text{molecular anisotropy}} \tag{33}$$

In the same way as in the OOP case, we can confine to a single direction and exchange the vectors for scalars. Doing that, we can further simplify by dividing by S_M:

$$\mu_B \cdot B + J \cdot S_S > K \tag{34}$$

From here, we can obtain the critical field B_C at which the sample starts to magnetizes for *K* that fulfills

$$K = \left| \mu_B \cdot B_C + J \cdot S_s(B_C) \right| \tag{35}$$

Putting the analysis of both magnetization directions together, and knowing that the molecule and substrate are antiferromagnetically coupled and the molecule has OOP anisotropy, we can calculate the anisotropy constant of the molecule and the coupling energy according to:

$$\begin{aligned} J &= \frac{\mu_B \cdot B_{OOP}}{S_S(B_{OOP})} \\ K &= |\mu_B \cdot B_{IP} + J \cdot S_s(B_{IP})| \end{aligned} \tag{36}$$

B_{OOP} and B_{IP} represents the critical fields in each direction. B_{OOP} is the non zero field at which the magnetization returns to zero, and $\vec{B}_{IP}$ is the prolongation of the linear growth of the magnetization to zero magnetization.

In our case, from Figure 83 we can determine the critical fields as $B_{OOP} = 1.10\,T$ and $B_{IP} = 1.25\,T$. This leads to a coupling J = -28μeV and a anisotropy constant K = 136μeV.

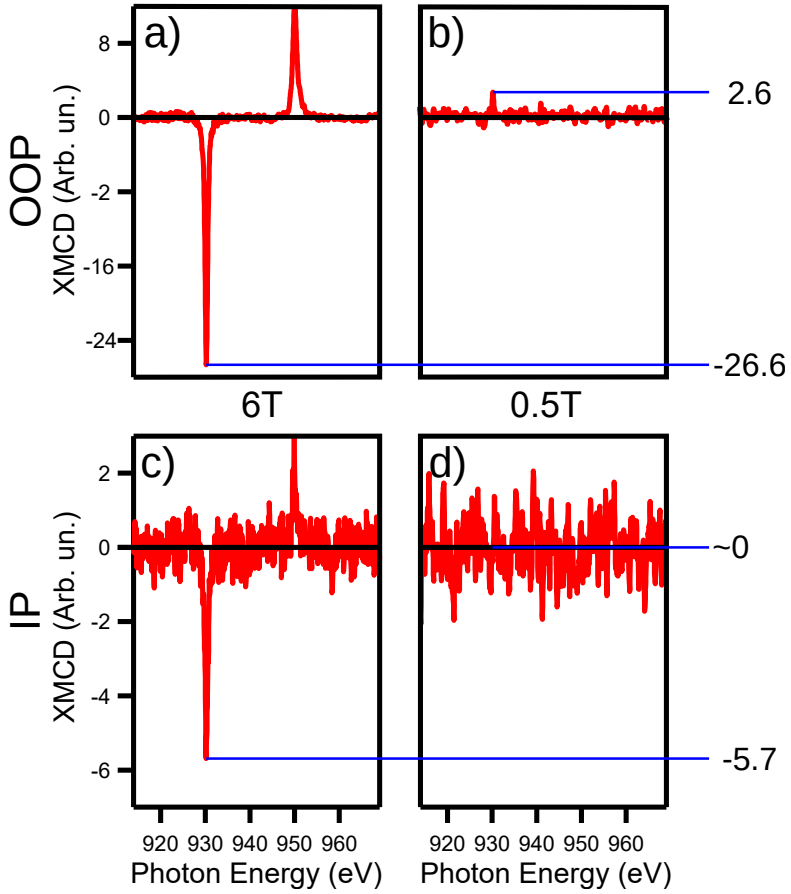

Figure 84: Detailed XMCD and XAS spectra of CuPc/GdAu₂. a),b) XMCD at an applied field of 6T and 0.5T in OOP geometry, c),d) in IP geometry, respectively. Spectra were taken at the Cu $L_{2,3}$ absorption edge. The inversion of the signal in OOP geometry relates directly with the the antiferromagnetic ordering of CuPc to the GdAu₂ magnetic moments.

The magnetism of the system of CuPc/HoAu₂ was analyzed in a similar way as previously shown in

the system CuPc/$GdAu_2$. Figure 85 displays XAS and XMCD measurements at the Cu $L_{2,3}$ edge of the sample CuPc/$HoAu_2$ at 6T and 4K. The measurements were carried out in both, IP and OOP geometries, respectively. We observe a clear decrease of the XMCD intensity of CuPc at IP geometry with respect to OOP geometry measurement. At 6T it is seen that the dichroic signal in IP direction is about 1/8 of the signal measured in OOP direction. This clearly indicates a strong OOP anisotropy of the CuPc adsorbed of $HoAu_2$. As in CuPc on $GdAu_2$, this can be explained by the adsorption in a planar geometry and the high anisotropy of CuPc with the easy axis perpendicular to the molecular plane. Importantly, the magnetization of CuPc in the IP direction is even lower than in CuPc/$GdAu_2$, being about one half. This is a first sign that the substrate $HoAu_2$ enhances the anisotropy of the CuPc molecule due to coincidence of their anisotropies. As it was previously commented, the non-flat background is likely to arise from EXAFS of the Au N_1 absorption edge.

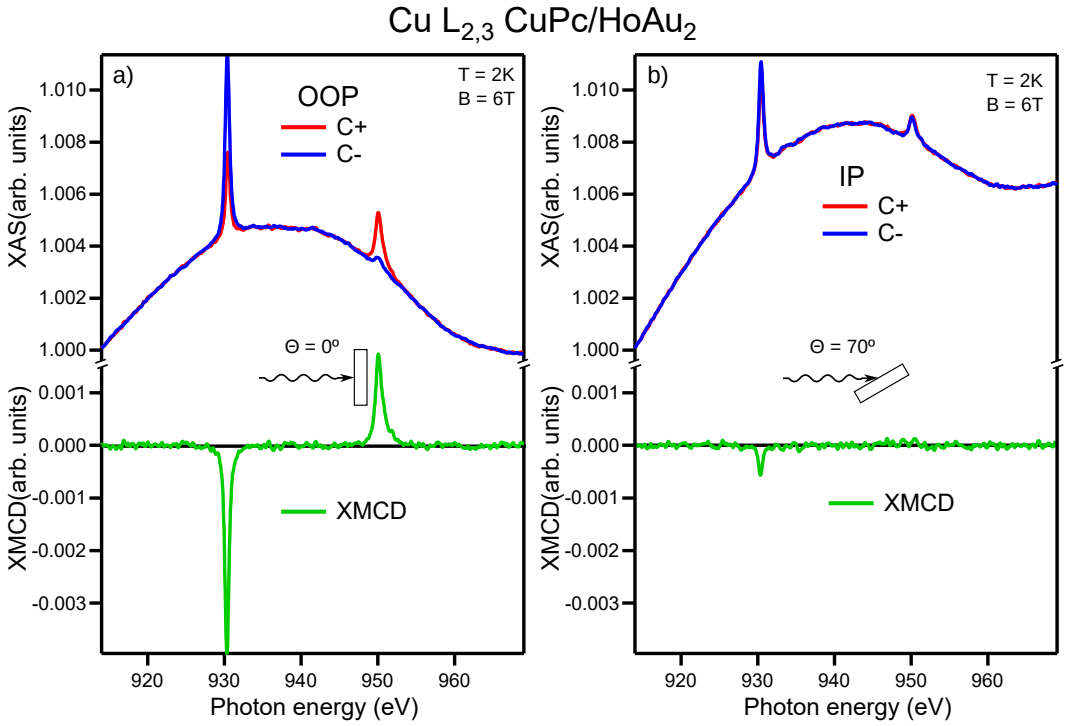

Figure 85: Cu XAS and XMCD spectra of CuPc/$HoAu_2$ measured at the Cu $L_{2,3}$ edge at 6T and 4K in a) OOP , and b) IP geometries. Red (blue) color is used for the XAS spectra measured with C+(C-) circular polarized light, green for the dichroic XMCD spectra [C+]-[C-].

Figure 86 shows the XMCD loops of CuPc/$HoAu_2$. The XMCD loops measured on the Cu L_3 edge are marked in blue (OOP geometry) and red (IP geometry). The XMCD loops measured on the Ho M_5 transition are marked in light blue (OOP geometry) and orange (IP geometry). The $HoAu_2$ loops also match reasonably well with the loops of the clean $HoAu_2$ surface (section 5.3.1), which indicates that the absorption of the CuPc molecule on the surface does not have a significant effect on the $HoAu_2$ alloy. This is the same situation as previously observed in the case of CuPc/$GdAu_2$. Here, the CuPc loops measured on CuPc/$HoAu_2$ display two different magnetization behaviors depending on the magnetization direction. In the IP direction, there is no magnetization until a field of 2.4T. Above this value it grows linearly until 6T. In the case of the OOP direction, the

magnetization is anti-parallel to the substrate magnetization until an applied magnetic field of 0.60T. Above this field the magnetization grows linearly following the field direction until saturation at about 4.2T. Above this field the increase in magnetization is reduced due to its proximity to saturation. Zero-magnetization (zero XMCD signal) crossing is observed for an applied field of 1.05T. Figure 87 shows the XMCD spectra taken at 6T and 0.5T. They confirm the inversion of magnetization in the OOP direction, and zero or a very small magnetization in the IP direction at low fields.

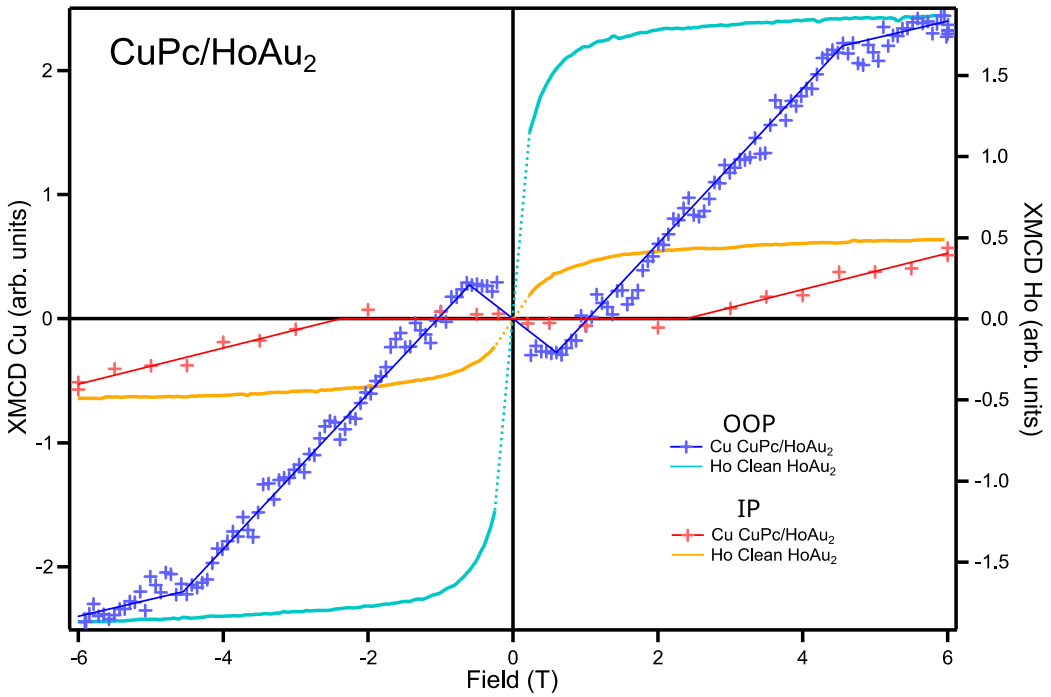

Figure 86: XMCD Hysteresis loop of CuPc and $HoAu_2$ in the CuPc/$HoAu_2$ system. The loops were measured at 4K. The XMCD loops were measured at the Cu L_3 edge for CuPc and at the Ho M_5 edge for the $HoAu_2$ surface. The XMCD loops of CuPc are marked in blue (OOP geometry) and red (IP geometry). XMCD loops of $HoAu_2$ are marked in light blue (OOP geometry) and orange (IP geometry). For the Cu measurements, solid lines has been drawn as visual guides.

Following the same argumentation as in the CuPc/$GdAu_2$ case we can determine two critical fields: $B_{OOP}=1.05\,T$ and $B_{IP}=2.20\,T$. From them we can estimate an anisotropy constant K = 190μeV and a coupling J =-30μeV. After comparing values of these constants with the case of the $GdAu_2$ surface, we can see two things. First, the anisotropy of the CuPc is larger in the system CuPc/$HoAu_2$, where $HoAu_2$ have an OOP easy axis of magnetization identical to the easy magnetization axis of CuPc. This can be understood, since the exchange coupling between them will minimize the energy more than in the case of an easy axis of anisotropy that is perpendicular between the two easy axes. Second, the coupling to the $GdAu_2$ alloy is of similar intensity than the coupling to $HoAu_2$ alloy. This second part is expected, and can be understood with some considerations. First, the coupling of CuPc with the alloy takes place with an imbalance of the spin (spin polarization) on the valence band of $REAu_2$ alloy. Second, the spin polarization near E_F of

both alloys is similar. The latter was shown in section 5.2.1.2 and it is caused by the shared trivalent RE electronic structure. To resume, the CuPc shows similar coupling to both ferromagnetic surface compounds due to its shared electronic structure. The shared easy axis direction in CuPc/$HoAu_2$ reinforces the magnetic anisotropy of the molecule. In both substrates, the response of the ferromagnetic substrate is unaffected.

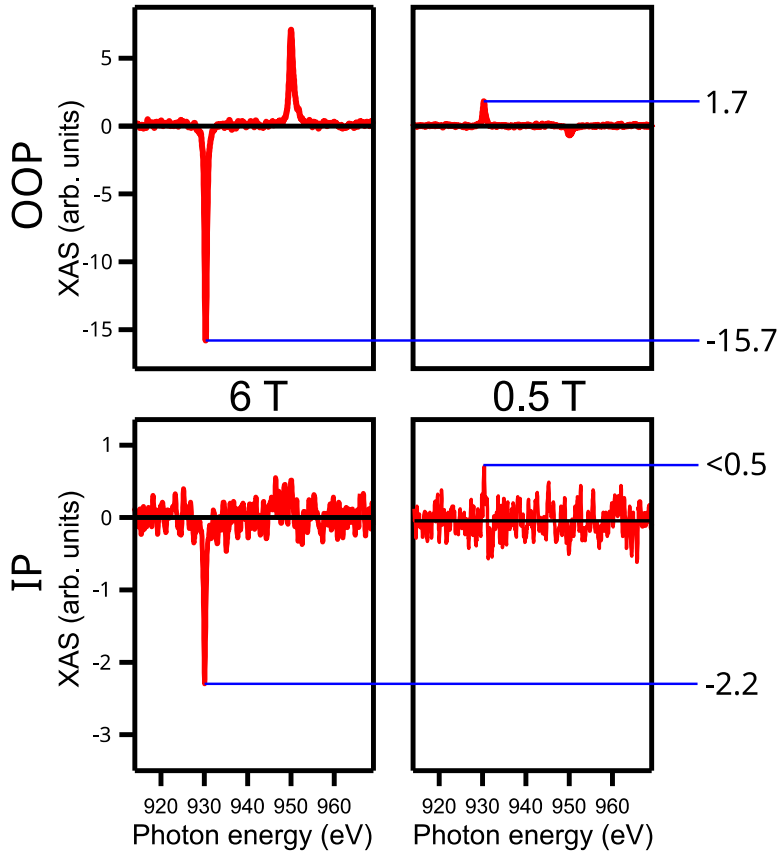

Figure 87: Detailed XMCD and XAS spectra of CuPc/$HoAu_2$. a),b) XMCD at an applied field of 6T and 0.5T in OOP geometry, c),d) in IP geometry, respectively. Spectra were taken at the Cu $L_{2,3}$ absorption edge. The inversion of the signal in OOP geometry relates directly to an antiferromagnetic ordering of CuPc to the $HoAu_2$ magnetic moments. In in-plane geometry and 0.5T the XMCD values are too small even after very long measurement times to extract a clear positive or negative value at the L_3 energy position.

7.2 $TbPc_2$/$REAu_2$ system

7.2.1 Structure analysis

1ML of $TbPc_2$ molecules was adsorbed on several $REAu_2$ surface compounds. In particular, the growth of $TbPc_2$ on the surface compounds was studied on $HoAu_2$ and $EuAu_2$ surfaces by low-energy electron diffraction (LEED) and scanning tunneling microscopy (STM). The main reason for this selection of the RE materials is that these substrates have an OOP easy axis of magnetization

that, as will be shown in next section, favors the OOP easy axis in $TbPc_2$.

Figure 88 displays the LEED pattern of $TbPc_2$ grown on a $HoAu_2$ surface. In this system $TbPc_2$ grows with three different rotational domains, as it is typically observed in phthalocyanine molecules on several noble metals and in CuPc adsorbed on $REAu_2$ surfaces, as was been previously shown. In Figure 88 the surface unit cell of $TbPc_2$ appears marked by a purple line. The green and orange lines represent the unit cells of the other two rotational domains, which are rotated by 60º degree respect each other.

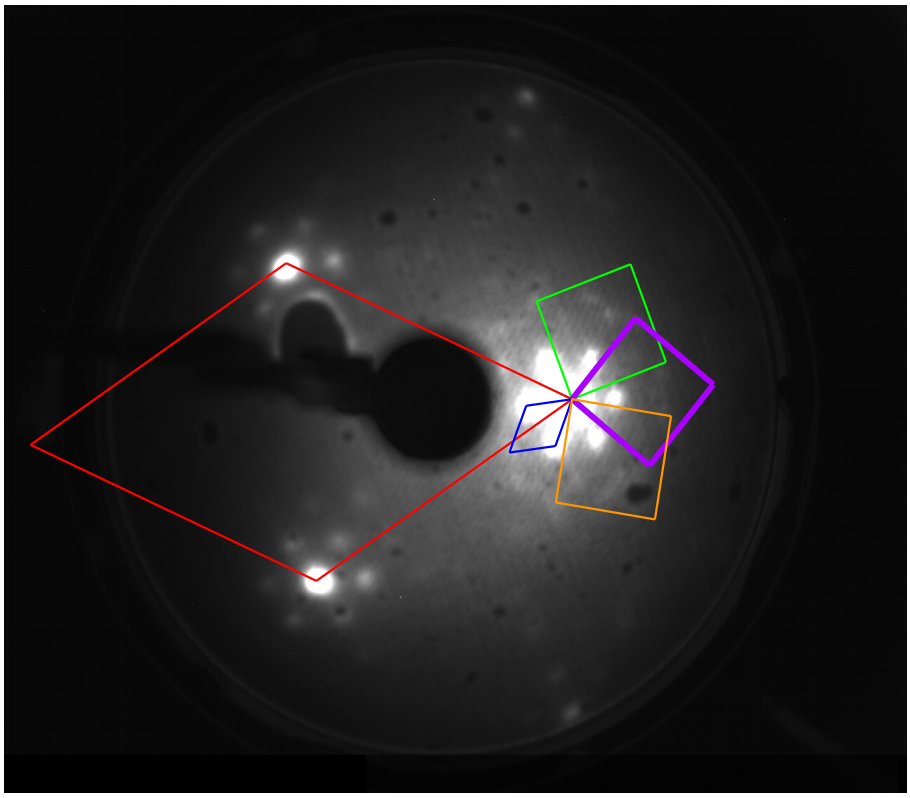

Figure 88: LEED patterns of a $TbPc_2$ monolayer grown on $HoAu_2$ surface alloy. The surface unit cells of the three equivalent rotational domains of $TbPc_2$ are displayed (green, purple and orange). The surface unit cell of $HoAu_2$ is marked in red, while the unit cell of its Moiré is marked in blue. All of them together contribute to the observed pattern. The LEED image was slightly rotated off-normal to be able to observe the (0,0) spot, electron energy was 15eV.

The ordering of the $TbPc_2$ molecules on the $HoAu_2$ surface has been further investigated by scanning tunneling microscopy (STM). Figures 89a) and b) show the areas of the sample with the three different rotational domains, with the 60° rotation between them. As commented above, this is due to the superposition of molecules with 4-fold symmetry over substrates with 3-fold symmetry. Fig. 89c) shows an area that is focused on one of these domains while Figure 89d) is the self correlation function (SCF), which is a direct assessment of the repetition (periodicity) in that image. In this case, the lattice of the domains results to be rhomboid with a lattice parameter $a = (1.53 \pm 0.04)\,nm$ and θ = 88° between the two lattice vectors. Considering this arrangement,

the packing density of the $TbPc_2$ overlayer results to be of about 0.45 molecules/nm^2, slightly lower than the value obtained in CuPc on $REAu_2$ surfaces (RE: Ho, Gd, Yb) (0.49 molecules/nm^2). It should be noted that there are molecules grown in a second layer that are randomly located as it is seen in Figure 89c). A profile analysis performed on several of such molecules grown on top of the first $TbPc_2$ layer is shown in Fig 89e). The results indicate that there are two heights of these molecules, one corresponding to 0.4nm expected to be intact $TbPc_2$ and the other one of 0.2nm. For the latter, there are two possible explanations. They could be single Pc structures from broken $TbPc_2$ molecules during the evaporation[214], or triple-deckers (Tb_2Pc_3) forming part of the first layer[215]. The growth of molecules in a second layer (first option with 0.4nm height) indicates that the molecule-molecule interaction pins the molecule and prevent them (at least partially) to move to island borders. Such type of growth concerning the second $TbPc_2$ layer has been also observed on Au(111) and Cu(111) surfaces[216].

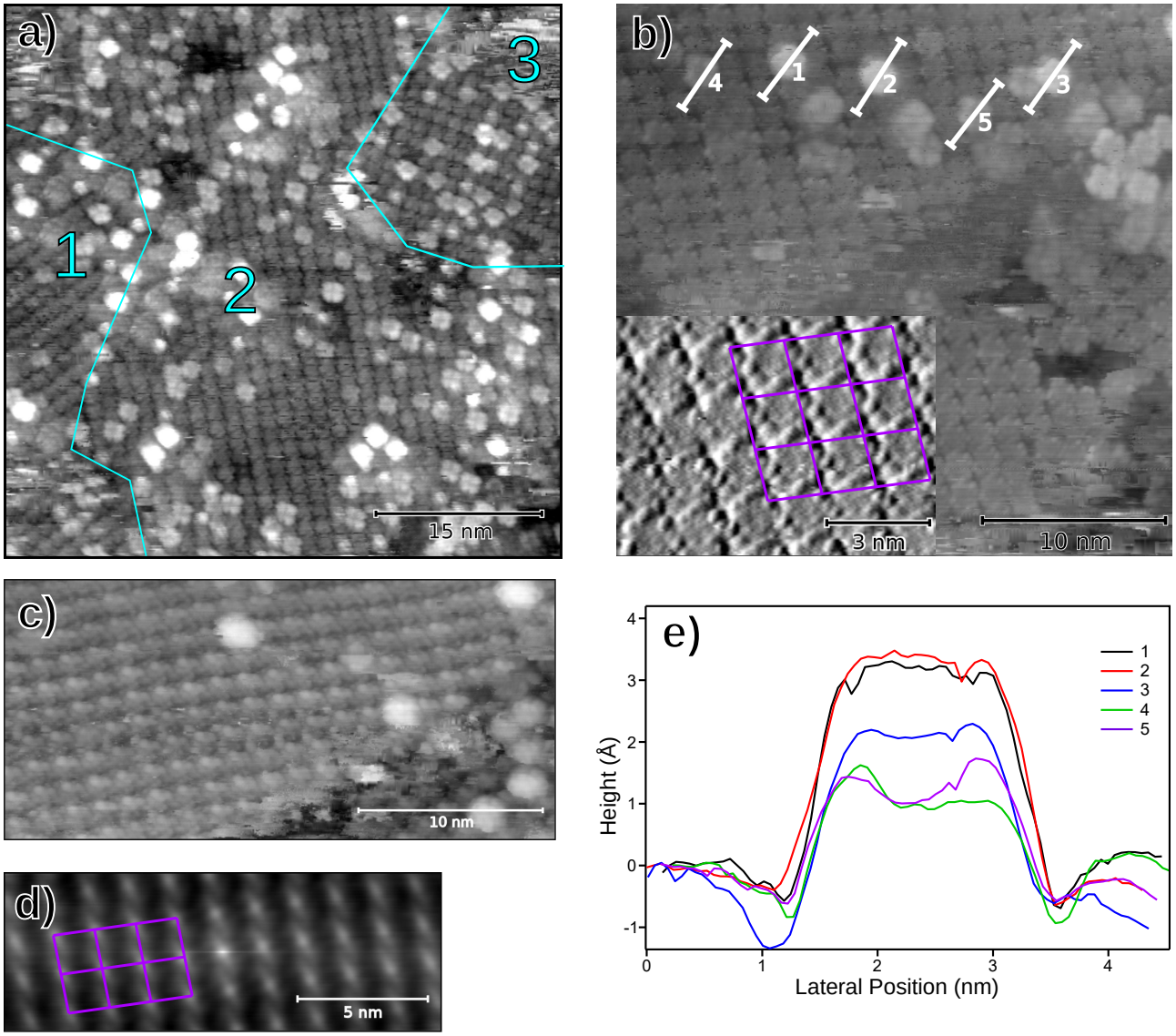

Figure 89: STM images of 1 ML of $TbPc_2$ on $HoAu_2$. a) Area of the sample revealing three different rotational domains, the domain borders are marked in cyan. (image size 50×50nm², U = 1V, I = 0.3nA) b) Area of the sample of a single domain for an incomplete molecular layer (image size 30 ×30nm², U = 1V, I = 0.3nA). Although the layer is not complete, second layer molecules and broken or triple-decker formation can be observed. The zoom (inset) reveal the molecular arrangement. c) Large scan area with a single domain of the $TbPc_2$ layer on $HoAu_2$ (image size 30×15nm², U = 1V, I = 0.3nA). d) SCF transformation applied to the STM micrograph shown in c) with the molecular lattice marked in purple. e) height profiles taken along the paths marked in b).

For the case of $TbPc_2$ on $EuAu_2$ we do not observe the same diffraction pattern and unit cell of the $TbPc_2/HoAu_2$ system. Instead, a ring-like feature is detected. Such a LEED pattern reveals the existence of an average distance between the molecules, but does not show preferential ordering of the molecules. This ring can be produced in several ways. First, it can indicate an amorphous growth of the layer. In this case, the average distance between the molecules will be fixed, but slight distortions in the angles between the molecules would prevent the formation of a periodic layer. A second option is the formation of periodic domains, but with the domains not presenting preferential

directions. As a result of such an arrangement, the seen ring would be formed by the superposition of spots corresponding to many domains oriented in all possible directions. Figure 90 shows the evolution of the LEED pattern for different evaporation times, detecting the formation of a ring pattern after 20 minutes of evaporation. After 30 minutes, the ring around the (0,0) diffraction spot becomes sharper. If the evaporation continues, the ring becomes again blurrier, indicating that a second layer is growing on top of the first layer that did not reveal sharp spots. The $TbPc_2$ growth on $EuAu_2$ contrasts with the ordered growth observed on $HoAu_2$. A possible explanation for such difference could be a difference in the interaction with the alloy due to the divalent character of Eu. The lack of one electron in the valence band of the substrate could change the absorption distance or modify the energy difference between the adsorption positions, causing that the molecule does not find preferential growth positions or directions. A similar difference in molecule adsorption due to divalent character of the RE in the substrate surface alloy was also seen for CuPc growth on $YbAu_2$. From the relation of the ring radius R and the spot distances of the $EuAu_2$ substrate, we can extract roughly R = 1.6nm. This value exceeds slightly the $TbPc_2$ lattice constant on $HoAu_2$. This means that molecules are not close enough to order. We also carried out STM measurements of the $TbPc_2/EuAu_2$ system. Nevertheless, images were not conclusive and revealed blurry images. We assign this fact to the above mentioned mobility of $TbPc_2$ molecules. In order to overcome such mobility we tried to cool down our variable temperature STM with liquid nitrogen but even in this case, we were unable to get presentable images.

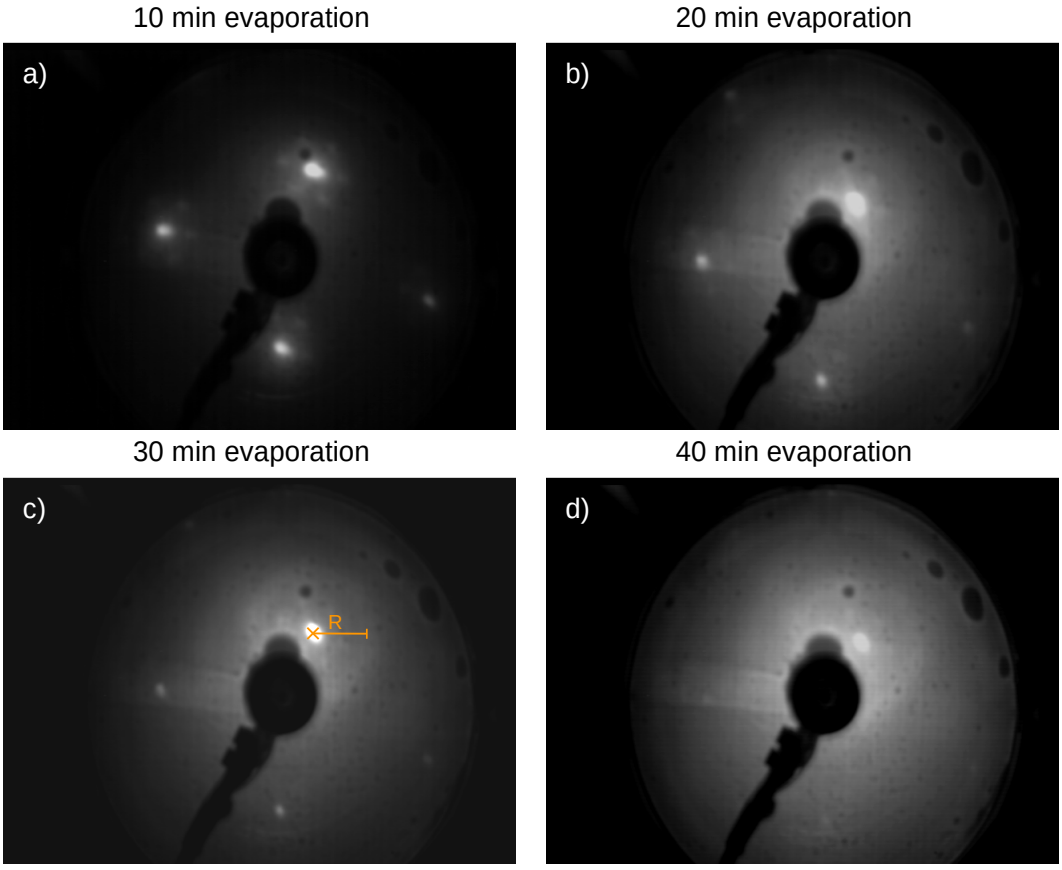

Figure 90: Evolution of the LEED pattern as a function of evaporation time for $TbPc_2$ molecules on $EuAu_2$. a) 10 min evaporation, the substrate LEED spot intensity diminishes. a) 20min evaporation, the molecules start to form a blurry ring, marking an average distance R between the molecules. c) 30min evaporation, the molecules ring becomes sharper, while the substrate spots are barely visible. We considered this thickness as a ML of molecules. d) 40min evaporation, the molecules ring becomes more blurry, indicating that the order of molecules has degraded. The substrate spots have nearly vanished. This indicates an excess of molecules of the first layer and formation of molecules on top. The evaporator was kept running constantly all time. The evaporation rate was calibrated prior to this experiment on Au(111) to form a $TbPc_2$ layer in 30min on Au(111). LEED energy was set to 20eV.

7.2.2 Electronic structure

The valence band of the $TbPc_2$ molecules on the $REAu_2$ surface alloys has been studied by ARPES photoemission at our home lab ($TbPc_2/HoAu_2$) and at Cassiopée beamline in Soleil synchrotron ($TbPc_2/EuAu_2$) with the sample cooled to 80K (liquid N_2). Figure 91 shows the photoemission results for normal and 45° emission angles of 1ML of $TbPc_2$ on $HoAu_2$ and $EuAu_2$ as well as on pure Au(111). The latter one is used as a reference to estimate and compare changes in the valence band structures among the $TbPc_2/REAu_2$ samples. In the reference case, i.e., $TbPc_2$ on Au(111), we see three different molecular levels at 0.44eV, 0.87eV and 1.11eV binding energy. According to the literature the molecular level at 0.44eV is assigned to the single occupied molecular orbital

(SOMO)[217–219]. The other two molecular levels at 0.87eV and 1.11eV are assigned to the HOMO levels HOMO and HOMO-1. There are several explanations for the presence of two HOMO levels. The first possibility is that in the sample there are not only $TbPc_2$ molecules but also the mentioned TbPc or Tb_2Pc_3 molecules that present different molecular orbitals. The possibility of coexistence of both molecules on the surface was seen on the STM images of our $TbPc_2/HoAu_2$ sample (section 7.2.1) and was reported by several authors in the literature[214,215]. Another possibility is the change of the alignment of levels (or even charging of the molecule) in a compact phase (ordered islands) with respect to isolated molecules. This has been also discussed in the literature[218]. According to the latter manuscript, the peak at 0.87eV would correspond to the HOMO of the isolated molecules while the ones at 0.44eV and 1.11eV would correspond to SOMO and HOMO of the ordered molecular layers. In our figure we will use this last assignation to the levels without confirming or rejecting one of the two options. Our investigations of $TbPc_2$ on $HoAu_2$ shows a similar electronic structure, but only with two molecular levels at 0.40 eV (SOMO) and 1.20 eV (HOMO). The intermediate level seen as on pure Au is missing. The exact HOMO positions have been obtained after peak fit analysis using Lorentzian peaks. The SOMO-HOMO difference here amounts to 0.8eV similar to the Au case (~0.7eV). We therefore interpret the level as the named SOMO and HOMO features. In the case of $TbPc_2$ on $EuAu_2$ we detected three molecular features like in the case of Au(111). These features are found at 0.1eV, 0.6eV and 1eV. The first molecular level could be again related to the SOMO and the other two levels to two different HOMO levels of TbPc (or Tb_2Pc_3) and $TbPc_2$ species. The two HOMO contributions could be also caused, like in $TbPc_2$/Au(111), by two phases, one of isolated molecules with an HOMO at 0.6eV binding energy and a compact phase with a HOMO at 1eV. The $TbPc_2$ molecules resulted particularly fragile under UV radiation. Therefore, after the exposition of $TbPc_2$ to the UV light for the photoemission measurements, after several minutes the molecular damage was so strong that the molecular levels had disappeared. Such a behavior was not observed for CuPc. A series of ten scans was measured on the $TbPc_2/EuAu_2$ samples, where each scan took 2-3 minutes. Then the sample position was slightly changed and the series was repeated. Several new positions were used to get enough statistics for the presented photoemission data. The first scan on each new position still revealed molecular features, but the following scans clearly indicate a gradual degradation of the molecular levels. Finally, at the last scan the molecular levels were completely gone, and only the features of the substrate $EuAu_2$ were observed. In order to better observe the molecular levels of $TbPc_2$ in this system a subtraction of the first and last scan (with and without molecular features) has been carried out. The result is shown in the bottom part of Figure 91c) and gave rise the levels mentioned above.

It is observed that the molecular levels measured in the case of $TbPc_2$/Au(111) are not the same than the $TbPc_2$/REAu(111) alloys, particularly in the case of Eu. The shift in the energy levels between the surfaces can be explained to different effects that take place at the interface and are related to several effects including the possibility of charge transfer, change of the surface dipole due to Pauli push-back effect, or another vacuum level alignment. This difference could be accentuated in the case of $EuAu_2$, as its divalent character could cause a higher work function reductions with respect to Au(111) or $HoAu_2$. Due to the strong character of the change and the few studies available on the $TbPc_2$ molecule, further experiments and simulations will be necessary to draw better conclusions.

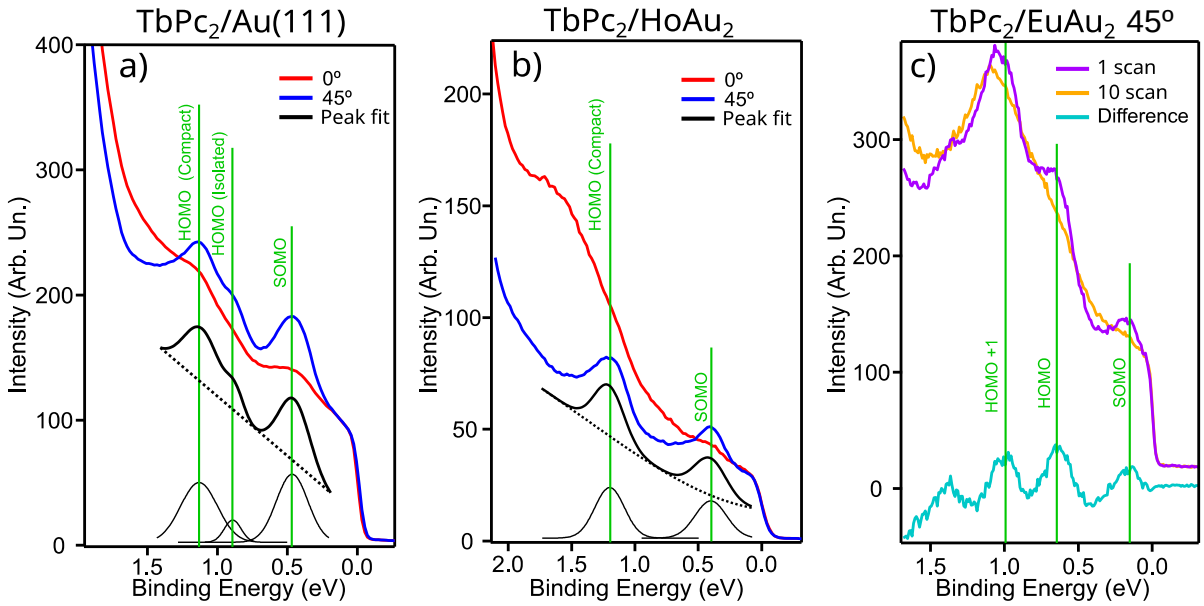

Figure 91: Photoemission measurements for $TbPc_2/REAu_2$ samples in comparison to $TbPc_2$/Au(111). a), b), c) Photoemission results at different emission angles θ=0° and 45° of 1ML $TbPc_2$ on Au(111), $HoAu_2$ and $EuAu_2$ surfaces. In the first two measurements, $TbPc_2$/Au(111) and $TbPc_2/HoAu_2$ the peaks were identified by peak fit analysis for the spectra at 45º emission angle. Both measurements have been carried out with He I_α (21.22eV) light. In the case of $EuAu_2$, the $TbPc_2$ molecule levels were identified by subtracting the beam damaged spectra (10º scan), experiments were carried out using a photon energy of 26eV.

7.2.3 Magnetic properties

7.2.3.1 $TbPc_2/HoAu_2$ system

XAS and XMCD measurements were performed on the $TbPc_2/HoAu_2$ sample at 6T and 2K in both IP and OOP geometries at BOREAS beamline of ALBA synchrotron in Barcelona. Here, specially the Tb and Ho $M_{4,5}$ absorption edges were considered. The results of the experiment are displayed in Figure 92. The non-flat background is likely due to the long-range EXAFS fluctuations of the Au N_1 transition. In the XAS spectra one observes a larger intensity in OOP geometry than in the IP one. The XAS peak structure in each geometry reveals different contributions. This probes that the $TbPc_2$ molecules are flat laying, as in the case of CuPc. The bonds of the Tb to the Pc corona causes a strong anisotropy of the Tb charge distribution, and hence the absorption probability of each subshell between different measurement geometries is not the same[42,84,214]. Additionally, it is observed that the dichroic signal is about three times more intense in the OOP measurement geometry than in the IP geometry in Tb M_5. The comparison to the Ho $M_{4,5}$ edge performed at 6T and 2K in OOP geometry is shown in Figure 92. The shape of the XMCD spectra measured at the Ho edge is the same as in the case of clean $HoAu_2$ shown in section 5.3.1. This indicates that Ho^{3+} valence state is preserved under molecule absorption. As expected, for this 6T applied field, both magnetizations follow the applied magnetic field.

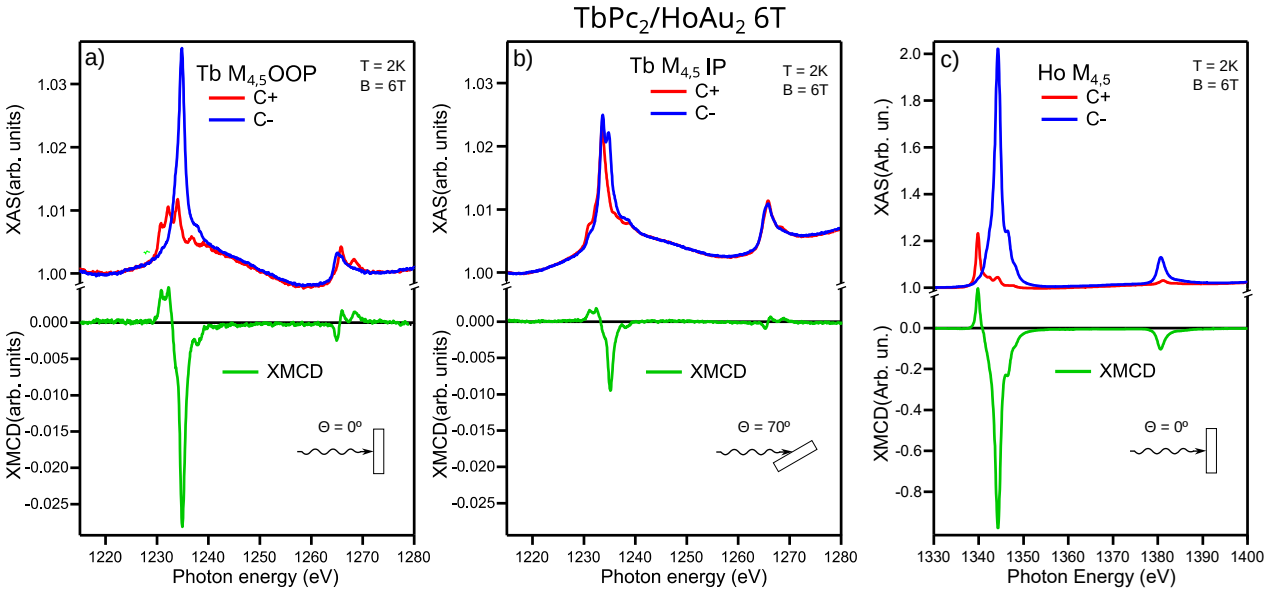

Figure 92: $M_{4,5}$ XAS and XMCD spectra of $TbPc_2/HoAu_2$ measured at 6T and 2K. a) OOP and b) IP geometry at Tb $M_{4,5}$ absorption edge, c) OOP geometry at Ho $M_{4,5}$ absorption edge. XAS of C+(C-) light are shown in red (blue), the difference XMCD spectra [C+]-[C-] are shown in green.

Figure 93 shows the XMCD loops of $TbPc_2/HoAu_2$ and compares it to $TbPc_2$/Au(111). Measurements were carried out at the Tb M_5 edge and are marked in red for $TbPc_2/HoAu_2$ and in black for $TbPc_2$/Au(111). Measurements at the Ho M_5 edge for the TbPc/$HoAu_2$ system are marked in blue. The $HoAu_2$ loops coincide with the loops measured on the clean $HoAu_2$, indicating that the adsorption of $TbPc_2$ molecules on this surface does not have much effect on the magnetic behavior of the $HoAu_2$ alloy.

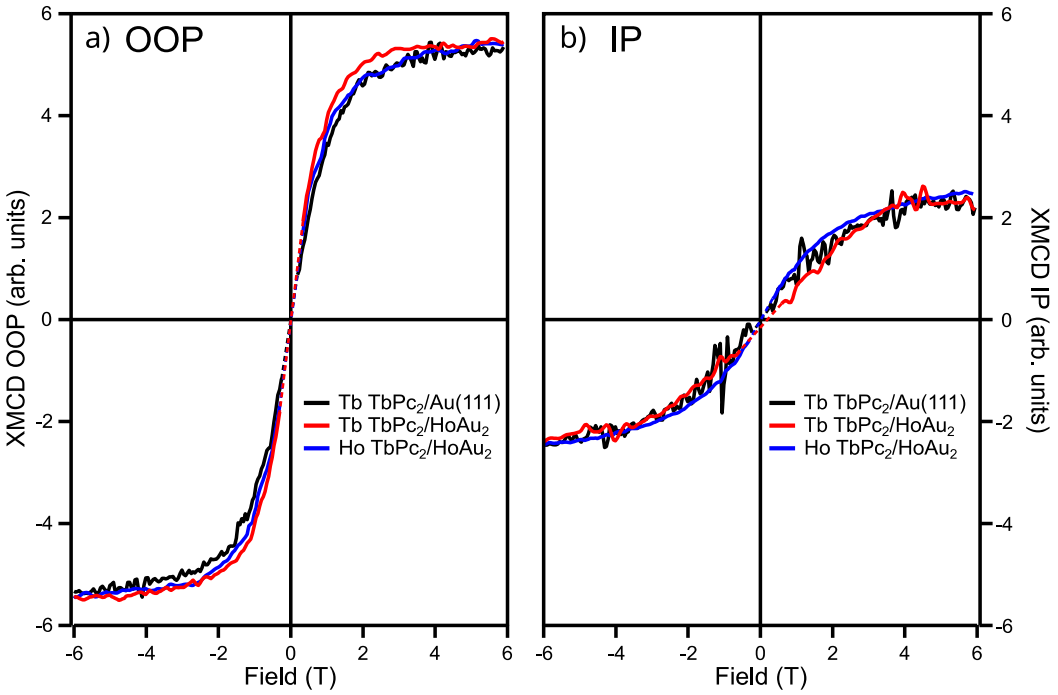

Figure 93: XMCD Hysteresis loop of $TbPc_2/HoAu_2$ compared to $TbPc_2/Au(111)$ measured at 2K on the energy position corresponding to the maximum peak of the M_5 transition for Ho and Tb. The loop of Ho (blue) and Tb (red) of the $TbPc_2/HoAu_2$ are close to the one of Tb (black) on Au(111).

Considering the magnetic behavior of $TbPc_2$/Au(111), it is important to remark that $TbPc_2$ on this substrate shows a strong anisotropy with a clear easy axis of magnetization in the OOP direction. Moreover, it shows a paramagnetic-like behavior but without any measurable opening in the hysteresis loop. The latter indicates that the contact with the metal quenches the remanence of the molecule. This quenching happens because the contact to the metal opens many paths to exchange angular momentum, which is equivalent to opening channels for the excited magnetic state to relax[87]. In the case of $TbPc_2/HoAu_2$ (red line) the loop reveals a small deviation from the Ho loop. Furthermore, it does not match perfectly the $TbPc_2$/Au(111) loop. The $HoAu_2$ substrate seems to induce slight modifications, this could attributed to an enhancement of the anisotropy of $TbPc_2$ due to a soft coupling with the substrate. But the measured difference is close to the assumable error of the experiment and would need to be improved in order to draw conclusions. It should be emphasized that pure $HoAu_2$ and $TbPc_2$ loops look already very similar, which is very unfortunate and makes it even more difficult to distinguish possible couplings between the layers. Therefore, a systems with larger differences between pure $REAu_2$ substrate and $TbPc_2$ loops has to be chosen. This is the case for $EuAu_2$ that we will discuss next.

7.2.3.2 $TbPc_2/EuAu_2$ system

XAS and XMCD measurements performed at 6T and 2K in OOP geometry measured at the Tb $M_{4,5}$ and Eu $M_{4,5}$ edges on the $TbPc_2/EuAu_2$ interface are shown in Figure 94. Again, the non-flat

background is likely to come from EXAFS of Au N_1 and Eu $M_{4,5}$. Due to the low amount of Tb atoms (approx. 0.5 atom/nm^2) the associated signal is relatively small and any background becomes very pronounced. The shape of the XMCD spectra of Eu is the same as it is in the clean $EuAu_2$ shown in section 5.3.4, which indicates that the Eu^{2+} valence state is preserved and no degradation has occurred during the deposition of the molecule.

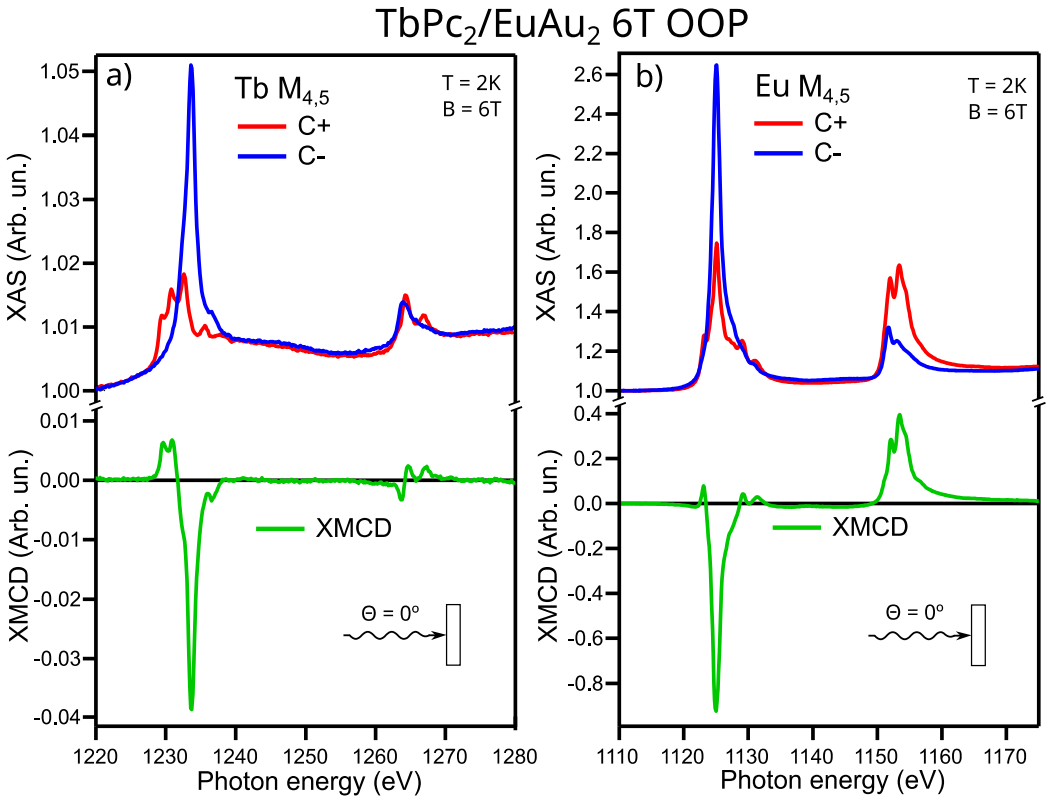

Figure 94: $M_{4,5}$ XAS and XMCD Spectra of $TbPc_2/EuAu_2$ measured at 6T and 2K. a),b) OOP measurements of Tb and Eu $M_{4,5}$ edges, respectively. The XAS spectra with C+(C-) circular polarization are marked in red (blue), green is used for the dichroic XMCD spectra [C+]-[C-].

Figure 95 shows the XMCD loops measured on $TbPc_2/EuAu_2$ and the $TbPc_2$/Au(111) interfaces. Measurements were performed at the Tb M_5 and Eu M_5 edges. Tb M_5 loops are represented in red for $TbPc_2/EuAu_2$ and in black for $TbPc_2$/Au(111). Additionally, in blue the Eu M_5 loop of the $TbPc_2/EuAu_2$ system is added. Due to the low signal-to-noise ratio of the Tb measurements, the loops in this case were measured manually point-by-point, that means that the data was acquired measuring the spectra at each field value. This way of measurement also solves the normalization problems close to zero applied field of the fast loop. The continuous loop corrected by these data points is shown in the inset. First, the Eu M_5 loops measured here coincides with the loops measured for the clean $EuAu_2$ shown in section 5.3.4. This indicate that the absorption of the $TbPc_2$ molecules on the surface does not have strong effects on the magnetic behavior of the $EuAu_2$ alloy. Second, it is very important to note the difference between the Tb M_5 loops of $TbPc_2$ in the systems $TbPc_2$/Au(111) and $TbPc_2/EuAu_2$. On $EuAu_2$ we see a strong rectangular like shape of the Tb loop. Especially, both samples reveal a different magnetization behavior below 1T. In the Tb loop

measured for $TbPc_2$/Au(111), the magnetization starts to decrease fast below 1T and at zero field, it barely has any magnetization. Meanwhile, in the loop measured on $TbPc_2/EuAu_2$ the magnetization starts to decrease only at 0.2 T and shows a clear remanence. For negative applied fields, it is seen that the magnetization switches direction following the magnetization of the $EuAu_2$ substrate. The zero-magnetization crossing takes place at -0.05 T. All these fact reveal that $TbPc_2$ is ferromagnetically coupled to the $EuAu_2$ substrate and follows its magnetization. Remember, there were only faint indications of a possible ferromagnetic coupling of $TbPc_2$ on $HoAu_2$, but here we observe a clear coupling although of weak intensity.

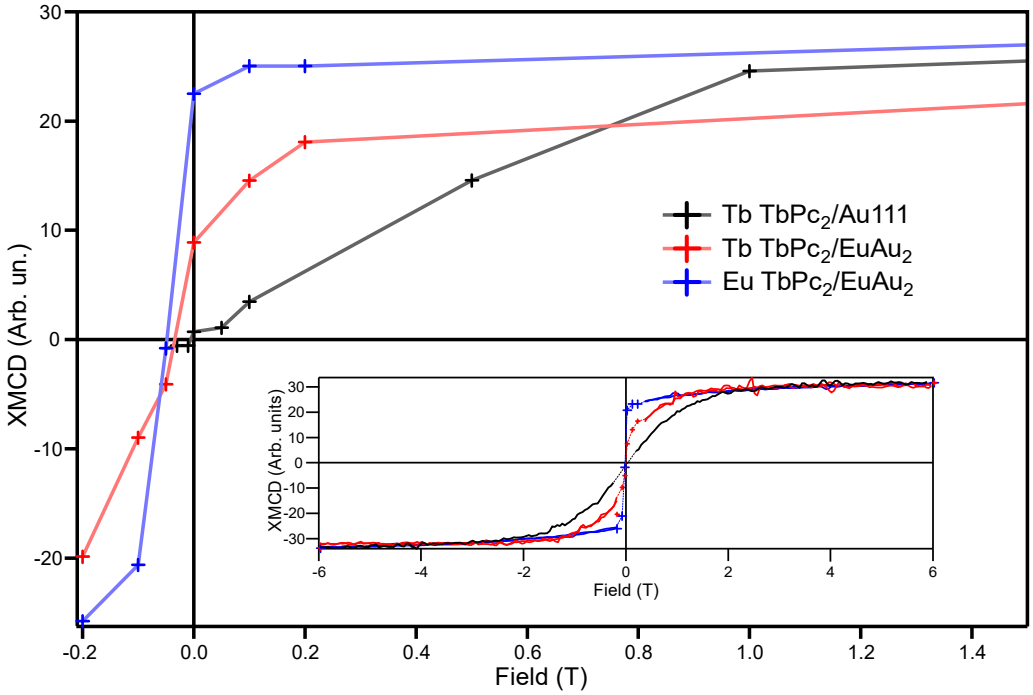

Figure 95: XMCD Hysteresis loop of $TbPc_2/EuAu_2$ compared to $TbPc_2$/Au(111) measured at 2K on the main peak of the M_5 transitions of Eu and Tb. The loops of Eu (blue) and Tb (red) of $TbPc_2/EuAu_2$ reveal weak ferromagnetic coupling and differ to Tb (black) of $TbPc_2$/Au(111). The inset shows the continuous scan on Eu and Tb M_5 signals of $TbPc_2/EuAu_2$ and $TbPc_2$/Au(111).

In order to prove the remanence, figure 96 displays the spectra taken at 6T, 0.2T and 0T. Here we can see in more detail the XMCD dichroism of each species (Tb, Eu) at selected fields. The XMCD dichroism of the Tb doesn't disappear at low field, but we see half the saturation magnetization at 0.2T and a quarter at 0T. In Eu, at 0.2T we have a 75% of the saturation magnetization while at 0T the magnetization is reduced to 66%. This confirms that Tb is coupled ferromagnetically to Eu, even if the coupling is much weaker than on 3d magnetic ordered substrates[80,92,93].

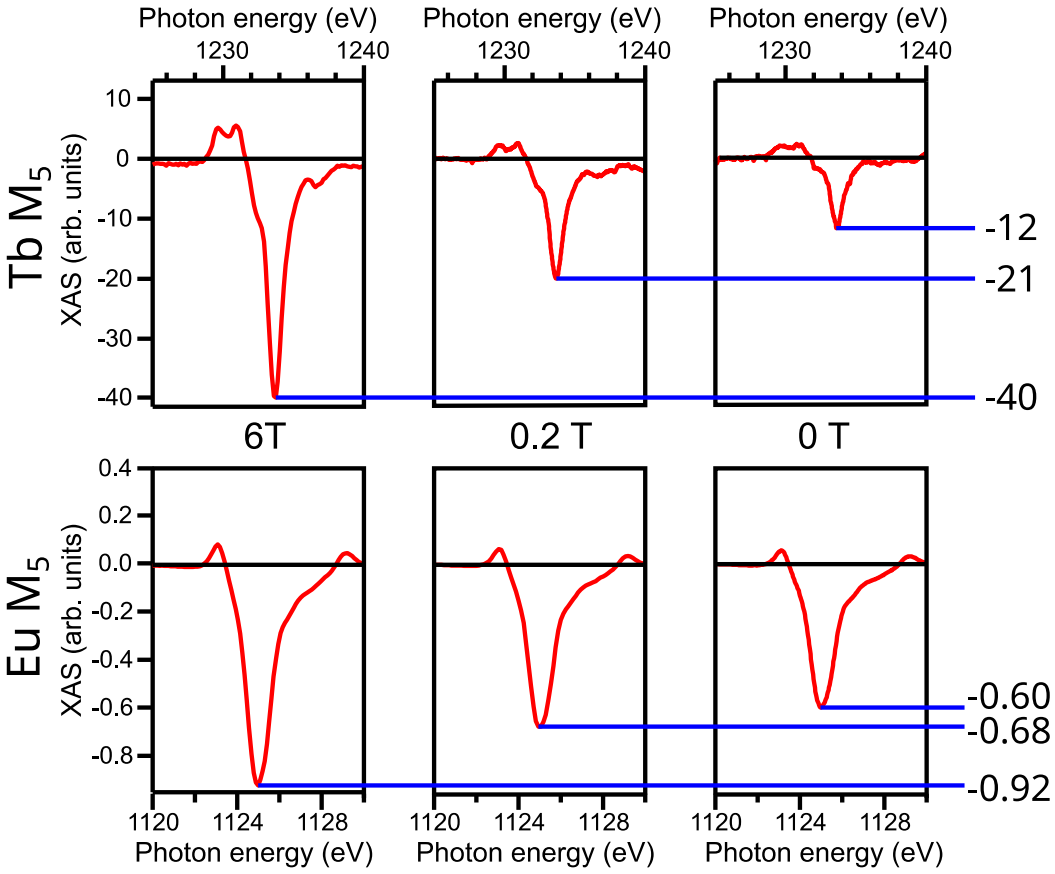

Figure 96: Detailed XMCD spectra at several applied magnetic fields (6T, 0.2T and 0T) for the M_5 transitions of Tb and Eu in OOP geometries in $TbPc_2/EuAu_2$. The measurements were performed at 4K.

Following the same considerations as in the $CuPc/REAu_2$ systems, that was assuming that the coupling of the molecule to the surface is isotropic and depreciating the coupling between molecules we will apply the same Hamiltonian of that system (Eq. 29). If we now apply it to zero field and we only consider as degree of freedom for the magnetization the OOP direction, we can simplify it to:

$$H = -J \cdot \vec{S}_M \cdot \vec{S}_S \tag{37}$$

Remember that $TbPc_2$ has only two possible states of magnetization, $J = \pm 6$. We can now apply the Maxwell-Boltzmann statistics (or what is the same, the Boltzmann model for a two-states system) and can calculate the exchange energy at the measurement temperature:

$$\frac{M_M(0)}{M_M(F_{sat})} = \frac{M_S(0)}{M_S(F_{sat})} \cdot \tanh\left(\frac{J}{k_B \cdot T}\right) \tag{38}$$

Here, $M_M(0)$ and $M_S(0)$ represent the magnetization at zero field of the molecule and the substrate, respectively, and $M_M(F_{sat})$ and $M_s(F_{sat})$ the magnetization of the molecule and substrate at saturation. T is the temperature, k_B the Boltzmann constant and J the coupling

energy. From the magnetization loops we can extract values $\frac{M_M(0)}{M_M(F_{sat})}=0.26$, $\frac{M_S(0)}{M_S(F_{sat})}=0.66$ at T = 2 K. As a result, we calculate a coupling energy of 35 μeV between $TbPc_2$ and $EuAu_2$. This coupling appears in $EuAu_2$ while for $HoAu_2$ the very small (if any) value is probably due to much higher spin polarization on the valence band of the alloy due to the hybridization to the Eu 4f orbital, as was shown in section 5.2.2.2.

7.2.3.3 $TbPc_2$/ $DyAu_2$ system

XAS and XMCD measurements were performed at 6T and 4K in OOP for the Tb and Dy transitions for the $TbPc_2/DyAu_2$ interface and are shown in Figure 97. As in the case of $TbPc_2/HoAu_2$, the shape of the XMCD spectra is consistent with the +3 valence states of Tb and Dy expected for the molecule and substrate materials[166]. The shape of the Dy XAS and XMCD spectra before and after molecular deposition is identical. This means that the magnetic state and anisotropy of $DyAu_2$ are unchanged.

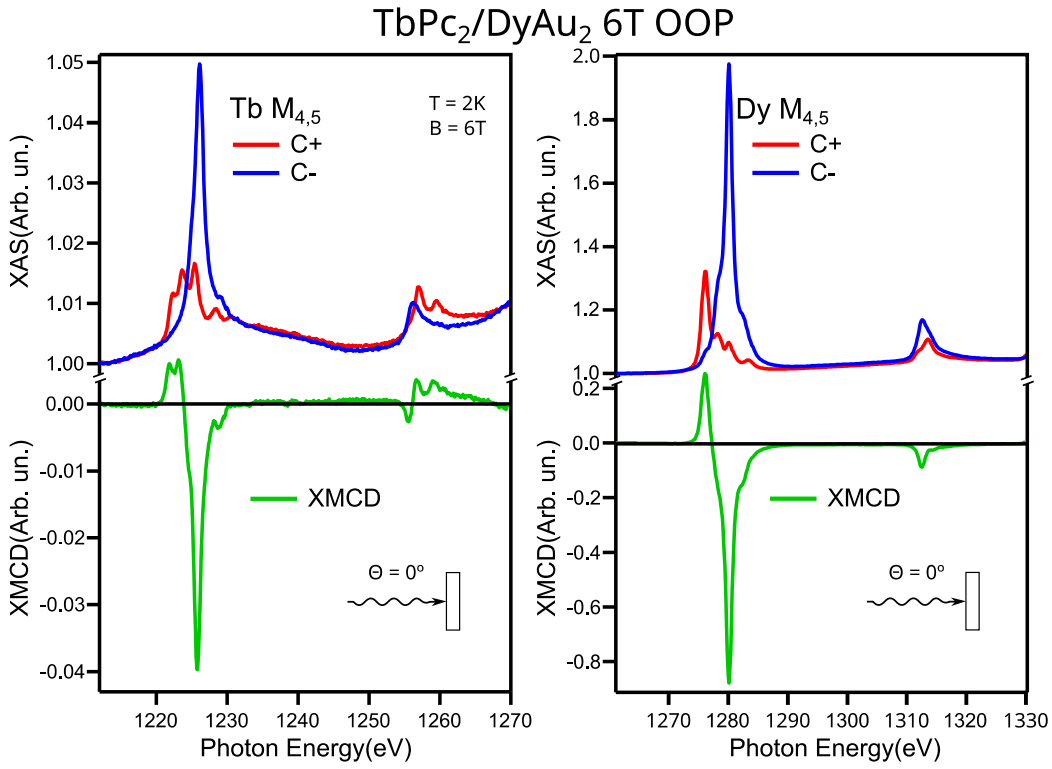

Figure 97: XAS and XMCD spectra of $TbPc_2/HoAu_2$ measured at 6T and 2K. a),b) OOP measurements of Tb and Dy $M_{4,5}$ transitions. We mark in red (blue) spectra for C+(C-) circular polarization, in green the dichroic XMCD spectra [C+]-[C-].

Figure 98 shows the XMCD loops of $TbPc_2/DyAu_2$. The measurements performed on the Dy and Tb M_5 edges are marked in blue and red, respectively, while the Tb loop of $TbPc_2$/Au(111) is marked in black. The $DyAu_2$ loops are similar to the ones measured for clean $DyAu_2$. The latter indicates that

the absorption of the $TbPc_2$ molecule on top does not destroy the ferromagnetism of the $DyAu_2$ surface alloy. The loops measured on the Tb M_5 edge of $TbPc_2/DyAu_2$ and $TbPc_2/Au$ are again similar. This indicates that $TbPc_2$ molecule is not affected by the adsorption on the $DyAu_2$ substrate. Here, we have the same unfortunate situation as before mentioned for the $HoAu_2$ case. When the magnetization loops alone are nearly identical, a possible coupling is very difficult to observe. Nevertheless, here we believe to see that the alloy and the $TbPc_2$ molecules do not reveal magnetic coupling. This observation is based on the facts that the substrate loop is unchanged and the molecular loop looks similar as on Au(111).

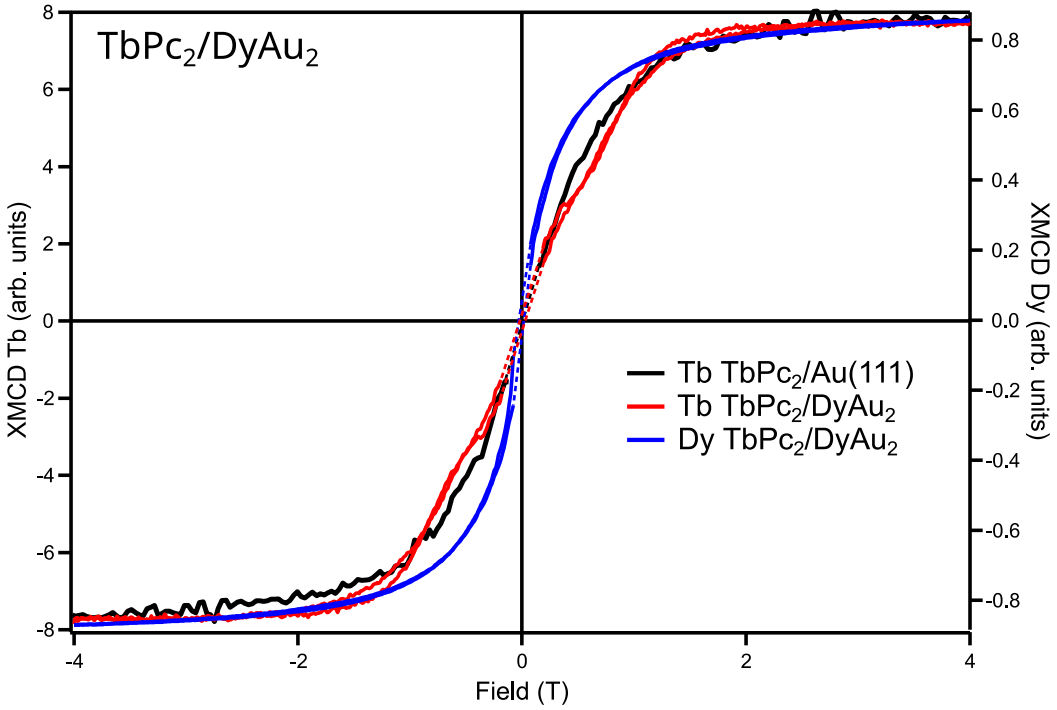

Figure 98: XMCD Hysteresis loops measured at 4 K on the $TbPc_2/DyAu_2$ surface. Both loops were measured at the M_5 transition of Dy and Tb. The loops of Tb (blue) and Dy (red) reveal clearly different behavior in the range of applied magnetic fields between 0 and 1T indicating that there is no magnetic coupling between molecule and substrate. For comparison, the pure $TbPc_2$ hysteresis loop on Au(111) is added in black.

The Curie temperatures of clean $DyAu_2$ surface alloy and the same substrate covered by the $TbPc_2$ molecular layer have been determined by the temperature dependence of the hysteresis loops. Figure 99 displays these measurements and the Arrot plot analysis (see inset of Figure 99). The loops show a smooth transition from a “square shape” toward linear paramagnetism as the temperature is increased. The Curie temperatures T_C have been extracted using the Arrot plot methodology (see section 5.3.2) and is shown in Figure 99b). The T_C is extracted as 24.5K and 27.3K, respectively, for the uncovered and molecular covered cases. This implies a very surprising T_C increase of ~3K upon deposition of $TbPc_2$. It contrasts to an observed Curie temperature decrease after PPP molecule adsorption on $GdAu_2$[51]. As a coupling to the $TbPc_2$ molecules to $DyAu_2$ has already been discarded, the T_C change can only be attributed to charge redistribution on the valence

band. Further studies will still be necessary to establish the exact nature of this change.

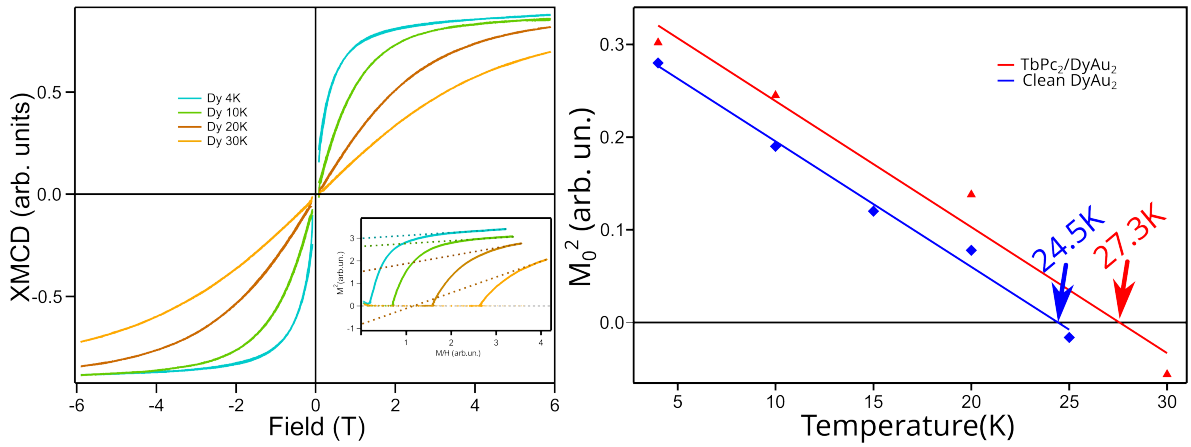

Figure 99: a) Temperature dependence of hysteresis loops in OOP geometry for Dy M_5 on $TbPc_2/DyAu_2$ sample. The inset shows the Arrot plot analysis. b) Fits of the resulting zero-field points in the Arrot plot analysis. The Curie temperature of $DyAu_2$ increases by approx. 3K after molecular adsorption.

Some final conclusion of the chapter should be given for the behavior of the $TbPc_2/REAu_2$ interfaces. First, deposition of the molecules onto $REAu_2$ surface alloys opens decoherence channels quenching the remanence of the $TbPc_2$ molecule observed on isolating surfaces like MgO[89] or SiO_2[220]. The second conclusion we can draw is that the magnetic behavior of the RE-Au_2 surface alloys is stable enough to not be affected significantly by the physisorption of the $TbPc_2$ molecules even in one case we observe a slight increase of the Curie temperature. Third, the magnetic coupling of the $TbPc_2$ molecule to the magnetic moments of $REAu_2$ is weak and conditioned by the valency of the RE metal of the alloy, being ferromagnetic in the case of divalent RE ($EuAu_2$) and nearly non-existent in the case of trivalent $REAu_2$ ($HoAu_2$ and $DyAu_2$). We additionally observed a slight increase of the $TbPc_2$ anisotropy after absorption on $HoAu_2$ surface.

8 Conclusions

In this thesis we have studied the magnetic properties of the RE-NM_2 surface alloys and their interfaces with magnetic molecules. In order to do so, two noble metal surfaces were used, namely Au(111) and Ag(111). As RE, we have chosen Sm, Eu, Gd, Ho, Dy and Yb. The molecules that we used for the molecule-RE-NM_2 interaction were CuPc and $TbPc_2$.

All RE-NM_2 surface compounds display a structure that can be described as a $(\sqrt{3}\times\sqrt{3})R30°$ reconstruction with a Moiré modulation. However, we find exceptions in two systems, $EuAu_2$ and $HoAg_2$, which do not reveal the same surface reconstruction. In the $EuAu_2$ surface it is found that the distortion induced by the larger atom radii of Eu cannot be relaxed by the Moiré lattice formation. In this $EuAu_2$ system, the surface stress is relaxed by the formation of a "vacant" lattice. In the case of $HoAg_2$, the Moiré modulation is exchanged by formation of almost hexagonal tiles separated by dislocation lines that show a long range order but without a discernible short range order.

In terms of electronic structure, the RE-NM_2 surface compounds can be classified according to the valence state of the RE in the compound. XPS and XAS spectroscopy measurements have shown that Sm (almost), Gd, Ho and Dy have a trivalent valence state of the surface compounds RE-NM_2, while Eu and Yb (almost) reveal a divalent valence state. We have found that the valence state of the RE atoms has a direct implication in the electronic structure of the surface compounds. In the case of the trivalent ones, we observe that they share the same electronic structure formed of s and d bands in $SmAu_2$, $GdAu_2$, $HoAu_2$, and $DyAu_2$. Calculations have shown that the common electronic structure found in these compounds is responsible for the introduction of an unexpected strong band anisotropy that favor an IP easy axis of magnetization. In the case of the compounds using Ag(111) substrate we also observe that the trivalent RE atoms display a shared band structure formed by s and d orbitals. The latter is the case of $SmAg_2$, $GdAg_2$ and $HoAg_2$. Additionally, by high resolution angle resolved photoemission we observe that the compounds $GdAg_2$ and $SmAg_2$ display a band opening of the s,d bands below the Curie temperature T_C that depends on the magnetization direction (IP in $GdAg_2$ and OOP in $SmAg_2$). This is a characteristic feature of these alloys that indicates the IP band contribution to the anisotropy of the RE-Au_2 and RE-Ag_2 compounds.

In the case of the compounds formed with divalent REs, namely $EuAu_2$ and $YbAu_2$, we have detected two fundamental characteristics that differ from the case of the trivalent REs: i) the lack of one electron in the valence band induces a downward shift of the Fermi level and ii) the 4f band is closer to the Fermi level and hybridizes with the valence band. This creates a heavy fermion like band. In the particular case of $EuAu_2$, both characteristics induce a strong band anisotropy favoring an OOP easy axis. In the case of $YbAu_2$, the divalent state leads to a complete 4f shell and the removal of any magnetic behavior.

Concerning the magnetic properties, it has been shown that the electronic 2D confinement found in the surface alloys produces a giant anisotropy. This anisotropy is of magneto-crystalline nature and it has two different contribution: one is the crystal field, which is determined by the orbital shape of the RE and the substrate chosen, Au(111) or Ag(111). The second is the band anisotropy,

determined by the valence state of the REs. For the crystal field contribution it has been found that in $SmAg_2$ and $HoAg_2$ the easy axis is interchanged with respect to $SmAu_2$ and $HoAu_2$ respectively, indicating that the quadrupolar term induced by the structure has changed its sign. The sum of both contributions define the total anisotropy and the easy axis of magnetization of the RE surface compounds. $GdAu_2$, $SmAu_2$ and $HoAg_2$ reveal IP easy axis. On the other hand, $HoAu_2$, $DyAu_2$, $EuAu_2$ and $SmAg_2$ have an OOP easy axis. Specially remarkable is the huge coercivity observed in $SmAg_2$, caused by the giant anisotropy that makes it behave as a 2D Ising ferromagnet. In all RE surface compounds mentioned above, their Curie temperature T_C was below 35K, without a clear correlation with the RE or substrate. It should be mention that the extraordinary high T_C values found in $GdAg_2$ is a quite particular case. Other compounds like $SmAg_2$ and $HoAg_2$ did not show T_C values of such magnitude despite being alloyed with Ag(111).

After the growth of the organic molecules (CuPc and $TbPc_2$) on the $REAu_2$ surfaces we have found different scenarios depending on the molecule. The structure of the CuPc ML deposited on the alloys is well ordered and commensurate with the substrate. Photoemission and XPS measurements reveal that CuPc is physisorbed on the $REAu_2$ surfaces (RE: Ho, Gd, Yb) without any sign of charge transfer between molecule and substrate. However, a Pauli repulsion between CuPc and the substrates was detected. We noticed that the behavior of the hybrid interface is in the Schottky–Mott limit, which means that the molecule orbitals are pinned to the vacuum level. Moreover, we observe a shift of the CuPc molecular levels that depends on the work function of the pristine $REAu_2$ surface compounds, finding that in the case of the trivalent REs (Ho and Gd) the particular shift of the molecule levels of CuPc gives place to an ambipolar injection barrier. Considering the magnetic behavior of the molecules grown on $REAu_2$ substrates, it has been demonstrated that the CuPc shows a weak antiferromagnetic coupling with the $GdAu_2$ and $HoAu_2$ substrates. The strong OOP anisotropy of the CuPc molecule is only slightly modulated by the easy axis of the alloy substrate on which it is adsorbed.

$TbPc_2$ molecules grow in a different manner. This molecule is much larger in size than CuPc and therefore the molecule-molecule interaction becomes much more important. In the case of $TbPc_2$ on $HoAu_2$ we observe a commensurate growth with slightly less density of molecules than on CuPc. Often, and independent of the amount of $TbPc_2$ evaporated, isolated molecules can be found on top of the $TbPc_2$ islands (second layer formation), indicating that the molecule-molecule interaction via Pc planes is quite strong inhibiting them to move toward the clean substrate. In the case of $TbPc_2$ ML on $EuAu_2$, the growth of $TbPc_2$ molecules is again different, and the molecules reveal a disordered growth that it is non commensurate with the substrates.

About the magnetic behavior of the $TbPc_2$ molecule, its high magnetic moment and high anisotropy remain also unchanged upon adsorption on the $REAu_2$ surfaces, but the remanence of the molecule is destroyed. On the trivalent $REAu_2$ surfaces, no clear sign of exchange coupling is detected. This probably results from the small spin polarization of the valence band in the alloys to which the molecule would have to couple. In the case of the divalent surface compound $EuAu_2$, $TbPc_2$ reveals a ferromagnetic coupling to the substrate. Additionally, it is observed that the adsorption of $TbPc_2$ on $DyAu_2$ induces a small but clear increase in the Curie temperature of $DyAu_2$.

In summary, in this thesis we carried out an extended analysis of the structure, electronic properties and magnetic behavior of the RE-NM_2 surface compounds and their role as substrates for the design of hybrid metal-organic interfaces. Furthermore, the electronic and magnetic properties of the prepared metal-organic interfaces have been studied, searching for the effect of specific RE atoms on the magnetic and electronic properties of the designed interfaces. The results show the robustness of the properties of the alloy, and the possibility of engineering desired magnetic properties of the alloys by simple methods, like the substitution of the RE atoms by other ones. Moreover, it has been shown that the alloying can be used for the modification of the injection barriers in metal-organic interfaces while the spin state of the molecules can be fixed by exchange coupling to the substrate. This could allow further developments in molecular spin valves. Finally, we have shown that it is possible to join the $TbPc_2$ single molecule magnet to a ferromagnetic substrate without causing coupling. This suggest that the introduction of a decoupling insulator could lead to organic spin valve devices exploiting the remanence of the $TbPc_2$ molecule.

9 Bibiography

(1) Moore, G. E. Cramming More Components onto Integrated Circuits, Reprinted from Electronics, Volume 38, Number 8, April 19, 1965, Pp.114 Ff. *IEEE Solid-State Circuits Soc. Newsl.* **2006**, *11* (3), 33–35. https://doi.org/10.1109/N-SSC.2006.4785860.

(2) Ratnesh, R. K.; Goel, A.; Kaushik, G.; Garg, H.; Chandan; Singh, M.; Prasad, B. Advancement and Challenges in MOSFET Scaling. *Mater. Sci. Semicond. Process.* **2021**, *134*, 106002. https://doi.org/10.1016/j.mssp.2021.106002.

(3) Zhang, Y.; Dong, Y.; Chen, K.; Dang, K.; Yao, Y.; Wang, B.; Ma, J.; Liu, W.; Wang, X.; Zhang, J.; Hao, Y. High-Performance Gallium Nitride High-Electron-Mobility Transistors with a Thin Channel and an AlN Back Barrier. *Appl. Phys. Lett.* **2023**, *122* (14), 142105. https://doi.org/10.1063/5.0134633.

(4) Wu, Y.; Farmer, D. B.; Xia, F.; Avouris, P. Graphene Electronics: Materials, Devices, and Circuits. *Proc. IEEE* **2013**, *101* (7), 1620–1637. https://doi.org/10.1109/JPROC.2013.2260311.

(5) Zia, R.; Schuller, J. A.; Chandran, A.; Brongersma, M. L. Plasmonics: The next Chip-Scale Technology. *Mater. Today* **2006**, *9* (7), 20–27. https://doi.org/10.1016/S1369-7021(06)71572-3.

(6) Nikitov, S. A.; Kalyabin, D. V.; Lisenkov, I. V.; Slavin, A. N.; Barabanenkov, Y. N.; Osokin, S. A.; Sadovnikov, A. V.; Beginin, E. N.; Morozova, M. A.; Sharaevsky, Y. P.; Filimonov, Y. A.; Khivintsev, Y. V.; Vysotsky, S. L.; Sakharov, V. K.; Pavlov, E. S. Magnonics: A New Research Area in Spintronics and Spin Wave Electronics. *Phys.-Uspekhi* **2015**, *58* (10), 1002. https://doi.org/10.3367/UFNe.0185.201510m.1099.

(7) Baibich, M. N.; Broto, J. M.; Fert, A.; Van Dau, F. N.; Petroff, F.; Etienne, P.; Creuzet, G.; Friederich, A.; Chazelas, J. Giant Magnetoresistance of (001)Fe/(001)Cr Magnetic Superlattices. *Phys. Rev. Lett.* **1988**, *61* (21), 2472–2475. https://doi.org/10.1103/PhysRevLett.61.2472.

(8) Binasch, G.; Grünberg, P.; Saurenbach, F.; Zinn, W. Enhanced Magnetoresistance in Layered Magnetic Structures with Antiferromagnetic Interlayer Exchange. *Phys. Rev. B* **1989**, *39* (7), 4828–4830. https://doi.org/10.1103/PhysRevB.39.4828.

(9) Hirohata, A.; Yamada, K.; Nakatani, Y.; Prejbeanu, I.-L.; Diény, B.; Pirro, P.; Hillebrands, B. Review on Spintronics: Principles and Device Applications. *J. Magn. Magn. Mater.* **2020**, *509*, 166711. https://doi.org/10.1016/j.jmmm.2020.166711.

(10) Urdampilleta, M.; Klyatskaya, S.; Cleuziou, J.-P.; Ruben, M.; Wernsdorfer, W. Supramolecular Spin Valves. *Nat. Mater.* **2011**, *10* (7), 502–506. https://doi.org/10.1038/nmat3050.

(11) Nguyen, T. D.; Ehrenfreund, E.; Vardeny, Z. V. Spin-Polarized Light-Emitting Diode Based on an Organic Bipolar Spin Valve. *Science* **2012**, *337* (6091), 204–209. https://doi.org/10.1126/science.1223444.

(12) Sun, X.; Vélez, S.; Atxabal, A.; Bedoya-Pinto, A.; Parui, S.; Zhu, X.; Llopis, R.; Casanova, F.; Hueso, L. E. A Molecular Spin-Photovoltaic Device. *Science* **2017**, *357* (6352), 677–680. https://doi.org/10.1126/science.aan5348.

(13) Comstock, M. J.; Levy, N.; Kirakosian, A.; Cho, J.; Lauterwasser, F.; Harvey, J. H.; Strubbe, D. A.; Fréchet, J. M. J.; Trauner, D.; Louie, S. G.; Crommie, M. F. Reversible Photomechanical Switching of Individual Engineered Molecules at a Metallic Surface. *Phys. Rev. Lett.* **2007**, *99* (3), 038301. https://doi.org/10.1103/PhysRevLett.99.038301.

(14) Barraud, C.; Seneor, P.; Mattana, R.; Fusil, S.; Bouzehouane, K.; Deranlot, C.; Graziosi, P.;

Hueso, L.; Bergenti, I.; Dediu, V.; Petroff, F.; Fert, A. Unravelling the Role of the Interface for Spin Injection into Organic Semiconductors. *Nat. Phys.* **2010**, *6* (8), 615–620. https://doi.org/10.1038/nphys1688.
(15) Cinchetti, M.; Dediu, V. A.; Hueso, L. E. Activating the Molecular Spinterface. *Nat. Mater.* **2017**, *16* (5), 507–515. https://doi.org/10.1038/nmat4902.
(16) Corso, M.; Verstraete, M. J.; Schiller, F.; Ormaza, M.; Fernández, L.; Greber, T.; Torrent, M.; Rubio, A.; Ortega, J. E. Rare-Earth Surface Alloying: A New Phase for GdAu2. *Phys. Rev. Lett.* **2010**, *105* (1), 2–5. https://doi.org/10.1103/PhysRevLett.105.016101.
(17) Ormaza, M.; Fernández, L.; Ilyn, M.; Magaña, A.; Xu, B.; Verstraete, M. J.; Gastaldo, M.; Valbuena, M. A.; Gargiani, P.; Mugarza, A.; Ayuela, A.; Vitali, L.; Blanco-Rey, M.; Schiller, F.; Ortega, J. E. High Temperature Ferromagnetism in a GdAg2 Monolayer. *Nano Lett.* **2016**, *16* (7), 4230–4235. https://doi.org/10.1021/acs.nanolett.6b01197.
(18) Bazarnik, M.; Abadia, M.; Brede, J.; Hermanowicz, M.; Sierda, E.; Elsebach, M.; Hänke, T.; Wiesendanger, R. Atomically Resolved Magnetic Structure of a Gd-Au Surface Alloy. *Phys. Rev. B* **2019**, *99* (17), 174419. https://doi.org/10.1103/PhysRevB.99.174419.
(19) Mousavion, S.; Yu, K. M.; Maniraj, M.; Lyu, L.; Knippertz, J.; Stadtmüller, B.; Aeschlimann, M. Atomic and Mesoscopic Structure of Dy-Based Surface Alloys on Noble Metals. *New J. Phys.* **2022**, *24* (3), 033048. https://doi.org/10.1088/1367-2630/ac5c17.
(20) Huang, B.; Clark, G.; Navarro-Moratalla, E.; Klein, D. R.; Cheng, R.; Seyler, K. L.; Zhong, D.; Schmidgall, E.; McGuire, M. A.; Cobden, D. H.; Yao, W.; Xiao, D.; Jarillo-Herrero, P.; Xu, X. Layer-Dependent Ferromagnetism in a van Der Waals Crystal down to the Monolayer Limit. *Nature* **2017**, *546* (7657), 270–273. https://doi.org/10.1038/nature22391.
(21) Gong, C.; Li, L.; Li, Z.; Ji, H.; Stern, A.; Xia, Y.; Cao, T.; Bao, W.; Wang, C.; Wang, Y.; Qiu, Z. Q.; Cava, R. J.; Louie, S. G.; Xia, J.; Zhang, X. Discovery of Intrinsic Ferromagnetism in Two-Dimensional van Der Waals Crystals. *Nature* **2017**, *546* (7657), 265–269. https://doi.org/10.1038/nature22060.
(22) Ising, E. Beitrag zur Theorie des Ferromagnetismus. *Z. Für Phys.* **1925**, *31* (1), 253–258. https://doi.org/10.1007/BF02980577.
(23) Onsager, L. Crystal Statistics. I. A Two-Dimensional Model with an Order-Disorder Transition. *Phys. Rev.* **1944**, *65* (3–4), 117–149. https://doi.org/10.1103/PhysRev.65.117.
(24) Mermin, N. D.; Wagner, H. Absence of Ferromagnetism or Antiferromagnetism in One- or Two-Dimensional Isotropic Heisenberg Models. *Phys. Rev. Lett.* **1966**, *17* (22), 1133–1136. https://doi.org/10.1103/PhysRevLett.17.1133.
(25) Bander, M.; Mills, D. L. Ferromagnetism of Ultrathin Films. *Phys. Rev. B* **1988**, *38* (16), 12015–12018. https://doi.org/10.1103/PhysRevB.38.12015.
(26) Kosterlitz, J. M.; Thouless, D. J. Ordering, Metastability and Phase Transitions in Two-Dimensional Systems. *J. Phys. C Solid State Phys.* **1973**, *6* (7), 1181. https://doi.org/10.1088/0022-3719/6/7/010.
(27) Legrand, E.; Plumier, R. Neutron Diffraction Investigation of Antiferromagnetic K2NiF4. *Phys. Status Solidi B* **1962**, *2* (3), 317–320. https://doi.org/10.1002/pssb.19620020306.
(28) Néel, L. L'anisotropie Superficielle Des Substances Ferromagnétiques. *Comptes Rendus Hebd. Seances Acad. Sci.* **1953**, No. 237 (23), 1468–1470.
(29) Bennett, A. J.; Cooper, B. R. Origin of the Magnetic "Surface Anisotropy" of Thin Ferromagnetic Films. *Phys. Rev. B* **1971**, *3* (5), 1642–1649. https://doi.org/10.1103/PhysRevB.3.1642.
(30) Grundy, P. J. Magnetic Layers: Anisotropy. In *Encyclopedia of Materials: Science and Technology*; Buschow, K. H. J., Cahn, R. W., Flemings, M. C., Ilschner, B., Kramer, E. J., Mahajan, S., Veyssière, P., Eds.; Elsevier: Oxford, 2001; pp 4788–4792.

https://doi.org/10.1016/B0-08-043152-6/00836-6.
(31) Gradmann, U. Struktur und Ferromagnetismus sehr dünner, epitaktischer Ni-Flächenschichten. *Ann. Phys.* **1966**, *472* (1–2), 91–106. https://doi.org/10.1002/andp.19664720110.
(32) Gradmann, U.; Müller, J. Very Thin (2–200 Å) Ferromagnetic NiFe Films. *J. Appl. Phys.* **1968**, *39* (2), 1379–1381. https://doi.org/10.1063/1.1656313.
(33) *Electron probabilities for gadolinium*. Encyclopædia Britannica. https://www.britannica.com/science/rare-earth-element/Electronic-structure-and-ionic-radius#/media/1/491579/187149 (accessed 2023-05-05).
(34) Kutzelnigg, W.; Morgan, J. D. Hund's Rules. *Z. Für Phys. At. Mol. Clust.* **1996**, *36* (3), 197–214. https://doi.org/10.1007/BF01426405.
(35) Menth, A.; Nagel, H.; Perkins, R. S. NEW HIGH-PERFORMANCE PERMANENT MAGNETS BASED ON RARE EARTH-TRANSITION METAL COMPOUNDS. *Ann Rev Mater Sci 19788 21-47*.
(36) Tawara, Y.; Senno, H. Sintered Magnets of Copper- and Iron-Modified Cerium Cobalt. *IEEE Trans. Magn.* **1972**, *8* (3), 560–561. https://doi.org/10.1109/TMAG.1972.1067360.
(37) Comstock, R. L. Review Modern Magnetic Materials in Data Storage. *J. Mater. Sci. Mater. Electron.* **2002**, *13* (9), 509–523. https://doi.org/10.1023/A:1019642215245.
(38) Jensen, J.; Mackintosh, A. R. Novel Magnetic Phases in Holmium. *J. Magn. Magn. Mater.* **1992**, *104–107*, 1481–1484. https://doi.org/10.1016/0304-8853(92)91421-O.
(39) Alkhafaji, M. T.; Ali, N. Magnetic Phase Diagram of Dysprosium. *J. Alloys Compd.* **1997**, *250* (1), 659–661. https://doi.org/10.1016/S0925-8388(96)03039-3.
(40) Mason, M. G.; Lee, S. T.; Apai, G.; Davis, R. F.; Shirley, D. A.; Franciosi, A.; Weaver, J. H. Particle-Size-Induced Valence Changes in Samarium Clusters. *Phys. Rev. Lett.* **1981**, *47* (10), 730–733. https://doi.org/10.1103/PhysRevLett.47.730.
(41) McGuire, T. R.; Shafer, M. W. Ferromagnetic Europium Compounds. *J. Appl. Phys.* **1964**, *35* (3), 984–988. https://doi.org/10.1063/1.1713568.
(42) Tang, J.; Zhang, P. A Basis for Lanthanide Single-Molecule Magnets. In *Lanthanide Single Molecule Magnets*; Tang, J., Zhang, P., Eds.; Springer: Berlin, Heidelberg, 2015; pp 1–39. https://doi.org/10.1007/978-3-662-46999-6_1.
(43) Cavallin, A.; Fernández, L.; Ilyn, M.; Magaña, A.; Ormaza, M.; Matena, M.; Vitali, L.; Ortega, J. E.; Grazioli, C.; Ohresser, P.; Rusponi, S.; Brune, H.; Schiller, F. Magnetism and Morphology of Co Nanocluster Superlattices on $GdAu_2$/Au(111)-(13x13). *Phys. Rev. B* **2014**, *90* (23), 235419. https://doi.org/10.1103/PhysRevB.90.235419.
(44) Fernández, L.; Blanco-Rey, M.; Ilyn, M.; Vitali, L.; Magaña, A.; Correa, A.; Ohresser, P.; Ortega, J. E.; Ayuela, A.; Schiller, F. Co Nanodot Arrays Grown on a GdAu2 Template: Substrate/Nanodot Antiferromagnetic Coupling. *Nano Lett.* **2014**, *14* (6), 2977–2981. https://doi.org/10.1021/nl403471z.
(45) Fernández, L.; Ilyn, M.; Magaña, A.; Vitali, L.; Ortega, J. E.; Schiller, F. Growth of Co Nanomagnet Arrays with Enhanced Magnetic Anisotropy. *Adv. Sci.* **2016**, *3* (9), 1600187. https://doi.org/10.1002/advs.201600187.
(46) Ormaza, M.; Fernández, L.; Lafuente, S.; Corso, M.; Schiller, F.; Xu, B.; Diakhate, M.; Verstraete, M. J.; Ortega, J. E. $LaAu_2$ and $CeAu_2$ Surface Intermetallic Compounds Grown by High-Temperature Deposition on Au(111). *Phys. Rev. B* **2013**, *88* (12), 125405. https://doi.org/10.1103/PhysRevB.88.125405.
(47) Ormaza Saezmiera, M. Ph.D. Thesis: Rare Earth/Noble Metal Surface Alloys, UPV-EHU, 2013.
(48) Correa, A.; Xu, B.; Verstraete, M. J.; Vitali, L. Strain-Induced Effects in the Electronic and

Spin Properties of a Monolayer of Ferromagnetic GdAg2. *Nanoscale* **2016**, *8* (45), 19148–19153. https://doi.org/10.1039/C6NR06398E.
(49) Schumacher, S.; Huttmann, F.; Petrović, M.; Witt, C.; Förster, D. F.; Vo-Van, C.; Coraux, J.; Martínez-Galera, A. J.; Sessi, V.; Vergara, I.; Rückamp, R.; Grüninger, M.; Schleheck, N.; Meyer zu Heringdorf, F.; Ohresser, P.; Kralj, M.; Wehling, T. O.; Michely, T. Europium underneath Graphene on Ir(111): Intercalation Mechanism, Magnetism, and Band Structure. *Phys. Rev. B* **2014**, *90* (23), 235437. https://doi.org/10.1103/PhysRevB.90.235437.
(50) Blanco-Rey, M.; Castrillo-Bodero, R.; Ali, K.; Gargiani, P.; Bertran, F.; Sheverdyaeva, P. M.; Ortega, J. E.; Fernandez, L.; Schiller, F. Effect of the Valence State on the Band Magnetocrystalline Anisotropy in Two-Dimensional Rare-Earth/Noble-Metal Compounds. *Phys. Rev. Res.* **2022**, *4* (1), 013237. https://doi.org/10.1103/PhysRevResearch.4.013237.
(51) Abadía, M.; Ilyn, M.; Piquero-Zulaica, I.; Gargiani, P.; Rogero, C.; Ortega, J. E.; Brede, J. Polymerization of Well-Aligned Organic Nanowires on a Ferromagnetic Rare-Earth Surface Alloy. *ACS Nano* **2017**, *11* (12), 12392–12401. https://doi.org/10.1021/acsnano.7b06374.
(52) Feng, B.; Zhang, R.-W.; Feng, Y.; Fu, B.; Wu, S.; Miyamoto, K.; He, S.; Chen, L.; Wu, K.; Shimada, K.; Okuda, T.; Yao, Y. Discovery of Weyl Nodal Lines in a Single-Layer Ferromagnet. *Phys. Rev. Lett.* **2019**, *123* (11), 116401. https://doi.org/10.1103/PhysRevLett.123.116401.
(53) Kobayashi, K. Moiré Pattern in Scanning Tunneling Microscopy: Mechanism in Observation of Subsurface Nanostructures. *Phys. Rev. B* **1996**, *53* (16), 11091–11099. https://doi.org/10.1103/PhysRevB.53.11091.
(54) Gaviria-Posada, J. C. P. Master Thesis, UPV-EHU, 2013.
(55) Bean, C. P.; Livingston, J. D. Superparamagnetism. *J. Appl. Phys.* **2009**, *30* (4), S120–S129. https://doi.org/10.1063/1.2185850.
(56) Dediu, V. A.; Hueso, L. E.; Bergenti, I.; Taliani, C. Spin Routes in Organic Semiconductors. *Nat. Mater.* **2009**, *8* (9), 707–716. https://doi.org/10.1038/nmat2510.
(57) Naber, W. J. M.; Faez, S.; Wiel, W. G. van der. Organic Spintronics. *J. Phys. Appl. Phys.* **2007**, *40* (12), R205. https://doi.org/10.1088/0022-3727/40/12/R01.
(58) Geng, R.; Luong, H. M.; Daugherty, T. T.; Hornak, L.; Nguyen, T. D. A Review on Organic Spintronic Materials and Devices: II. Magnetoresistance in Organic Spin Valves and Spin Organic Light Emitting Diodes. *J. Sci. Adv. Mater. Devices* **2016**, *1* (3), 256–272. https://doi.org/10.1016/j.jsamd.2016.08.006.
(59) Cinchetti, M.; Heimer, K.; Wüstenberg, J.-P.; Andreyev, O.; Bauer, M.; Lach, S.; Ziegler, C.; Gao, Y.; Aeschlimann, M. Determination of Spin Injection and Transport in a Ferromagnet/Organic Semiconductor Heterojunction by Two-Photon Photoemission. *Nat. Mater.* **2009**, *8* (2), 115–119. https://doi.org/10.1038/nmat2334.
(60) Lach, S.; Altenhof, A.; Tarafder, K.; Schmitt, F.; Ali, Md. E.; Vogel, M.; Sauther, J.; Oppeneer, P. M.; Ziegler, C. Metal–Organic Hybrid Interface States of A Ferromagnet/Organic Semiconductor Hybrid Junction as Basis For Engineering Spin Injection in Organic Spintronics. *Adv. Funct. Mater.* **2012**, *22* (5), 989–997. https://doi.org/10.1002/adfm.201102297.
(61) Javaid, S.; Bowen, M.; Boukari, S.; Joly, L.; Beaufrand, J.-B.; Chen, X.; Dappe, Y. J.; Scheurer, F.; Kappler, J.-P.; Arabski, J.; Wulfhekel, W.; Alouani, M.; Beaurepaire, E. Impact on Interface Spin Polarization of Molecular Bonding to Metallic Surfaces. *Phys. Rev. Lett.* **2010**, *105* (7), 077201. https://doi.org/10.1103/PhysRevLett.105.077201.
(62) Droghetti, A.; Thielen, P.; Rungger, I.; Haag, N.; Großmann, N.; Stöckl, J.; Stadtmüller, B.; Aeschlimann, M.; Sanvito, S.; Cinchetti, M. Dynamic Spin Filtering at the Co/Alq3 Interface Mediated by Weakly Coupled Second Layer Molecules. *Nat. Commun.* **2016**, *7* (1), 12668.

https://doi.org/10.1038/ncomms12668.
(63) Ma'Mari, F. A.; Moorsom, T.; Teobaldi, G.; Deacon, W.; Prokscha, T.; Luetkens, H.; Lee, S.; Sterbinsky, G. E.; Arena, D. A.; MacLaren, D. A.; Flokstra, M.; Ali, M.; Wheeler, M. C.; Burnell, G.; Hickey, B. J.; Cespedes, O. Beating the Stoner Criterion Using Molecular Interfaces. *Nature* **2015**, *524* (7563), 69–73. https://doi.org/10.1038/nature14621.
(64) Moorsom, T.; Wheeler, M.; Mohd Khan, T.; Al Ma'Mari, F.; Kinane, C.; Langridge, S.; Ciudad, D.; Bedoya-Pinto, A.; Hueso, L.; Teobaldi, G.; Lazarov, V. K.; Gilks, D.; Burnell, G.; Hickey, B. J.; Cespedes, O. Spin-Polarized Electron Transfer in Ferromagnet C_{60} Interfaces. *Phys. Rev. B* **2014**, *90* (12), 125311. https://doi.org/10.1103/PhysRevB.90.125311.
(65) Takada, J. T. J. Organic-Inorganic Hetero Nanosystems as an Approach to Molecular Optoelectronics. *Jpn. J. Appl. Phys.* **1995**, *34* (7S), 3864. https://doi.org/10.1143/JJAP.34.3864.
(66) Takada, J.; Awaji, H.; Koshioka, M.; Nakajima, A.; Nevin, W. A. Organic–Inorganic Multilayers: A New Concept of Optoelectronic Material. *Appl. Phys. Lett.* **1992**, *61* (18), 2184–2186. https://doi.org/10.1063/1.108289.
(67) Pirriera, M. D.; Puigdollers, J.; Voz, C.; Stella, M.; Bertomeu, J.; Alcubilla, R. Optoelectronic Properties of CuPc Thin Films Deposited at Different Substrate Temperatures. *J. Phys. Appl. Phys.* **2009**, *42* (14), 145102. https://doi.org/10.1088/0022-3727/42/14/145102.
(68) Murtaza, I.; Qazi, I.; Karimov, K. S. CuPc/C60 Heterojunction Thin Film Optoelectronic Devices. *J. Semicond.* **2010**, *31* (6), 064005. https://doi.org/10.1088/1674-4926/31/6/064005.
(69) Warner, M.; Din, S.; Tupitsyn, I. S.; Morley, G. W.; Stoneham, A. M.; Gardener, J. A.; Wu, Z.; Fisher, A. J.; Heutz, S.; Kay, C. W. M.; Aeppli, G. Potential for Spin-Based Information Processing in a Thin-Film Molecular Semiconductor. *Nature* **2013**, *503* (7477), 504–508. https://doi.org/10.1038/nature12597.
(70) Heutz, S.; Mitra, C.; Wu, W.; Fisher, A. J.; Kerridge, A.; Stoneham, M.; Harker, A. H.; Gardener, J.; Tseng, H.-H.; Jones, T. S.; Renner, C.; Aeppli, G. Molecular Thin Films: A New Type of Magnetic Switch. *Adv. Mater.* **2007**, *19* (21), 3618–3622. https://doi.org/10.1002/adma.200701458.
(71) Carniato, S.; Luo, Y.; Ågren, H. Theoretical Study of the Near-Edge Cu L x-Ray Absorption Spectrum of Copper Phthalocyanine. *Phys. Rev. B* **2001**, *63* (8), 085105. https://doi.org/10.1103/PhysRevB.63.085105.
(72) Mugarza, A.; Robles, R.; Krull, C.; Korytár, R.; Lorente, N.; Gambardella, P. Electronic and Magnetic Properties of Molecule-Metal Interfaces: Transition-Metal Phthalocyanines Adsorbed on Ag(100). *Phys. Rev. B - Condens. Matter Mater. Phys.* **2012**, *85* (15), 1–13. https://doi.org/10.1103/PhysRevB.85.155437.
(73) Chen, X.; Fu, Y.-S.; Ji, S.-H.; Zhang, T.; Cheng, P.; Ma, X.-C.; Zou, X.-L.; Duan, W.-H.; Jia, J.-F.; Xue, Q.-K. Probing Superexchange Interaction in Molecular Magnets by Spin-Flip Spectroscopy and Microscopy. *Phys. Rev. Lett.* **2008**, *101* (19), 197208. https://doi.org/10.1103/PhysRevLett.101.197208.
(74) Gao, L.; Ji, W.; Hu, Y. B.; Cheng, Z. H.; Deng, Z. T.; Liu, Q.; Jiang, N.; Lin, X.; Guo, W.; Du, S. X.; Hofer, W. A.; Xie, X. C.; Gao, H.-J. Site-Specific Kondo Effect at Ambient Temperatures in Iron-Based Molecules. *Phys. Rev. Lett.* **2007**, *99* (10), 106402. https://doi.org/10.1103/PhysRevLett.99.106402.
(75) Fu, Y.-S.; Ji, S.-H.; Chen, X.; Ma, X.-C.; Wu, R.; Wang, C.-C.; Duan, W.-H.; Qiu, X.-H.; Sun, B.; Zhang, P.; Jia, J.-F.; Xue, Q.-K. Manipulating the Kondo Resonance through Quantum Size Effects. *Phys. Rev. Lett.* **2007**, *99* (25), 256601. https://doi.org/10.1103/PhysRevLett.99.256601.
(76) Zhao, A.; Li, Q.; Chen, L.; Xiang, H.; Wang, W.; Pan, S.; Wang, B.; Xiao, X.; Yang, J.; Hou,

J. G.; Zhu, Q. Controlling the Kondo Effect of an Adsorbed Magnetic Ion Through Its Chemical Bonding. *Science* **2005**, *309* (5740), 1542–1544. https://doi.org/10.1126/science.1113449.
(77) Stepanow, S.; Mugarza, A.; Ceballos, G.; Moras, P.; Cezar, J. C.; Carbone, C.; Gambardella, P. Giant Spin and Orbital Moment Anisotropies of a Cu-Phthalocyanine Monolayer. *Phys. Rev. B* **2010**, *82* (1), 014405. https://doi.org/10.1103/PhysRevB.82.014405.
(78) Gargiani, P. Ph.D. Thesis: Control the Electronic and Magnetic States of Organometallic Nanostructures Supported on Metals, Università di Roma "La Sapienza," 2011.
(79) *File:Copper phthalocyanine.svg - Wikipedia*. https://en.wikipedia.org/wiki/File:Copper_phthalocyanine.svg (accessed 2023-04-03).
(80) Lodi Rizzini, A.; Krull, C.; Mugarza, A.; Balashov, T.; Nistor, C.; Piquerel, R.; Klyatskaya, S.; Ruben, M.; Sheverdyaeva, P. M.; Moras, P.; Carbone, C.; Stamm, C.; Miedema, P. S.; Thakur, P. K.; Sessi, V.; Soares, M.; Yakhou-Harris, F.; Cezar, J. C.; Stepanow, S.; Gambardella, P. Coupling of Single, Double, and Triple-Decker Metal-Phthalocyanine Complexes to Ferromagnetic and Antiferromagnetic Substrates. *Surf. Sci.* **2014**, *630*, 361–374. https://doi.org/10.1016/j.susc.2014.07.008.
(81) Ishikawa, N.; Sugita, M.; Ishikawa, T.; Koshihara, S.; Kaizu, Y. Mononuclear Lanthanide Complexes with a Long Magnetization Relaxation Time at High Temperatures: A New Category of Magnets at the Single-Molecular Level. *J. Phys. Chem. B* **2004**, *108* (31), 11265–11271. https://doi.org/10.1021/jp0376065.
(82) Ishikawa, N.; Sugita, M.; Ishikawa, T.; Koshihara, S.; Kaizu, Y. Lanthanide Double-Decker Complexes Functioning as Magnets at the Single-Molecular Level. *J. Am. Chem. Soc.* **2003**, *125* (29), 8694–8695. https://doi.org/10.1021/ja029629n.
(83) Ishikawa, N. Single Molecule Magnet with Single Lanthanide Ion. *Polyhedron* **2007**, *26* (9), 2147–2153. https://doi.org/10.1016/j.poly.2006.10.022.
(84) Gao, S. *Molecular Nanomagnets and Related Phenomena*; Springer, 2015.
(85) Woodruff, D. N.; Winpenny, R. E. P.; Layfield, R. A. Lanthanide Single-Molecule Magnets. *Chem. Rev.* **2013**, *113* (7), 5110–5148. https://doi.org/10.1021/cr400018q.
(86) Branzoli, F.; Carretta, P.; Filibian, M.; Graf, M. J.; Klyatskaya, S.; Ruben, M.; Coneri, F.; Dhakal, P. Spin and Charge Dynamics in$TbPc_2$ and $DyPc_2$ Single-Molecule Magnets. *Phys. Rev. B* **2010**, *82* (13), 134401. https://doi.org/10.1103/PhysRevB.82.134401.
(87) Studniarek, M.; Wäckerlin, C.; Singha, A.; Baltic, R.; Diller, K.; Donati, F.; Rusponi, S.; Brune, H.; Lan, Y.; Klyatskaya, S.; Ruben, M.; Seitsonen, A. P.; Dreiser, J. Understanding the Superior Stability of Single-Molecule Magnets on an Oxide Film. *Adv. Sci.* **2019**, *6* (22), 1901736. https://doi.org/10.1002/advs.201901736.
(88) Robaschik, P.; Fronk, M.; Toader, M.; Klyatskaya, S.; Ganss, F.; F. Siles, P.; G. Schmidt, O.; Albrecht, M.; Hietschold, M.; Ruben, M.; T. Zahn, D. R.; Salvan, G. Tuning the Magneto-Optical Response of TbPc 2 Single Molecule Magnets by the Choice of the Substrate. *J. Mater. Chem. C* **2015**, *3* (31), 8039–8049. https://doi.org/10.1039/C5TC01520K.
(89) Wäckerlin, C.; Donati, F.; Singha, A.; Baltic, R.; Rusponi, S.; Diller, K.; Patthey, F.; Pivetta, M.; Lan, Y.; Klyatskaya, S.; Ruben, M.; Brune, H.; Dreiser, J. Giant Hysteresis of Single-Molecule Magnets Adsorbed on a Nonmagnetic Insulator. *Adv. Mater.* **2016**, *28* (26), 5195–5199. https://doi.org/10.1002/adma.201506305.
(90) Margheriti, L.; Chiappe, D.; Mannini, M.; Car, P.; Sainctavit, P.; Arrio, M.-A.; de Mongeot, F. B.; Cezar, J. C.; Piras, F. M.; Magnani, A.; Otero, E.; Caneschi, A.; Sessoli, R. X-Ray Detected Magnetic Hysteresis of Thermally Evaporated Terbium Double-Decker Oriented Films. *Adv. Mater.* **2010**, *22* (48), 5488–5493. https://doi.org/10.1002/adma.201003275.
(91) Klar, D.; Klyatskaya, S.; Candini, A.; Krumme, B.; Kummer, K.; Ohresser, P.; Corradini, V.;

de Renzi, V.; Biagi, R.; Joly, L.; Kappler, J.-P.; del Pennino, U.; Affronte, M.; Wende, H.; Ruben, M. Antiferromagnetic Coupling of $TbPc_2$ Molecules to Ultrathin Ni and Co Films. *Beilstein J. Nanotechnol.* **2013**, *4*, 320–324. https://doi.org/10.3762/bjnano.4.36.
(92) Rizzini, A.; Krull, C.; Balashov, T.; Kavich, J.; Mugarza, A.; Miedema, P.; Thakur, P.; Sessi, V.; Klyatskaya, S.; Ruben, M.; Stepanow, S.; Gambardella, P. Coupling Single Molecule Magnets to Ferromagnetic Substrates. *Phys. Rev. Lett.* **2011**, *107*, 177205. https://doi.org/10.1103/PhysRevLett.107.177205.
(93) Nistor, C.; Krull, C.; Mugarza, A.; Stepanow, S.; Stamm, C.; Soares, M.; Klyatskaya, S.; Ruben, M.; Gambardella, P. Exchange Bias of $TbPc_2$ Molecular Magnets on Antiferromagnetic FeMn and Ferromagnetic Fe Films. *Phys. Rev. B* **2015**, *92* (18), 184402. https://doi.org/10.1103/PhysRevB.92.184402.
(94) Ashcroft, N. W.; Mermin, N. D. *Solid State Physics*; Holt, Rinehart and Winston, 1976.
(95) Anderson, P. W. Antiferromagnetism. Theory of Superexchange Interaction. *Phys. Rev.* **1950**, *79* (2), 350–356. https://doi.org/10.1103/PhysRev.79.350.
(96) Ruderman, M. A.; Kittel, C. Indirect Exchange Coupling of Nuclear Magnetic Moments by Conduction Electrons. *Phys. Rev.* **1954**, *96* (1), 99–102. https://doi.org/10.1103/PhysRev.96.99.
(97) Parkin, S. S. P.; Mauri, D. Spin Engineering: Direct Determination of the Ruderman-Kittel-Kasuya-Yosida Far-Field Range Function in Ruthenium. *Phys. Rev. B* **1991**, *44* (13), 7131–7134. https://doi.org/10.1103/PhysRevB.44.7131.
(98) Daalderop, G. H. O.; Kelly, P. J.; Schuurmans, M. F. H. First-Principles Calculation of the Magnetocrystalline Anisotropy Energy of Iron, Cobalt, and Nickel. *Phys. Rev. B* **1990**, *41* (17), 11919–11937. https://doi.org/10.1103/PhysRevB.41.11919.
(99) Wernsdorfer, W.; Thirion, C.; Demoncy, N.; Pascard, H.; Mailly, D. Magnetisation Reversal by Uniform Rotation (Stoner–Wohlfarth Model) in FCC Cobalt Nanoparticles. *J. Magn. Magn. Mater.* **2002**, *242–245*, 132–138. https://doi.org/10.1016/S0304-8853(01)01153-2.
(100) Kumar, D.; Narayan, J.; Sharma, A. K.; Kvit, A.; Jin, C.; Sankar, J. Tunable Magnetic Properties in Metal Ceramic Composite Thin Films. *MRS Online Proc. Libr. OPL* **2001**, *676*, Y3.17. https://doi.org/10.1557/PROC-676-Y3.17.
(101) Arrott, A. Criterion for Ferromagnetism from Observations of Magnetic Isotherms. *Phys. Rev.* **1957**, *108* (6), 1394–1396. https://doi.org/10.1103/PhysRev.108.1394.
(102) Zangwill, A. *Physics at Surfaces*; Cambridge University Press, 1988.
(103) Corso, M.; Fernández, L.; Schiller, F.; Ortega, J. E. Au(111)-Based Nanotemplates by Gd Alloying. *ACS Nano* **2010**, *4* (3), 1603–1611. https://doi.org/10.1021/nn901345s.
(104) Reinert, F.; Nicolay, G.; Schmidt, S.; Ehm, D.; Hüfner, S. Direct Measurements of the L-Gap Surface States on the (111) Face of Noble Metals by Photoelectron Spectroscopy. *Phys. Rev. B* **2001**, *63* (11), 115415. https://doi.org/10.1103/PhysRevB.63.115415.
(105) Hertz, H. Ueber Einen Einfluss Des Ultravioletten Lichtes Auf Die Electrische Entladung. *Ann. Phys.* **1887**, *267* (8), 983–1000. https://doi.org/10.1002/andp.18872670827.
(106) Einstein, A. Über Einen Die Erzeugung Und Verwandlung Des Lichtes Betreffenden Heuristischen Gesichtspunkt. *Ann. Phys.* **1905**, *322* (6), 132–148. https://doi.org/10.1002/andp.19053220607.
(107) Lindberg, B. J.; Hamrin, K.; Johansson, G.; Gelius, U.; Fahlman, A.; Nordling, C.; Siegbahn, K. Molecular Spectroscopy by Means of Esca. *Phys. Scr.* **1970**, *1* (5–6), 286–298. https://doi.org/10.1088/0031-8949/1/5-6/020.
(108) Chusuei, C. C.; Goodman, D. W. X-Ray Photoelectron Spectroscopy. In *Encyclopedia of Physical Science and Technology (Third Edition)*; Meyers, R. A., Ed.; Academic Press: New York, 2003; pp 921–938. https://doi.org/10.1016/B0-12-227410-5/00830-9.

(109) Chelvayohan, M.; Mee, C. H. B. Work Function Measurements on (100), (110) and (111) Surfaces of Silver. *J. Phys. C Solid State* **1982**, *15*, 2305–2312. https://doi.org/10.1088/0305-4608/3/9/016.
(110) Lerch, A.; Fernandez, L.; Ilyn, M.; Gastaldo, M.; Paradinas, M.; Valbuena, M. A.; Mugarza, A.; Ibrahim, A. B. M.; Sundermeyer, J.; Höfer, U.; Schiller, F. Electronic Structure of Titanylphthalocyanine Layers on Ag(111). *J. Phys. Chem. C* **2017**, *121* (45), 25353–25363. https://doi.org/10.1021/acs.jpcc.7b09147.
(111) Hieringer, W.; Flechtner, K.; Kretschmann, A.; Seufert, K.; Auw, W.; Barth, J. V.; Andreas, G.; Steinr, H.; Gottfried, J. M. The Surface Trans Effect : Influence of Axial Ligands on the Surface Chemical Bonds of Adsorbed Metalloporphyrins. **2010**, 6206–6222.
(112) Kelsall, R.; Hamley, I.; Geoghegan, M. *Nanoscale Science and Tecnology*.
(113) Hüfner, S. *Photoelectron Spectroscopy. Principles and Applications*; 1995.
(114) Hadjarab, F.; Erskine, J. L. Image Properties of the Hemispherical Analyzer Applied to Multichannel Energy Detection. *J. Electron Spectrosc. Relat. Phenom.* **1985**, *36* (3), 227–243. https://doi.org/10.1016/0368-2048(85)80021-9.
(115) Tusche, C.; Chen, Y.-J.; Schneider, C. M.; Kirschner, J. Imaging Properties of Hemispherical Electrostatic Energy Analyzers for High Resolution Momentum Microscopy. *Ultramicroscopy* **2019**, *206*, 112815. https://doi.org/10.1016/j.ultramic.2019.112815.
(116) Ponor. *Https://Commons.Wikimedia.Org/Wiki/File:Hemispherical_electron_energy_analyzer_for_ARPES_-_main_parts.Svg*; 2020. https://commons.wikimedia.org/wiki/File:Hemispherical_electron_energy_analyzer_for_ARPES_-_main_parts.svg (accessed 2023-01-04).
(117) Meitner, L. Über den Zusammenhang zwischen β- und γ-Strahlen. *Z. Für Phys.* **1922**, *9* (1), 145–152. https://doi.org/10.1007/BF01326963.
(118) Coster, D.; L. Kronig, R. D. New Type of Auger Effect and Its Influence on the X-Ray Spectrum. *Physica* **1935**, *2* (1), 13–24. https://doi.org/10.1016/S0031-8914(35)90060-X.
(119) Fano, U. Effects of Configuration Interaction on Intensities and Phase Shifts. *Phys. Rev.* **1961**, *124* (6), 1866–1878. https://doi.org/10.1103/PhysRev.124.1866.
(120) Tanaka, A.; Jo, T. Resonant 3d, 3p and 3s Photoemission in Transition Metal Oxides Predicted at 2p Threshold. *J. Phys. Soc. Jpn.* **1994**, *63* (7), 2788–2807. https://doi.org/10.1143/JPSJ.63.2788.
(121) Phenomena, R.; Electronics, S. RESONANT PHOTOEMISSION Sm AND Tb AT THE. *Energy* **1986**, *41* (1936), 59–66.
(122) Mishra, S. R.; Cummins, T. R.; Waddill, G. D.; Gammon, W. J.; van der Laan, G.; Goodman, K. W.; Tobin, J. G. Nature of Resonant Photoemission in Gd. *Phys. Rev. Lett.* **1998**, *81* (6), 1306–1309. https://doi.org/10.1103/PhysRevLett.81.1306.
(123) Haffner, S.; Olson, C. G.; Lynch, D. W. Evidence for Replicate 5p Core Levels in Photoelectron Spectra of Eu Metal Due to Nonconstant Kinetic-Energy Resonant Auger Decay. *Phys. Rev. B - Condens. Matter Mater. Phys.* **1999**, *60* (24), 16346–16349. https://doi.org/10.1103/PhysRevB.60.16346.
(124) Cohen-Tannoudji, C.; Diu, B.; Laloë, F. *Quantum Mechanics*; Wiley, 1977.
(125) Pellach, E.; Sar-el, H. Z. Vacuum UV Spectrum of Helium Lamp with Tubings of Different Diameters. *J. Electron Spectrosc. Relat. Phenom.* **1978**, *14* (4), 259–266. https://doi.org/10.1016/0368-2048(78)80002-4.
(126) Hannon, F.; Clarke, J.; Hill, C.; Muir, A.; Scott, D.; Shepherd, B. CONSTRUCTION OF AN APPLE-II TYPE UNDULATOR AT DARESBURY LABORATORY FOR THE SRS. **2004**.
(127) Sasaki, S. Analyses for a Planar Variably-Polarizing Undulator. *Nucl. Instrum. Methods Phys.*

Res. Sect. Accel. Spectrometers Detect. Assoc. Equip. **1994**, *347* (1), 83–86. https://doi.org/10.1016/0168-9002(94)91859-7.
(128) *CASSIOPEE | French national synchrotron facility*. https://www.synchrotron-soleil.fr/en/beamlines/cassiopee (accessed 2023-06-07).
(129) *BEAMLINE INFORMATION — en*. https://www.cells.es/en/beamlines/bl29-boreas (accessed 2023-06-07).
(130) Binnig, G.; Rohrer, H. Scanning Tunneling Microscopy. *Surf. Sci.* **1982**, *126* (126), 236–244. https://doi.org/10.1016/0039-6028(83)90716-1.
(131) Chen, C. J. *Introduction to Scanning Tunneling Microscopy*; Oxford series in optical and imaging sciences; Oxford University Press.
(132) Binnig, G.; Rohrer, H.; Gerber, Ch.; Weibel, E. Tunneling through a Controllable Vacuum Gap. *Appl. Phys. Lett.* **1982**, *40* (2), 178–180. https://doi.org/10.1063/1.92999.
(133) Bardeen, J. Tunnelling from a Many-Particle Point of View. *Phys. Rev. Lett.* **1961**, *6* (2), 57–59. https://doi.org/10.1103/PhysRevLett.6.57.
(134) Tersoff, J.; Hamann, D. R. Theory of the Scanning Tunneling Microscope. *Phys. Rev. B* **1985**, *31* (2), 805–813. https://doi.org/10.1103/PhysRevB.31.805.
(135) Oura, K. (Kenjiro). *Surface Science : An Introduction*; Berlin ; New York : Springer, 2003.
(136) Ponor. *Https://Commons.Wikimedia.Org/Wiki/File:Low-Energy_electron_diffraction_(LEED)_instrument_-_schematic_diagram.Svg*; 2020. https://commons.wikimedia.org/wiki/File:Low-energy_electron_diffraction_(LEED)_instrument_-_schematic_diagram.svg (accessed 2023-03-10).
(137) Kittel C. *Introduction to Solid State Physics*; Wiley, 1959.
(138) Crocombette, J. P.; Thole, B. T.; Jollet, F. Ph.D. Thesis: The Importance of the Magnetic Dipole Term in Magneto-Circular x-Ray Absorption Dichroism for 3d Transition Metal Compounds. *J. Phys. Condens. Matter* **1996**, *8* (22), 4095. https://doi.org/10.1088/0953-8984/8/22/013.
(139) Šipr, O.; Minár, J.; Ebert, H. On the Importance of the Magnetic Dipole Term Tz in Analyzing X-Ray Magnetic Circular Dichroism Spectra of Clusters. *Europhys. Lett.* **2009**, *87* (6), 67007. https://doi.org/10.1209/0295-5075/87/67007.
(140) Praetorius, C. M. Ph.D. Thesis: Ce $M_{4,5}$ XAS and XMCD as Local Probes for Kondo and Heavy Fermion Materials A Study of $CePt_5$/Pt(111) Surface Intermetallics, Julius-Maximilians-Universität of Würzburg.
(141) Thole, B. T.; van der Laan, G. Sum Rules for Magnetic Dichroism in Rare Earth 4f Photoemission. *Phys. Rev. Lett.* **1993**, *70* (16), 2499–2502. https://doi.org/10.1103/PhysRevLett.70.2499.
(142) Singha, A.; Baltic, R.; Donati, F.; Wäckerlin, C.; Dreiser, J.; Persichetti, L.; Stepanow, S.; Gambardella, P.; Rusponi, S.; Brune, H. 4f Occupancy and Magnetism of Rare-Earth Atoms Adsorbed on Metal Substrates. *Phys. Rev. B* **2017**, *96* (22), 224418. https://doi.org/10.1103/PhysRevB.96.224418.
(143) Sipr, O.; Minar, J.; Ebert, H. Influence of Spin-Orbit Coupling on the Magnetic Dipole Term. *Phys. Rev. B* **2016**, *94*. https://doi.org/10.1103/PhysRevB.94.144406.
(144) Carra, P.; Thole, B. T.; Altarelli, M.; Wang, X. X-Ray Circular Dichroism and Local Magnetic Fields. *Phys. Rev. Lett.* **1993**, *70* (5), 694–697. https://doi.org/10.1103/PhysRevLett.70.694.
(145) Seitz, M.; Oliver, A. G.; Raymond, K. N. The Lanthanide Contraction Revisited. *J. Am. Chem. Soc.* **2007**, *129* (36), 11153–11160. https://doi.org/10.1021/ja072750f.
(146) Que, Y.; Zhuang, Y.; Liu, Z.; Xu, C.; Liu, B.; Wang, K.; Du, S.; Xiao, X. Two-Dimensional

Rare Earth–Gold Intermetallic Compounds on Au(111) by Surface Alloying. *J. Phys. Chem. Lett.* **2020**, *11* (10), 4107–4112. https://doi.org/10.1021/acs.jpclett.0c00981.
(147) Iandelli, A.; Palenzona, A. Atomic Size of Rare Earths in Intermetallic Compounds. MX Compounds of CsCl Type. *J. Common Met.* **1965**, *9* (1), 1–6. https://doi.org/10.1016/0022-5088(65)90028-7.
(148) Hooks, D. E.; Fritz, T.; Ward, M. D. Epitaxy and Molecular Organization on Solid Substrates. *Adv. Mater.* **2001**, *13* (4), 227–241. https://doi.org/10.1002/1521-4095(200102)13:4<227::AID-ADMA227>3.0.CO;2-P.
(149) Spurgeon, P.; Lai, K. C.; Han, Y.; Evans, J.; Thiel, P. Fundamentals of Au(111) Surface Dynamics: Coarsening of 2D Au Islands. *J. Phys. Chem. C* **2020**, *124*, 7492. https://doi.org/10.1021/acs.jpcc.9b12056.
(150) Moulder, J. F.; Stickle, W. F.; Sobol, P. E.; Bomben, K. D. *Handbook of X-Ray Photoelectron Spectroscopy: A Reference Book of Standard Spectra for Identification and Interpretation of XPS Data*; 1992. https://doi.org/9780962702624.
(151) Thomson, A.; Attwood, D.; Gullikson, E.; Howells, M.; Kim, K.-J.; Kirz, J.; Kortright, J.; Lindau, I.; Pianetta, P.; Robinson, A.; Scofield, J.; Underwood, J.; Vaughan, D.; Williams, G.; Winick, H. *X-Ray Data Booklet*, 2nd edition.; Lawrence Berkeley National Laboratory.
(152) *Samarium (Sm), Z=62, & Samarium Compounds*. https://xps-database.com/samarium-sm-z62-samarium-compounds/ (accessed 2023-01-26).
(153) Gerken, F. Calculated Photoemission Spectra of the 4f States in the Rare-Earth Metals. *J. Phys. F Met. Phys.* **1983**, *13* (3), 703. https://doi.org/10.1088/0305-4608/13/3/021.
(154) Wertheim, G. K.; Crecelius, G. Divalent Surface State on Metallic Samarium. *Phys. Rev. Lett.* **1978**, *40* (12), 813–816. https://doi.org/10.1103/PhysRevLett.40.813.
(155) Thole, B. T.; Wang, X. D.; Harmon, B. N.; Li, D.; Dowben, P. A. Multiplet Fine Structure in the Photoemission of the Gadolinium and Terbium 5p Levels. *Phys. Rev. B* **1993**, *47* (14), 9098–9101. https://doi.org/10.1103/PhysRevB.47.9098.
(156) Lademan, W. J.; See, A. K.; Klebanoff, L. E.; van der Laan, G. Multiplet Structure in High-Resolution and Spin-Resolved x-Ray Photoemission from Gadolinium. *Phys. Rev. B* **1996**, *54* (23), 17191–17198. https://doi.org/10.1103/PhysRevB.54.17191.
(157) van der Laan, G.; Arenholz, E.; Navas, E.; Hu, Z.; Mentz, E.; Bauer, A.; Kaindl, G. Magnetic Circular Dichroism in 5p Photoemission from Gd and Tb Metal. *Phys. Rev. B* **1997**, *56* (6), 3244–3250. https://doi.org/10.1103/PhysRevB.56.3244.
(158) Mulhollan, G. A.; Garrison, K.; Erskine, J. L. Surface Magnetism of Gd(0001): Evidence of Ferromagnetic Coupling to Bulk. *Phys. Rev. Lett.* **1992**, *69* (22), 3240–3243. https://doi.org/10.1103/PhysRevLett.69.3240.
(159) Kaindl, G.; Höhr, A.; Weschke, E.; Vandré, S.; Schüßler-Langeheine, C.; Laubschat, C. Surface Core-Level Shifts and Surface States for the Heavy Lanthanide Metals. *Phys. Rev. B* **1995**, *51* (12), 7920–7923. https://doi.org/10.1103/PhysRevB.51.7920.
(160) Signorelli, A. J.; Hayes, R. G. X-Ray Photoelectron Spectroscopy of Various Core Levels of Lanthanide Ions: The Roles of Monopole Excitation and Electrostatic Coupling. *Phys. Rev. B* **1973**, *8* (1), 81–86. https://doi.org/10.1103/PhysRevB.8.81.
(161) Suzuki, K.; Enoki, T.; Bandow, S. Electronic Properties and Valence State of Sm in $(SmS)_{1.19}TaS_2$. *Phys. Rev. B* **1993**, *48* (15), 11077–11085. https://doi.org/10.1103/PhysRevB.48.11077.
(162) Fernandez, L.; Blanco-Rey, M.; Castrillo-Bodero, R.; Ilyn, M.; Ali, K.; Turco, E.; Corso, M.; Ormaza, M.; Gargiani, P.; Valbuena, M. A.; Mugarza, A.; Moras, P.; Sheverdyaeva, P. M.; Kundu, A. K.; Jugovac, M.; Laubschat, C.; Ortega, J. E.; Schiller, F. Influence of 4f Filling on Electronic and Magnetic Properties of Rare Earth-Au Surface Compounds. *Nanoscale* **2020**,

12 (43), 22258–22267. https://doi.org/10.1039/D0NR04964F.
(163) Wertheim, G. K.; Wernick, J. H.; Crecelius, G. Surface Effects on Valence in Rare-Earth Intermetallic Compounds. *Phys. Rev. B* **1978**, *18* (2), 875–879. https://doi.org/10.1103/PhysRevB.18.875.
(164) Lawrence, J. M.; Riseborough, P. S.; Parks, R. D. Valence Fluctuation Phenomena. *Rep. Prog. Phys.* **1981**, *44* (1), 1. https://doi.org/10.1088/0034-4885/44/1/001.
(165) Laubschat, C.; Kaindl, G.; Schneider, W.-D.; Reihl, B.; Mrtensson, N. Stability of 4f Configurations in Rare-Earth-Metal Compounds. *Phys. Rev. B* **1986**, *33* (10), 6675–6683. https://doi.org/10.1103/PhysRevB.33.6675.
(166) Thole, B. T.; van der Laan, G.; Fuggle, J. C.; Sawatzky, G. A.; Karnatak, R. C.; Esteva, J.-M. 3d X-Ray-Absorption Lines and the $3d^9 4f^{n+1}$ Multiplets of the Lanthanides. *Phys. Rev. B* **1985**, *32* (8), 5107–5118. https://doi.org/10.1103/PhysRevB.32.5107.
(167) Joy, P. A.; Date, S. K. Comparison of the Zero-Field-Cooled Magnetization Behavior of Some Ferromagnetic and Ferrimagnetic Systems. *J. Magn. Magn. Mater.* **2000**, *218* (2), 229–237. https://doi.org/10.1016/S0304-8853(00)00405-4.
(168) Hansen, M. F.; Mørup, S. Estimation of Blocking Temperatures from ZFC/FC Curves. *J. Magn. Magn. Mater.* **1999**, *203* (1), 214–216. https://doi.org/10.1016/S0304-8853(99)00238-3.
(169) Tcakaev, A.; Zabolotnyy, V. B.; Fornari, C. I.; Rüßmann, P.; Peixoto, T. R. F.; Stier, F.; Dettbarn, M.; Kagerer, P.; Weschke, E.; Schierle, E.; Bencok, P.; Rappl, P. H. O.; Abramof, E.; Bentmann, H.; Goering, E.; Reinert, F.; Hinkov, V. Incipient Antiferromagnetism in the Eu-Doped Topological Insulator Bi_2Te_3. *Phys. Rev. B* **2020**, *102* (18), 184401. https://doi.org/10.1103/PhysRevB.102.184401.
(170) Kinoshita, T.; Gunasekara, H.; Takata, Y.; Kimura, S.; Okuno, M.; Haruyama, Y.; Kosugi, N.; Nath, K.; Wada, H.; Mitsuda, A.; Shiga, M.; Okuda, T. Spectroscopy Studies of Temperature-Induced Valence Transition on $EuNi_2(Si_{1-x}Ge_x)_2$ around Eu 3d-4f, 4d-4f and Ni 2p-3d Excitation Regions. *J. Phys. Soc. Jpn. - J PHYS SOC JPN* **2002**, *71*, 148–155. https://doi.org/10.1143/JPSJ.71.148.
(171) Holst, B.; Nohlen, M.; Wandelt, K.; Allison, W. Observation of an Adlayer-Driven Substrate Reconstruction in Cu-Pt(111). *Phys. Rev. B* **1998**, *58* (16), R10195–R10198. https://doi.org/10.1103/PhysRevB.58.R10195.
(172) Ling, W. L.; Hamilton, J. C.; Thürmer, K.; Thayer, G. E.; de la Figuera, J.; Hwang, R. Q.; Carter, C. B.; Bartelt, N. C.; McCarty, K. F. Herringbone and Triangular Patterns of Dislocations in Ag, Au, and AgAu Alloy Films on Ru(0001). *Surf. Sci.* **2006**, *600* (9), 1735–1757. https://doi.org/10.1016/j.susc.2006.01.055.
(173) Self-Organized Growth of Nanostructure Arrays on Strain-Relief Patterns. *Nature* **1998**. https://doi.org/10.1038/28804.
(174) Günther, C.; Vrijmoeth, J.; Hwang, R. Q.; Behm, R. J. Strain Relaxation in Hexagonally Close-Packed Metal-Metal Interfaces. *Phys. Rev. Lett.* **1995**, *74* (5), 754–757. https://doi.org/10.1103/PhysRevLett.74.754.
(175) Levine, D.; Steinhardt, P. J. Quasicrystals: A New Class of Ordered Structures. *Phys. Rev. Lett.* **1984**, *53* (26), 2477–2480. https://doi.org/10.1103/PhysRevLett.53.2477.
(176) Moras, P.; Theis, W.; Ferrari, L.; Gardonio, S.; Fujii, J.; Horn, K.; Carbone, C. Quasicrystalline Electronic States of a One-Dimensionally Modulated Ag Film. *Phys. Rev. Lett.* **2006**, *96* (15), 156401. https://doi.org/10.1103/PhysRevLett.96.156401.
(177) Rotenberg, E.; Theis, W.; Horn, K.; Gille, P. Quasicrystalline Valence Bands in Decagonal AlNiCo. *Nature* **2000**, *406* (6796), 602–605. https://doi.org/10.1038/35020519.
(178) Gordy, W. A New Method of Determining Electronegativity from Other Atomic Properties.

Phys. Rev. **1946**, *69* (11–12), 604–607. https://doi.org/10.1103/PhysRev.69.604.
(179) Andersen, J. N.; Chorkendorff, I.; Onsgaard, J.; Ghijsen, J.; Johnson, R. L.; Grey, F. Mixed Valence of Sm on Metal Single-Crystal Surfaces. *Phys. Rev. B* **1988**, *37* (9), 4809–4812. https://doi.org/10.1103/PhysRevB.37.4809.
(180) Juel, M.; Samuelsen, B. T.; Kildemo, M.; Raaen, S. Valence Variations of Sm on Polycrystalline Ag. *Surf. Sci.* **2006**, *600* (5), 1155–1159. https://doi.org/10.1016/j.susc.2006.01.010.
(181) Heimann, P.; Neddermeyer, H.; Roloff, H. F. Ultraviolet Photoemission for Intrinsic Surface States of the Noble Metals. *J. Phys. C Solid State Phys.* **1977**, *10* (1), L17–L21. https://doi.org/10.1088/0022-3719/10/1/004.
(182) Kröger, I.; Stadtmüller, B.; Stadler, C.; Ziroff, J.; Kochler, M.; Stahl, A.; Pollinger, F.; Lee, T.-L.; Zegenhagen, J.; Reinert, F.; Kumpf, C. Submonolayer Growth of Copper-Phthalocyanine on Ag(111). *New J. Phys.* **2010**, *12* (8), 083038. https://doi.org/10.1088/1367-2630/12/8/083038.
(183) Stadtmüller, B.; Kröger, I.; Reinert, F.; Kumpf, C. Submonolayer Growth of CuPc on Noble Metal Surfaces. *Phys. Rev. B* **2011**, *83* (8), 085416. https://doi.org/10.1103/PhysRevB.83.085416.
(184) Hermann, K.; Van Hove, M. A. LEEDPat. http://www.fhi-berlin.mpg.de/KHsoftware/LEEDpat/index.html.
(185) Andreev, T.; Barke, I.; Hövel, H. Adsorbed Rare-Gas Layers on Au(111): Shift of the Shockley Surface State Studied with Ultraviolet Photoelectron Spectroscopy and Scanning Tunneling Spectroscopy. *Phys. Rev. B* **2004**, *70* (20), 205426. https://doi.org/10.1103/PhysRevB.70.205426.
(186) Armbrust, N.; Schiller, F.; Güdde, J.; Höfer, U. Model Potential for the Description of Metal/Organic Interface States. *Sci. Rep.* **2017**, *7* (1), 46561. https://doi.org/10.1038/srep46561.
(187) *Visualizing the interface state of PTCDA on Au(111) by scanning tunneling microscopy - IOPscience*. https://iopscience.iop.org/article/10.1088/0957-4484/27/47/475707 (accessed 2022-11-11).
(188) Galbraith, M. C. E.; Marks, M.; Tonner, R.; Höfer, U. Formation of an Organic/Metal Interface State from a Shockley Resonance. *J. Phys. Chem. Lett.* **2014**, *5* (1), 50–55. https://doi.org/10.1021/jz402249b.
(189) Castrillo-Bodero, R.; Blanco-Rey, M.; Ali, K.; Ortega, J. E.; Schiller, F.; Fernández, L. Tuning the Carrier Injection Barrier of Hybrid Metal–Organic Interfaces on Rare Earth-Gold Surface Compounds. *Nanoscale* **2023**. https://doi.org/10.1039/D2NR06440E.
(190) Kröger, I.; Stadtmüller, B.; Kumpf, C. Submonolayer and Multilayer Growth of Titaniumoxide-Phthalocyanine on Ag(111). *New J. Phys.* **2016**, *18* (11), 113022. https://doi.org/10.1088/1367-2630/18/11/113022.
(191) Ueno, N.; Kera, S.; Sakamoto, K.; Okudaira, Koji. K. Energy Band and Electron-Vibration Coupling in Organic Thin Films: Photoelectron Spectroscopy as a Powerful Tool for Studying the Charge Transport. *Appl. Phys. A* **2008**, *92* (3), 495–504. https://doi.org/10.1007/s00339-008-4553-8.
(192) Kera, S.; Yamane, H.; Sakuragi, I.; Okudaira, K. K.; Ueno, N. Very Narrow Photoemission Bandwidth of the Highest Occupied State in a Copper-Phthalocyanine Monolayer. *Chem. Phys. Lett.* **2002**, *364* (1), 93–98. https://doi.org/10.1016/S0009-2614(02)01302-7.
(193) Kera, S.; Yamane, H.; Fukagawa, H.; Hanatani, T.; Okudaira, K. K.; Seki, K.; Ueno, N. Angle Resolved UV Photoelectron Spectra of Titanyl Phthalocynine Monolayer Film on Graphite. *J. Electron Spectrosc. Relat. Phenom.* **2007**, *156–158*, 135–138.

https://doi.org/10.1016/j.elspec.2006.11.016.
(194) Zhang, Y.; Learmonth, T.; Wang, S.; Matsuura, A. Y.; Downes, J.; Plucinski, L.; Bernardis, S.; O'Donnell, C.; Smith, K. E. Electronic Structure of the Organic Semiconductor Vanadyl Phthalocyanine (VO-Pc). *J. Mater. Chem.* **2007**, *17* (13), 1276–1283. https://doi.org/10.1039/B613274J.
(195) Doniach, S.; Sunjic, M. Many-Electron Singularity in X-Ray Photoemission and X-Ray Line Spectra from Metals. *J. Phys. C Solid State Phys.* **1970**, *3* (2), 285. https://doi.org/10.1088/0022-3719/3/2/010.
(196) Shirley, D. A. High-Resolution X-Ray Photoemission Spectrum of the Valence Bands of Gold. *Phys. Rev. B* **1972**, *5* (12), 4709–4714. https://doi.org/10.1103/PhysRevB.5.4709.
(197) Zhang, Y.; Wang, S.; Demasi, A.; Reid, I.; Piper, L. F. J.; Matsuura, A. Y.; Downes, J. E.; Smith, K. E. Soft X-Ray Spectroscopy Study of Electronic Structure in the Organic Semiconductor Titanyl Phthalocyanine (TiO-Pc). *J. Mater. Chem.* **2008**, *18* (15), 1792–1798. https://doi.org/10.1039/B717224A.
(198) Xiao, J.; Dowben, P. A. Changes in the Adsorbate Dipole Layer with Changing D-Filling of the Metal (II) (Co, Ni, Cu) Phthalocyanines on Au(111). *J. Phys. Condens. Matter* **2008**, *21* (5), 052001. https://doi.org/10.1088/0953-8984/21/5/052001.
(199) Borghetti, P.; El-Sayed, A.; Goiri, E.; Rogero, C.; Lobo-Checa, J.; Floreano, L.; Ortega, J. E.; De Oteyza, D. G. Spectroscopic Fingerprints of Work-Function-Controlled Phthalocyanine Charging on Metal Surfaces. *ACS Nano* **2014**, *8* (12), 12786–12795. https://doi.org/10.1021/nn5060333.
(200) Kim, J. W.; Kim, A. Absolute Work Function Measurement by Using Photoelectron Spectroscopy. *Curr. Appl. Phys.* **2021**, *31*, 52–59. https://doi.org/10.1016/j.cap.2021.07.018.
(201) Helander, M. G.; Greiner, M. T.; Wang, Z. B.; Lu, Z. H. Pitfalls in Measuring Work Function Using Photoelectron Spectroscopy. *Appl. Surf. Sci.* **2010**, *256* (8), 2602–2605. https://doi.org/10.1016/j.apsusc.2009.11.002.
(202) Koch, N. Energy Levels at Interfaces between Metals and Conjugated Organic Molecules. *J. Phys. Condens. Matter* **2008**, *20* (18), 184008. https://doi.org/10.1088/0953-8984/20/18/184008.
(203) Yan, L.; Watkins, N. J.; Zorba, S.; Gao, Y.; Tang, C. W. Thermodynamic Equilibrium and Metal-Organic Interface Dipole. *Appl. Phys. Lett.* **2002**, *81* (15), 2752–2754. https://doi.org/10.1063/1.1512826.
(204) Witte, G.; Lukas, S.; Bagus, P. S.; Wöll, C. Vacuum Level Alignment at Organic/Metal Junctions: "Cushion" Effect and the Interface Dipole. *Appl. Phys. Lett.* **2005**, *87* (26), 1–3. https://doi.org/10.1063/1.2151253.
(205) Goiri, E.; Borghetti, P.; El-Sayed, A.; Ortega, J. E.; de Oteyza, D. G. Multi-Component Organic Layers on Metal Substrates. *Adv. Mater.* **2016**, *28* (7), 1340–1368. https://doi.org/10.1002/adma.201503570.
(206) Ziroff, J.; Gold, P.; Bendounan, A.; Forster, F.; Reinert, F. Adsorption Energy and Geometry of Physisorbed Organic Molecules on Au(111) Probed by Surface-State Photoemission. *Surf. Sci.* **2009**, *603* (2), 354–358. https://doi.org/10.1016/j.susc.2008.11.019.
(207) Yamane, H.; Kosugi, N. Site-Specific Organic/Metal Interaction Revealed from Shockley-Type Interface State. *J. Phys. Chem. C* **2016**, *120* (42), 24307–24313. https://doi.org/10.1021/acs.jpcc.6b09207.
(208) Liu, Y.; Guo, J.; Zhu, E.; Liao, L.; Lee, S.-J.; Ding, M.; Shakir, I.; Gambin, V.; Huang, Y.; Duan, X. Approaching the Schottky–Mott Limit in van Der Waals Metal–Semiconductor Junctions. *Nature* **2018**, *557* (7707), 696–700. https://doi.org/10.1038/s41586-018-0129-8.
(209) Torrente, I. F.; Franke, K. J.; Pascual, J. I. Spectroscopy of C60 Single Molecules: The Role

of Screening on Energy Level Alignment. *J. Phys. Condens. Matter* **2008**, *20* (18), 184001. https://doi.org/10.1088/0953-8984/20/18/184001.
(210) Risteska, A.; Knipp, D. Organic Ambipolar Transistors and Circuits. In *Handbook of Visual Display Technology*; Chen, J., Cranton, W., Fihn, M., Eds.; Springer International Publishing: Cham, 2016; pp 971–995. https://doi.org/10.1007/978-3-319-14346-0_177.
(211) Kanagasekaran, T.; Shimotani, H.; Shimizu, R.; Hitosugi, T.; Tanigaki, K. A New Electrode Design for Ambipolar Injection in Organic Semiconductors. *Nat. Commun.* **2017**, *8* (1), 999. https://doi.org/10.1038/s41467-017-01047-9.
(212) Bisri, S. Z.; Takenobu, T.; Yomogida, Y.; Shimotani, H.; Yamao, T.; Hotta, S.; Iwasa, Y. High Mobility and Luminescent Efficiency in Organic Single-Crystal Light-Emitting Transistors. *Adv. Funct. Mater.* **2009**, *19* (11), 1728–1735. https://doi.org/10.1002/adfm.200900028.
(213) Gargiani, P.; Rossi, G.; Biagi, R.; Corradini, V.; Pedio, M.; Fortuna, S.; Calzolari, A.; Fabris, S.; Cezar, J. C.; Brookes, N. B.; Betti, M. G. Spin and Orbital Configuration of Metal Phthalocyanine Chains Assembled on the Au(110) Surface. *Phys. Rev. B* **2013**, *87* (16).
(214) Stepanow, S.; Honolka, J.; Gambardella, P.; Vitali, L.; Abdurakhmanova, N.; Tseng, T.-C. C.; Rauschenbach, S.; Tait, S. L.; Sessi, V.; Klyatskaya, S.; Ruben, M.; Kern, K. Spin and Orbital Magnetic Moment Anisotropies of Monodispersed Bis (Phthalocyaninato) Terbium on a Copper Surface. *J. Am. Chem. Soc.* **2010**, *132* (34), 11900–11901. https://doi.org/10.1021/ja105124r.
(215) Hellerstedt, J.; Cahlík, A.; Švec, M.; Torre, B. de la; Moro-Lagares, M.; Chutora, T.; Papoušková, B.; Zoppellaro, G.; Mutombo, P.; Ruben, M.; Zbořil, R.; Jelinek, P. On-Surface Structural and Electronic Properties of Spontaneously Formed Tb_2Pc_3 Single Molecule Magnets. *Nanoscale* **2018**, *10* (33), 15553–15563. https://doi.org/10.1039/C8NR04215B.
(216) Deng, Z.; Rauschenbach, S.; Stepanow, S.; Klyatskaya, S.; Ruben, M.; Kern, K. Self-Assembly of Bis(Phthalocyaninato)Terbium on Metal Surfaces. *Phys. Scr.* **2015**, *90*, 098003. https://doi.org/10.1088/0031-8949/90/9/098003.
(217) Vitali, L.; Fabris, S.; Conte, A. M.; Brink, S.; Ruben, M.; Baroni, S.; Kern, K. Electronic Structure of Surface-Supported Bis(Phthalocyaninato) Terbium(III) Single Molecular Magnets. *Nano Lett.* **2008**, *8* (10), 3364–3368. https://doi.org/10.1021/nl801869b.
(218) Komeda, T.; Isshiki, H.; Liu, J.; Katoh, K.; Yamashita, M. Variation of Kondo Temperature Induced by Molecule–Substrate Decoupling in Film Formation of Bis(Phthalocyaninato)Terbium(III) Molecules on Au(111). *ACS Nano* **2014**, *8* (5), 4866–4875. https://doi.org/10.1021/nn500809v.
(219) Schwöbel, J.; Fu, Y.; Brede, J.; Dilullo, A.; Hoffmann, G.; Klyatskaya, S.; Ruben, M.; Wiesendanger, R. Real-Space Observation of Spin-Split Molecular Orbitals of Adsorbed Single-Molecule Magnets. *Nat. Commun.* **2012**, *3* (1), 953. https://doi.org/10.1038/ncomms1953.
(220) Mannini, M.; Bertani, F.; Tudisco, C.; Malavolti, L.; Poggini, L.; Misztal, K.; Menozzi, D.; Motta, A.; Otero, E.; Ohresser, P.; Sainctavit, P.; Condorelli, G. G.; Dalcanale, E.; Sessoli, R. Magnetic Behaviour of TbPc2 Single-Molecule Magnets Chemically Grafted on Silicon Surface. *Nat. Commun.* **2014**, *5* (1), 4582. https://doi.org/10.1038/ncomms5582.